Stud shear connectors for composite beams.

A thesis submitted to the Department of Engineering

of the University of Warwick for the degree of

Doctor of Philosophy by

Deric John Oehlers.

March 1980

i

Stud shear connectors for composite beams.

A thesis submitted to the Department of Engineering

of the University of Warwick for the degree of

Doctor of Philosophy by

Deric John Oehlers.

March 1980

To my wife and children

SUMMARY

The published results of push tests were analysed statistically in order to determine the main parameters that affect the strength of stud shear connectors. The results of the statistical analysis were used to design a series of seventy-nine push tests. A finite element analysis program was developed which allowed for the interaction between the tensile and compressive failure of concrete and hence predicted the variation in the bearing strength of concrete prisms of varying size and with varying amounts of lateral restraint, when subjected to concentrated loads.

A combination of theoretical and empirical analyses was used to determine the load at which the stud broke, the strength of concrete prisms which were subjected to patch loads of varying size and eccentricity and hence the strength of concrete slabs, the effect of lateral forces and transverse reinforcement on the strength of the stud and the slab, the strength of shear connections in which the reinforcement is looped around the stud and the load-slip curve for a stud shear connection.

CONTENTS

Chapter Eleven CONCLUSIONS

LIST OF TABLES

LIST OF FIGURES

ACKNOWLEDGEMENTS

This research contract was sponsored by the Science Research Council. I would like to thank my supervisor, Professor R. P. Johnson, for his guidance, criticism and encouragement.

NOTATION

A_c area of concrete prism, l_c X h_t

A_m transformed area of splitting zone, concrete prism or shear plane

A_p area of patch load, b_a X h_a

A_r cross-sectional area of a group of transverse reinforcement; area of reinforcement crossing the shear plane

A_s cross-sectional area of the shank of the stud

A_{sh} area of the shear plane

A_{sp} area of splitting zone

A_w cross-sectional area of the weld collar

a_b angle of crack

a_c angle between the local and global co-ordinate systems

B regression coefficient

b_a width of applied load

b_c effective width of slab; diameter of concrete cylinder

b_d effective width of a double strip load; effective width of a group

b_t total width of slab

C correlation coefficient; concrete split

c_b minimum cover to transverse reinforcement at the bottom of the slab

D_g elasticity matrix in the global co-ordinate system

D_l elasticity matrix in the local co-ordinate system

d_s diameter of the shank of the stud; diameter of a reinforcing bar

d_w diameter of the weld collar

E_c isotropic modulus of elasticity of concrete; tangent modulus of elasticity of concrete

E_s modulus of elasticity of steel

E_x modulus of elasticity of an orthotropic concrete in a direction parallel to the x axis

E_y modulus of elasticity of an orthotropic concrete in a direction parallel to the y axis

e strain

e_l longitudinal compressive failure strain of concrete

e_t lateral tensile failure strain of concrete

e_x strain in a direction parallel to the x axis

e_y strain in a direction parallel to the y axis

F normal force

F_b force in the reinforcement behind the stud

F_f force in the reinforcement in front of the stud

F_l lateral tensile force at the experimental failure load

F_{sh} yield strength of reinforcement crossing the shear plane

F_t yield strength of transverse reinforcement in the splitting zone

f stress; lateral stress

f_a axial stress

f_b mean bearing stress

f_{ca} cube strength of concrete cured in air

f_{cc} compressive strength of an unrestrained concrete element, $0.4E_c e_l$

f_{ct} split tensile strength of concrete cured in water

f_{cu} cube strength of concrete cured in water

f_{cy} cylinder strength of concrete

f_f maximum flexural stress

f_g lateral global stress; mean lateral stress between strip loads

f_l lateral stress in concrete induced by laterally applied forces

f_m maximum lateral stress induced by concentrated loads

f_{md} modulus of rupture strength

f_{rt} amount of transverse reinforcement; percentage of transverse reinforcement in the slab

f_{ru} ultimate tensile strength of the reinforcement

f_{ry} yield strength of transverse reinforcement

f_{su} ultimate tensile strength of the stud

f_{sy} yield strength of the stud

f_t tensile strength of concrete

f_X stress in direction parallel to the X axis

f_x stress in direction parallel to the x axis

f_Y stress in direction parallel to the Y axis; laterally applied stress

f_y stress in direction parallel to the y axis

G modulus of shear

h_a depth of patch load

h_c thickness of the concrete slab; effective depth of prism

h_f height of failure zone measured from the flange

h_r height of transverse reinforcement

h_s height of stud; effective height of stud

h_{sh} height of shank

h_t depth of prism

h_w height of weld collar

K_a change in shear strength with axial load

K_d total lateral tensile force / longitudinally applied load

K_e change in the shear strength with the concrete stiffness

K_f change in the shear strength with the cube strength

K_h change in the shear strength with the height of the shank

K_l change in the shear strength with the length of the slab

K_s mean lateral tensile stress over the splitting zone / maximum lateral tensile stress

K_{sp} K_s/K_d

K_w change in the shear strength with the height of the weld collar

K_Y increase in strength due to eccentricity along the Y axis

K_Z increase in strength due to eccentricity along the Z axis

L reinforcement looped around the stud

L_g lateral global force

l distance from the bearing surface; distance from the discontinuity in the shear flow; distance from the maximum lateral stress; studs longitudinally spaced

l_b length of slab behind the stud or concentrated load

l_c length of concrete cylinder or prism; length of slab in front of the stud or concentrated load

l_m distance from the bearing surface to the maximum lateral tensile stress

l_p distance from the centre of the stud to the base of the push specimen; effective length of the slab; shear span

l_r distance from the transverse reinforcement to the stud

l_s distance from the base of the stud measured along the axis of the stud

l_t lateral distance from the line of action of the applied load

l_z length of the splitting zone

n aggregate interlock factor; number of independent variables

P concentrated load

P_a axial load at the base of the stud

P_{cp} load at which the concrete fails in compression

P_e experimentally determined maximum shear strength of a stud; experimentally determined load; maximum experimental load

P_{ea} experimentally determined maximum axial load

P_{sg} theoretical splitting strength of a single strip load

P_{sh} maximum theoretical shear strength; shank failure load

P_{sp} splitting strength of an unreinforced prism / number of studs or strip loads

P_{sr} load at which the slab fails in shear

P_{st} theoretical strength of the standard push test

P_u theoretical or empirical ultimate strength

P_Y strength of a hypothetical strip load in which the force is dispersed in the Y direction

P_{yr} load at which the reinforcement fails

P_Z strength of a hypothetical strip load in which the force is dispersed in the Z direction

p probability of occurrence

pf_y yield strength of transverse reinforcement / area of shear plane

q longitudinal shear flow / h_s

q_{xy} shear strain

R slab transversely reinforced

S significance of regression coefficient; shank failed

S_h highly significant

S_n not significant

S_p probably significant

S_s significant

s single stud

s_c internal diameter of the bend of the looped reinforcement

s_p slip

s_r longitudinal spacing of transverse reinforcement

s_s longitudinal spacing of studs or strip loads

T the number of standard errors that the regression coefficient is from zero

T_{xy} shear stress; maximum shear stress

t studs transversely spaced

t_s transverse spacing of studs

U unreinforced

v Poisson's ratio of the isotropic concrete

v_{cu} ultimate shear strength

v_s Poisson's ratio for steel

v_x Poisson's ratio of an orthotropic concrete in a direction parallel to the x axis

v_y Poisson's ratio of an orthotropic concrete in a direction parallel to the y axis

X independent variable; abscissa of global co-ordinate system

x abscissa of local co-ordinate system

Y dependent variable; ordinate of global co-ordinate system; in a direction parallel to the Y axis

y ordinate of local co-ordinate system; direction of maximum tensile strain; in a direction parallel to the y axis

P_{yr}	load at which the reinforcement fails
P_Z	strength of a hypothetical strip load in which the force is dispersed in the Z direction
p	probability of occurrence
pf_y	yield strength of transverse reinforcement / area of shear plane
q	longitudinal shear flow / h_s
q_{xy}	shear strain
R	slab transversely reinforced
S	significance of regression coefficient; shank failed
S_h	highly significant
S_n	not significant
S_p	probably significant
S_s	significant
s	single stud
s_c	internal diameter of the bend of the looped reinforcement
s_p	slip
s_r	longitudinal spacing of transverse reinforcement
s_s	longitudinal spacing of studs or strip loads
T	the number of standard errors that the regression coefficient is from zero
T_{xy}	shear stress; maximum shear stress
t	studs transversely spaced
t_s	transverse spacing of studs
U	unreinforced
v	Poissons ratio of the isotropic concrete
v_{cu}	ultimate shear strength
v_s	Poissons ratio for steel
v_x	Poissons ratio of an orthotropic concrete in a direction parallel to the x axis
v_y	Poissons ratio of an orthotropic concrete in a direction parallel to the y axis
X	independent variable; abscissa of global co-ordinate system
x	abscissa of local co-ordinate system
Y	dependent variable; ordinate of global co-ordinate system; in a direction parallel to the Y axis
y	ordinate of local co-ordinate system; direction of maximum tensile strain; in a direction parallel to the y axis

Chapter One

INTRODUCTION

1.1 SCOPE OF INVESTIGATION

It is standard practice in North America and Europe to determine the properties of stud shear connectors from push tests of the kind shown in Fig. 1.1. However, these tests have also shown that the ultimate strengths are dependant upon several parameters: the thickness of the flange[1], the area of the shank of the stud[2], the height of the stud[3,4], the width of the slab[5], the compressive strength of the concrete[2,6], the stiffness of the concrete[2], the tensile strength of the stud[3,7,8], the amount of transverse reinforcement[5], the position of the studs[9] and the constraints imposed upon the slab[10-13].

The object of this research project was to study the behaviour of studs in push tests, in order that their load-slip curves could be predicted for different values of the above parameters. The behaviour of studs in beams has been inferred, but these results have neither been confirmed experimentally nor by a theoretical analysis of studs in beams.

1.2 SEQUENCE OF RESEARCH

Stud shear connectors fail in four modes:

1. Failure of the shank of the stud.
2. Embedment or pull-out failure.
3. Splitting of the slab.
4. Failure of the slab along planes of maximum shear.

All of these modes are affected by the amount and position of the transverse reinforcement.

Empirically derived rules for the strength of stud shear connectors and the amount of transverse reinforcement are compared in Chapter Two. In Chapter Three the results of push tests are analysed statistically in order to determine the prevalence of the different failure modes and the main parameters which affect the strength; the results of this analysis were used to plan a series of push tests, Chapter Five. The different modes of failure were analysed by using a finite element computer program, Chapter Four. The effect of shear and axial forces on the shank of the stud, Modes 1 and 2, are analysed in Chapter Six and splitting failure in Chapter Seven. The effect of transverse reinforcement and lateral forces on the splitting and shank failure loads are determined in Chapter Eight and the effect of concentrations of reinforcement along the plane of maximum shear in Chapter Nine. In Chapter Ten, load-slip curves are derived which take account of the different methods of failure.

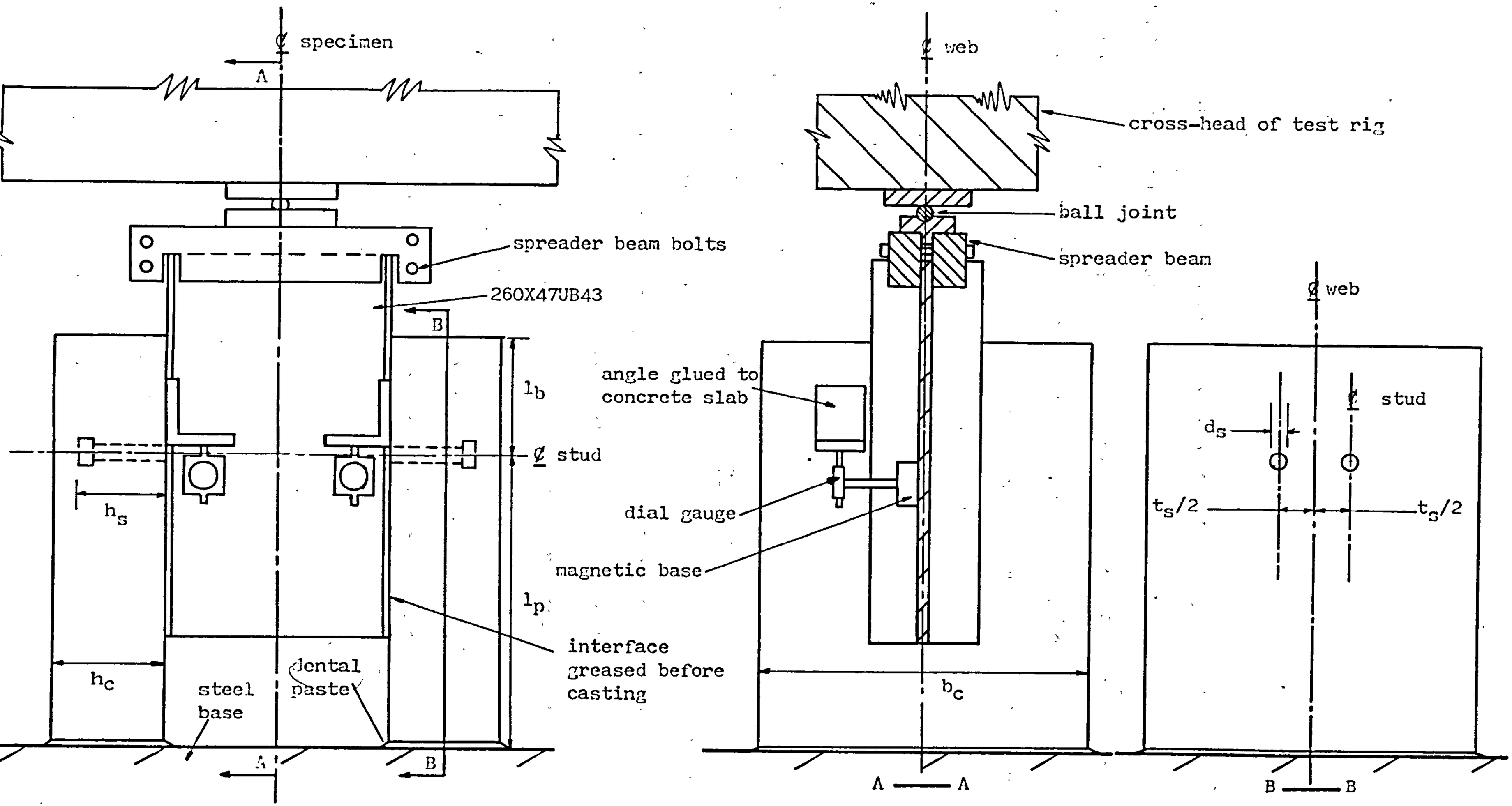

Fig. 1.1 Test rig and push specimen.

Chapter Two

THE STATE OF THE ART

2.1 LITERATURE REVIEW

Viest[14] reviewed the research from 1920 to 1958, Teraszkiewicz[12] up to 1961 and Davies[15] from 1940 to 1966. Chapman[16] discussed the behaviour of composite sections and shear connectors in 1964. Iyengar[17] wrote a comprehensive state of the art, up to 1977, which included a review of literature and also followed the development of design practices throughout the world. Present design practices in Great Britain are fully covered by Johnson and Buckby[18,19] and in the United States of America by the Council of Tall Buildings and Urban Habitat[20].

2.2 STUD SHEAR CONNECTORS

2.2.1 Empirically determined ultimate strengths

A comparison is made in Fig. 2.1 of various empirically derived rules for the ultimate strength, P_u, of a 19X100mm stud in normal density concrete. It is assumed throughout this chapter that the concrete cylinder strength is equal to 85% of the cube strength, f_{cu}, and that the relationship between f_{cu} and the modulus of elasticity of concrete, E_c, is as given by CP110[21]. The units of N and mm will be used throughout this thesis in equations which are dimensionally incorrect.

In 1962 Slutter and Driscoll[3] recommended that

$$P_u = 71.1 d_s^2 f_{cu}^{0.5} \leqslant A_s f_{su} \qquad (2.1)$$

when $f_{cu} \leqslant 28\ N/mm^2$ and $h_s/d_s > 4.2$

$$\text{or} \quad P_u = 16.8 h_s d_s f_{cu}^{0.5} \leqslant A_s f_{su} \qquad (2.2)$$

when $f_{cu} \leqslant 28\ N/mm^2$ and $h_s/d_s < 4.2$

where d_s = diameter of the shank of the stud

A_s = cross-sectional area of the shank of the stud

f_{su} = ultimate tensile strength of the stud

h_s = height of the stud

It was assumed in CP117:1965[8] that there was a linear variation between P_u and f_{cu} provided that the yield strength of the stud, f_{sy}, was greater than 386 N/mm^2 and f_{su} was greater than 494 N/mm^2.

In 1971 Ollgaard, Slutter and Fisher[2] determined that

$$P_u = 1.74 A_s f_{cu}^{0.3} E_c^{0.44} \qquad (2.3)$$

and proposed the following simplified relationship

$$P_u = 0.46 A_s (f_{cu} E_c)^{0.5} \qquad (2.4)$$

with an upper bound to the connector strength at

$$(f_{cu} E_c)^{0.5} = 974$$

In 1971 Menzies[6] suggested that CP117[8] overestimated the strength and proposed the reduced values given in the Bridge Code[7], which uses the same recommendation as CP117[8] for the strength of the stud material.

In 1975 deVries and Stark[22] found that the strength became constant at high concrete strengths

$$P_u \leqslant 0.7 A_s f_{su} \qquad (2.5)$$

The draft European recommendations[23], 1978, give the strength as Equ. 2.4 with the upper bound as Equ. 2.5 for studs with $h_s/d_s \geqslant 4.2$.

The range of strengths given by the above relationships is clearly shown in Fig. 2.1. It will be shown in Chapters Six, Seven and Eight that this is due to the different parameters, Sect. 1.1, and modes of failure, Sect. 1.2, of the push tests.

2.2.2 Theoretical analyses

Gogoi[24] analysed a stud as a cantilever in an elastic foundation and Van Dalen[25] assumed it to be pinned at the base. Van Dalen[25] used the results, Figs. 2.2 and 2.3, to show the ability of a stud to transmit increasing shear loads as a plastic hinge is formed around the flange-shank interface. The results are compared in Chapter Six with that of a finite element analysis.

2.3 TRANSVERSE REINFORCEMENT

A comparison is made in Fig. 2.4 of design rules which give the ultimate shear strength of the concrete, v_{cu}, in terms of the strength of transverse reinforcement per unit area of shear plane, pf_y. It is assumed, in the comparison, that $f_{cu} = 30\ N/mm^2$ and that there is a single row of studs.

It is stated in CP117:1965[8] that the shear strength is dependent upon the strength of the concrete and transverse reinforcement

$$v_{cu} = 0.233f_{cu}^{0.5} + pf_y \qquad (2.6)$$

with an upper bound which is dependent on the strength of the concrete

$$v_{cu} \not> 0.623f_{cu}^{0.5} \qquad (2.7)$$

with a further proviso for a minimum amount of reinforcement at the bottom of the slab

$$pf_y' > 0.5pf_y \qquad (2.8)$$

where pf_y' is derived from the amount of bottom steel only.

The shear friction theory proposed by Birkeland[26] and Mast[27], 1968, assumed that the coefficient of friction across a crack in a shear plane

was 1.4 and that the normal force across the crack was pf_y.

$$v_{cu} = 1.4pf_y \qquad (2.9)$$

when $pf_y \leqslant 0.13f_{cu}$.

In 1969 Davies[28] developed empirical rules which were derived from the first appearance of splitting in composite beams.

$$v_{cu} = 0.354f_{cu}^{0.5} + 1.2pf_y \qquad (2.10)$$

In 1969 Hofbeck, Ibrahim and Mattock[29] determined the ultimate shear that could be transferred across a cracked plane

$$v_{cu} = 1.96 + 0.8pf_y \qquad (2.11)$$

The first term is the shear strength due to aggregate interlock and dowel action and the second due to friction across the plane. They found that there was an upper limit to this linear variation which depended upon the compressive strength of the concrete, beyond which the shear plane acted as uncracked.

In 1972 Mattock and Hawkins[30] proposed a lower bound to Equ. 2.11,

$$v_{cu} = 1.38 + 0.8pf_y \qquad (2.12)$$

with a maximum shear strength of

$$v_{cu} = 0.25f_{cu} \qquad (2.13)$$

and a minimum amount of reinforcement

$$pf_y \geqslant 1.38 \text{ N/mm}^2$$

In 1969 Johnson[31,32] concluded that CP117 was unduly conservative and in 1975[18] proposed a new ultimate strength design method based on

the work of Mattock and Hawkins, Equs. 2.12 and 2.13. These rules are now used in the Bridge Code[7], the draft European recommendations[23] and in the United States of America[20] and can therefore be considered to supersede all previous design rules. They are, however, not applicable to regions of high concentrations of reinforcement, i.e. when $v_{cu} > 0.25f_{cu}$, Equ. 2.13. The transfer of shear in these regions is analysed in Chapter Nine.

2.4 DISCUSSION

It will be shown in the statistical analysis, Chapter 3, that the variation due to the experimental error, coefficient of variation of 7.9%, is considerably smaller than the variation between each series of experimental results, Fig. 2.1; the latter must therefore be due to the different parameters and restraints, Sect. 1.1, and modes of failure, Sect. 1.2, of the push tests. No attempt has therefore been made to compare each series of push tests directly, instead, the results were analysed statistically as a whole and only parameters which could be quantified were included in the analysis, Table 3.1; hence only the results of push tests which were fully restrained at the base and made of normal density concrete were used. In compiling the list of parameters, it was found that most research workers only considered as important the compressive strength of the concrete and the cross-sectional area of the stud. The height of the weld collar was never measured, the tensile strength of the concrete and that of the stud and the stiffness of the concrete were rarely measured and the transverse reinforcement was seldom fully anchored and the amount and position rarely stated; although most of these parameters were kept constant during a series of tests the effect they had on the magnitude of the strengths could not be determined. The mode of failure

was rarely stated posibly because it is difficult to distinguish between splitting and shank failure in a laterally reinforced specimen. If splitting occurs first then the two sides of the slab are held together by the reinforcement and hence the load reduces as the concrete crushes, due to the reduced lateral restraint, until the shank breaks; the maximum strength is therefore determined by the splitting strength although failure would appear to have been caused by the stud breaking. The distinction may have been more obvious if the falling branch of the load-slip curve had been determined by applying increasing displacements instead of applying increasing loads which was the usual procedure.

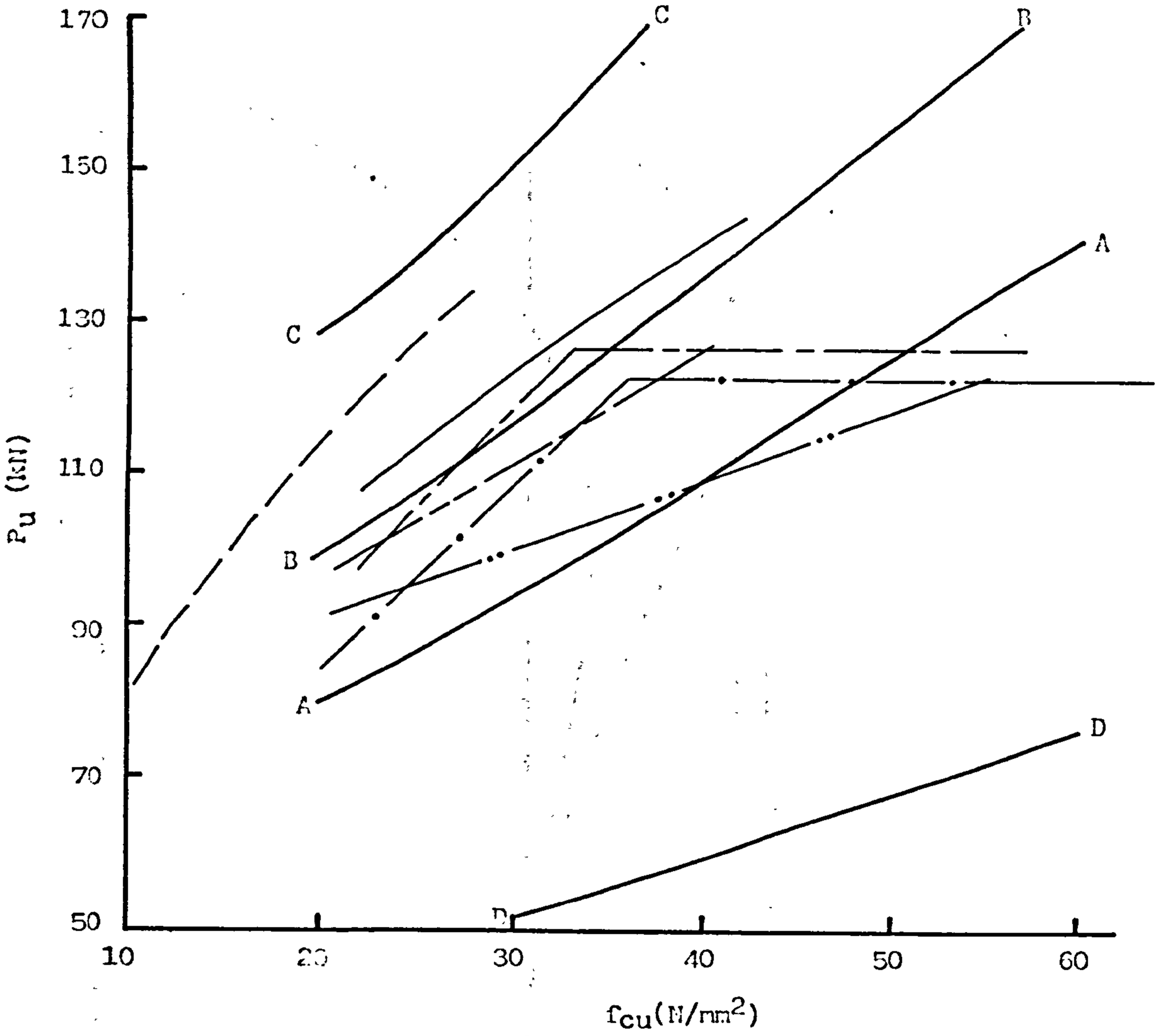

Slutter and Driscoll, Equ. 2.1
CP117, Ref. 8
Ollgaard, Slutter, Fisher, Equ. 2.3
Ollgaard, Slutter, Fisher, Equ. 2.4
Menzies, Ref. 6
Draft European recommendations, assumes f_{su} = 620 N/mm^2, Ref. 23

A ——— A Equ. 6.2, f_{su} = 500 N/mm^2
B ——— B Equ. 6.2, f_{su} = 620 N/mm^2
C ——— C Upper bound to push tests
D ——— D Lower bound to push tests

Fig. 2.1 Strength of 19X100mm studs in normal density concrete.

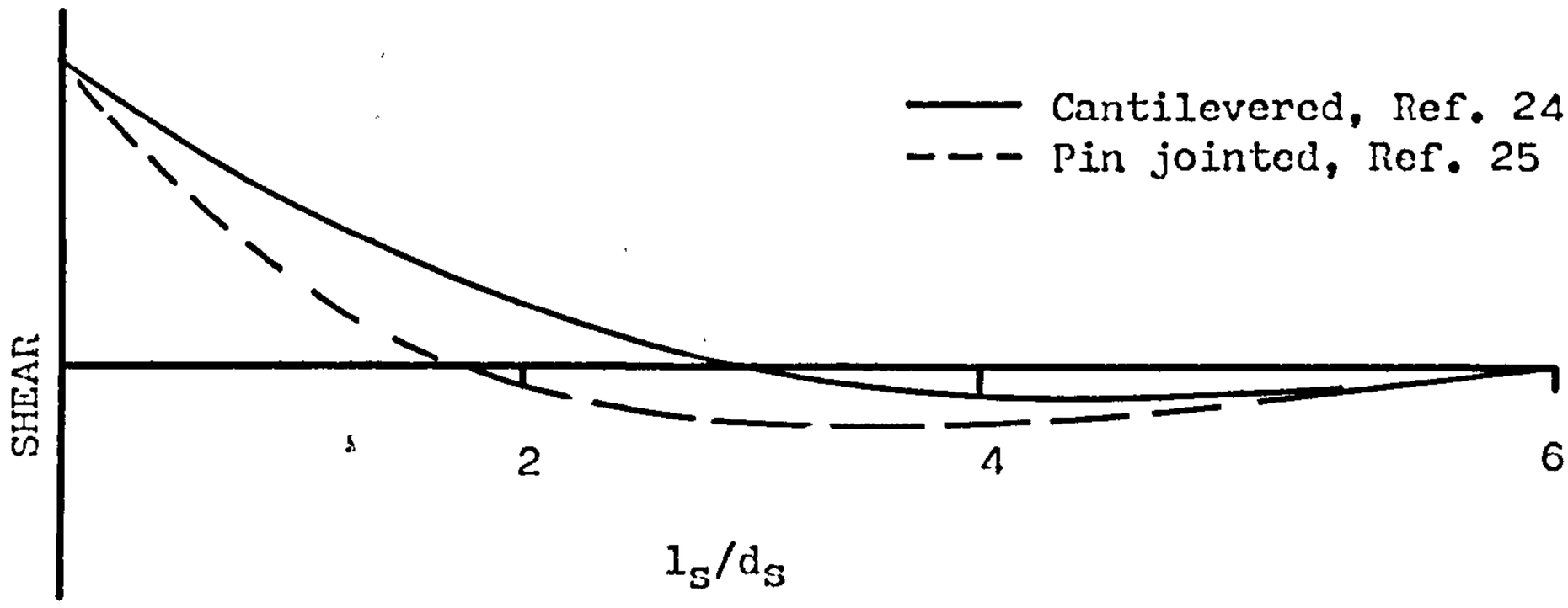

Fig. 2.2 Theoretical distribution of shear along the shank.

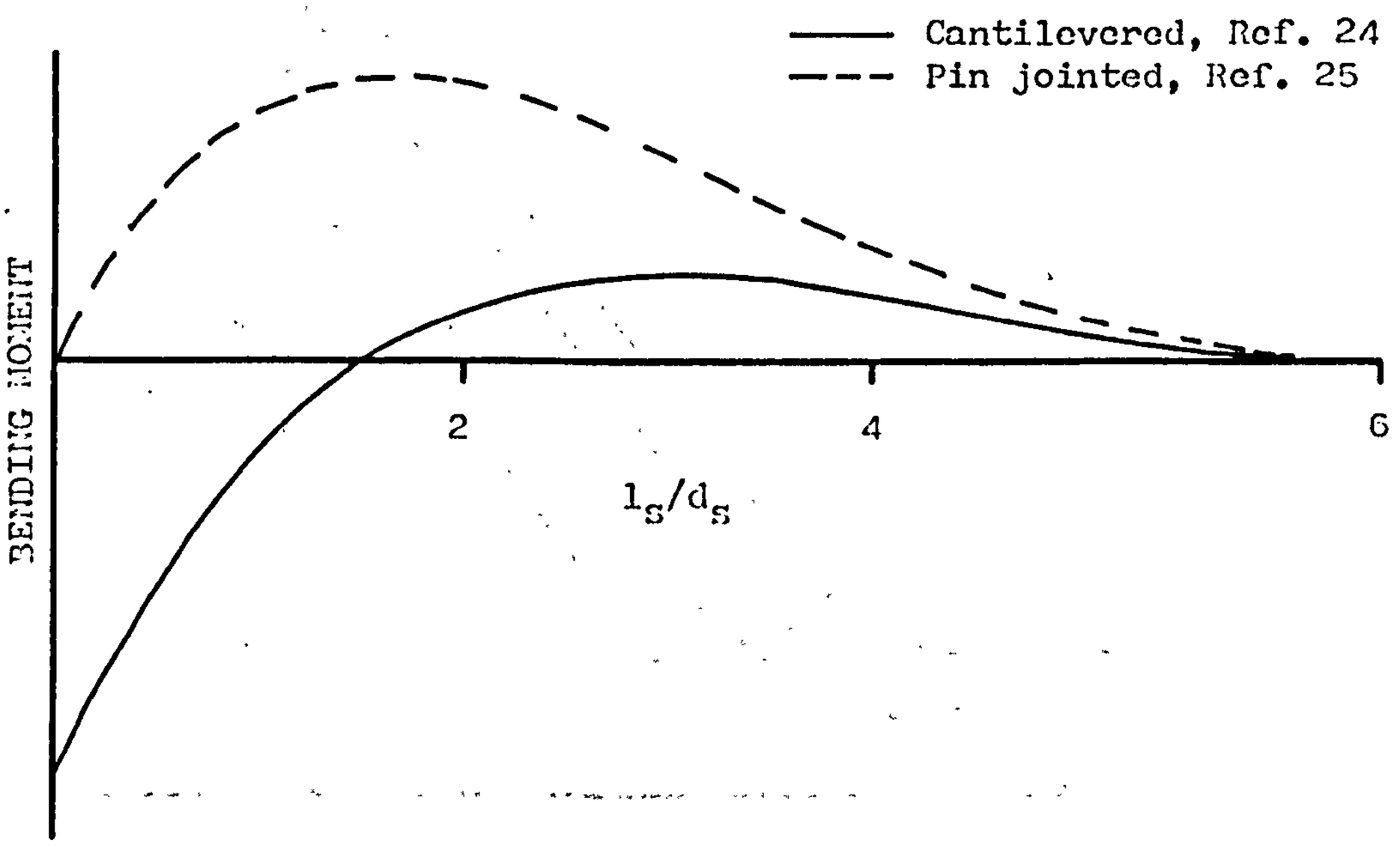

Fig. 2.3 Theoretical distribution of the bending moments along the shank.

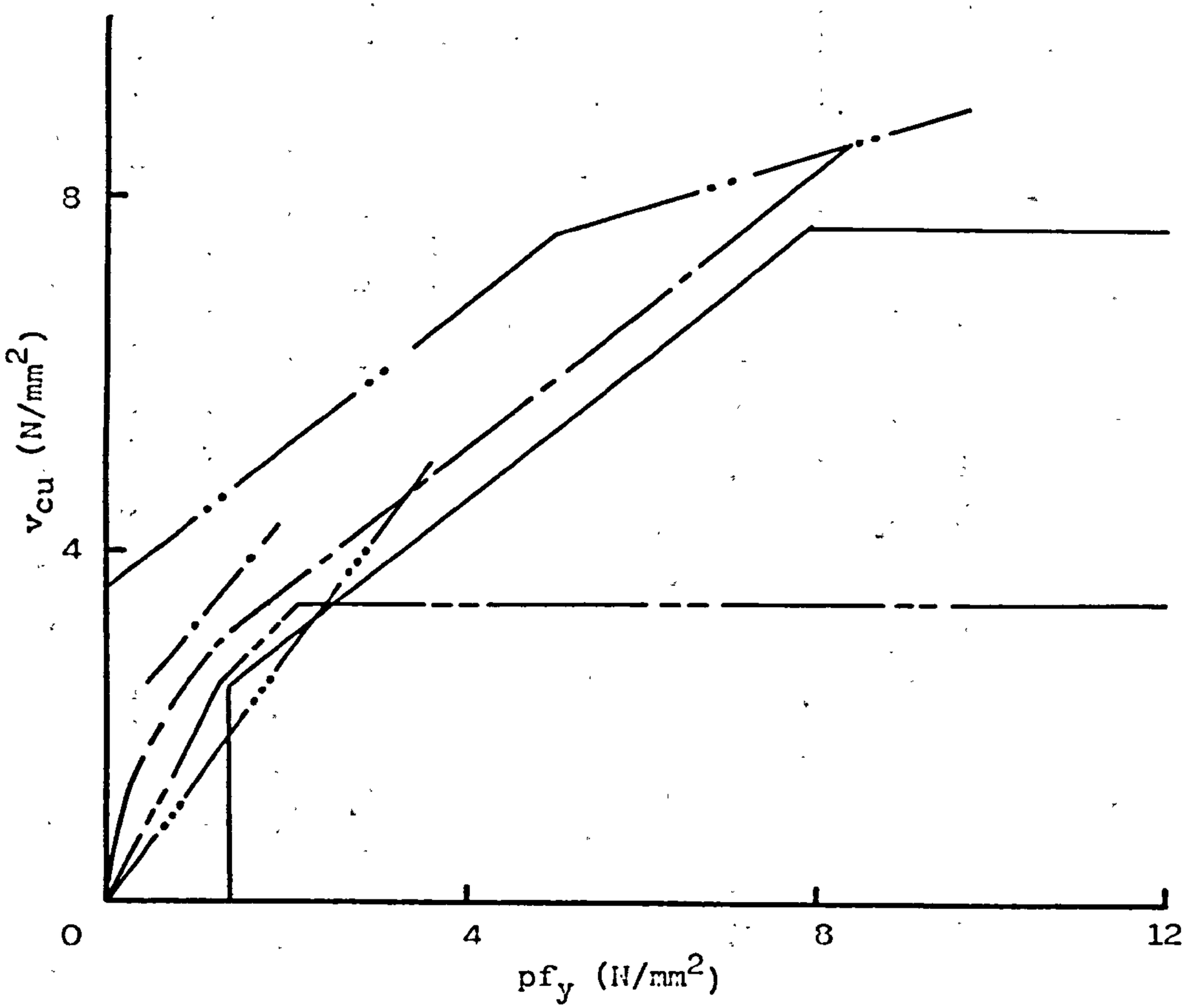

Fig. 2.4 Empirical rules for transverse reinforcement.

Chapter Three

A STATISTICAL ANALYSIS OF PUSH TESTS

3.1 INTRODUCTION

One hundred and twenty-five push tests have been analysed statistically in order to determine the main parameters which affect the maximum strength of stud shear connectors. The strengths and properties of the push tests are given in Sect. 3.2, a statistical computer program is described in Sect. 3.3, and the statistical analysis is described in Sect. 3.4.

3.2 PUSH TESTS

The statistical analysis was restricted to specimens of the type shown in Figs. 1.1, 3.1 and 3.2 whose slabs were made from aggregate of normal density. There was only enough information to describe the following parameters of the specimen, Table 3.1.

Thickness of the concrete slab, h_c, (Fig. 1.1).

Effective length of the slab, l_p, (Figs. 1.1 and 3.1).

Effective width of the slab, b_c, (Figs. 1.1 and 3.2). When the slab was haunched, the effective width was assumed to be equal to the minimum width of the slab.

Height of the stud, h_s, (Fig. 1.1).

Diameter of the shank of the stud, d_s, (Fig. 1.1).

Transverse spacing of the studs, t_s, (Fig. 1.1). When there were single studs, the transverse spacing was assumed to be equal to zero.

Cube strength of the concrete cured in water, f_{cu}. When the cylinder strength of the concrete, f_{cy}, was only given, it was assumed that $f_{cu} = 1.18 f_{cy}$.

Cube strength of concrete cured in air, f_{ca}.

Split tensile strength of the concrete, f_{ct}.

The above parameters were used as the independent variables in the statistical regression analysis; the dependent variable being the maximum experimental load, P_e. No attempt was made to quantify the amount of transverse reinforcement, f_{rt}, as it was considered to be dependent upon such parameters as the position, strength and anchorage, the values of which were indeterminate. Instead, the specimens have been classified as reinforced, R, or unreinforced, U, and placed in groups in which the reinforcement is constant.

3.3 REGRESSION ANALYSIS COMPUTER PROGRAM

A computer program has been developed which uses the standard mathematical procedures, described by Davies[43], to minimize the residual variance about the regression. The program functions in three modes: multi-variable linear regression analysis, curvilinear regression analysis and a multi-variable curvilinear regression analysis.

3.3.1 Multi-variable linear regression analysis

The dependent variable, Y, is assumed to be a linear function of several independent variables, X,

$$Y = f(X_1, X_2, \ldots, X_n) \qquad (3.1)$$

$$\text{i.e. } Y = B_0 + B_1X_1 + B_2X_2 + \ldots + B_nX_n$$

where the regression coefficients are B and n is the number of independent variables. The program analyses the data n times, increasing the number of independent variables from one to n and including them in the order in which they are input, Equ. 3.1.

A thorough regression analysis requires that all combinations of the independent variables are tested in order to find the best fit. Since this is impracticable, combinations of variables were tested and those which were the most significant and least related to the other independent variables, were used in further combinations to test the significance of other variables.

The significance of a regression coefficient was determined by calculating the number of standard errors of the regression coefficient from zero, T. The relationship between independent variables, X_1 and X_2, was determined from their correlation coefficient, $C[\overline{X}_1, X_2]$. It was assumed that these statistics were not significant, S_n, when the probability of occurrence, p, was greater than 0.05, that they were probably significant, S_p, when $p < 0.05$ and $p > 0.01$, that they were significant, S_s, when $p < 0.01$ and $p > 0.001$, and that they were highly significant, S_h, when $p < 0.001$.

3.3.2 Curvilinear regression analysis

The dependent variable is assumed to be a linear function of powers of one independent variable, i.e.

$$Y = B_0 + B_1X + B_2X^2 + \ldots + B_nX^n$$

The analysis is the same as that of the multi-variable linear regression, each power being treated as an independent variable, except that the correlation coefficient will always be highly significant as the powers are directly related.

3.3.3 Multi-variable curvilinear regression analysis

The dependent variable is assumed to be a linear function of powers of several independent variables, such as

$$Y = B_0 + B_1X_1 + B_2X_1^2 + B_3X_1^3 + B_4X_2 + B_5X_2^2 + \ldots\ldots$$

The analysis is similar to that of the curvilinear regression analysis except that as each variable is included the significance is tested and if it did not reach a specified value that variable would be excluded.

3.4 STATISTICAL ANALYSIS

The analysis consisted of determining the significance of the independent variables, comparing different types of statistical regressions, an analysis of the variance and an analysis of the different modes of failure.

3.4.1 Significance of variables

The significance of the independent variables was determined by analysing different groups of variables as multi-variable linear regressions.

The following relation, which contained the variables which were thought to be most important, was first analysed.

$$P_e = f(d_s, b_c, h_c, f_{ct}, h_s)$$

When f_{ct} had not been measured, Table 3.1, the following empirical relationships[6,33] were assumed.

$$f_{cu} = 1.2f_{ca}$$

$$f_{ct} = 0.92 + 0.06f_{cu}$$

Three of the regressions which were analysed are given below.

$$P_u = -89 + 8.2d_s + 0.054b_c + 0.13h_c \qquad (3.2)$$

T: 12.3 5.0 2.3

S_h S_h - S_p

$$P_u = -98 + 7.9d_s + 0.052b_c + 0.11h_c + 4.7f_{ct} \qquad (3.3)$$

T: 12.0 4.8 2.0 2.2

S_h S_h S_p S_p

$$P_u = -100 + 7.7d_s + 0.049b_c + 0.08h_c + 3.3f_{ct} + 0.18h_s \qquad (3.4)$$

T: 11.4 4.5 1.4 1.4 1.4

S_h S_h S_n S_n S_n

$$C\,\underline{/}\bar{d}_s, h_c\underline{\_}\bar{/} = 0.2(S_p)$$

$$C\,\underline{/}\bar{d}_s, h_s\underline{\_}\bar{/} = -0.25(S_s)$$

$$C\,\underline{/}\bar{h}_c, h_s\underline{\_}\bar{/} = -0.33(S_h) \qquad C\,\underline{/}\bar{f}_{ct}, h_s\underline{\_}\bar{/} = -0.42(S_h)$$

The statistics of Equs. 3.2 and 3.3 showed that there was no significant correlation between the independent variables and that d_s and b_c were highly significant and h_c and f_{ct} were probably significant.

The inclusion of h_s, Equ. 3.4, was not only found to be not significant but caused h_c and f_{ct} to become not significant, while d_s and b_c remained highly significant. It was also found that h_s had a highly significant correlation with h_c and f_{ct}. The problem was therefore to determine which of the independent variables, f_{ct}, h_c and h_s, really caused a change in P_e. There was a significant correlation between d_s and h_s and since d_s had already been found to be highly significant it was assumed that h_s did not have any real effect on P_e. It was therefore concluded that the reduction in the significance of h_c and f_{ct} was due to their correlation with h_s, i.e. the properties of the specimens were altered

in such a manner that an increase in h_s was accompanied by a reduction in f_{ct} and h_c, and that h_s was not significant.

The effect of t_s and l_p was determined from an analysis of the following relations.

$$P_u = f(t_s, d_s, b_c, h_c, f_{ct}, h_s)$$

$$P_u = f(d_s, f_{ct}, b_c, h_c, l_p)$$

It was found that t_s and l_p were not significant in all of the combinations.

The following relation was analysed in order to determine the significance of f_{cu}.

$$P_e = f(f_{cu}, d_s, b_c, h_c) \qquad (3.5)$$

The result was

$$P_u = -94 + 7.9d_s + 0.052b_c + 0.12h_c + 0.26f_{cu} \qquad (3.6)$$

T:	12.0	4.8	2.1	1.9
	S_h	S_h	S_p	S_n

Residual variance = 406 kN^2

A similar analysis using f_{ct} instead of f_{cu}, Equ. 3.3, gave a residual variance of 402 $(kN)^2$. A comparison of the residual variances of Equs. 3.3 and 3.6 showed that the difference was not significant.

The change in the significance of f_{cu} with d_s was determined by analysing $P_e = f(f_{cu})$ for constant values of d_s.

when d_s = 13mm $\quad P_u = 55 + 0.033f_{cu}$ (3.7)

T:	0.43
	S_n

when d_s = 16mm $\quad P_u = 31 + 1.34f_{cu}$ (3.8)

T:	2.69
	S_s

when $d_s = 19mm$ $P_u = 81 + 0.54f_{cu}$ (3.9)

T: 2.09

S_p

The results are plotted in Figs. 3.4 to 3.6 with the variations given by the Bridge Code[7] and CP117[8]. The regressions and variations are in general agreement, although the scatter can be very large. The results are further discussed in Sect. 3.4.4.

3.4.2 Regression functions

A comparison has been made of different types of regressions based on the four independent variables f_{cu}, d_s, b_c and h_c, Equ. 3.5.

3.4.2.1 Multi-variable linear regression

The scatter of the experimental results about the regression, Equ. 3.6, is shown in Fig. 3.3. The lower-bound 90% confidence limit occurs at $0.65P_u$.

3.4.2.2 Multi-variable curvilinear regression

The following relation was analysed at two levels of significance.

$$P_e = f(d_s, d_s^2, d_s^3, f_{cu}, f_{cu}^2, f_{cu}^3, b_c, b_c^2, b_c^3, h_c, h_c^2, h_c^3)$$

When only variables which were highly significant were included then

$$P_u = -41 + 7.6d_s + 0.039b_c + 2.1 \times 10^{-4}b_c^2 - 0.23 \times 10^{-6}b_c^3 \quad (3.10$$

Residual variance = 306 kN^2

when only variables which were significant or highly significant were included then

$$P_u = -92 + 7.3d_s + 2.1f_{cu} - 0.018f_{cu}^2 + 0.034b_c + 1.9 \times 10^{-4}b_c^2 - 0.22 \times 10^{-6}b_c^3 \qquad (3.11)$$

Residual variance = 259 kN^2

A comparison of the residual variances in Equs. 3.6 and 3.11 showed the improvement to be significant. The lower-bound 90% confidence limit of Equ. 3.11 occurred at $0.72P_u$.

3.4.2.3 Logarithmic multi-variable linear regression

The previous regression analyses assumed that the strength changed by a constant amount as an independent variable changed. The following relation assumes that the strength changes by a constant proportion.

$$P_e = B_0\, d_s^{B1} f_{cu}^{B2} b_c^{B3} h_c^{B4}$$

The relation, which was analysed in its logarithmic form as a multi-variable linear regression, gave the following results.

$$P_u = 0.095 d_s^{1.5} f_{cu}^{0.13} b_c^{0.20} h_c^{0.17}$$

T: 15.1 2.4 6.5 2.1

S_h S_p S_h S_p

Residual variance = 339 kN^2

The lower-bound 90% confidence limit occurred at $0.68P_u$. A comparison with the multi-variable linear regression, Equ. 3.6, showed an increase in the significance of all the variables except h_c, which remained the same.

3.4.3 Analysis of the variance

The residual variance about the regressions, Sect. 3.4.2, can be considered to consist of two components: that due to experimental error and that due to the variance between each series of push tests. The latter is therefore the variance due to some unaccounted variable.

3.4.3.1 Experimental error

The experimental error was determined from the residual variance within groups of specimens in which most of the variables were constant; the rest of the variables were assumed to vary linearly. The following relations were analysed as multi-variable linear regressions.

$P_e = f(f_{cu})$ when h_c, b_c, f_{rt} and d_s were constant

$P_e = f(f_{cu}, b_c)$ when h_c, f_{rt} and d_s were constant

The best estimate of the variance was found to be 50 $(kN)^2$ which gave a coefficient of variation of the experimental error of 7.9%. Since the sum of squares of the deviates about a linear regression will always be equal to or greater than that about a curvilinear regression, the above estimate is an over-estimation of the experimental error.

3.4.3.2 Distribution of the variance about multi-variable regressions.

It will now be assumed that the residual variance, which is unaccounted for after allowing for the variances due to f_{cu}, d_s, b_c, h_c and the experimental error, is primarily due to the variation in the transverse reinforcement between samples.

The distribution of variance, Table 3.2, about $P_e = f(f_{cu})$ at constant values of d_s, showed that the variance due to f_{rt} increased with the diameter of the stud; 13mm studs were not affected by the

transverse reinforcement nor by the variations in the size of the slab, b_c and h_c, whereas the variance due to f_{rt} for 19mm studs was ten times the experimental variance and that due to the size of the slab, b_c and h_c, was four times the experimental variance.

The distribution of variances for the multi-variable linear regression, Equ. 3.6, and the multi-variable curvilinear regression, Equ. 3.10, is given in Table 3.3. Although the variations between P_e and h_c and f_{cu} were found to be probably significant, their contribution to the variance is less than 7% of the total variance. The main effect of using a curvilinear regression was to increase the variance due to b_c.

3.4.4 Modes of failure

The prevalence of different failure modes can be determined from the statistical analyses if the following assumptions are made.

The maximum strength is dependent upon the shear strength of the shank of the stud, P_{sh}, i.e. upon its cross-sectional area. P_{sh} is therefore proportional to d_s^2.

The load at which the slab splits, P_{sp}, is dependent upon the effective height of the stud, which may be considered to be proportional to d_s, and the strength of the concrete. P_{sp} is therefore proportional to d_s and f_{cu}.

The load at which the concrete fails in compression, P_{cp}, is dependent upon the bearing area of the stud which is itself dependent upon the effective height and width of the stud. P_{cp} is therefore proportional to d_s^2 and f_{cu}.

3.4.4.1 13mm studs

Since the concrete strength, Equ. 3.7, was not significant and the variance due to b_c and h_c, and f_{rt}, Table 3.2, was negligible, it may

therefore be assumed that the strength is not dependent upon the transverse reinforcement, shape of slab and compressive strength of the concrete. This implies that the strength of 13mm studs is not determined by P_{sp} nor P_{cp} and must therefore be dependent upon the shear strength of the shank of the stud, P_{sh}.

3.4.4.2 16mm and 19mm studs

Since P_{sp} is proportional to d_s and P_{sh} is proportional to d_s^2, as d_s increases, P_{sp} occurs at a lower proportion of P_{sh}. This implies that the effect of the concrete strength reduces as d_s increases, which explains the reduction in the significance of the concrete in Equs. 3.8 and 3.9. If it is assumed that the load on the transverse reinforcement increases rapidly after splitting has occurred, then this would explain the increase in the variance attributable to f_{rt}, Table 3.2, as d_s increases.

3.5 SUMMARY

The behaviour of stud shear connectors in push tests can be summarized as follows.

The diameter of the stud and the width of the slab are highly significant. The depth of the slab and the strength of the concrete are probably significant. The height of the stud, the transverse spacing of the studs and the length of the slab are not significant. The strength bears a non-linear relationship with the width of the slab. The effect of the transverse reinforcement and the size of the slab increases with the diameter of the stud. The coefficient of variation of the experimental error is 7.9%. The strength of 13mm studs is independent of the strength of the concrete, size of the slab and the transverse reinforcement. The strength of 19mm studs is dependent upon the strength of the concrete, size of the slab and the transverse reinforcement.

Table 3.1 Published results and properties of push tests.

d_s mm	P_e kN	f_{ca} *	f_{cu} *	f_{ct} *	f_{rt} *	b_c mm	l_p mm	h_c mm	t_s mm	h_s mm	Ref. No.
13	54	67			U	204	330	152	102	101	34
13	58	56			"	"	"	"	"	"	"
13	50	56			"	"	"	"	"	"	"
13	57	56			"	"	"	"	"	"	"
13	60		35		R	305	254	152	64	102	35
13	65		35		"	"	"	"	"	57	"
13	47		35		R	90	160	200	0	65	5
13	47		35		"	"	"	"	"	"	"
13	51		35		"	125	"	"	"	"	"
13	51		35		"	"	"	"	"	"	"
13	58		35		"	165	"	"	"	"	"
13	58		35		"	"	"	"	"	"	"
13	40		35		"	90	"	"	"	"	"
13	40		35		"	"	"	"	"	"	"
13	62	42			R	305	305	152	76	102	1
13	64	38			"	"	"	"	"	"	"
13	65	40			"	"	"	"	"	"	"
13	62	42			"	"	"	"	"	"	"
13	69	44			"	"	"	"	"	"	"
13	69	38			"	"	"	"	"	"	"
13	71	38			"	"	"	"	"	"	"
13	59		21	1.9	R	300	250	150	39	65	36
13	59		21	1.9	"	"	"	"	"	"	"
13	55		20	1.6	"	"	"	"	"	"	"
13	55		20	1.6	"	"	"	"	"	"	"
13	57		21	1.7	"	"	"	"	"	"	"
13	60		21	1.7	"	"	"	"	"	"	"
13	59		21	1.9	U	"	"	"	"	"	"
13	56		21	1.9	R	"	"	"	"	"	"
13	54	44			U	610	572	152	102	102	37
13	63	33			R	"	"	178	"	"	"
13	50	27			U	610	330	152	102	51	38
13	56	36			"	"	"	"	"	"	"
13	57	28			"	"	"	"	"	75	"
13	49	30			"	"	"	"	"	102	"
13	54	45			"	"	"	"	"	"	"
13	48	45			"	"	"	"	"	"	"
16	67		30		R	400	225	190	90	120	39
16	68		30		"	"	"	"	"	"	"
16	71		30		"	"	"	"	"	"	"
16	57		30		"	130	"	"	"	"	"
16	52		30		"	"	"	"	"	"	"
16	50		30		"	"	"	"	"	"	"
16	102	33			R	305	305	152	76	102	1
16	109	37			"	"	"	"	"	"	"

* N/mm^2

Table 3.1 continued.

d_s mm	P_e kN	f_{ca} *	f_{cu} *	f_{ct} *	f_{rt} *	b_c mm	l_p mm	h_c mm	t_s mm	h_s mm	Ref. No.
16	98	29			"	305	305	152	76	102	1
16	99	33			"	"	"	"	"	"	"
16	93	32			"	"	"	"	"	"	"
16	85	44			U	610	572	152	102	102	37
16	103	33			R	"	"	178	"	"	"
16	78	25		3.1	U	610	330	152	102	102	33
16	85	41			"	"	"	"	"	"	"
16	79	39			"	"	"	"	"	"	"
16	83	39			"	"	"	"	"	"	"
19	98	17	22		R	305	250	230	77	102	6
19	97	17	22		"	"	"	"	"	"	"
19	97	17	22		"	"	"	"	"	"	"
19	127	51	54		"	"	"	"	"	"	"
19	127	51	54		"	"	"	"	"	"	"
19	127	51	54		"	"	"	"	"	"	"
19	82	67			U	204	330	150	102	101	34
19	105	67			"	"	"	"	"	"	"
19	76	56			"	"	"	"	"	"	"
19	89	56			"	"	"	"	"	"	"
19	125		36		R	305	254	152	64	102	35
19	123		39		R	"	"	"	"	"	"
19	127		38		"	"	"	"	"	"	"
19	113		25		"	"	"	"	"	"	"
19	119		39		"	"	"	"	"	"	"
19	103		35		"	"	"	"	"	77	"
19	111		42		"	"	"	"	"	51	"
19	125	45		2.9	R	503	356	152	102	75	40
19	129	46		3.0	"	"	"	"	"	"	"
19	82	40		1.9	"	"	"	"	"	"	"
19	82	40		1.9	"	"	"	"	"	"	"
19	160	37			R	406	305	152	102	102	1
19	159	31			"	"	"	"	"	"	"
19	156	35			"	"	"	"	"	"	"
19	141	35			"	"	"	"	"	"	"
19	143	36			"	"	"	"	"	"	"
19	161	31			"	"	"	"	"	"	"
19	145	31			"	"	"	"	"	"	"
19	149	36			"	"	"	"	"	"	"
19	172	35			"	"	"	"	"	"	"
19	70	41	40		R	133	229	203	76	102	41
19	77	41	32		"	172	"	"	"	"	"
19	83	41	37		"	197	"	"	"	"	"
19	87	47	45		"	133	"	"	"	"	"
19	87	49	47		"	153	"	"	"	"	"
19	90	51	49		"	172	"	"	"	"	"

* N/mm^2

Table 3.1 continued.

d_s mm	P_c kN	f_{ca} *	f_{cu} *	f_{ct} *	f_{rt} *	b_c mm	l_p mm	h_c mm	t_s mm	h_s mm	Ref. No.
19	95	53	48		"	197	229	203	76	102	41
19	100	52	53		"	222	"	"	"	"	"
19	101	52	49		"	248	"	"	"	"	"
19	59		29	2.6	U	105	550	100	0	75	33
19	76		32	2.7	"	"	"	"	"	"	"
19	81		29	2.6	"	"	"	"	"	"	"
19	84		31	2.6	"	"	"	"	"	"	"
19	81		30	2.6	"	"	"	"	"	"	"
19	78		33	2.7	"	129	"	"	"	"	"
19	84		29	2.6	"	151	"	"	"	"	"
19	80		29	2.6	"	179	"	"	"	"	"
19	84		31	2.7	"	203	"	"	"	"	"
19	71		31	2.6	"	148	"	"	39	"	"
19	64		32	2.7	"	176	"	"	"	"	"
19	77		35	2.8	"	216	"	"	"	"	"
19	73		32	2.7	"	252	"	"	"	"	"
19	60		36	2.9	"	150	"	"	"	"	"
19	90		24	2.3	R	300	"	"	0	"	"
19	68		29	2.5	"	"	"	"	39	"	"
19	131	47			U	610	572	152	102	102	37
19	144	33			R	"	"	178	"	"	"
19	110	41			R	"	"	152	"	"	"
19	86	39			U	610	330	152	102	51	38
19	98	22			"	"	"	"	"	76	"
19	108	43			"	"	"	"	"	"	"
19	94	24			"	"	"	"	"	102	"
19	93	29		3.1	"	"	"	152	"	"	"
19	100	31		3.0	"	"	"	"	"	"	"
19	131	40			"	"	"	152	"	102	"
19	69		22	1.9	U	300	330	150	57	75	36
19	86		22	1.8	"	"	"	"	"	"	"
19	72		22	1.8	R	"	"	"	39	"	"
19	145		58		R	305	230	152	64	75	42
19	138		58		"	"	"	"	"	"	"
19	150		55		"	"	"	"	"	"	"
19	96		61		"	"	"	"	"	"	"
19	97		43		"	"	"	"	"	"	"
22	143	47			U	610	572	152	102	102	37
22	167	43			R	"	"	178	"	"	"
22	133	40			R	610	572	152	102	102	38

* N/mm^2

Table 3.2 Distribution of the residual variance about the function $P_e = f(f_{cu})$ when d_s is constant.

d_s (mm)	Residual variance due to (kN^2)		
	Experimental error	Slab dimensions b_c and h_c	f_{rt}
13	50	3	0
16	50	58	133
19	50	193	522

Table 3.3 Distribution of the variance about the multi-variable linear regression, Equ. 3.6, and the multi-variable curvilinear regression, Equ. 3.10.

Variable	Sum of squares $(kN)^2$	
	Equ. 3.6	Equ. 3.10
d_s	59,927	61,099
f_{rt}	43,440	25,239
b_c	9,259	23,993
f_{cu}	4,319	8,414
h_c	1,798	0
Experimental error	5,311	5,311
Total	124,050	124,050

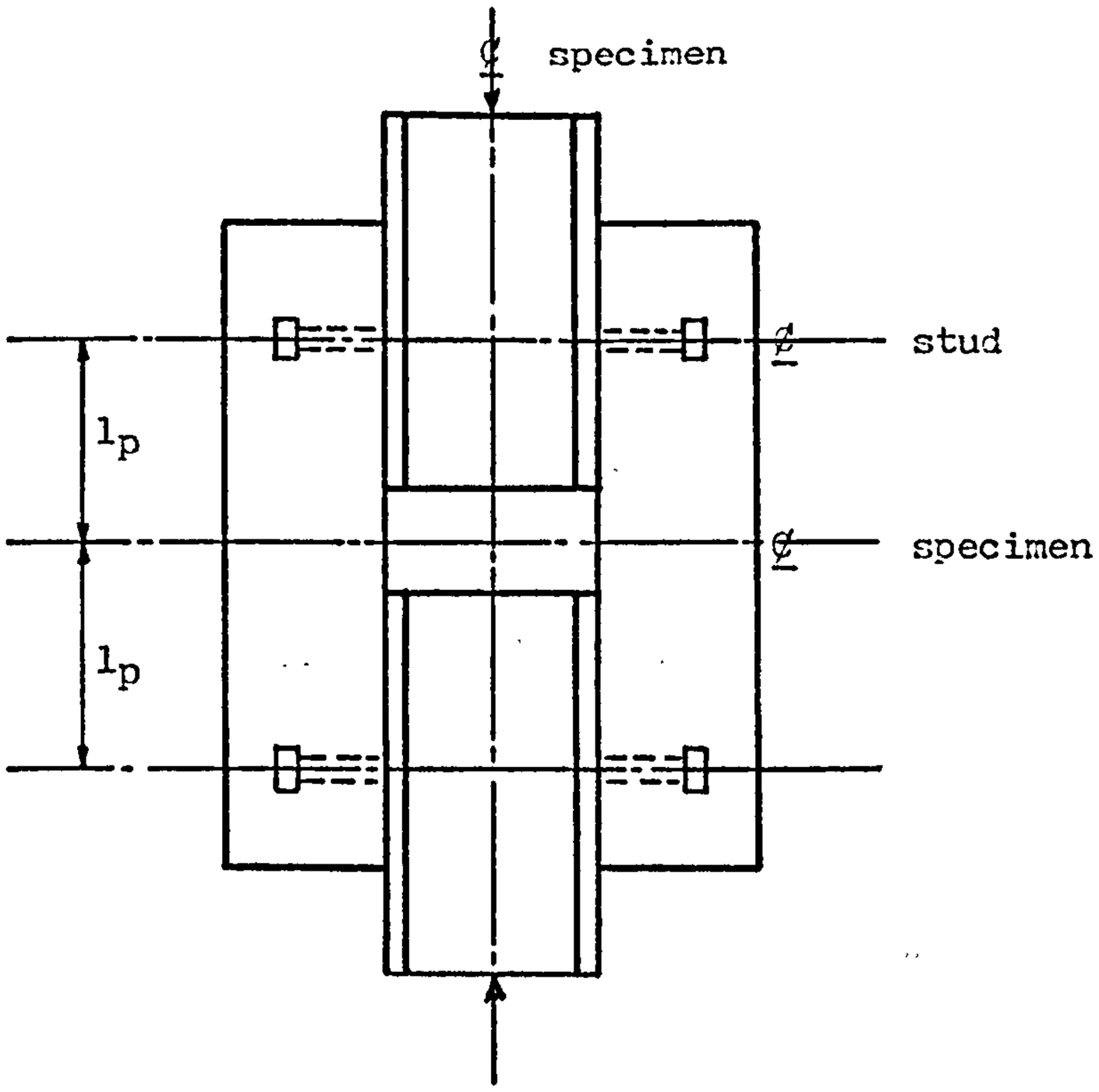

Fig. 3.1 Push specimen designed by Teraszkiewcz[12].

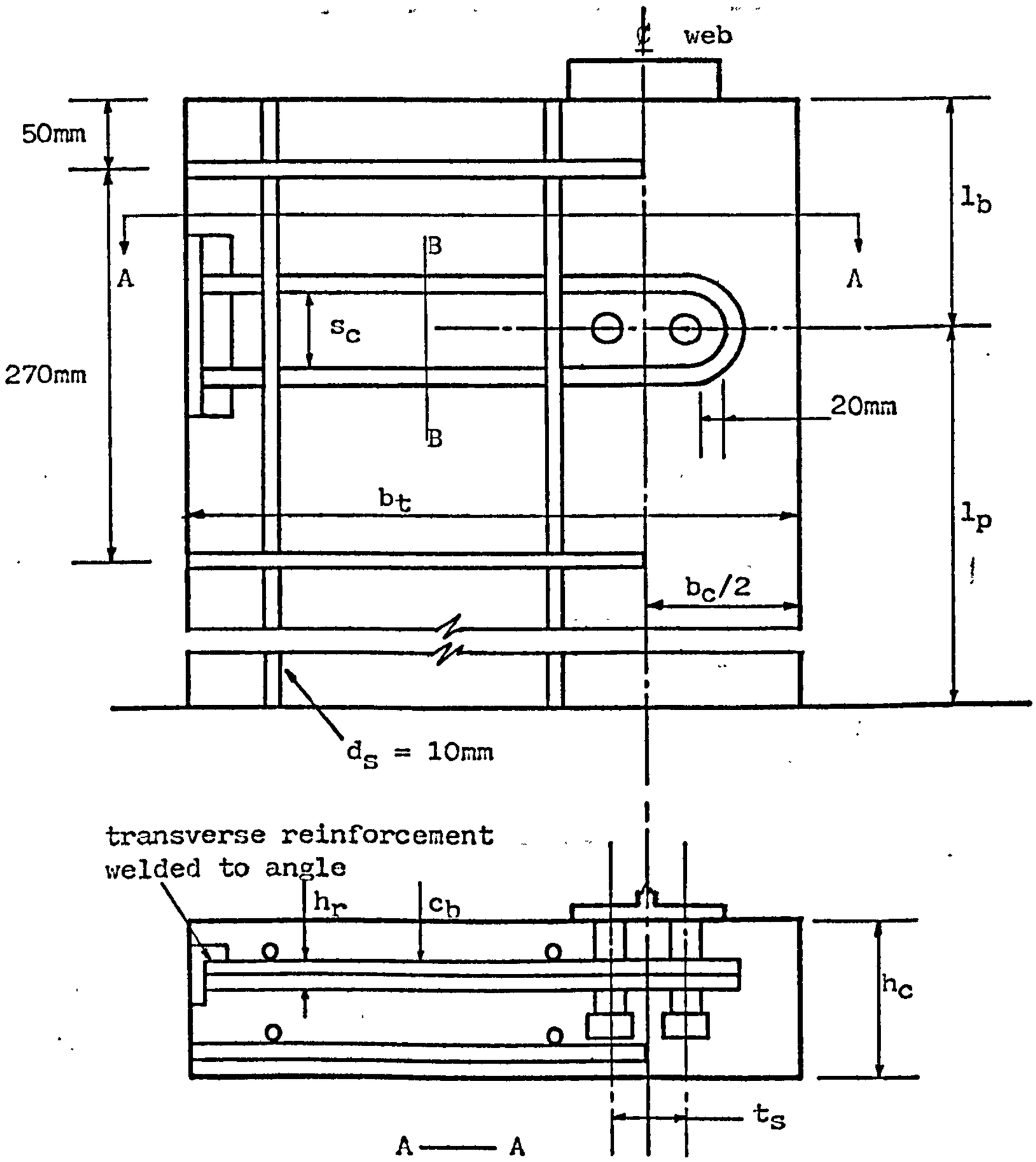

Fig. 3.2 Push specimen designed to represent a composite I-beam[33]

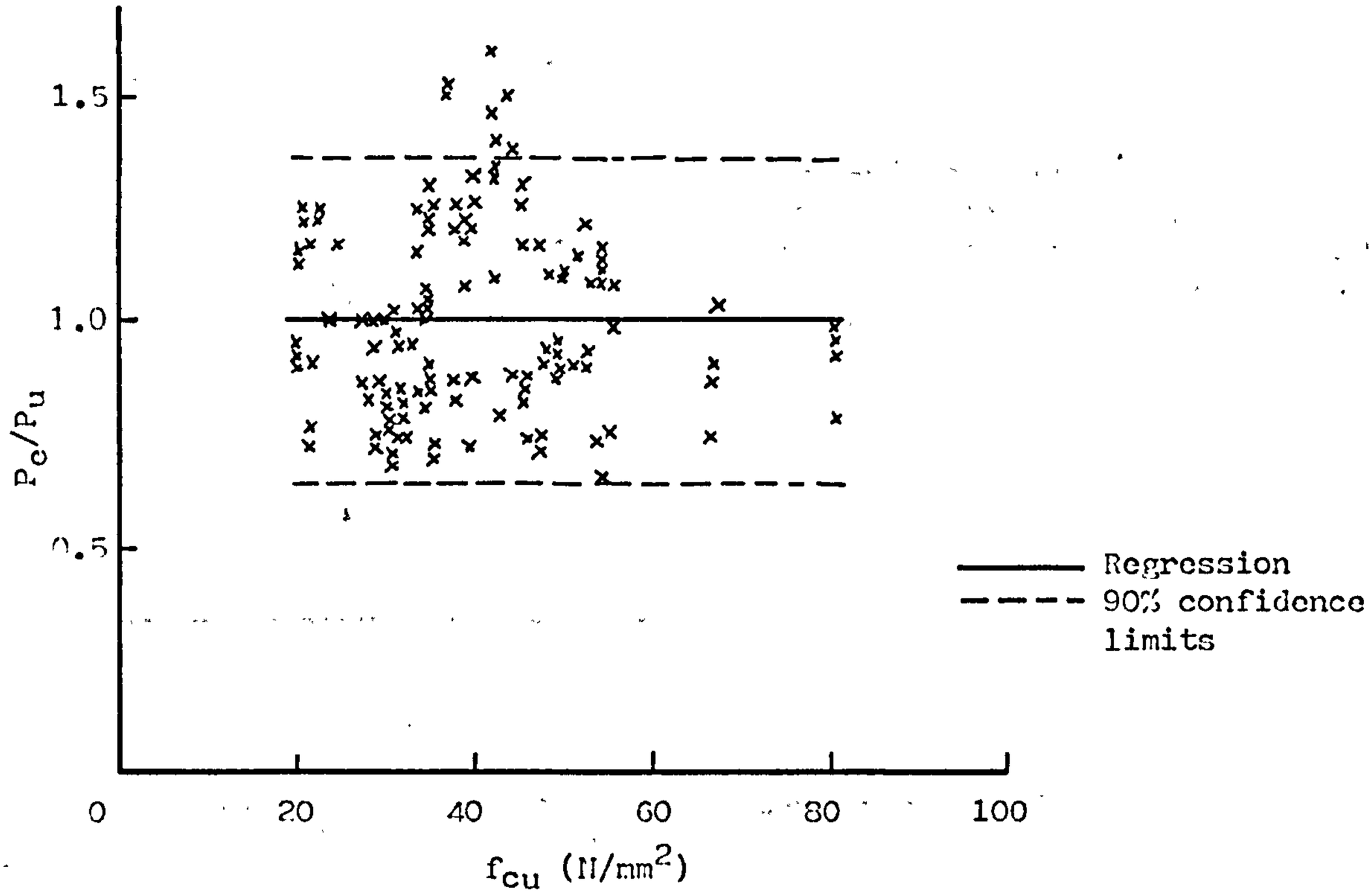

Fig. 3.3 Scatter about the multi-variable linear regression.

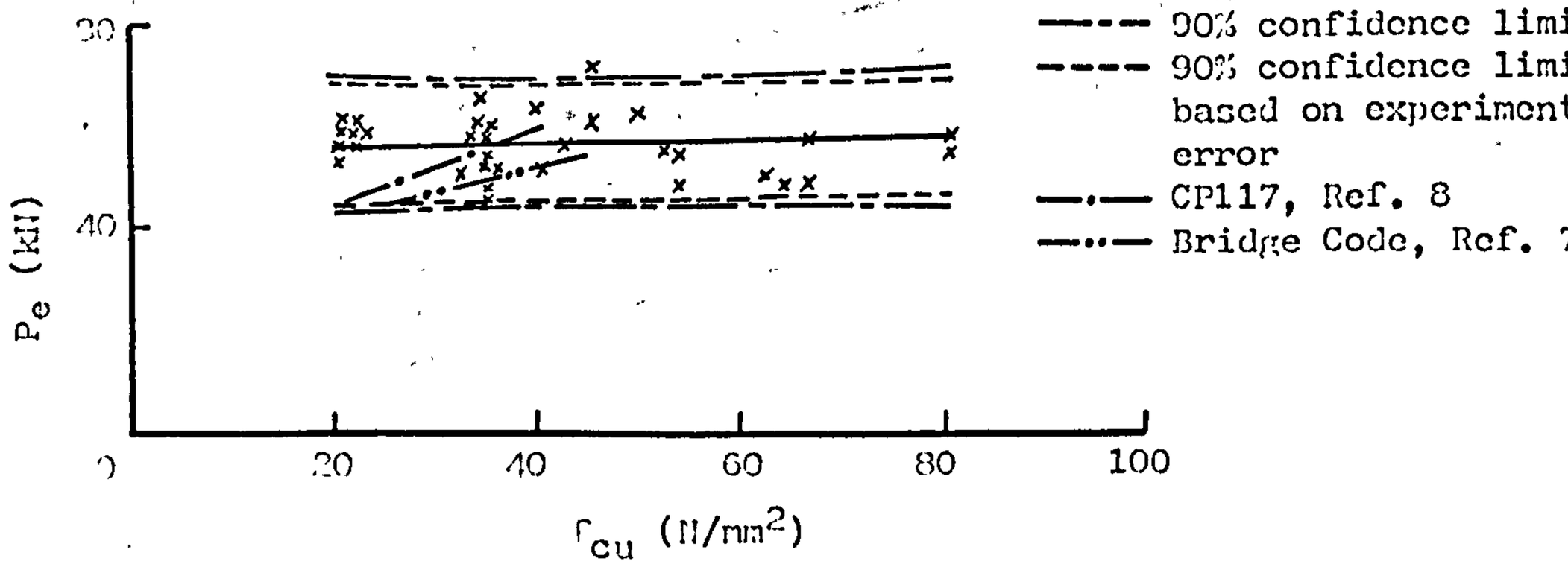

Fig. 3.4 Regression analysis of the strengths of 13mm stud shear connectors.

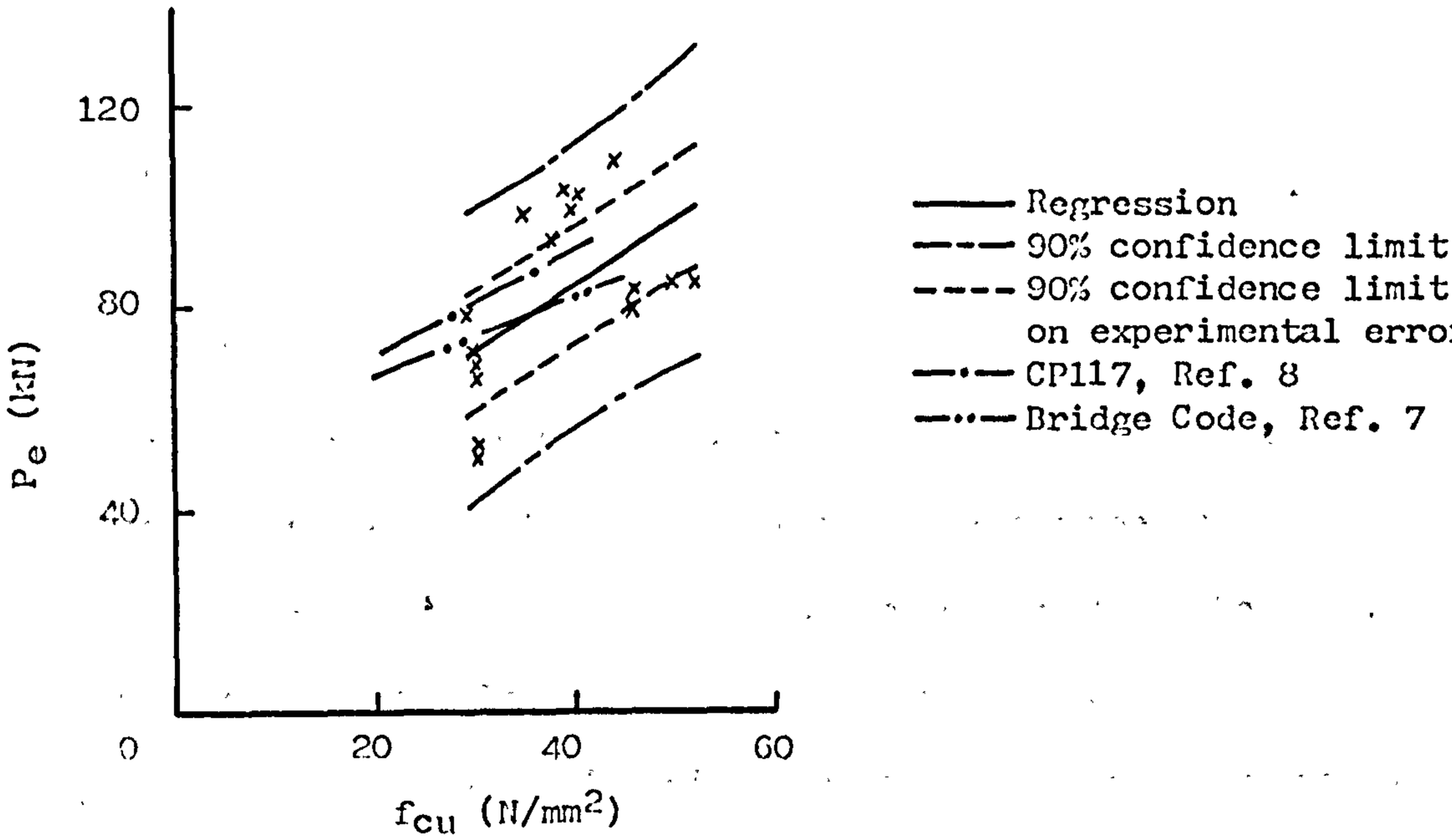

Fig. 3.5 Regression analysis of the strengths of 16mm stud shear connectors.

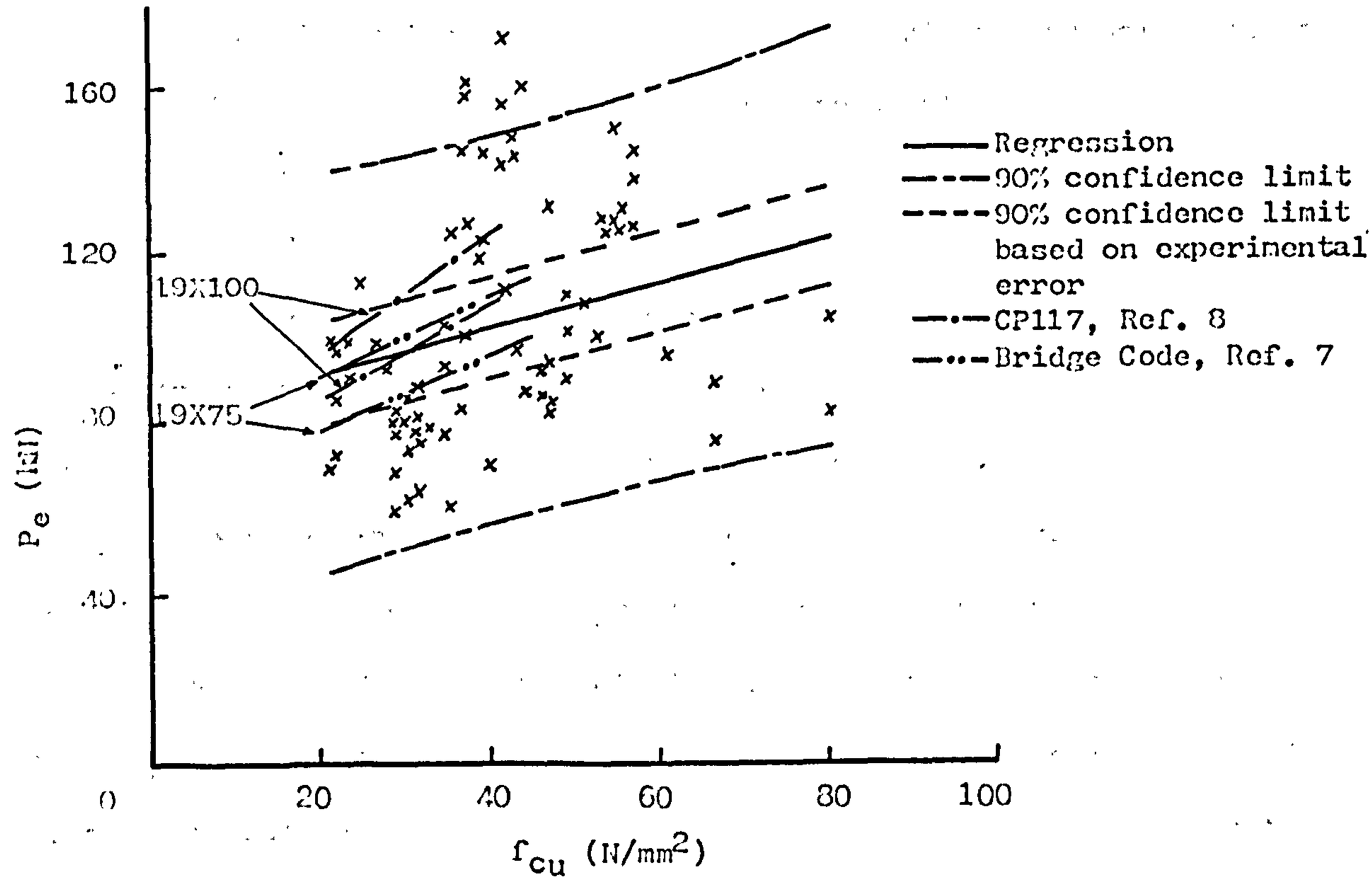

Fig. 3.6 Regression analysis of the strengths of 19mm stud shear connectors.

Chapter Four

A FINITE ELEMENT COMPUTER PROGRAM

4.1 INTRODUCTION

A finite element computer program has been developed in order to analyse the various failure modes of stud shear connectors.

The basic routines of the program are described in Sect. 4.2. The procedures which simulate tensile failure of the concrete are described in Sect. 4.3, and those which simulate tensile and compressive failure of the concrete are described in Sect. 4.4.

The nomenclature used is shown in Fig. 4.2. Tensile stresses and strains are positive. The line of action of the main compressive force in a specimen will be referred to as the longitudinal direction and it will be denoted by the direction of the X axis. The longitudinal direction of an element will refer to the direction of the minimum principal stress and it will be denoted by the direction of the x axis.

4.2 BASIC ROUTINES OF THE PROGRAM

The finite element analysis program uses the standard two dimensional plane stress triangular element for isotropic materials, as described by Zienkiewicz[52]. The flow diagram is shown in Fig. 4.1.

The rectangular co-ordinates of the grid system, Fig. 4.2, are input and from these the program automatically forms and numbers the triangular elements and nodes in the sequence shown. The isotropic material properties and thicknesses are input for each element in numerical order, followed by the external constraints, i.e. loads or displacements, applied to the nodes. The material properties of the failed elements and their failure criteria are discussed in Sects. 4.3 and 4.4.

The overall stiffness matrix is formed from the isotropic material properties and then with the initial constraints solved to give, if required, the standard finite element analysis of an elastic isotropic material, which will be referred to as Mode 1. The first element to fail is determined by comparing the principal stresses or strains of each element with the specified failure criteria. That element which requires the smallest proportional change in the initial constraints to reach its next failure criterion will fail first. The term fail is used to imply a change in the material properties, not necessarily a complete disintegration or collapse as given by zero stiffness. The internal stresses and strains, and external nodal forces and displacements are then output, where required, at the constraints at which the element failed, by factoring the original analysis by the proportional change already calculated. This procedure is possible because the analysis is always linearly elastic. The stiffness matrix of the failed element is then removed from the overall stiffness matrix. The properties of this element are then changed and the new stiffness matrix, derived from the new properties, added to the overall stiffness matrix.

The program repeats this routine for a specified number of iterations or until the specimen has reached a critical state, such as yielding of the steel or a large reduction in overall stiffness.

4.3 TENSILE STRESS FAILURE OF CONCRETE

This procedure, which allows the concrete to fail only in tension, will be referred to as Mode 2.

The procedure uses, with only minor modifications, a method developed by Arnaouti[51] which alters the elasticity matrix of an element to allow for the development of tensile cracks and the subsequent reduction in stiffness. His method assumes that the element cracks when the principal

tensile stress reaches a specific value, such as the split tensile strength of the concrete. The stiffness across the crack is reduced to zero and the shear stiffness reduced by a factor n which allows for the aggregate interlock across the crack, the value of which is determined from experimental work.

A record is kept within the program, in an integer array /CRACK/, of the state of failure of each element. The concrete is first assumed to be isotropic and hence the elasticity matrix in the global co-ordinate system, D_g, is given by /CRACK/ = 0

$$D_g = \frac{E_c}{1-v^2}\begin{bmatrix} 1 & v & 0 \\ v & 1 & 0 \\ 0 & 0 & (1-v)/2 \end{bmatrix}$$

where E_c = modulus of elasticity of the concrete

v = Poisson's ratio of the concrete

When an element cracks, Fig. 4.2, the elasticity matrix in the local co-ordinate system, D_1, becomes

/CRACK/ = 1

$$D_1 = \frac{E_c}{1-v^2}\begin{bmatrix} 1 & 0 & 0 \\ 0 & 0 & 0 \\ 0 & 0 & n(1-v)/2 \end{bmatrix}$$

which is then transformed into the overall co-ordinate system by using the standard transformation matrix with a_c, the angle between the co-ordinate systems.

When an element cracks for a second time, its shear strength is assumed to reduce by the factor n again and a_c is taken as the mean of the angles of the two cracks.

$$/\overline{\text{CRACK}}/ = 2$$

$$D_1 = \frac{E_c}{1-\nu^2}\begin{bmatrix} 0 & 0 & 0 \\ 0 & 0 & 0 \\ 0 & 0 & n^2(1-\nu)/2 \end{bmatrix}$$

When a third crack is formed, $/\overline{\text{CRACK}}/ = 3$, the element is assumed to have disintegrated completely, i.e. zero stiffness, and therefore all the coefficients of the elasticity matrix are made zero.

4.4 COMPRESSIVE AND TENSILE FAILURE OF CONCRETE

This procedure, which allows the concrete to fail in tension and compression, will be referred to as Mode 3.

An attempt has been made to simulate the compressive failure of concrete in a finite element analysis. For this to represent compressive failure under all conditions it must at least simulate the behaviour of concrete cylinders under standard uniaxial compressive tests, from which the following characteristics have been observed.

4.4.1 Characteristics to be simulated

The specimen[44] can be considered to be initially linearly elastic.

Longitudinal cracking develops when the lateral strain is of the same order as the tensile strain at failure in modulus of rupture tests[55], and is accompanied by a reduction in the overall longitudinal stiffness[44]. This is referred to as the discontinuity point of the concrete. The formation of these cracks is described by Baker[49] and their propagation illustrated experimentally by Liw[47].

The specimen continues to resist increasing load and become less stiff up to overall strains in the region[44,53] of 2000 to 2500 microstrains. The value of this strain would appear to depend on the gauge length over which the strains are measured[44].

The failed specimen exhibits a type of necking[44]. At failure the specimen consists of two cones of solid concrete. The cones are surrounded by longitudinal strips of concrete, which can be broken away by hand, and between the cones a small region over which the concrete has totally disintegrated. It is clear that concrete cylinders do not fail uniformly.

4.4.2 Hypothesis for a mechanism of compressive failure

The following failure mechanism, which is based on two parameters, is proposed.

Longitudinal cracks which start to form at a specific lateral strain, e_t, are shown diagrammatically in Fig. 4.3. This concertina action causes the longitudinal stiffness to appear to reduce more rapidly than the lateral stiffness.

It is important to differentiate between this type of cracking, which is caused by tensile strains produced by compressive forces and their Poisson effect, and that due to tensile forces. In the latter case, when one crack is formed, the stiffness perpendicular to the crack reduces to zero and hence the tensile force and its associated strain in the uncracked portion of concrete reduces to zero and no further cracks are formed. In the former case, the formation of one crack will not reduce the lateral strain in the concrete since it is caused by the compressive forces and their Poisson effect. In theory an infinite number of cracks would form but instead the element is assumed to crack as in Fig. 4.3.

These cracked elements fail at a specific longitudinal strain e_1. In theory an uncracked element can resist unlimited compressive strains. At the specified longitudinal strain the cracked elements can be considered to be analogous to columns. They buckle, transferring the load to the central core.

A concrete element is therefore considered to disintegrate completely

only when first the lateral tensile strain induced by compressive forces reaches a critical value and then the longitudinal compressive strain exceeds another critical value. This may be considered to be a type of instability failure.

4.4.3 Shear modulus and elasticity matrix of orthotropic materials

Since the mechanism of compressive failure requires the material to be orthotropic the elasticity matrix and shear modulus, G, have been derived below using the nomenclature and co-ordinate system of Fig. 4.4.

4.4.3.1 Elasticity matrix of an orthotropic material in plane stress

$$e_x = f_x/E_x - v_x f_y/E_y$$

$$e_y = f_y/E_y - v_y f_x/E_x$$

$$q_{xy} = T_{xy}/G$$

hence

$$D_1 = \frac{1}{1-v_y v_x} \begin{bmatrix} E_x & E_x v_x & 0 \\ E_y v_y & E_y & 0 \\ 0 & 0 & G(1-v_y v_x) \end{bmatrix}$$

4.4.3.2 Shear modulus of an orthotropic material

The shear modulus of an orthotropic material is derived below by considering the deformation of an element in pure shear, as detailed by Timoshenko[56].

$$\tan(\pi/4 - q_{xy}/2) = (1+e_y)/(1+e_x)$$

$$= (1 - v_y f_x/E_x + f_y/E_y)/(1 - v_x f_y/E_y + f_x/E_x)$$

since $T_{xy} = f_x = -f_y$

$$\tan(\pi/4-q_{xy}/2) = (1-T_{xy}(1/E_y+v_x/E_x))/(1+T_{xy}(1/E_x+v_x/E_y))$$

hence $$q_{xy}/T_{xy} = B+A-(q_{xy}(B-A))/2$$

where $$A = 1/E_y+v_y/E_x$$

and $$B = 1/E_x+v_x/E_y$$

since $q_{xy}(B-A)/2$ is much less than B+A

$$G = 1/(B+A) = E_xE_y/(E_y(1+v_y)+E_x(1+v_x))$$

4.4.4 Sequence of failure

The sequence in which an element can fail and the consequent change in its material properties is shown in Fig. 4.5. The failure criteria and material properties are derived in Sect. 4.4.5. The direction at which an element first fails is used to fix the local co-ordinate system of that element; the ordinate being in the direction of the maximum principal strain. The possibility of subsequent failures occurring in this element are calculated in this direction.

4.4.4.1 Isotropic element, /CRACK/ = 0

An element, which is first assumed to have isotropic material properties, can fail when either the tensile strength of the concrete, f_t, or the lateral tensile strain of failure, e_t, is reached. Because the relationship between f_t and e_t, and the longitudinal compressive stress, f_x, are not known, Sect. 4.4.5.2, the following conditions of failure are assumed.

When the lateral stress, f_y, is compressive then the element fails when the lateral strain, e_y, reaches e_t. Otherwise, when f_y is tensile, the element fails when $-vf_x/E_c = e_t$, which has the effect of ignoring the tensile strain produced by the tensile stress as it would disappear if

f_t were exceeded.

The element fails when $f_y = f_t$.

4.4.4.2 A split element, /CRACK/ = 1

The isotropic element is assumed to split into two segments when the tensile failure stress is reached. The stiffness across the crack, E_y, is therefore reduced to zero and, because the change in the Poisson ratio is not known, v is also reduced to zero in all failed elements. In order to reduce computation time only one tensile stress crack is formed in an element.

Further failure can only occur when the local tensile strain in the concrete, $-ve_x$, reaches e_t, i.e. the width of the crack is ignored in deriving the lateral tensile strain.

4.4.4.3 Tensile failure strain reached, /CRACK/ = 2

When the lateral strain of failure is reached the stiffness in the direction of the compressive stress, E_x, is reduced to $0.4E_c$, Sect. 4.4.5.3.

Further failure can occur when either the tensile strength of the concrete is reached i.e. $f_y = f_t$ or when the longitudinal compressive strain of failure, e_1, is reached i.e. $e_x = e_1$.

4.4.4.4 Tensile failure strain and stress reached, /CRACK/ = 3

The stiffness in the direction of the compressive force, E_x, is reduced to $0.4E_c$, and across the crack to zero.

Further failure can only occur when $e_x = e_1$.

4.4.4.5 Complete disintegration, /CRACK/ = 4

Only elements which have reached their tensile failure strains

are assumed to disintegrate completely when the longitudinal compressive strain of failure, e_1, is reached. The stiffness in all directions is then reduced to zero.

4.4.5 Material properties and failure criteria

The various material properties and failure criteria which are required for the finite element analysis are determined below.

4.4.5.1 Isotropic material properties

The isotropic modulus of elasticity of the concrete, E_c, is assumed to be equal to the tangent modulus, as determined by BS1881[57]. The Poisson ratio is assumed to be constant at 0.15, since Anson and Newman[46] showed that it hardly varied over the range of normal concrete mixes.

4.4.5.2 Tensile strain and stress failure

Of the two standard concrete tensile tests in use[57], the modulus of rupture and the split tensile test, only the modulus of rupture fails at a strain caused solely by tensile forces; since in the split tensile test, the region of failure is subject to lateral tensile strains which are induced by the longitudinally applied compressive forces. This may be the reason why the split tensile strength is less than the modulus of rupture strength, but as the effect has not been quantified experimentally the tensile strain and stress at failure are calculated from the modulus of rupture test by using the tangent modulus of the isotropic material.

4.4.5.3 Orthotropic properties after tensile strain failure

Unlike splitting, $\underline{/}\overline{\text{CRACK}}\underline{/} = 1$ in Fig. 4.5, tensile strain failure, $\underline{/}\overline{\text{CRACK}}\underline{/} = 2$, can occur when the lateral forces are compressive as well as tensile. If it is assumed that a series of longitudinal cracks are

formed which are not continuous, as compared with a split, then the lateral stiffness will depend on the lateral forces; compressive lateral forces will cause the longitudinal cracks to close and the stiffness to increase, whereas, the stiffness when tensile lateral forces are exerted will depend on the extent and continuity of the cracks. Furthermore, the lateral tensile strength of the concrete will also depend on the extent and continuity of the cracks; the reduction in strength is not known but can be considered to be represented by the split tensile strength as opposed to the modulus of rupture strength. Two elements should therefore be formed when lateral tensile strain failure occurs, however, in order to simplify the program and since the change in the lateral stiffness and strength is not known it was assumed that the lateral stiffness and strength remained the same after lateral tensile strain failure. The longitudinal stiffness after tensile strain failure was reduced in order to represent the secant stiffness of the concrete at the maximum load.

The theoretical extent of cracking at the discontinuity point of Barnard's experimental specimen[44] and the development of the central core are shown in Fig. 4.7, which uses the nomenclature of Figs. 4.2 and 4.5. Only a quarter of the specimen is analysed as it is symmetrical about its centre lines. The program had not then been adapted to allow for the tensile stress failure of the concrete. The sudden theoretical reduction in the longitudinal stiffness by 60% only causes a gradual reduction in the overall stiffness, Fig.4.6.

4.4.5.4 Compressive strain failure

Those elements which had previously reached their tensile failure strain are assumed to disintegrate at a longitudinal compressive strain, e_1, of 0.0035, as used in CP110[21]. No attempt was made to simulate the gradual failure of concrete since, if the mechanism is as hypothesized, it would require a non-linear analysis. Instead, it is assumed that the stiffness of the concrete in all directions reduces to zero.

The theoretical extent of cracking of Barnard's specimen at the maximum load, which occurred when the first element disintegrated, is shown in Fig. 4.8. Further displacement to the theoretical specimen was accompanied by a reduction in the applied load and the formation of a band of concrete which had totally disintegrated, Fig. 4.9. The specimen collapsed, i.e. the stiffness and hence load reduced to zero, when the band had completely formed. A similar effect was observed experimentally

by Barnard[44]. It is apparent, Fig. 4.6, that the strain at which the concrete disintegrates is dependent upon the gauge length over which it is measured.

4.4.6 Validation of the hypothesis for compressive failure

Theoretical variations in strength have been compared with experimental variations in order to determine the accuracy of the hypothesis for the compressive failure of concrete.

It is virtually impossible to simulate the stress distribution and constraints of a three dimensional experiment on a two dimensional finite element program. Furthermore, the program only allows for tensile strain failure in the X - Y plane. The magnitude of these effects are considered at the beginning of each section.

Since it is generally agreed that the present methods of determining the strengths and properties of concrete[57] are not an absolute measure, the finite element programs have been used throughout this thesis to determine only the variations in strength, which are mainly affected by the relative change in an independent variable. The theoretical variations have therefore been plotted in terms of an absolute strength which can be or is determined experimentally.

All of the analyses, which use Mode 3, assume the following concrete material properties and failure criteria which were derived from Barnard's[44] specimen.

Failure criteria:

Tensile strain failure of concrete; $e_t = 145X10^{-6}$

Compressive strain failure of concrete; $e_1 = -3500X10^{-6}$

Tensile stress failure of concrete; $f_t = 3.92\ N/mm^2$

Concrete properties:

	E_x (N/mm^2)	E_y (N/mm^2)	v_x	v_y
/CRACK/ = 0	27000	27000	0.15	0.15
/CRACK/ = 1	27000	0	0	0
/CRACK/ = 2	10800	27000	0	0
/CRACK/ = 3	10800	0	0	0
/CRACK/ = 4	0	0	0	0

4.4.6.1 Triaxial compression tests

The finite element analysis only considers failure in the x-y plane, hence

$$e_y = -vf_x/E_c+f_y/E_c \qquad (4.1)$$

A cube of concrete in a triaxial compression test is subject to stresses from three dimensions, hence

$$e_y = -vf_x/E_c+f_y/E_c-vf_z/E_c$$

since $f_y = f_z$ in a triaxial compression test

$$e_y = -vf_x/E_c+f_y(1-v)/E_c \qquad (4.2)$$

Therefore the error in determining the load at which tensile strain failure occurs, by using the two dimensional program, is given by vf_y/E_c. The difference is shown in Figs. 4.10 and 4.11 where f_x and f_y have been plotted in terms of the compressive strength of an unrestrained element, f_{cc}, i.e. $0.4E_ce_1$.

The experimental results of triaxial compression tests on cylinders of concrete by Balmer, Jones and McHenry[54], and Hobbs, Pomeroy and Newman[50] are shown in Figs. 4.10 and 4.11. In these tests the lateral restraint, f_y, was active since it was maintained at a constant stress as the

longitudinal force, f_b, was applied. These results have been compared with theoretical analyses in which the lateral forces were increased in proportion to the imposed longitudinal displacements i.e. passive resistance. The constraints were the same as in Fig. 4.7. The computer program had not been adapted to allow for the tensile stress failure of the concrete. A previous analysis, using Mode 2, showed that tensile stress failure only occurred at extremely high loads, when the load was applied as a uniform displacement, because f_X was fairly uniform and hence f_Y, which is caused by the dispersal of f_X, was very small.

The results, Figs. 4.10 and 4.11, agree reasonably well at low lateral restraints i.e. $f_Y < 0.3f_{cy}$ but as f_Y increases they become increasingly unconservative and follow the load at which tensile strain failure first occurs in an element, Equ. 4.1. The difference between the finite element analysis and Equ. 4.1 is due to the non uniformity of the stresses within the specimen which are caused by the constraints of the platen.

There is a reserve of strength in a specimen when tensile strain failure of an element occurs at a compressive strain below the compressive strain failure, e_1, and no reserve when it occurs above it. When there is a reserve of strength then further cracking can occur with an increase in load and the variation, Fig. 4.11, is not directly proportional to Equ. 4.1. However, when there is no reserve of strength then the specimen begins to disintegrate and hence the load reduces as soon as the tensile strain of failure is reached and the variations of Figs. 4.10 and 4.11 are directly proportional to Equ. 4.1. The effect of this on the distribution of cracks as the specimen begins to collapse is shown in Fig. 4.12; the extent of cracking reduces as f_Y increases.

An attempt was made to simulate the constraints of a triaxial test specimen by applying a load to the centre of the steel platen, Fig. 4.13. The actual dimensions of the rig used in the triaxial tests of Balmer,

Jones and McHenry[54] are not known although the report states that one platen was a spherical bearing. The results of an analysis without lateral forces, Fig. 4.13, showed that the cracking pattern and the failure load were similar to the analysis, Fig. 4.12, in which the specimen was displaced uniformly, however, the stresses at the edges were 18% less than at the centre. The variation in strength, Figs. 4.10 and 4.11, gave a much closer correlation with the experimental results; the divergence at very high bearing stresses may be due to the non-linear behaviour of the platens. It would therefore appear that the curved relationship between the longitudinal failure load and the lateral restraining forces obtained from triaxial experiments may, in some cases, be a property of the apparatus and not a material property.

The theoretical distribution of cracks in a triaxial compression specimen, in which the load is applied to the centre of the platen, is shown in Fig. 4.14. The combination of the increased longitudinal compressive stress at the centre and hence larger lateral tensile strains with the lateral tensile strains developed at the centre in order to balance the dispersal of the forces, due to the non-uniformity of loading, caused failure to initiate at the centre directly under the platen. A central core was not formed. The failed region is remote from the laterally applied forces whose effects are further reduced by the platen stiffness and hence the lateral forces have a smaller effect on the increase in bearing strength, Figs. 4.10 and 4.11, than in the theoretical specimen with the uniform displacement.

4.4.6.2 Platen restraint

Since the external lateral forces are zero, the lateral stresses within the specimen, f_y, tend towards zero and hence the combination of stresses used in the finite element analysis to determine the load at

which the tensile failure strain is reached, Equ. 4.1, are very nearly the same as in the experiments, Equ. 4.2. There is therefore no significant error in comparing the two dimensional theoretical analysis with the three dimensional experiment.

The theoretical and experimental variation, reported by Price[45], between the mean bearing strength, f_b, and the length of the concrete cylinder, l_c, in terms of its diameter, b_c, is shown in Fig. 4.15. The constraints on the theoretical specimen are the same as in Fig. 4.7. The program did not allow for the tensile stress failure of the concrete. There appears to be a reasonable agreement between the variations.

4.4.6.3 Bearing strength of strip loads

When a specimen is subject to strip loads, Fig. 4.17, the forces can be considered to be dispersed only in the X - Y plane and hence the specimen would appear to be suitable for a two dimensional finite element analysis. The program does not consider the lateral strains in the z direction which are given by

$$e_z = -vf_x/E_c - vf_y/E_c$$

as f_z is assumed to be zero as there is no dispersal of force in this direction. As f_y is normally tensile due to the dispersal of the forces, e_y (Equ. 4.1) will usually be greater than e_z and therefore the error in ignoring e_z when determining the load at which e_t is reached may be considered to be insignificant.

The finite element results are compared with the experimental results of Niyogi[58] and the empirical variations of Williams[59] in Fig. 4.16. The Mode 3 program was used as it allowed for the tensile stress failure caused by the dispersal of the forces. The finite element results are plotted in terms of the crushing strength of an unrestrained element, f_{ce}.

There is a reasonable agreement between the variations, the finite element analysis being conservative at low values of b_a/b_c.

4.4.7 Summary

A two dimensional, plane stress, finite element program has been written which allows the concrete to fail in tension and compression. Concrete is assumed to fail in tension when the principal tensile stress reaches a critical value and to fail in compression when first the lateral tensile strain induced by compressive forces reaches a critical value and then the longitudinal compressive strain exceeds another critical value.

In order to remain an elastic analysis the program assumes sudden changes in stiffness when various failure criteria are reached. This may not occur in practice. However, the procedures predict quite well the distribution of cracks, the effect of platen restraint, the triaxial strength of concrete cylinders and the bearing strength under strip loads.

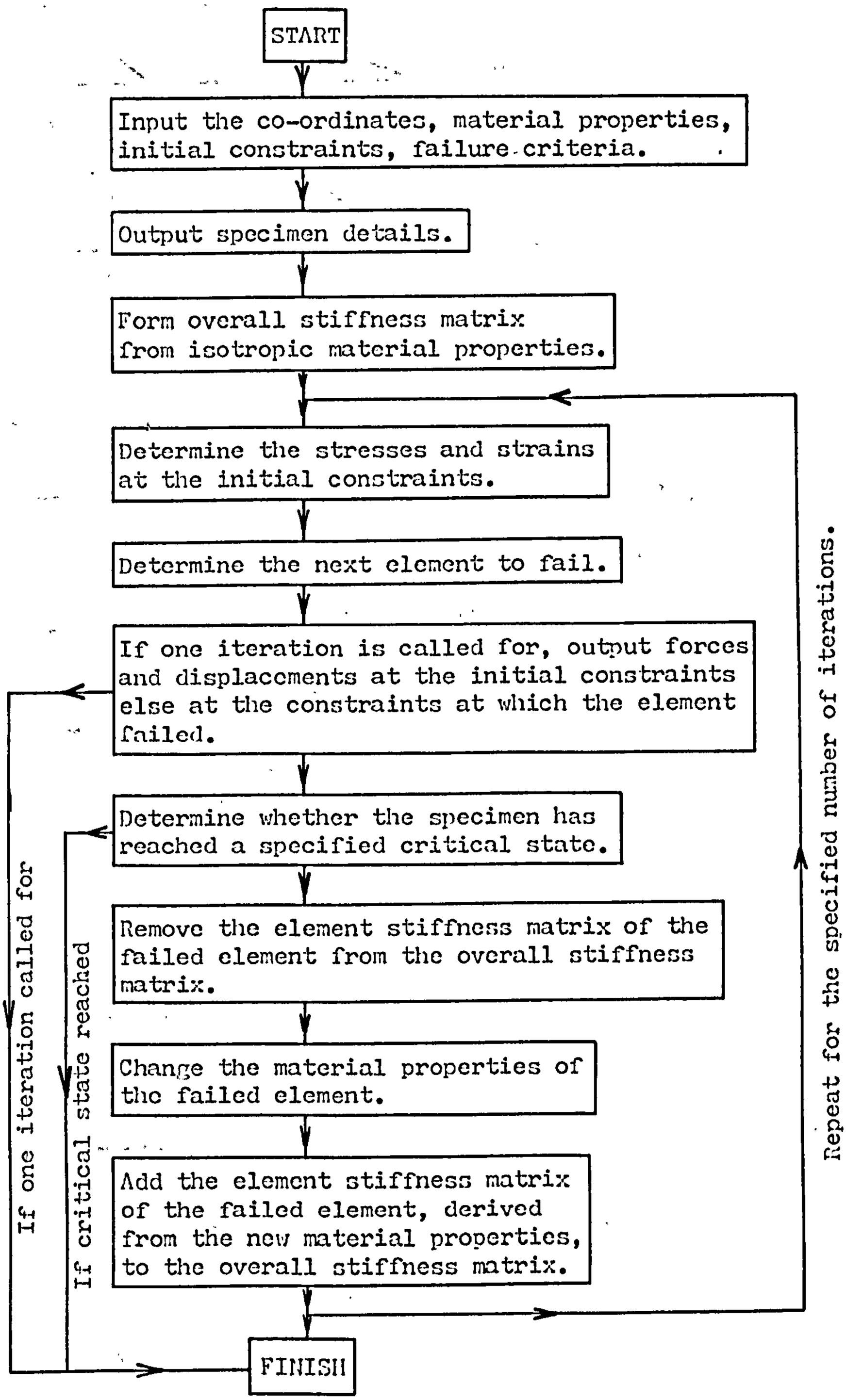

Fig. 4.1 Flow diagram of the finite element program.

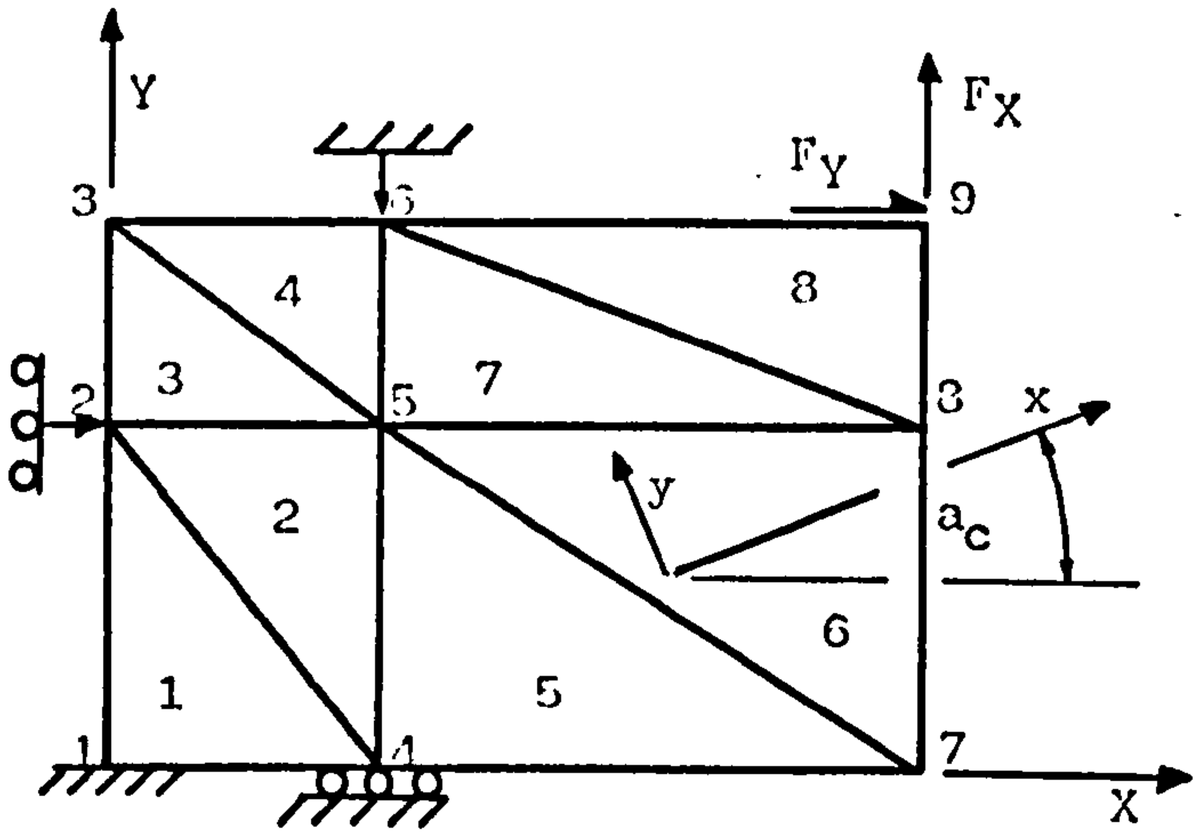

X,Y global axes
x,y local axes
a_c angle between co-ordinate systems
crack
node fully restrained
node fully restrained in Y direction only, free to slide in X direction
F_X resultant of constraint in X direction
constraint applied to node in Y direction, fully restrained in X direction
constraint applied to node in X direction, free to slide in Y direction

Fig. 4.2 A finite element simulation.

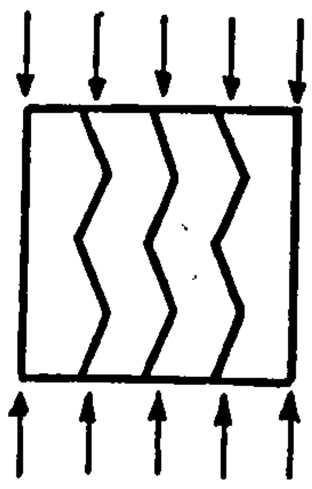

Fig. 4.3 Schematic representation of cracking induced by compressive forces.

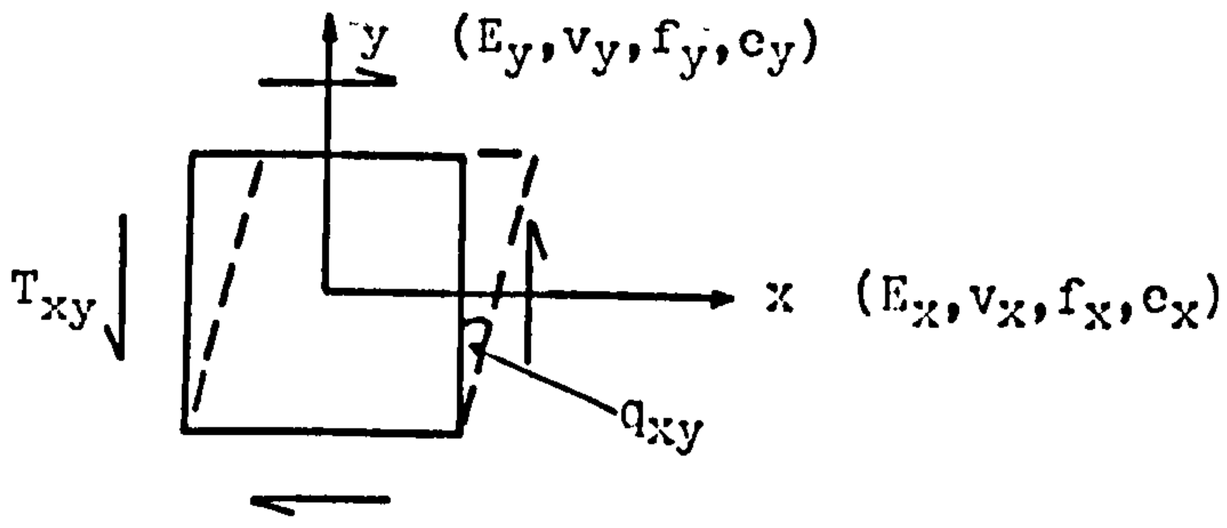

Fig. 4.4 Orthotropic properties of the concrete.

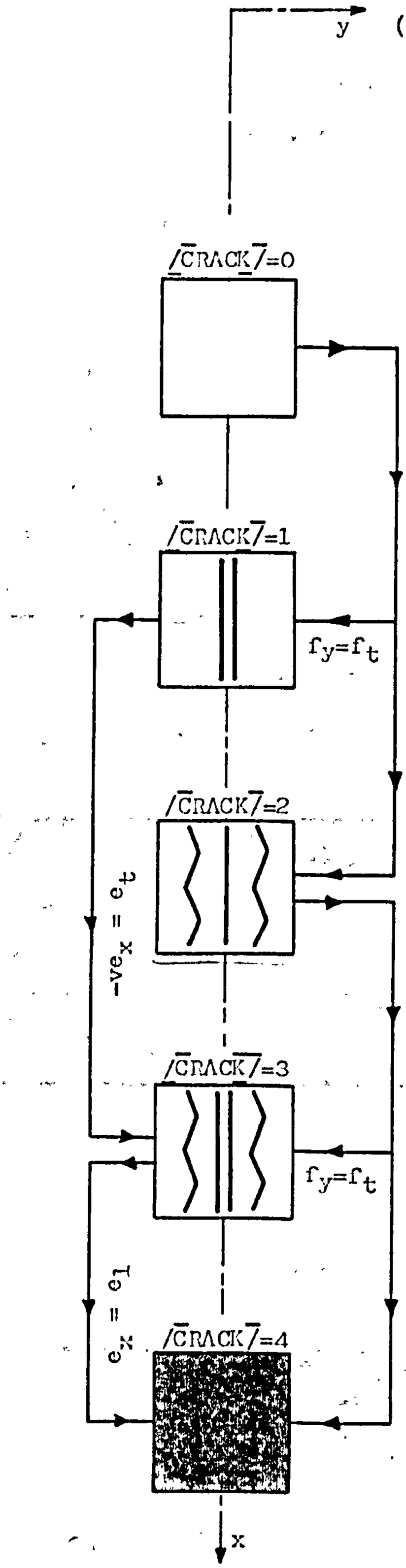

Material properties

$E_x = E_y = E_c$

$v_x = v_y = v$

$E_x = E_c$

$E_y = v_x = v_y = 0$

$E_x = 0.4E_c$ $E_y = E_c$

$v_x = v_y = 0$

$E_x = 0.4E_c$

$E_y = v_x = v_y = 0$

$E_x = E_y = v_x = v_y = 0$

Fig. 4.5 Sequence of failure of a concrete element.

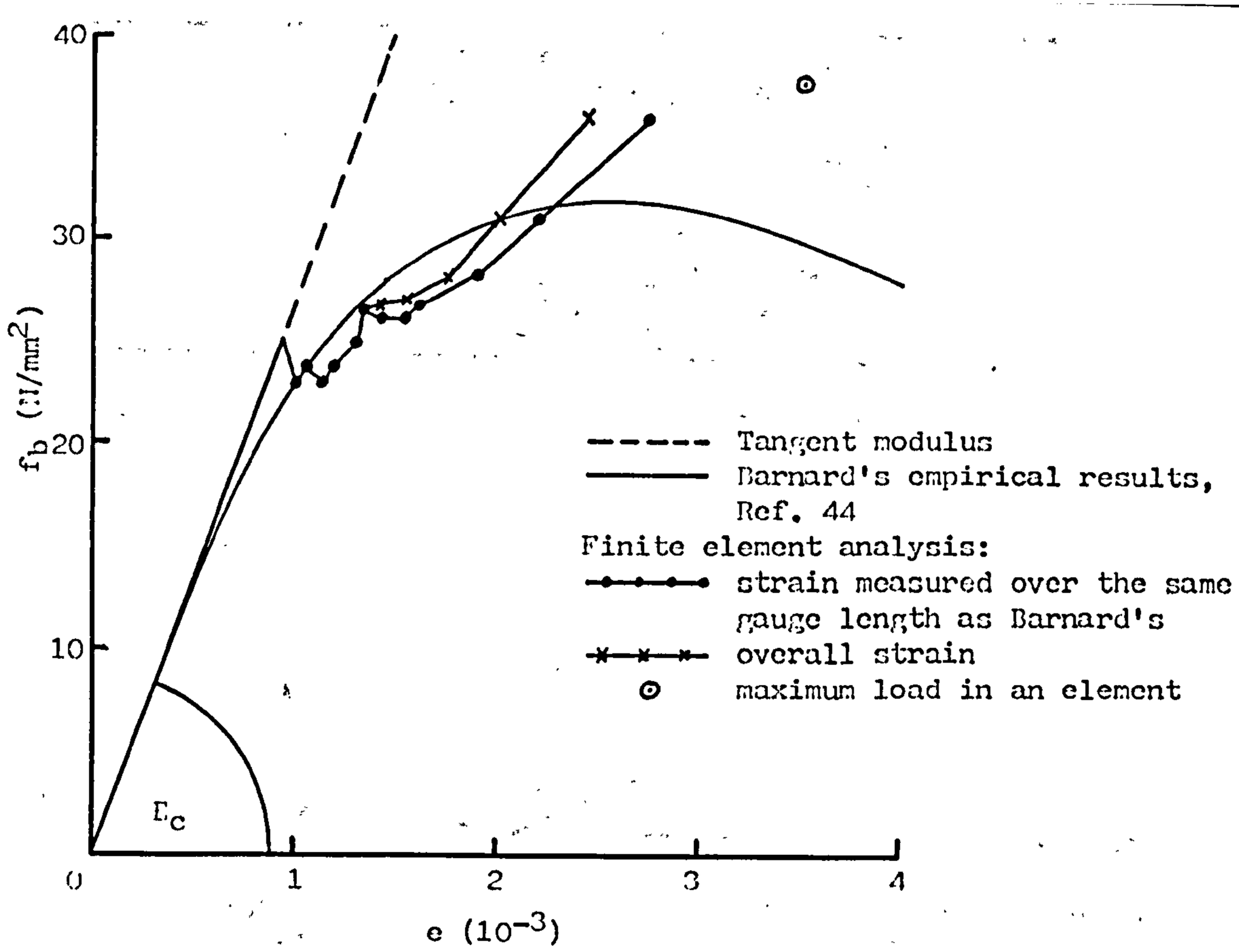

Fig. 4.6 Simulation of Barnard's stress-strain curve for concrete.

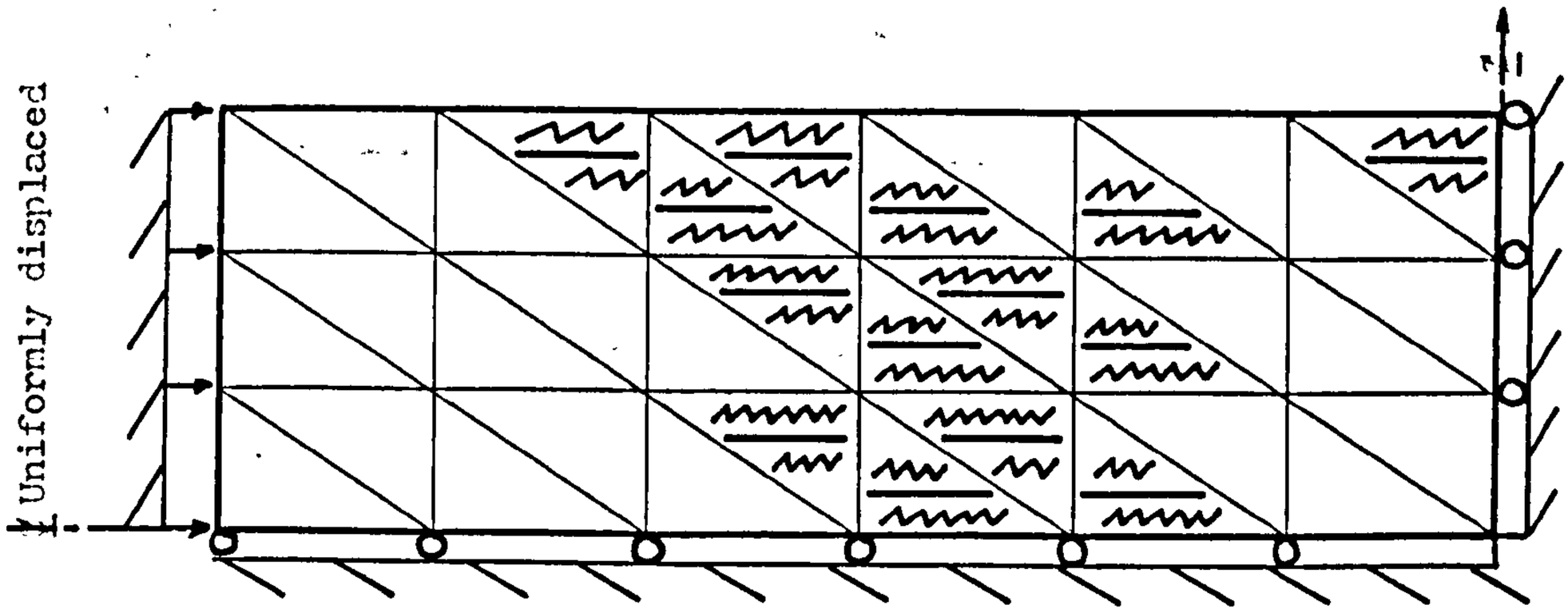

Fig. 4.7 Theoretical analysis of Barnard's specimen.
Failure of the concrete at the discontinuity point.

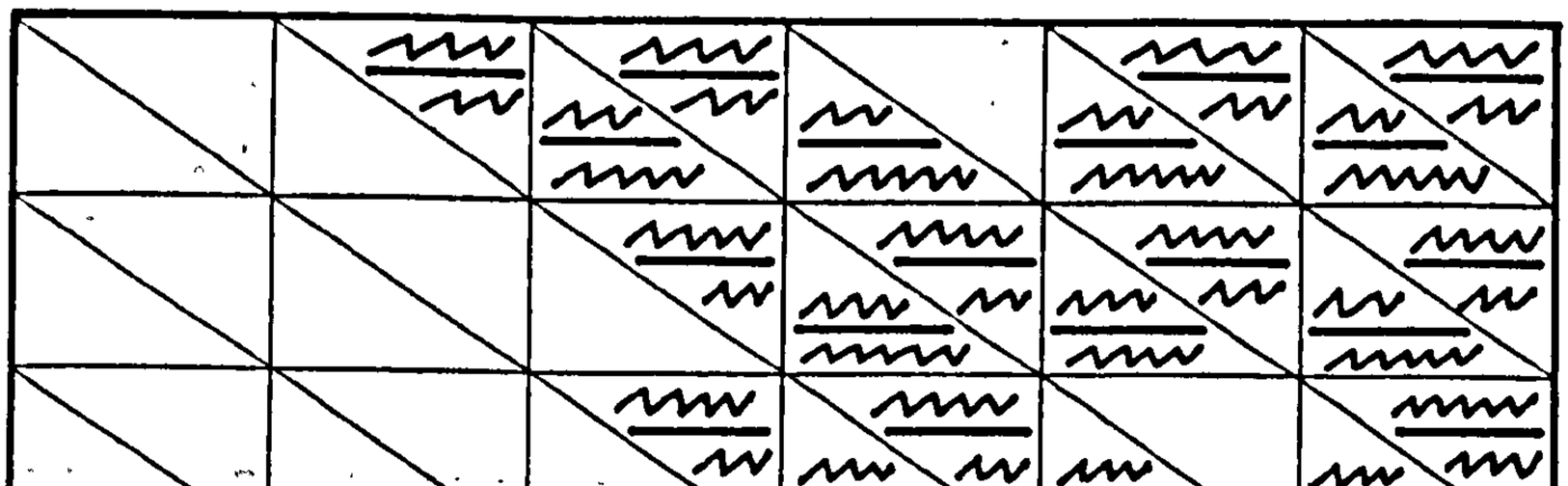

Fig. 4.8 Theoretical analysis of Barnard's specimen.
Failure of the concrete at the maximum load.

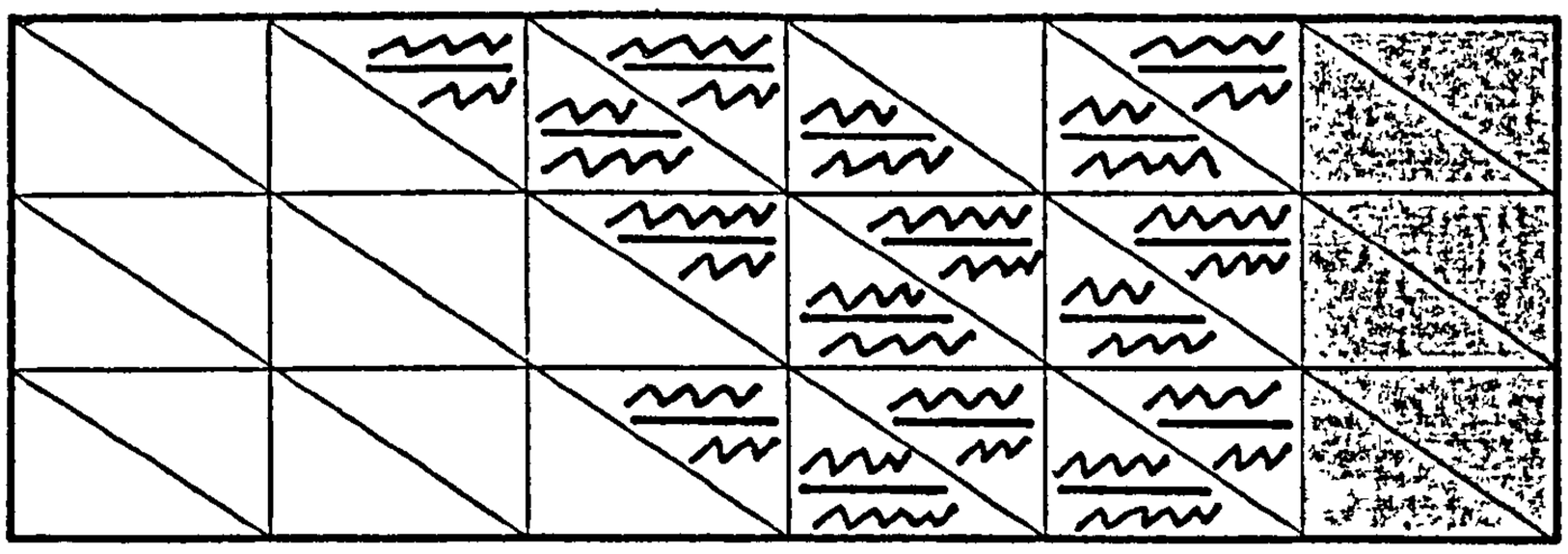

Fig. 4.9 Theoretical analysis of Barnard's specimen.
Failure of the concrete at the collapse of the specimen.

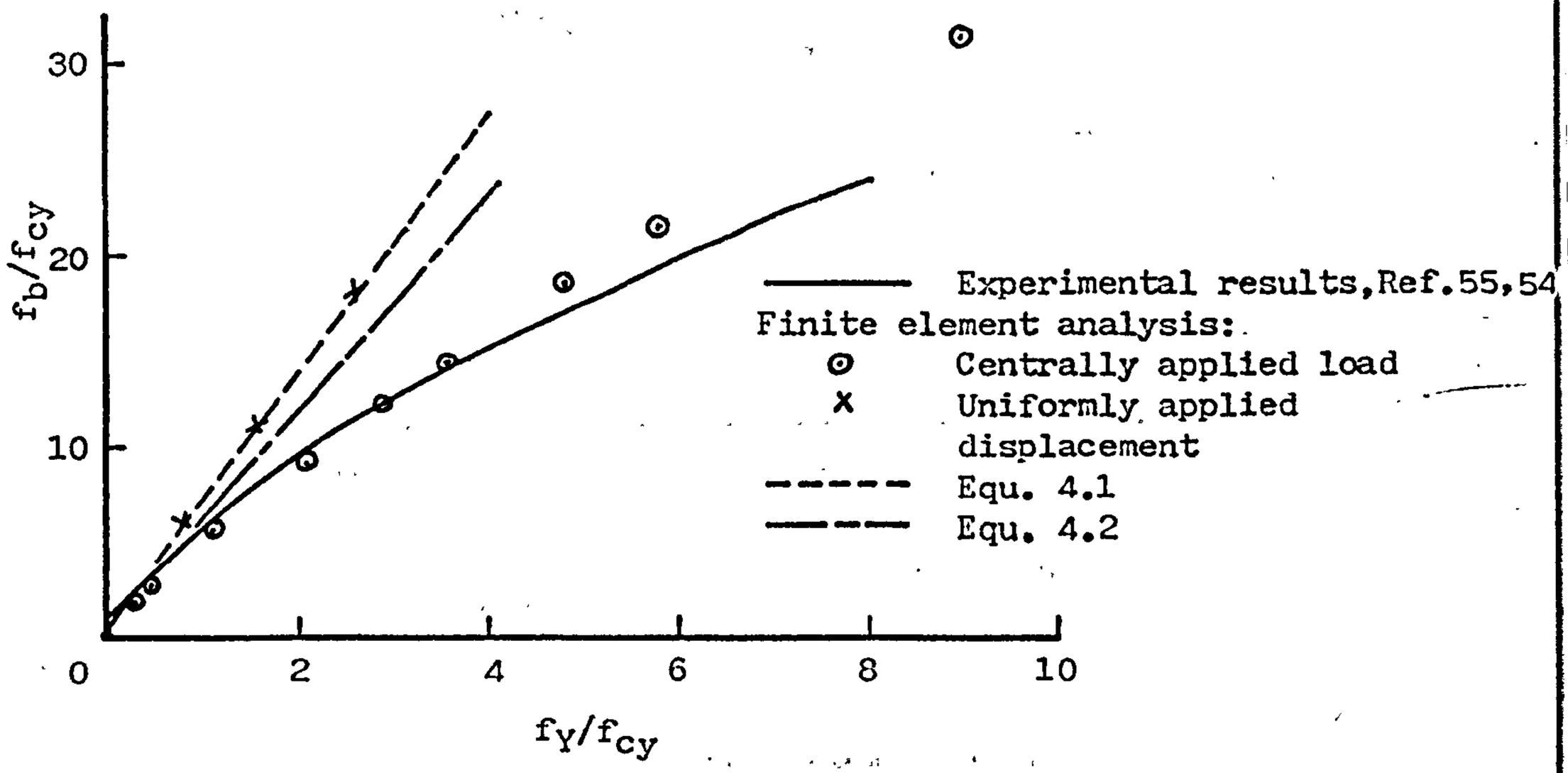

Fig. 4.10 Theoretical and experimental results of triaxial compression tests.

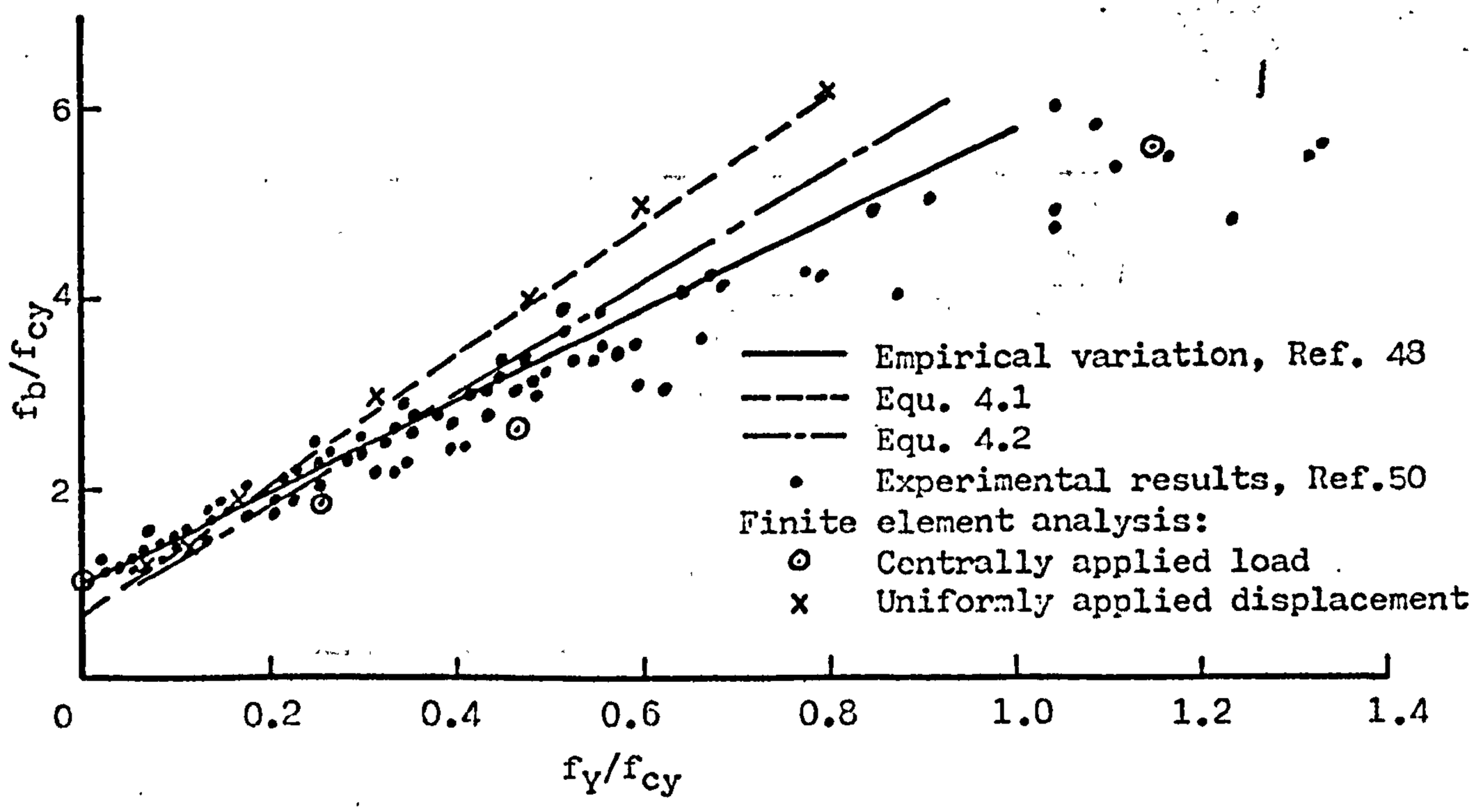

Fig. 4.11 Theoretical and experimental results of triaxial compression tests at low lateral stresses.

Cracking near collapse.
Maximum load:
f_X is equivalent to f_{cy}
as $f_Y = 0$

Cracking at collapse.
Maximum load:
$f_X = 1.20 f_{cy}$,
$f_Y = 0.07 f_{cy}$

Cracking at collapse.
Maximum load:
$f_X = 1.38 f_{cy}$,
$f_Y = 0.12 f_{cy}$

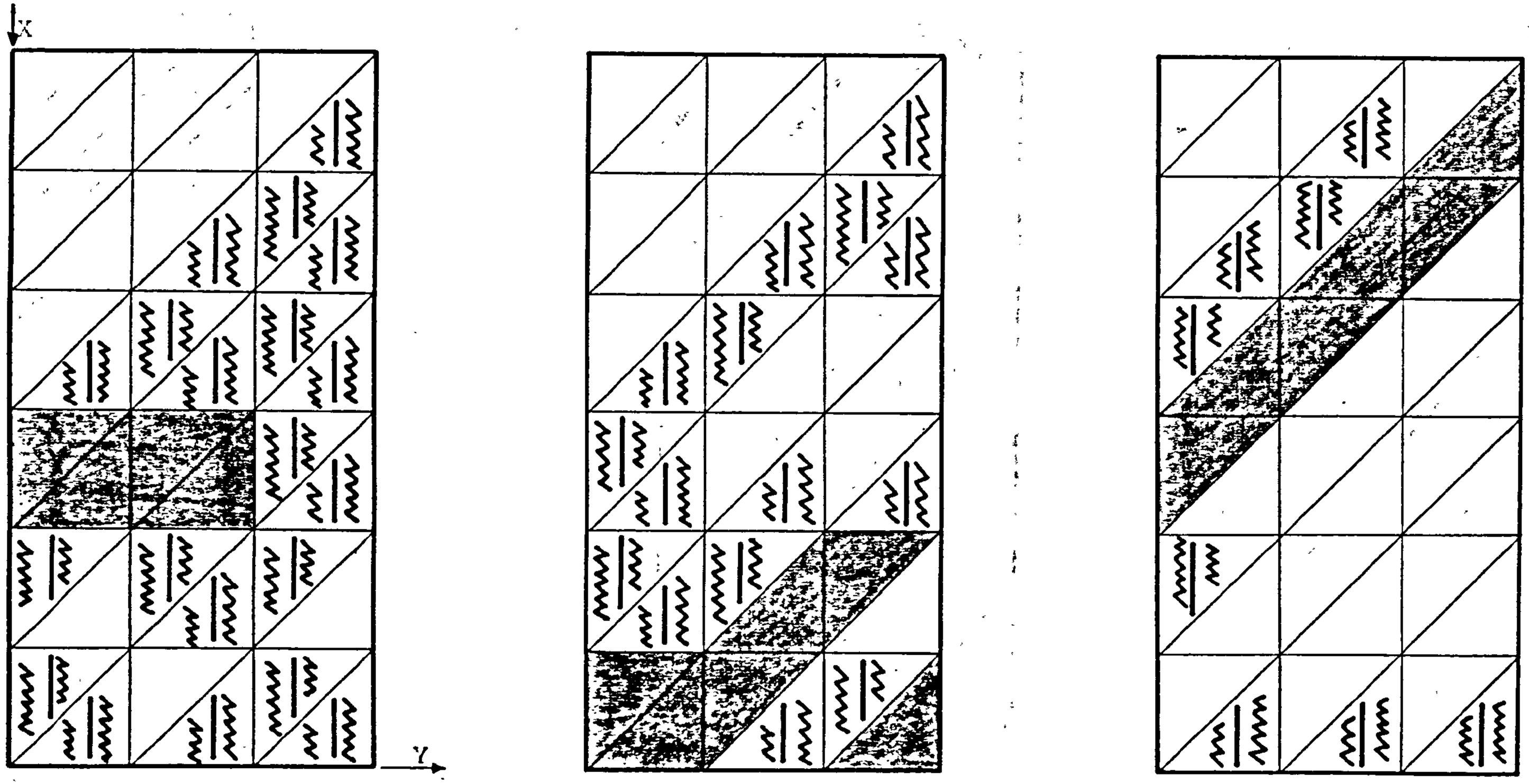

Fig. 4.12 Uniform displacement applied in a theoretical triaxial compression test.

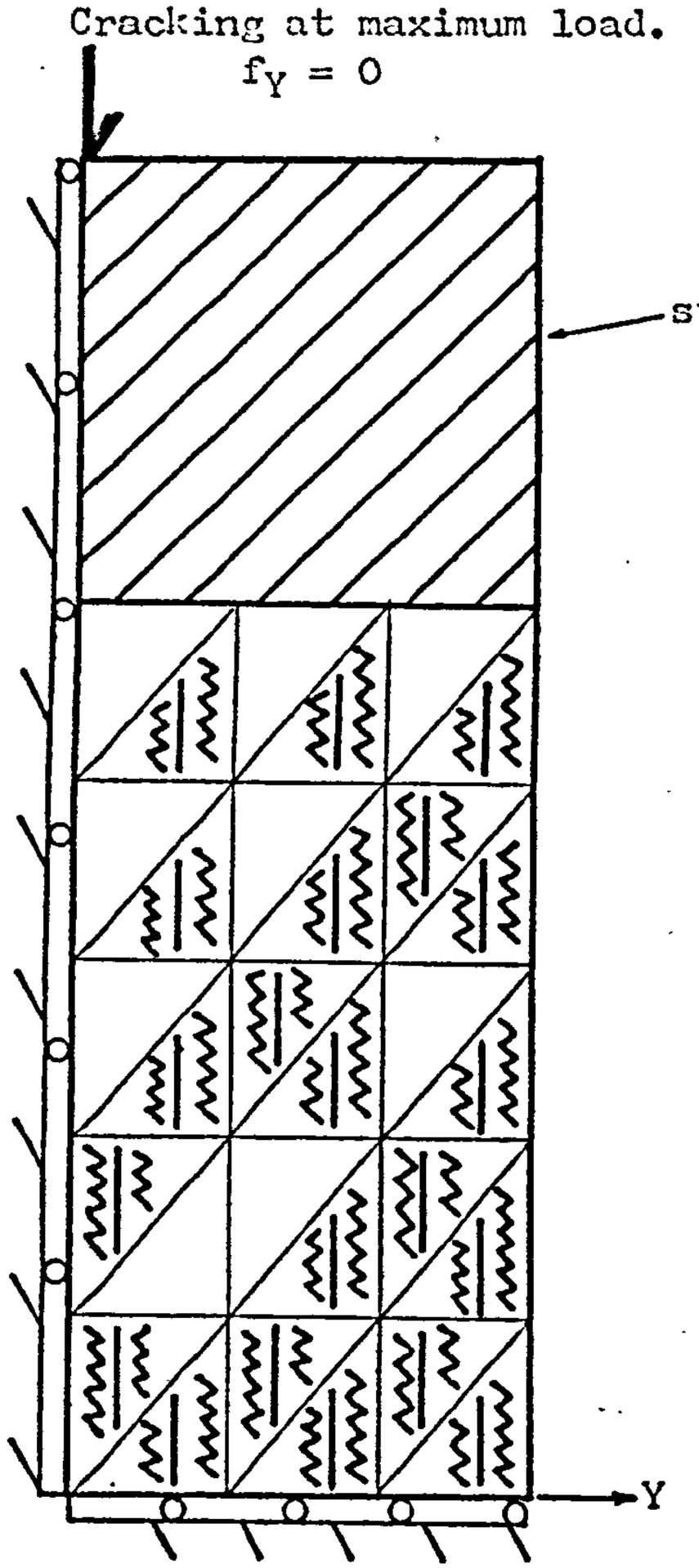

Fig. 4.13 Load applied to the centre of the platen of a theoretical specimen.

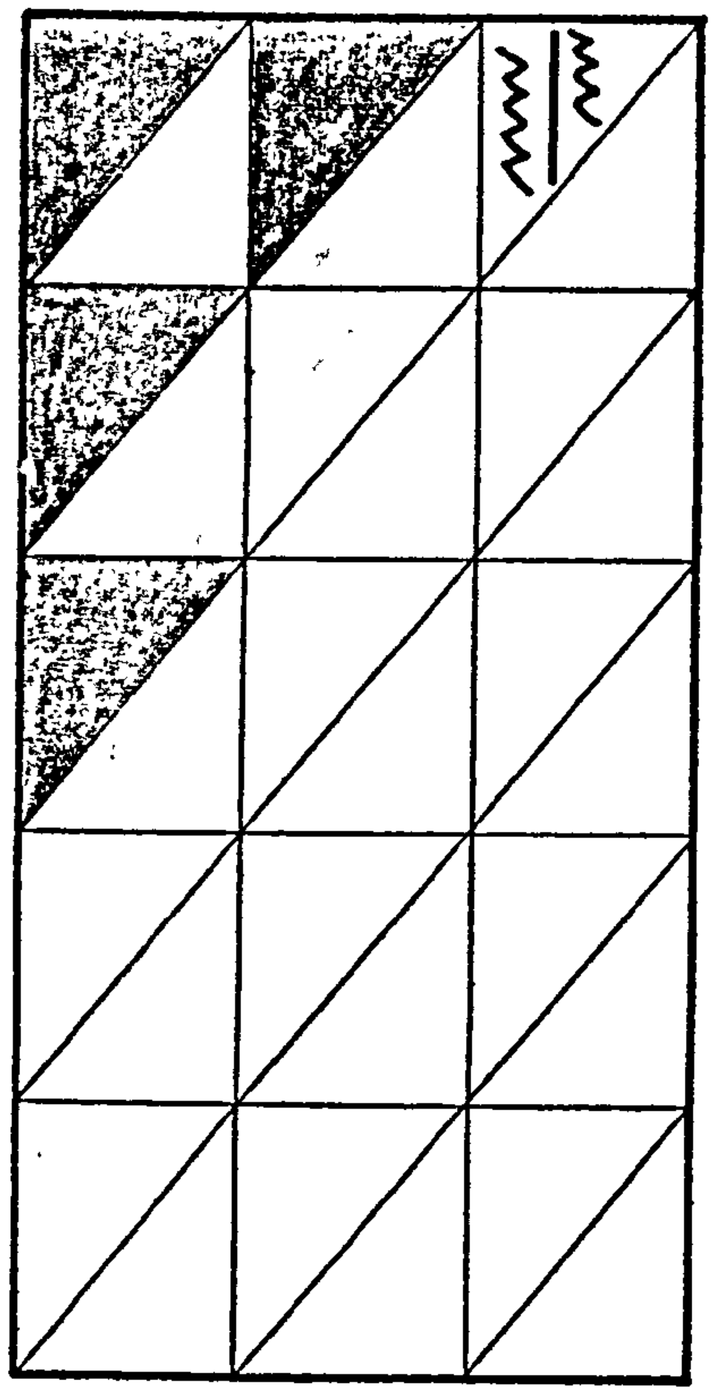

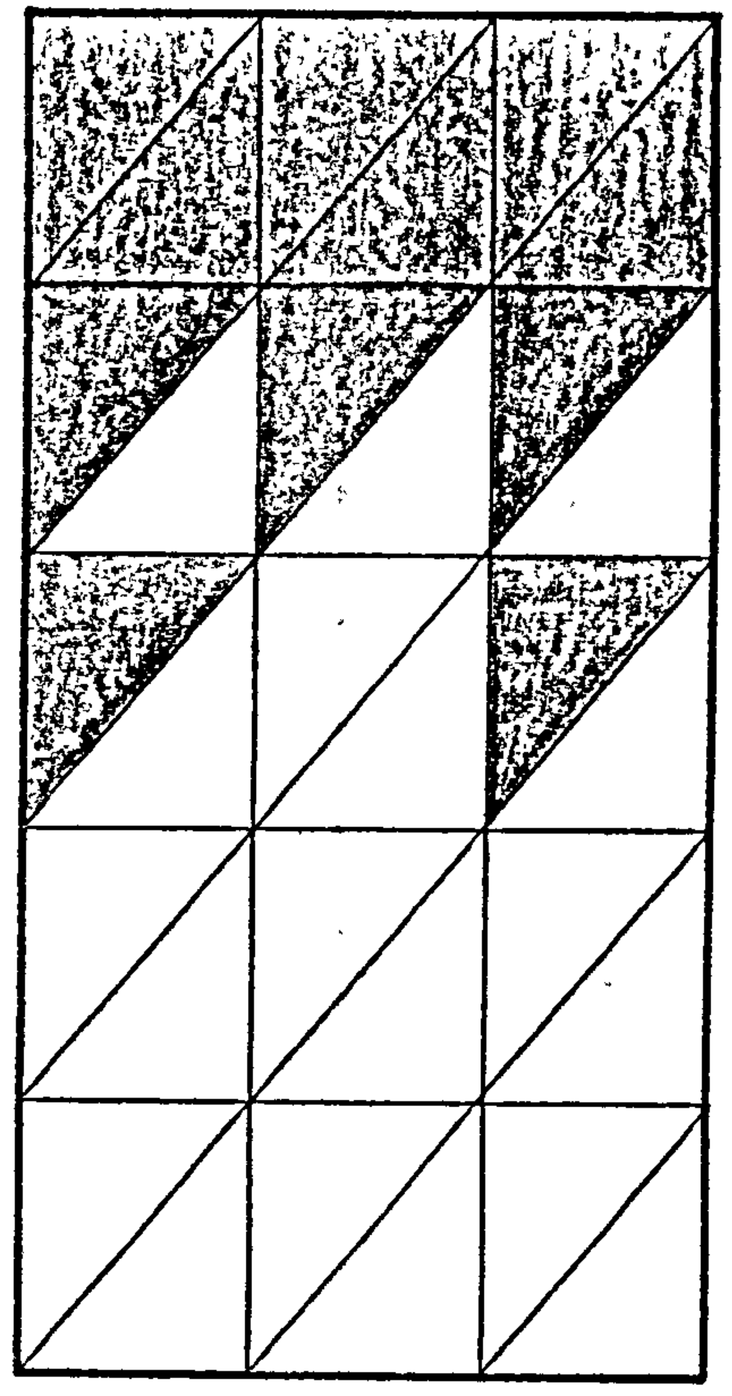

Fig. 4.14 Load applied to the centre of the platen in a theoretical triaxial compression test.

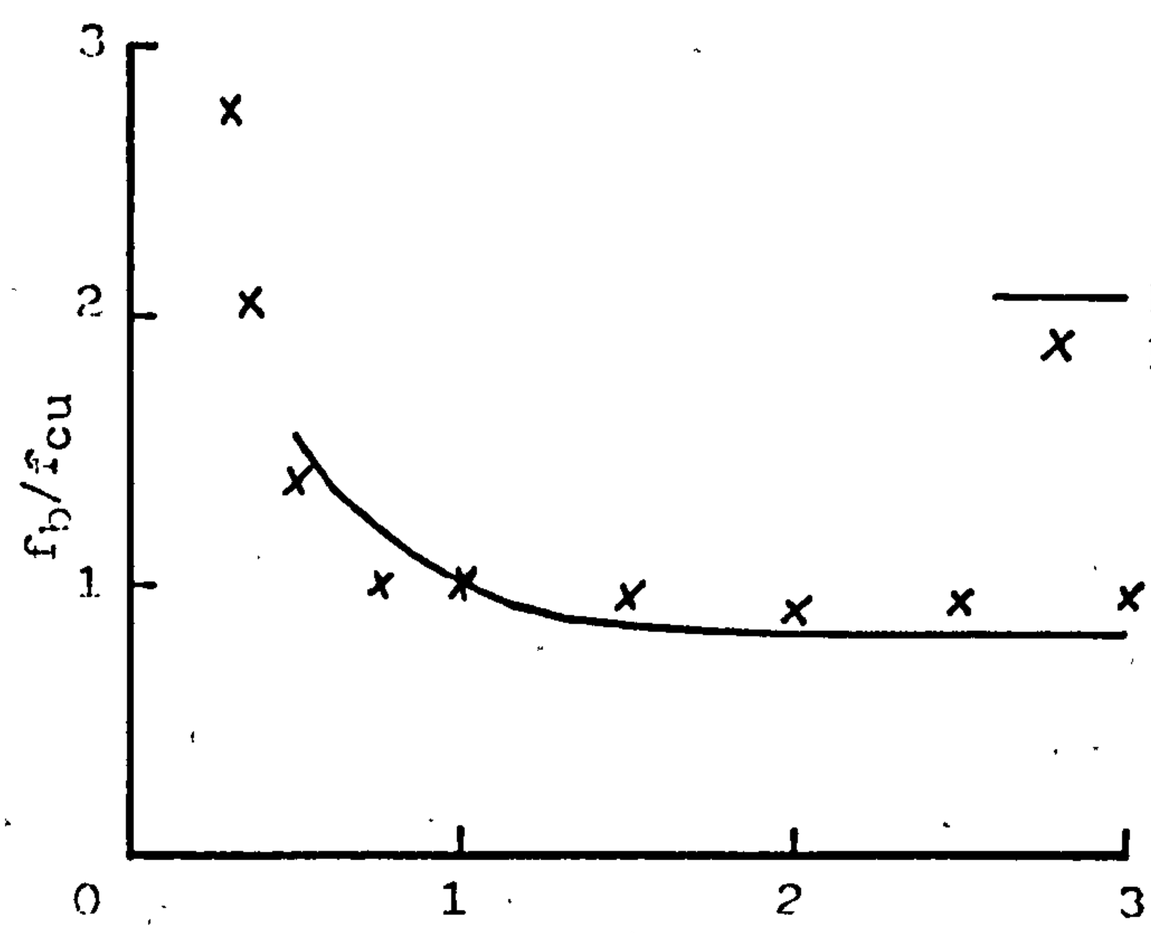

Fig. 4.15 Theoretical and experimental effect of the platen restraint.

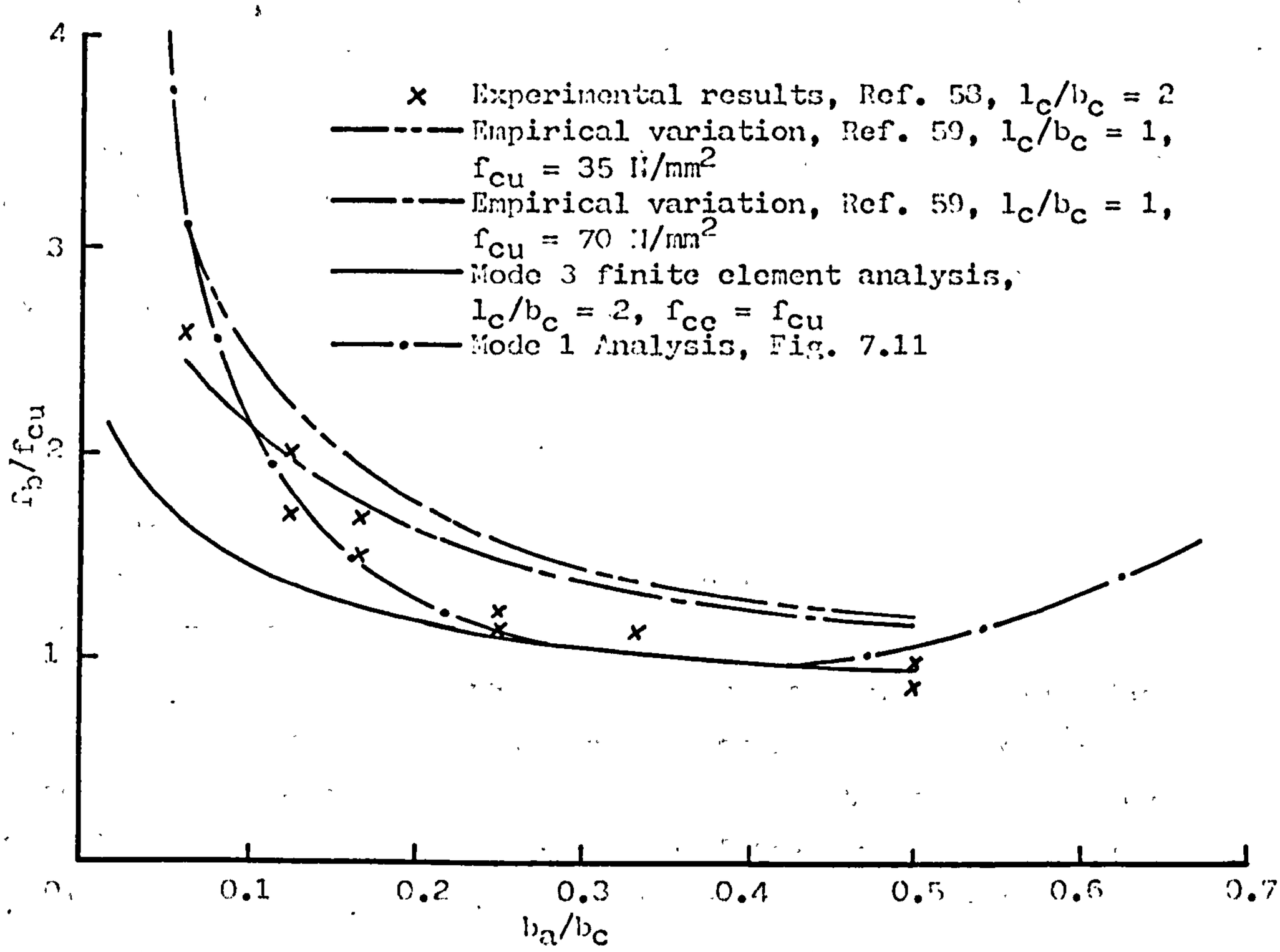

Fig. 4.16 Theoretical and experimental bearing strengths of concentric strip loads.

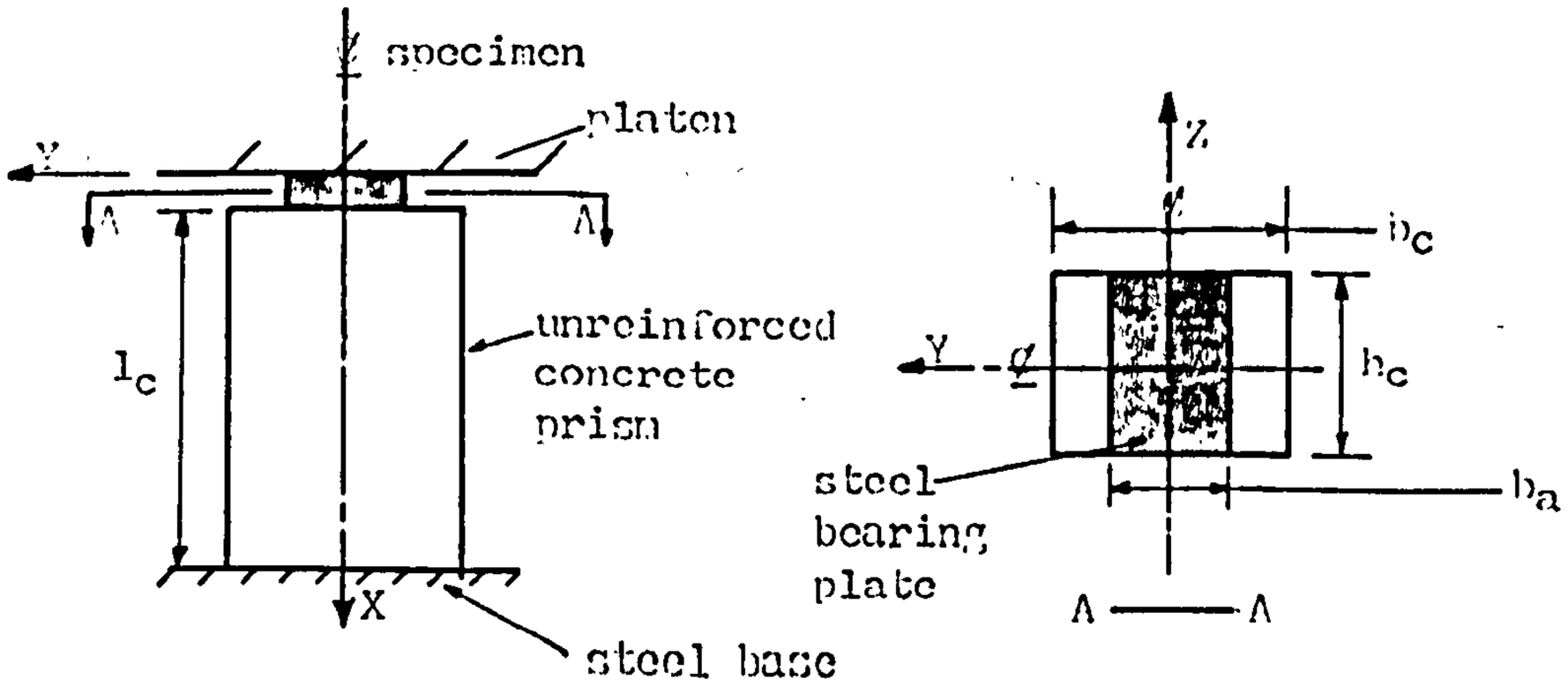

Fig. 4.17 Prism subjected to a concentric strip load.

Chapter Five

THE EXPERIMENTAL WORK

5.1 INTRODUCTION

The manufacture, testing procedures, material properties, specimen constraints, maximum strengths and failure modes of a series of tests are described in this chapter. The results are used, in Chapters Six to Ten, either to validate a finite element analysis or to determine empirical relationships between two dimensional finite element analyses and the three dimensional experiments.

It was concluded from the literature review, Sect 2.4, and statistical analysis, Chapter 3, that the variation between the empirically derived rules, Fig. 2.1, was not due to experimental error which was found to be comparatively small but due to the different modes of failure, splitting of the slab and failure of the shank of the stud, and the effect upon these of the parameters and restraints of the push tests. A series of push tests was therefore devised in order to analyse each of these modes of failure separately.

5.2 MANUFACTURE AND TESTING PROCEDURE

5.2.1 Push tests

The flanges of the steel beams were greased and the specimens cast in the upright position, Fig. 1.1.

A typical test rig and specimen is shown in Fig. 1.1. The slabs were bedded to the steel base using dental paste. The spreader beams, which were simply supported by the flanges, were butted against the web and the ball joint was placed at the centre of the flanges. The load was applied by raising the base at a constant rate of 5½mm/hour; the cross-head being stationary. The slips were measured with dial gauges at the level of the studs. The total load was automatically registered on a dial of the rig.

5.2.2 Eccentric strip loads on concrete prisms

The concrete prisms, Fig. 5.33, were cast in steel moulds.

The specimen, Fig. 5.33, was tested by using the same procedure and rig as used in a split tensile test[57].

5.3 MATERIAL PROPERTIES

5.3.1 Concrete

5.3.1.1 Mix design

The concrete consisted of a normal-density gravel of maximum size 10mm, zone 3 sand and Rapid Hardening Portland cement. The variation between the cube strength and water/cement ratio is shown in Fig. 5.23. The aggregates were tested according to BS812[60].

5.3.1.2 Variation of properties

The variation between the cube strength of the concrete, f_{cu}, and the split tensile strength, f_{ct}, modulus of rupture strength, f_{md}, modulus of elasticity, E_c, cylinder strength, f_{cy}, and density are given in Figs. 5.22, 5.24 to 5.26. The cube strengths, split cylinder strengths and densities are the mean of three results, the modulus of rupture strengths and the cylinder strengths are the mean of two results and the modulus of elasticity results are individual results. The materials were tested according to BS1881[57].

5.3.2 Studs

The studs were supplied by Crompton Parkinson and welded with equipment manufactured by them.

5.3.2.1 Dimensions of welded studs and their ferrules

The dimensions, Table 5.1, are each a mean of over twenty measurements. An ideal weld was considered to be one in which the weld collar was of a uniform depth and fully homogeneous with the shank, Fig. 5.10. When the weld collar was not fully homogeneous, Fig. 5.11, or not uniform, Fig. 5.9, the mean depth of the weld collar which was fully homogeneous was measured. During welding the molten metal must

have eroded the inside of the ferrule as the diameter of the weld collar was slightly greater than the internal diameter of the ferrule. However, the variation was small; the measurements ranged from 96% to 103% of the mean. The molten metal did not and is not intended to fill the full internal depth of the ferrule; this not only caused large variations between the depths of weld collars, the measurements ranged from 73% to 128% of the mean, but also variations in the depth of the individual weld collars, Fig. 5.9.

5.3.2.2 Strength of welded studs

The specimens, Fig. 5.15, were tested by applying an axial tensile force through the head of the stud and the flange of the beam. The majority of the specimens, Table 5.2, failed along the shank of the stud, Fig. 5.15,however, two failed at the weld-collar/shank interface at 108% and 95% of the mean shank failure load. The strength of the weld material was tested by turning down the collar to 18.5mm, in which case the stud failed along the shank, and to 15.1mm ($0.79d_s$), Fig. 5.21. The mean axial strengths, Table 5.3, were inversely proportional to the diameter of the stud and the strength of the weld collar was 13% stronger than the mean axial strength of the stud. It would appear that the flange material, which is mild steel, does not reduce the strength of the weld.

5.3.2.3 Coupon tests

The coupons, which were taken from the shanks of unwelded studs, were tested according to BS18[61]. A typical stress-strain relationship is shown in Fig. 5.27. The strengths, Table 5.3,were almost the same as those of the welded studs.

5.4 UNREINFORCED PUSH TESTS

5.4.1 Specimens which failed due to splitting

The studs were still intact after the concrete had split into two.

5.4.1.1 Single studs

The details of the specimens are given in Table 5.4.

The cracking pattern was the same as in the lightly reinforced specimen, Fig. 5.1, except that the slab parted about the longitudinal crack at the maximum load. The lateral cracks were visible before the maximum load was reached and the longitudinal cracks, behind and in front of the stud, i.e. the split, which were only visible when or soon after the maximum load was reached, spread very rapidly causing the slab to split into two and the load to reduce to zero.

5.4.1.2 Longitudinally spaced studs

The details of the specimens are given in Table 5.5.

The cracking pattern for specimens in which the studs were widely spaced is shown in Fig. 5.3. Splitting occurred at the maximum load, the concrete had disintegrated in the triangle in front of the studs and the lateral cracks were either non-existent or very localized. The split was vertical, Fig. 5.4.

The cracking pattern for specimens in which the studs were closely spaced is shown in Fig. 5.5. The slab split, at the maximum load, below the bottom stud and above the top stud and between the studs the slab parted along planes of maximum shear.

5.4.1.3 Laterally spaced studs

The details of the specimen are given in Table 5.6.

The cracking pattern, Fig. 5.2, was similar to that of a single

stud; the lateral cracks formed first and the longitudinal cracks formed at the maximum load.

5.4.1.4 Staggered studs

The details of the specimens are given in Table 5.7.

The slab split below the bottom stud and above the top stud at the maximum load. Between the studs, Figs. 5.6 and 5.7, the slab parted along the planes of maximum shear and the remaining concrete showed signs of splitting. When the studs were narrowly spaced, Fig. 5.6, the shear planes criss-crossed forming struts between the studs, and when the studs were widely spaced, Fig. 5.7, the concrete sheared along longitudinal planes at the outer edges of the studs.

5.4.2 Specimens which failed across the shank

The details of the specimens are given in Table 5.8. The height of the failure zone, h_f, was measured at the position at which the stud first cracked, Fig. 5.11.

The studs broke at the weld-collar/shank interface, Figs. 5.10 and 5.11, and had hardly any permanent deformation, Fig. 5.8. The slab exhibited only localized failure, Fig. 5.17, about the front of the stud; the cavity, Fig. 5.17, was probably gouged out by the weld collar as the specimen failed.

5.4.3 Effect of base restraint and weld collar

The details of the specimens are given in Table 5.9.

The specimens in which the weld collar was removed, Fig. 5.12, failed at the flange/shank interface, Fig. 5.13. The shank had hardly any permanent deformation, Fig. 5.12.

Those specimens which did not have the weld collar removed failed when the slab split, Fig. 5.14; a triangle of concrete broke away at the front with the usual split behind the stud.

The extra passive lateral restraint, Fig. 5.30, did not change the failure mode but did increase the strengths.

5.5 REINFORCED PUSH TESTS

5.5.1 Transverse reinforcement fully anchored

The details of the specimens are given in Table 5.10.

In most of the specimens the split was visible at the top of the slab soon after the maximum load was reached, and in all of the specimens the split was visible along the soffit, Fig. 5.1, when it was exposed at the end of the experiment. The strength reduced gradually after the maximum load was reached and even when the load had reduced to half the maximum load the studs were found to be intact, but they had a large permanent deformation. The lateral cracks occurred before the maximum load.

5.5.2 Uniformly distributed transverse reinforcement

The details of the specimens are given in Table 5.11.

The studs broke at the weld-collar/shank interface. The mode of failure is described in Sect. 5.4.2.

5.5.3 Specimens reinforced according to the standard push test of the Bridge Code[7]

The details of the specimens are given in Table 5.12.

The studs broke at the weld-collar/shank interface and the slabs showed signs of splitting.

5.6 PUSH TESTS WITH REINFORCEMENT LOOPED AROUND THE STUD

The lateral cracks, Figs. 5.18 and 5.19, which occurred first, were followed by either the longitudinal crack, Fig. 5.18, which caused the concrete cover to the studs to break away, or by wedges of concrete, Fig. 5.19, breaking away; both failure mechanisms exposed the stud and the transverse reinforcement, Fig. 5.20. The reinforcement formed a cone of concrete around the studs, which separated from the concrete behind it.

5.6.1 Single studs

The details of the specimens are given in Table 5.13.

The slab split along the centre line of the stud.

5.6.2 Double studs

The details of the specimens are given in Table 5.14.

5.7 ECCENTRIC STRIP LOADS ON CONCRETE PRISMS

The details of the specimens are given in Table 5.15.

The specimens failed due to splitting.

Table 5.1 The mean dimensions of welded studs and their ferrules.

Details:
The diameter of the weld collar was measured above the notches produced by the gas vents.

Type of stud	22X100	19X100	19X75	13X65
Height of stud (mm)	100	99½	75½	64
Diameter of shank (mm)	22.18	18.95	18.95	12.76
Diameter of head (mm)	34.9	29.9	29.9	25.3
Height of shank (mm)	83.0	87.3	63.3	56.6
Diameter of weld collar (mm)	29.0	25.9	25.9	16.8
Height of weld collar (mm)	6.9	5.0	5.0	3.2
Internal diameter of ferrule (mm)	27.7	23.4	23.4	16.6
Internal depth of ferrule (mm)	10.1	9.9	9.9	4.3

Table 5.2 Tensile tests on welded studs.

Type of stud	P_{ea} (kN)	Position of failure zone
13X65	81	Along shank
13X65	82	Along shank
19X100	171	Along shank
19X100	169	Along shank
19X100	184	At weld-collar/shank interface
22X100	223	Along shank
22X100	229	Along shank
22X100	215	At weld-collar/shank interface
19X100*1	169	Along shank
19X100*2	125	In area of reduced diameter

*1 Weld collar turned down to a diameter of 18.46mm
*2 Weld collar turned down to a diameter of 15.06mm

Table 5.3 The mean strength of the stud material.

Type of stud	Tests on welded studs		Coupons from shank	
	No. of specimens	f_{su} (N/mm^2)	No. of coupons	f_{su} (N/mm^2)
13X65	2	639		
19X100	3	620	2	611
22X100	3	576	1	562
19X100*	1	703		

* Weld collar turned down to a diameter of 15.06mm.

Table 5.1 The mean dimensions of welded studs and their ferrules.

Details:
The diameter of the weld collar was measured above the notches produced by the gas vents.

Type of stud	22X100	19X100	19X75	13X65
Height of stud (mm)	100	99½	75½	64
Diameter of shank (mm)	22.18	18.95	18.95	12.76
Diameter of head (mm)	34.9	29.9	29.9	25.3
Height of shank (mm)	83.0	87.3	63.3	56.6
Diameter of weld collar (mm)	29.0	25.9	25.9	16.8
Height of weld collar (mm)	6.9	5.0	5.0	3.2
Internal diameter of ferrule (mm)	27.7	23.4	23.4	16.6
Internal depth of ferrule (mm)	10.1	9.9	9.9	4.3

Table 5.2 Tensile tests on welded studs.

Type of stud	P_{ea} (kN)	Position of failure zone
13X65	81	Along shank
13X65	82	Along shank
19X100	171	Along shank
19X100	169	Along shank
19X100	184	At weld-collar/shank interface
22X100	223	Along shank
22X100	229	Along shank
22X100	215	At weld-collar/shank interface
19X100*1	169	Along shank
19X100*2	125	In area of reduced diameter

*1 Weld collar turned down to a diameter of 18.46mm
*2 Weld collar turned down to a diameter of 15.06mm

Table 5.3 The mean strength of the stud material.

Type of stud	Tests on welded studs		Coupons from shank	
	No. of specimens	f_{su} (N/mm^2)	No. of coupons	f_{su} (N/mm^2)
13X65	2	639		
19X100	3	620	2	611
22X100	3	576	1	562
19X100*	1	703		

* Weld collar turned down to a diameter of 15.06mm.

Table 5.4 Push tests. Unreinforced slabs with single studs which failed due to splitting.

Details:
Specimen as in Fig. 1.1, except that a single stud was placed along the centre line of the web. $l_p/b_c = 2$. $l_b = 150mm$.

Specimen No.	Type of stud	f_{cu} (N/mm^2)	f_{ct} (N/mm^2)	b_c (mm)	h_c (mm)	P_e (kN)
UCs1	19X75	27	2.4	152	111	57
UCs2	19X75	31	2.3	252	105	57
UCs3	19X75	27	2.4	358	102	69
UCs4	19X100	32	2.0	151	131	61
UCs5	19X100	32	2.0	190	126	58
UCs6	19X100	25	2.0	256	126	65
UCs7	19X100	25	2.0	299	126	71
UCs8	19X100	37	3.0	300	127	87
UCs9	19X100	46	3.2	300	128	117
UCs10	19X100	55	3.6	300	128	125
UCs11	19X100	62	3.8	300	127	130
UCs12	19X100	64	4.3	300	127	131
UCs13	19X100	32	2.0	360	126	72
UCs14	19X100	32	2.8	399	126	89
UCs15	19X100	53	3.8	401	176	129
UCs16	22X100	32	2.3	168	130	65
UCs17	22X100	31	2.3	229	127	50
UCs18	22X100	32	2.3	300	126	94
UCs19	22X100	30	2.5	360	126	85
UCs20	22X100	30	2.3	399	125	94
UCs21	13X65	36	3.2	100	90	37
UCs22	13X65	36	3.2	100	90	38

where U = Unreinforced slab
C = Concrete split
s = single stud per slab

Table 5.5 Push tests. Unreinforced slabs with longitudinally spaced studs which failed due to splitting.

Details:
Specimen as in Fig. 1.1, except that the studs were longitudinally spaced, Fig. 5.28, along the centre line of the web. 19X100 studs. $b_c = 300mm$. $h_c = 127mm$. $l_p = 950mm$. $l_b = 50mm$.

Specimen No.	s_s (mm)	No. of studs	f_{cu} (N/mm^2)	f_{ct} (N/mm^2)	P_e (kN)
UC11	60	6	32	2.6	25
UC12	100	5	34	2.7	37
UC13	150	5	28	2.1	43
UC14	300	3	32	2.6	71

where l = studs longitudinally spaced

Table 5.6 Push tests. Unreinforced slabs with laterally spaced studs which failed due to splitting.

Details:
Specimen as in Fig. 1.1. 19X100 studs. b_c = 300mm. h_c = 127mm. l_p = 600mm. l_b = 150mm.

Specimen No.	t_s (mm)	f_{cu} (N/mm^2)	f_{ct} (N/mm^2)	P_c (kN)
UCt1	40	35	2.6	86
UCt2	100	37	2.9	80

where t = studs transversely spaced

Table 5.7 Push tests. Unreinforced slabs with staggered studs which failed due to splitting.

Details:
Specimen as in Fig. 1.1, except that the studs were staggered, Fig. 5.29, about the centre line of the web. 6 No. 19X100 studs. b_c = 300mm. h_c = 127mm. l_p = 950mm. l_b = 50mm. s_s = 50mm.

Specimen No.	t_s (mm)	f_{cu_2} (N/mm^2)	f_{ct_2} (N/mm^2)	P_c (kN)
UC1t1	20	35	2.7	23
UC1t2	20	32	2.7	27
UC1t3	40	36	3.0	39

Table 5.8 Push tests. Unreinforced slabs with single studs which failed across the shank.

Details:
Specimen as in Fig. 1.1, except that a single stud was placed along the centre line of the web. l_b = 150mm.

Specimen No.	Type of stud	f_{cu} (N/mm^2)	f_{ct} (N/mm^2)	b_c (mm)	h_c (mm)	l_p (mm)	h_f (mm)	P_c (kN)
USs1	13X65	36	2.8	400	115	450	4.0	51
USs2	13X65	36	2.8	400	115	450	4.8	56
USs3	13X65	28	2.2	400	115	450	-	42
USs4	13X65	33	2.9	400	115	450	3.9	51
USs5	19X100	61	3.9	400	175	800	4.9	141
USs6	19X100	65	4.0	400	175	555	6.0	169
USs7	19X100	63	4.0	400	175	555	5.9	163
USs8	22X100	69	4.6	400	175	555	-	205

where S = studs failed across the shank

Table 5.9 Push Tests. Effect of the base restraint and weld collar.

Details:
Specimen as in Fig. 1.1, except that a single stud was placed along the centre line of the web. 1 No. 19X100 stud. b_c = 300mm. h_c = 150mm. l_p = 120mm. l_b = 200mm.

Specimen No.	f_{cu} (N/mm^2)	f_{ct} (N/mm^2)	P_e (kN)	Type of failure
UCs23	55	3.5	153	Concrete failed
UCs24	55	3.5	172	Concrete failed
USs9	63	3.5	129	Shank failed
USs10	63	3.5	153	Shank failed

——— Weld collar removed
– – – Extra passive lateral restraint (Fig. 5.30)

Table 5.10 Push tests. Transverse reinforcement fully anchored. Slabs split.

Details:
Specimen as in Fig. 1.1, except that a single stud was placed along the centre line of the web. Transverse reinforcement as in Fig. 5.31. 1 No. 19X100 stud. b_c = 300mm. h_c = 127mm. l_p = 600mm. l_b = 150mm. Mild steel reinforcement.

Specimen No.	A_r (mm^2)	No. of groups	f_{ry} (N/mm^2)	f_{ru} (N/mm^2)	l_r (mm)	s_r (mm)	f_{cu} (N/mm^2)	f_{ct} (N/mm^2)	c_b (mm)	P_e (kN)
RCs1	36	1	308	470	119		25	2.0	20	63
RCs2	72	1	308	470	119		30	2.3	20	93
RCs3	107	1	308	470	119		25	2.0	20	77
RCs4	125	1	331	588	123		32	2.9	20	97
RCs5	156	1	331	588	116		32	2.9	20	100
RCs6	125	1	331	588	119		35	2.6	44	106
RCs7	57	1	308	470	220		31	2.6	20	93
RCs8	28	2	308	470	119	110	31	2.6	20	97
RCs9	72	2	308	470	119	110	29	2.5	20	95
RCs10	62	5	331	588	76	49	37	3.2	44	103

where R = slab reinforced
A_r = cross-sectional area of a group of transverse reinforcement

Table 5.11 Push tests. Uniformly distributed transverse reinforcement. Studs failed across shank.

Details:
Specimen as in Fig. 1.1, except that a single stud was placed along the centre line of the web. Transverse reinforcement as in Fig. 5.32.
19X100 stud. b_c = 300mm. h_c = 127mm. l_p = 600mm. l_b = 150mm.
High yield reinforcement.

Specimen No.	A_r (mm^2)	l_r (mm)	s_r (mm)	f_{cu} (N/mm^2)	f_{ct} (N/mm^2)	f_{md} (N/mm^2)	c_b (mm)	h_f (mm)	P_c (kN)
RSs1	50	24	30	36	2.5	4.4	15	7.2	135
RSs2	79	24	30	36	2.5	4.4	15	4.9	133
RSs3	157	24	33	29	2.6	3.6	15	6.1	122
RSs4	157	39	60	29	2.6	3.6	15	7.4	131
RSs5	79	24	30	34	2.6	4.3	30	7.5	133
RSs6	79	24	30	34	2.6	4.3	45	7.0	142

Table 5.12 Push tests. Specimens reinforced according to the standard push test of the Bridge Code[7].

Details:
Specimen as in Fig. 1.1. 19X75 studs. b_c = 300mm. h_c = 100mm.
l_p = 545mm. l_b = 195mm.

Specimen No.	No. of studs	t_s (mm)	f_{cu} (N/mm^2)	f_{ct} (N/mm^2)	f_{md} (N/mm^2)	P_c (kN)
RCs11	1	0	24	2.0	3.2	90
RCt1	2	39	29	2.2	3.9	68

Table 5.13 Push tests. Transverse reinforcement looped around a single stud.

Details:
Specimen as in Fig. 3.2, except that a single stud was placed along the centre line of the web. 19X75 stud. f_{ry} = 380 N/mm^2. s_c = 60mm. Mild steel reinforcement.

Specimen No.	A_r (mm^2)	h_r (mm)	c_b (mm)	l_p (mm)	l_b (mm)	h_c (mm)	b_t (mm)	b_c (mm)	f_{cu} *	f_{ct} *	f_{md} *	P_c (kN)
Ls1	0	0	15	545	195	100	352	105	29	2.7	4.1	59
Ls2	101	8	15	545	195	100	352	105	32	2.8	3.3	76
Ls3	201	16	15	545	195	100	352	105	29	2.9	3.8	89
Ls4	302	24	15	545	195	100	351	104	31	2.7	3.9	99
Ls5	402	16	15	545	195	100	352	105	30	2.5	3.4	89
Ls6	101	8	15	545	195	100	364	129	33	2.9	4.0	73
Ls7	101	8	15	545	195	100	375	151	29	2.8	3.2	84
Ls8	101	8	15	545	195	100	389	179	29	2.5	3.9	80
Ls9	101	8	15	545	195	100	401	203	31	2.7	3.7	84
Ls10	217	16	25	600	150	125	170	80	29	2.6	3.8	76
Ls11	217	16	32	600	150	125	170	80	28	2.4	3.7	75
Ls12	217	16	45	600	150	125	170	80	29	2.6	3.8	61
Ls13	472	30	18	600	150	125	170	80	28	2.4	3.7	100

* (N/mm^2)

where L = reinforcement looped around the stud
A_r = area of reinforcement crossing the plane B–B, Fig. 3.2

Table 5.14 Push tests. Transverse reinforcement looped around a double stud.

Details:
Specimen as in Fig. 3.2. 2 No. 19X75 studs. h_c = 100mm. l_p = 545mm. l_b = 195mm. s_c = 60mm. t_s = 39mm. c_b = 15mm. h_r = 8mm. f_{ry} = 380mm.

Specimen No.	A_r (mm^2)	b_t (mm)	b_c (mm)	f_{cu} (N/mm^2)	f_{ct} (N/mm^2)	f_{md} (N/mm^2)	P_c (kN)
Lt1	0	375	150	36	2.8	3.8	60
Lt2	101	374	148	31	2.8	3.7	71
Lt3	101	388	176	32	2.8	3.7	64
Lt4	101	408	216	35	2.8	4.3	77
Lt5	101	426	252	32	2.7	4.2	73

where A_r = area of reinforcement crossing the plane B-B, Fig. 3.2

Table 5.15 Eccentric strip loads on concrete prisms.

Details:
Specimen as in Fig. 5.33. h_c = 150mm. b_t = 150mm. l_c = 300mm. b_a/b_c = 0.12. f_{ct} = 2.9 N/mm^2.

Specimen No.	b_c/b_t	P_c (kN)
UC1	1	168
UC2	0.825	156
UC3	0.639	123
UC4	0.483	110
UC5	0.280	69

where P_c = the mean of three tests

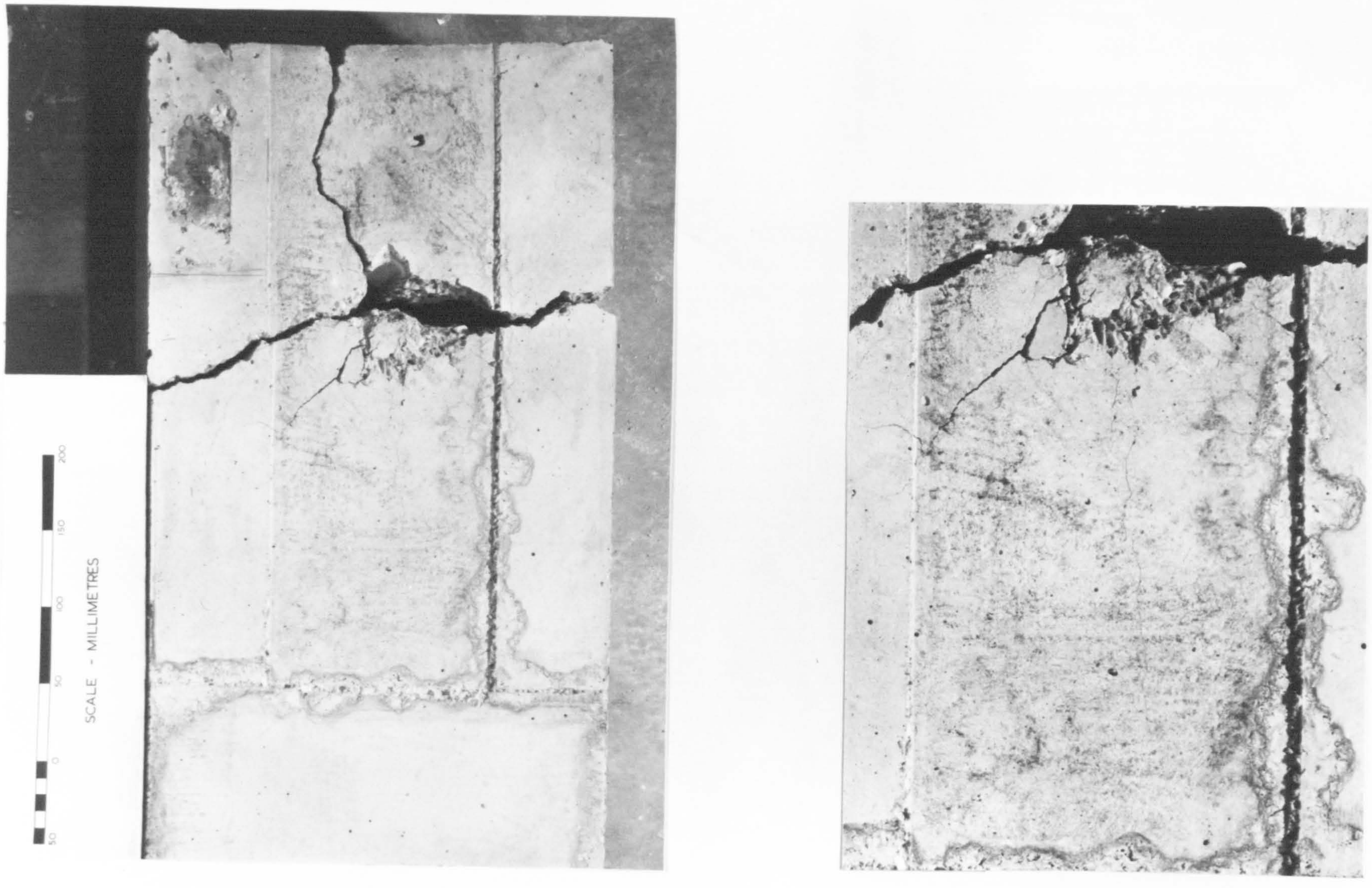

Fig. 5.1 Failure of a lightly reinforced slab.

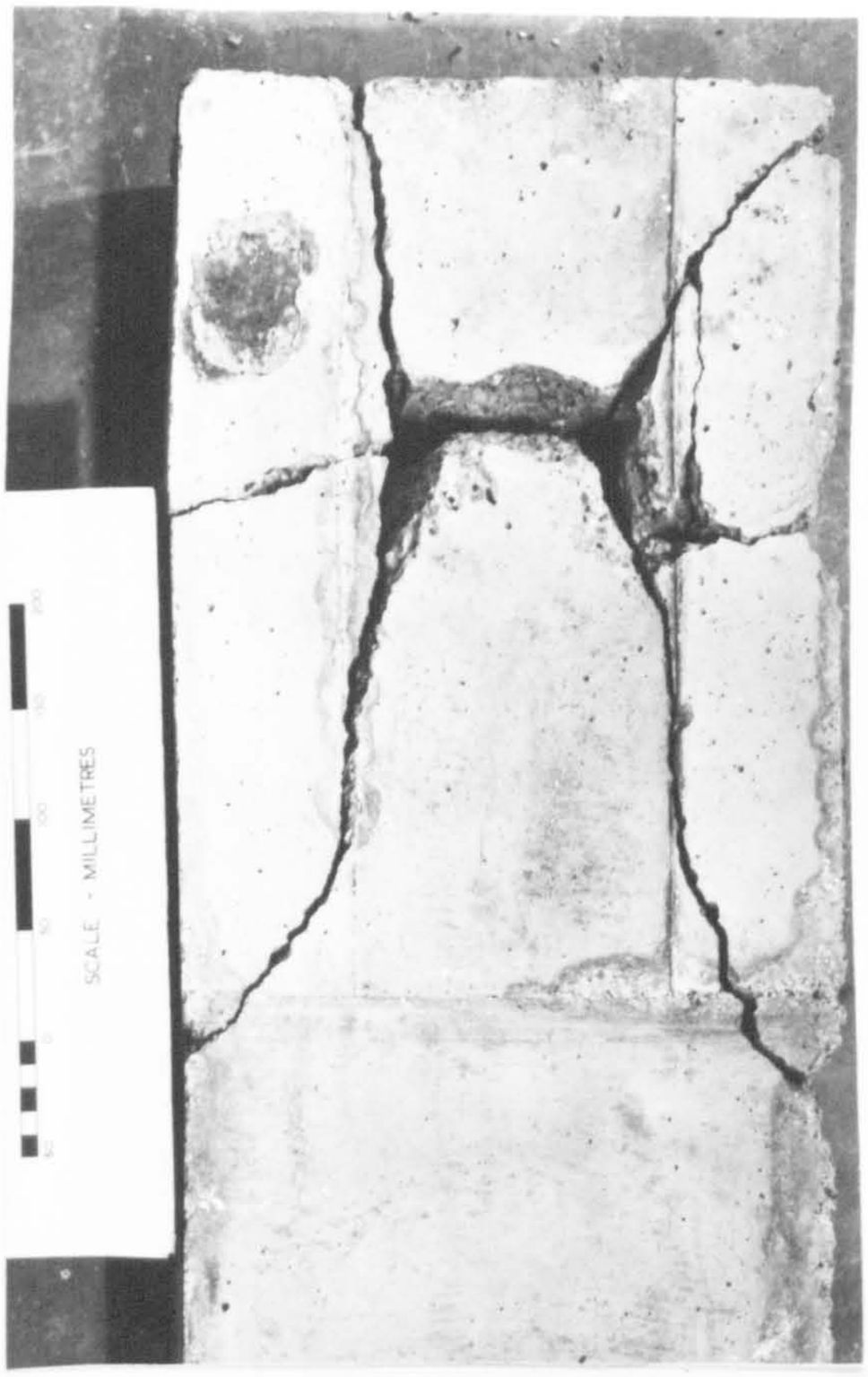

Fig. 5.2 Laterally spaced studs.

Fig. 5.3 Longitudinally spaced studs.

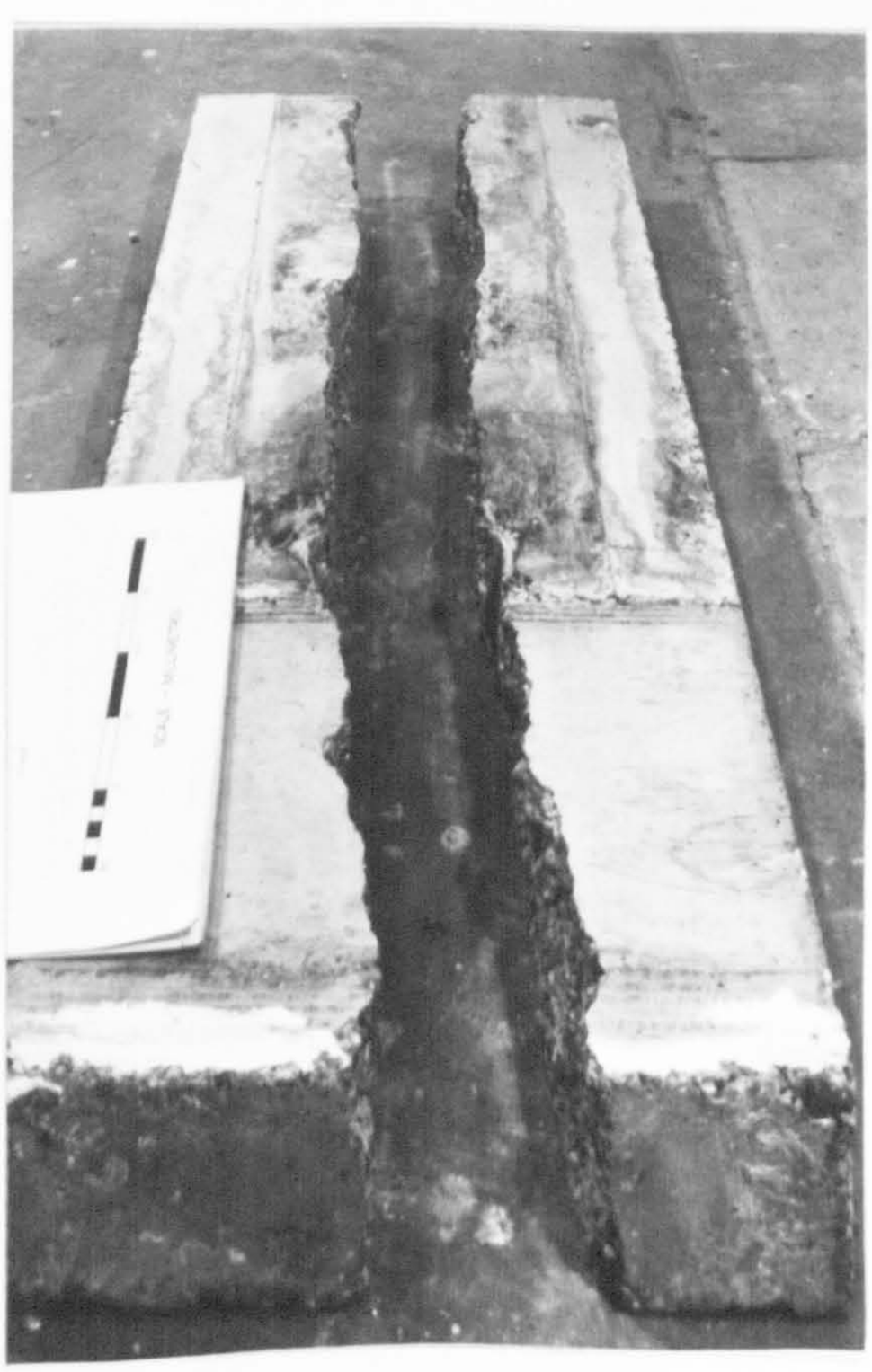

Fig. 5.4 Vertical split.

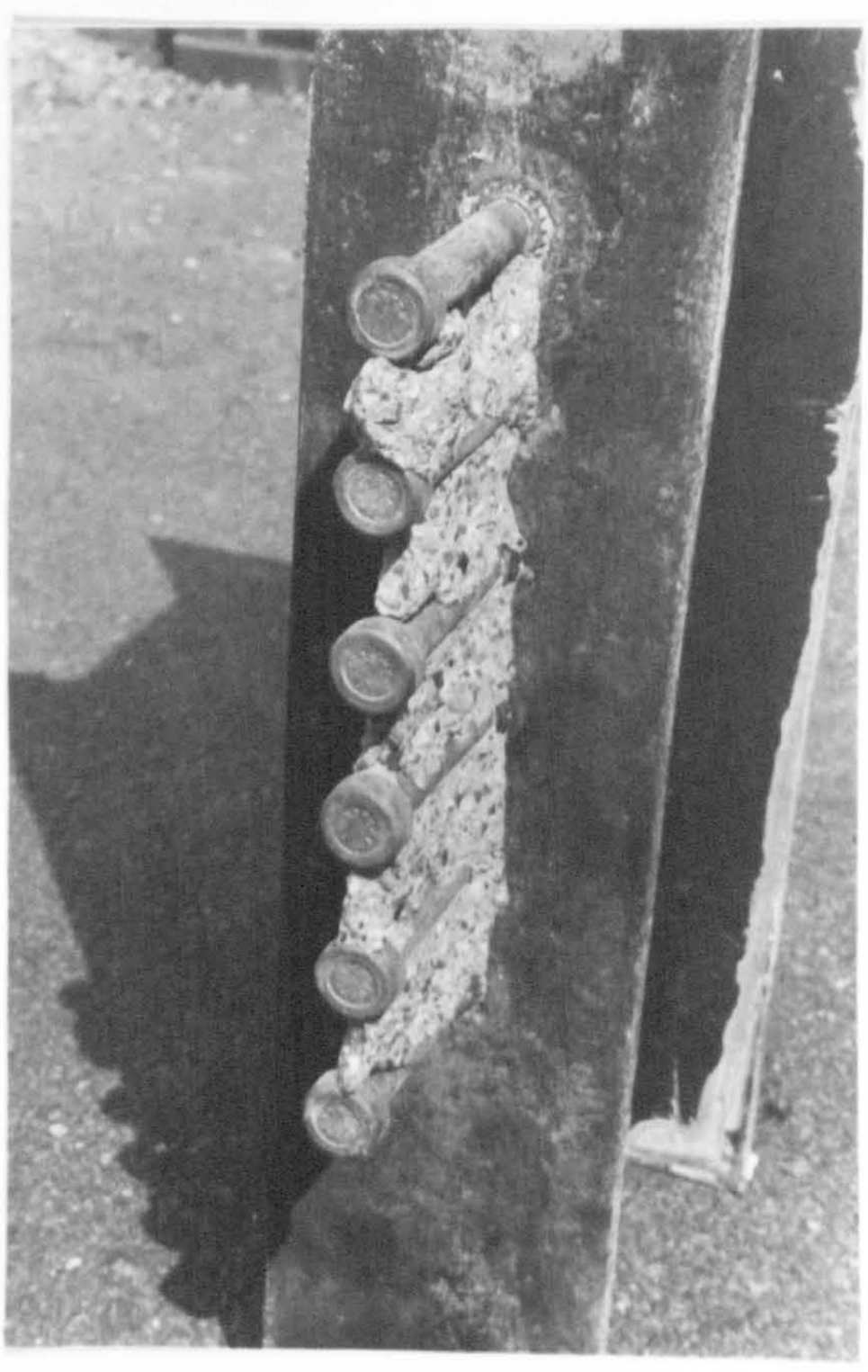

Fig. 5.5 Shear failure of concrete.

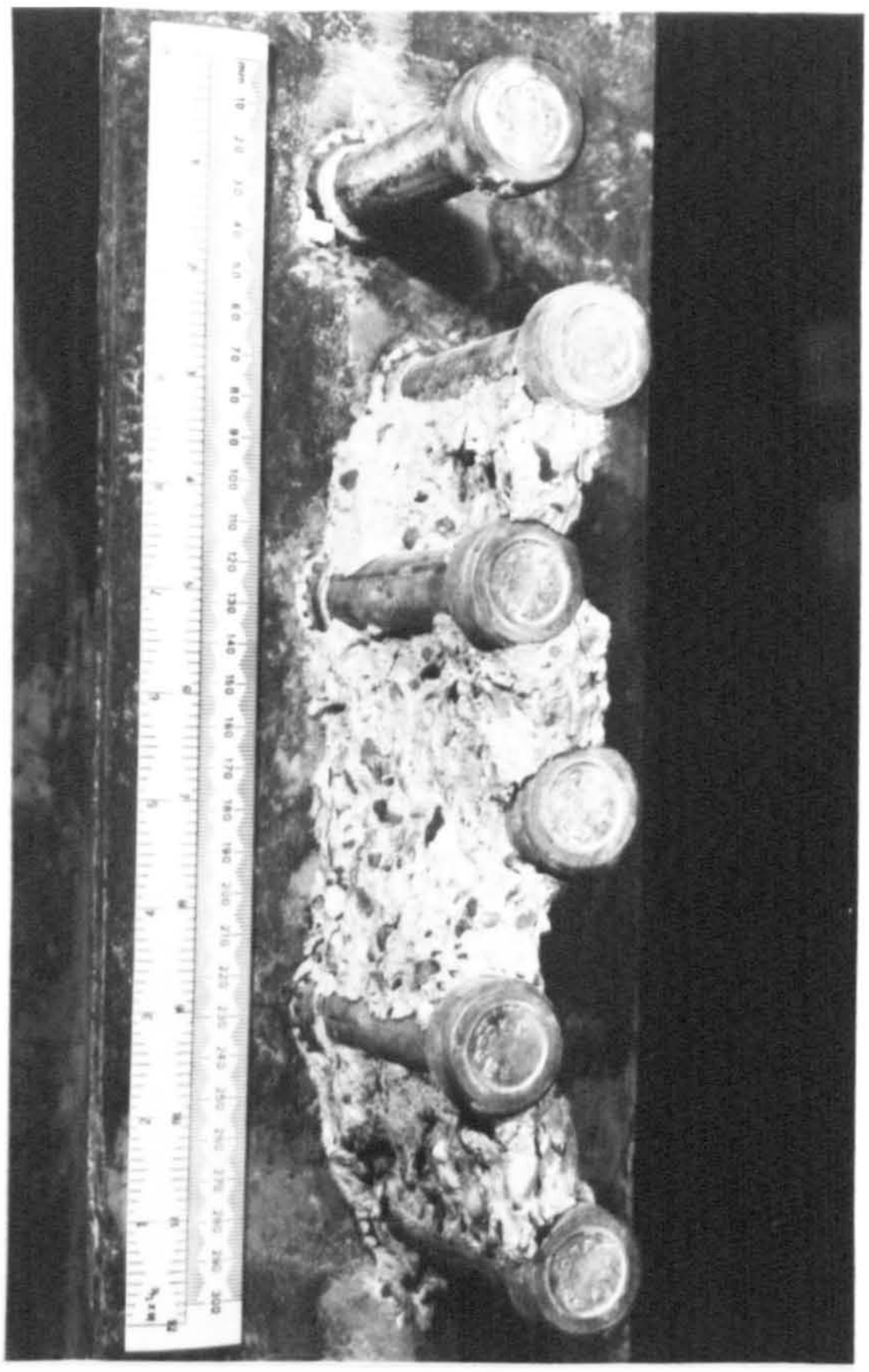

Fig. 5.6 Narrowly staggered studs.

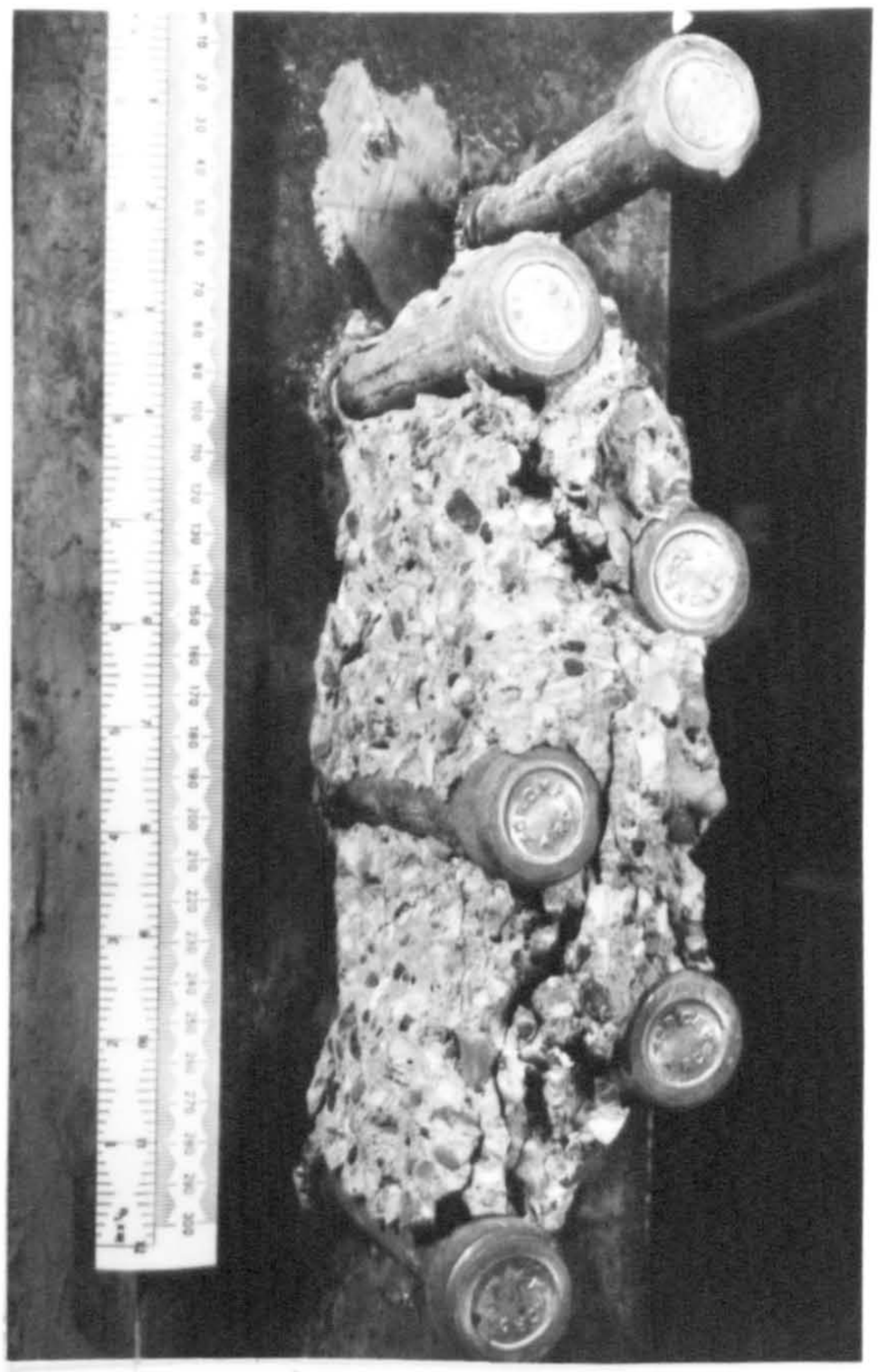

Fig. 5.7 Widely staggered studs.

Fig. 5.8 The shank after failure.

Fig. 5.9 Variation in the height of the weld-collar.

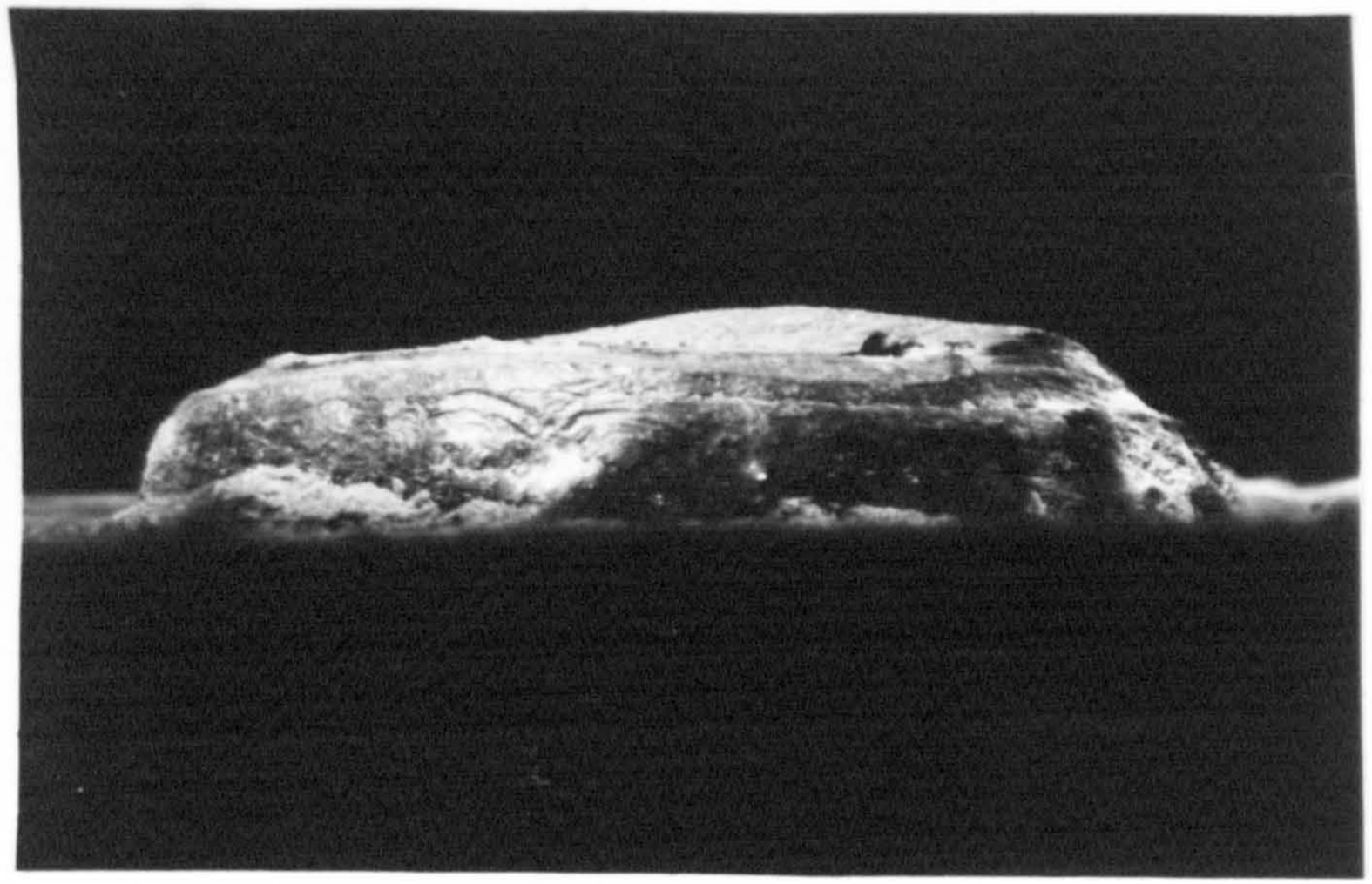

Fig. 5.10 The weld-collar after failure.

Fig. 5.11 Failure of the stud.

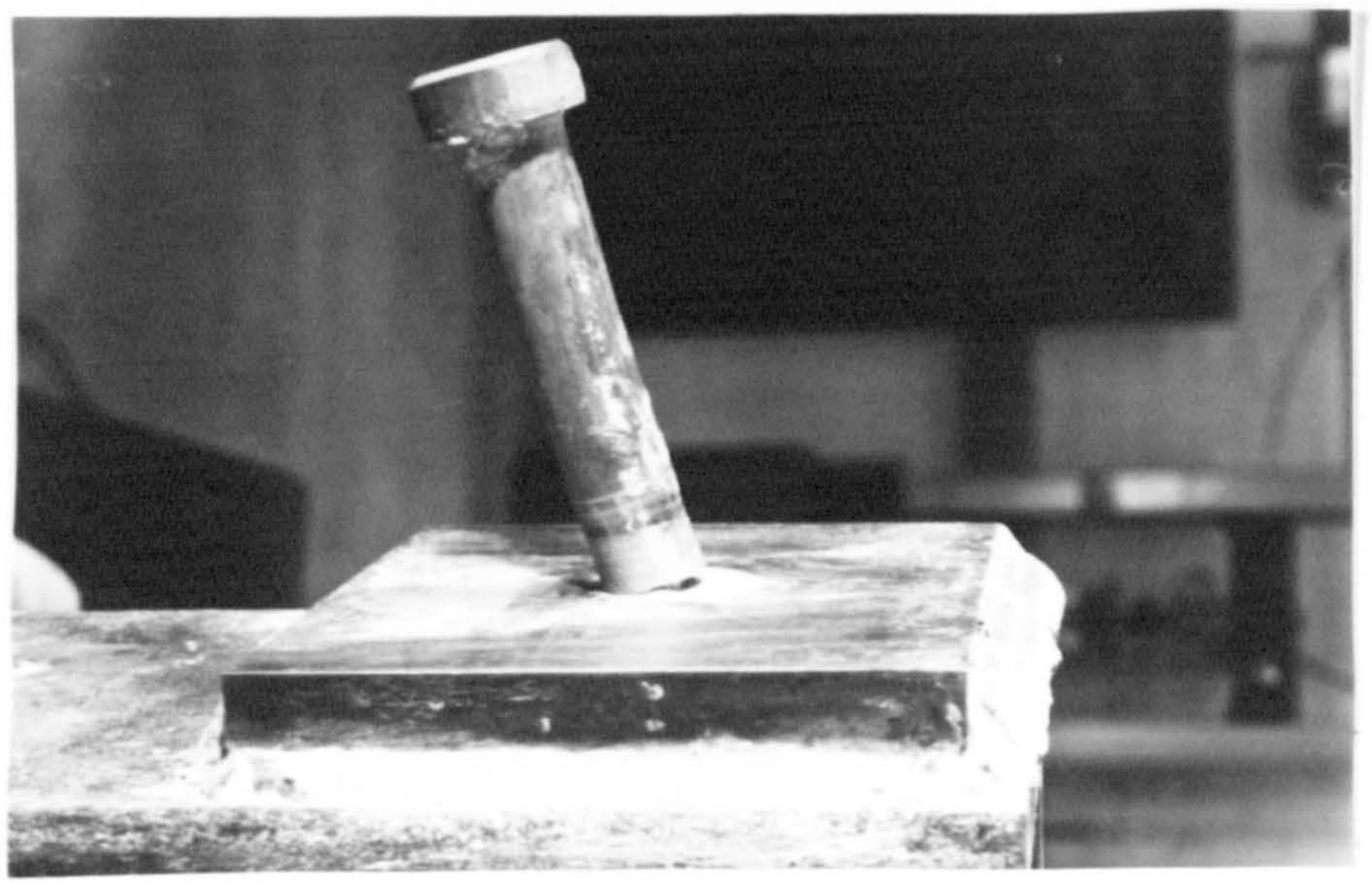

Fig. 5.12 Weld-collar removed.

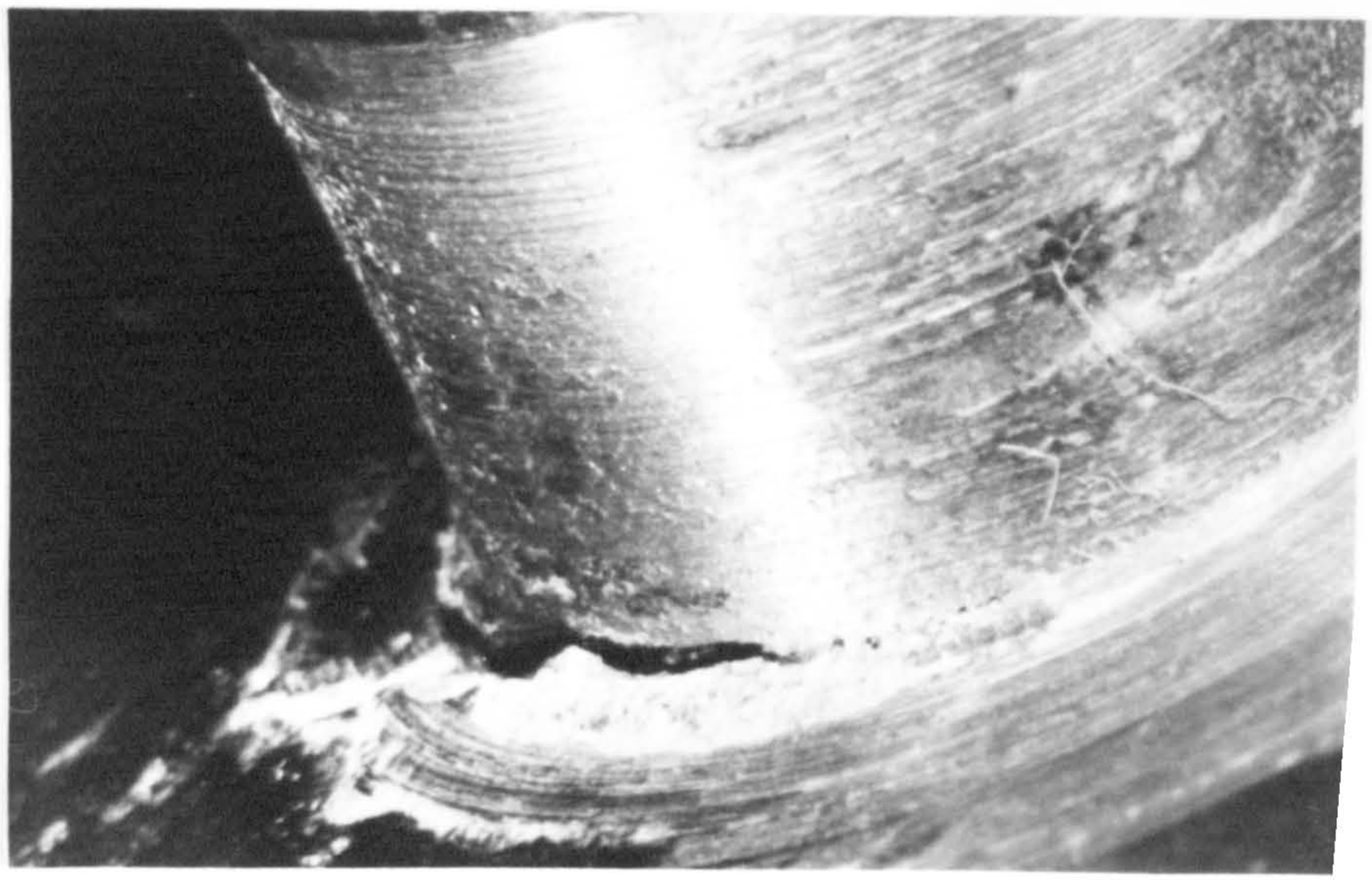

Fig. 5.13 Failure at the shank/flange interface.

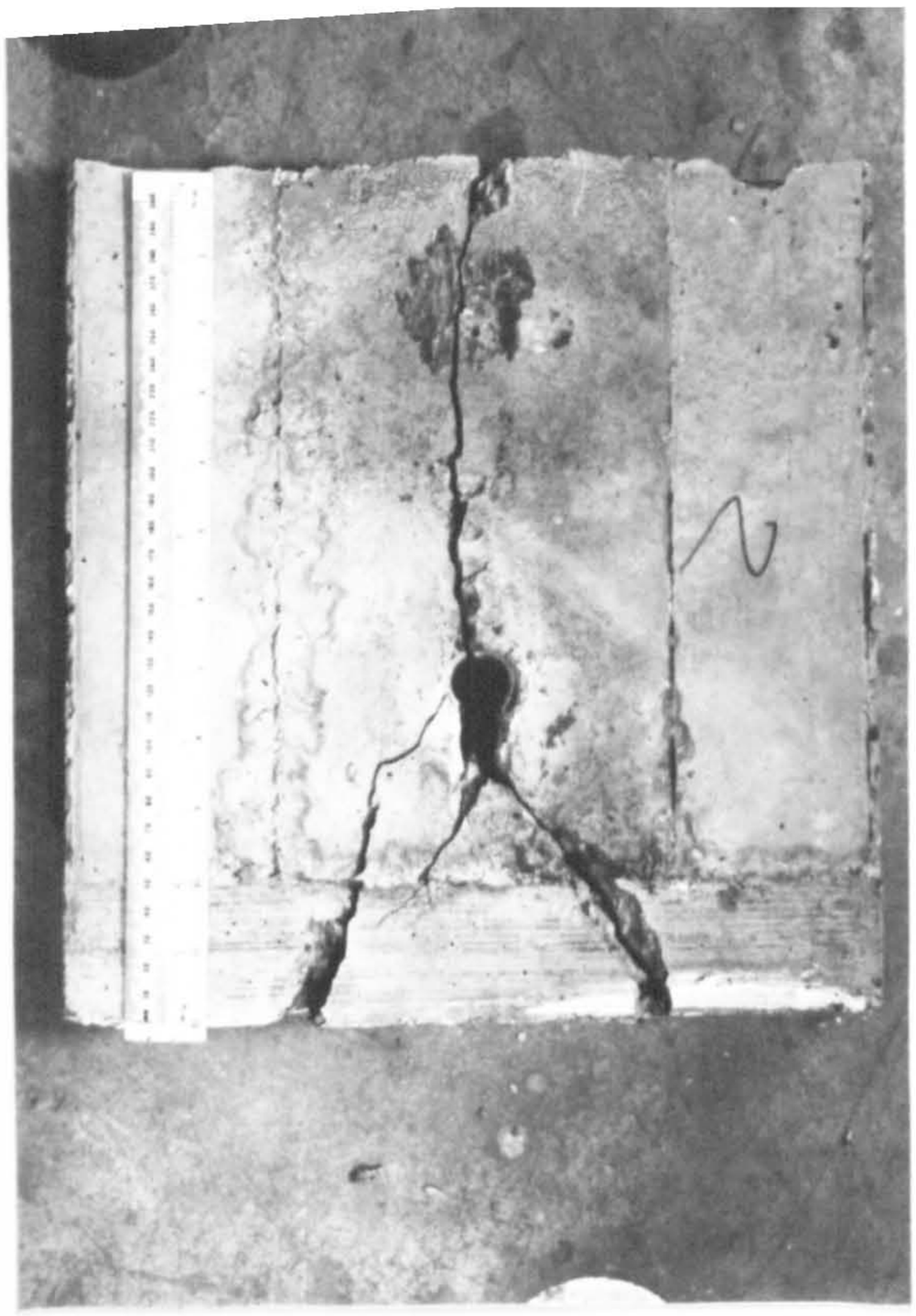

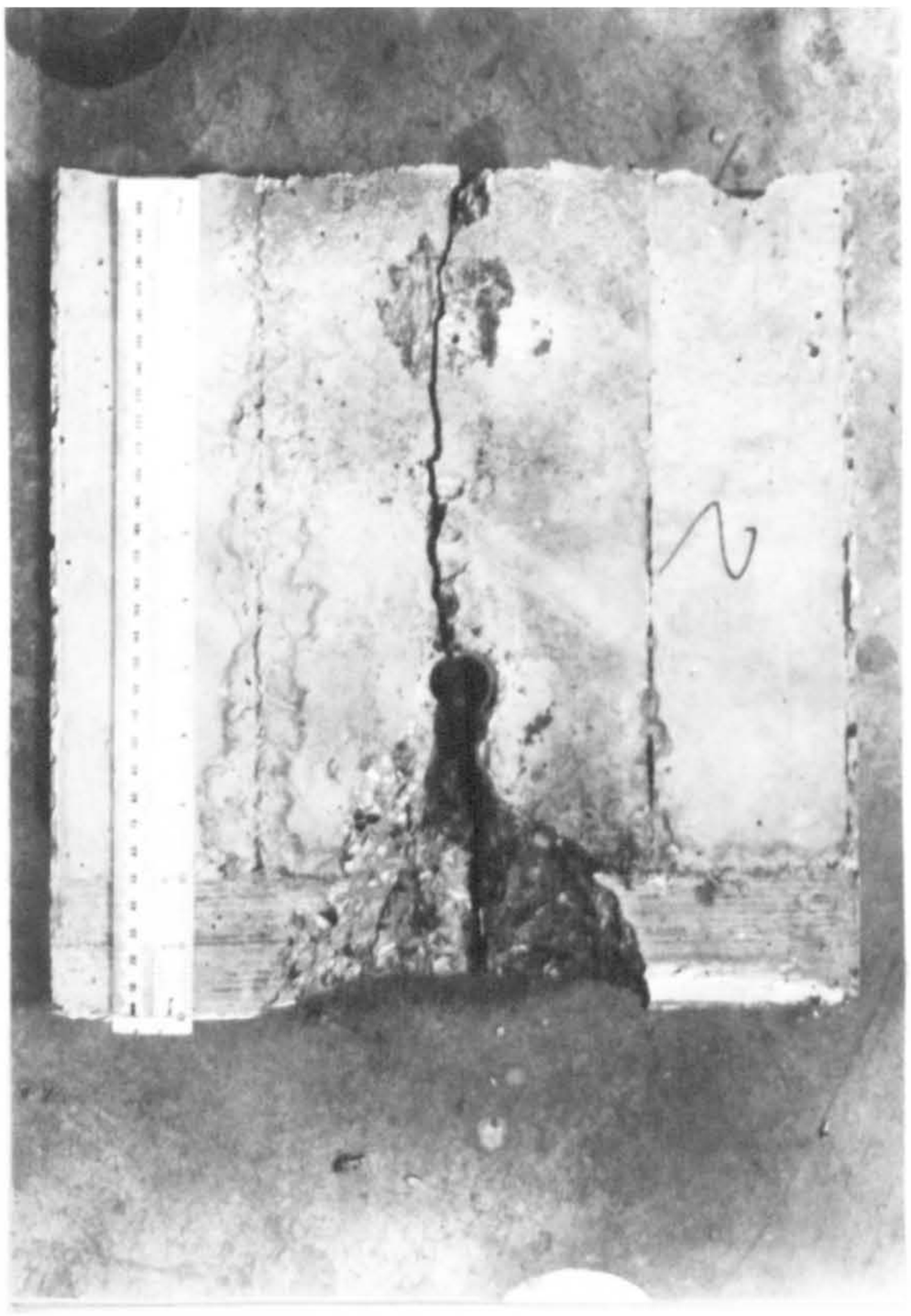

Fig. 5.14 The effect of the base restraint.

Fig. 5.15 Tensile test on a welded stud.

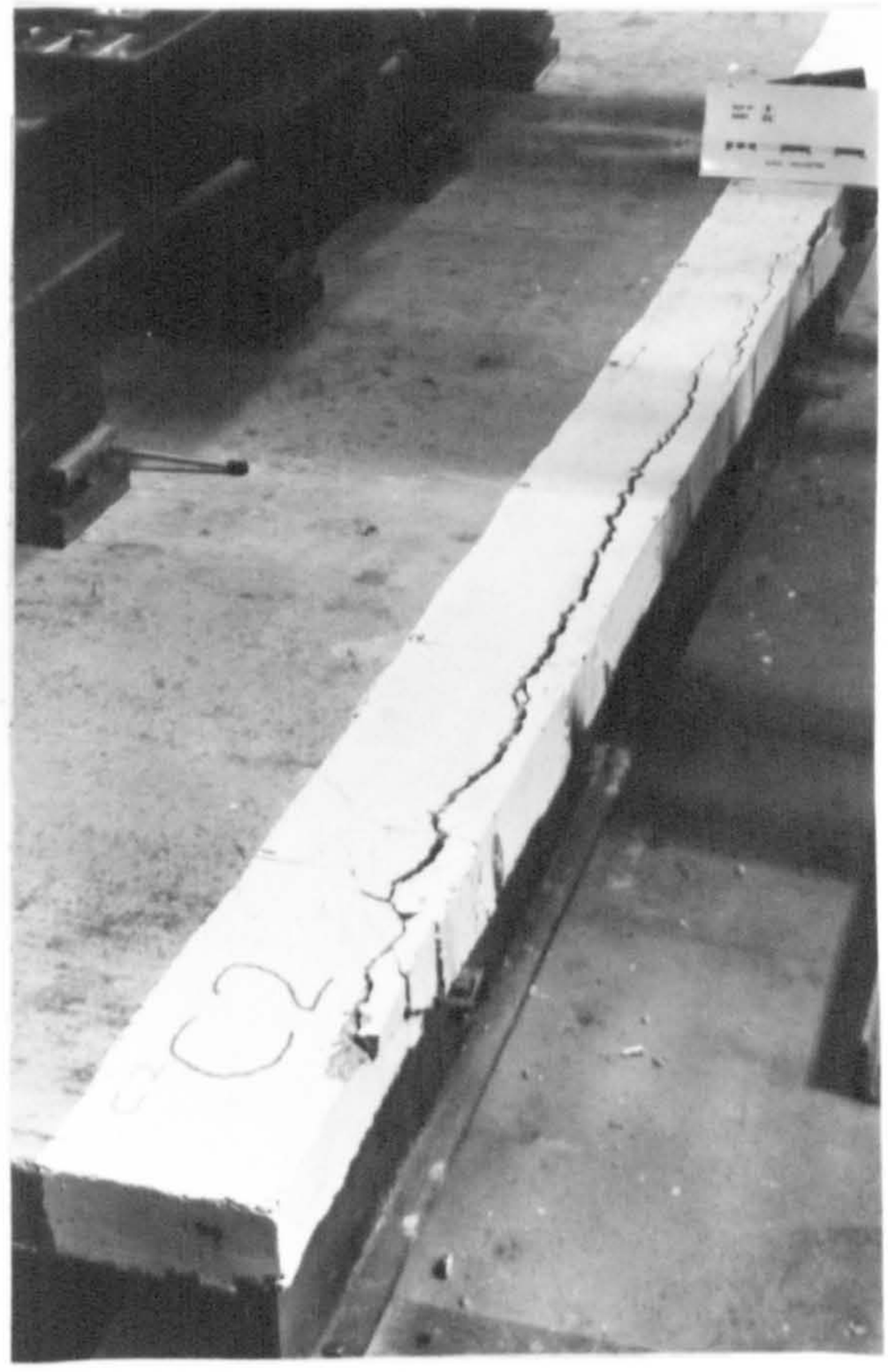

Fig. 5.16 Splitting in a composite L-beam.

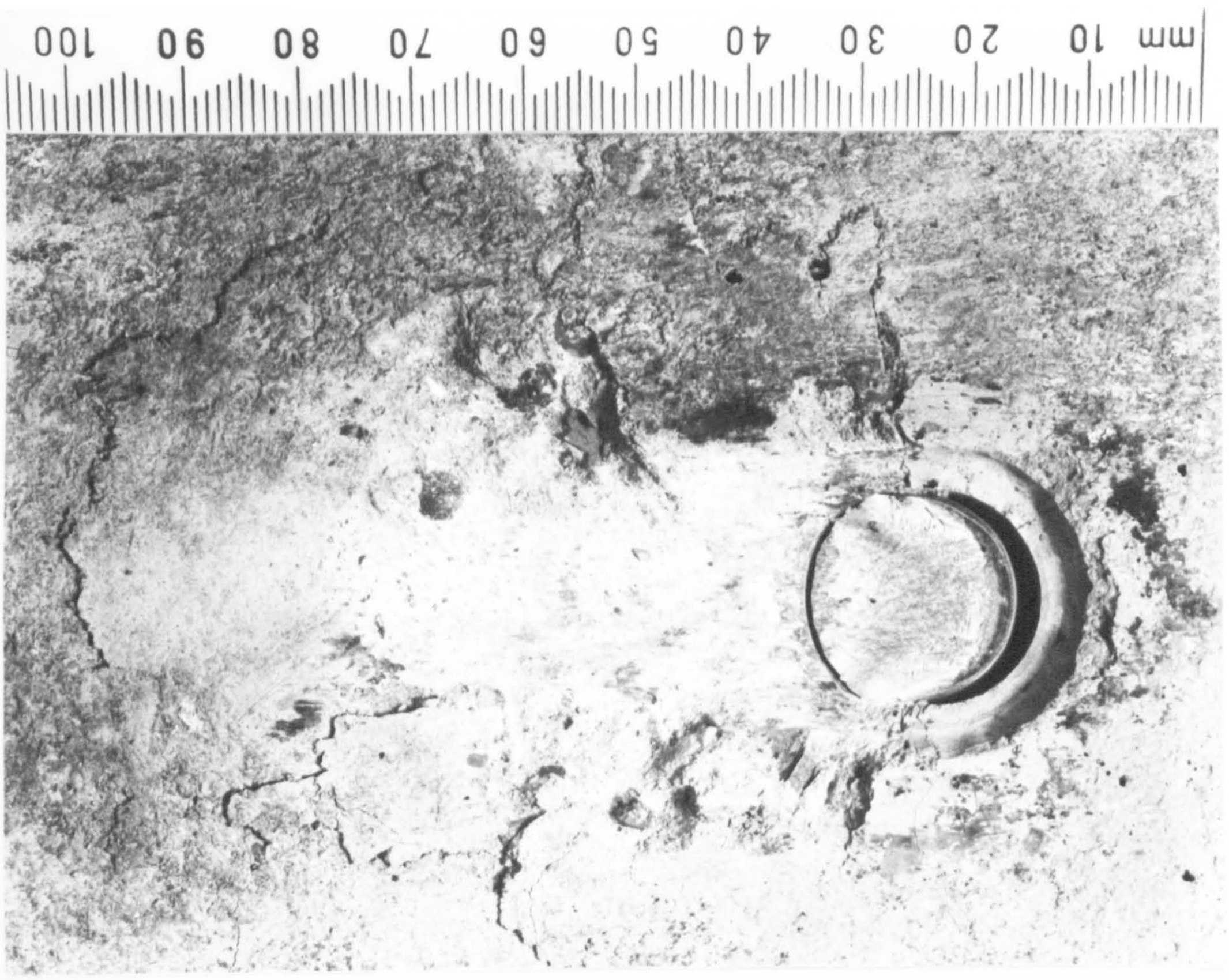

Fig. 5.17 The local cracking of the concrete around a stud.

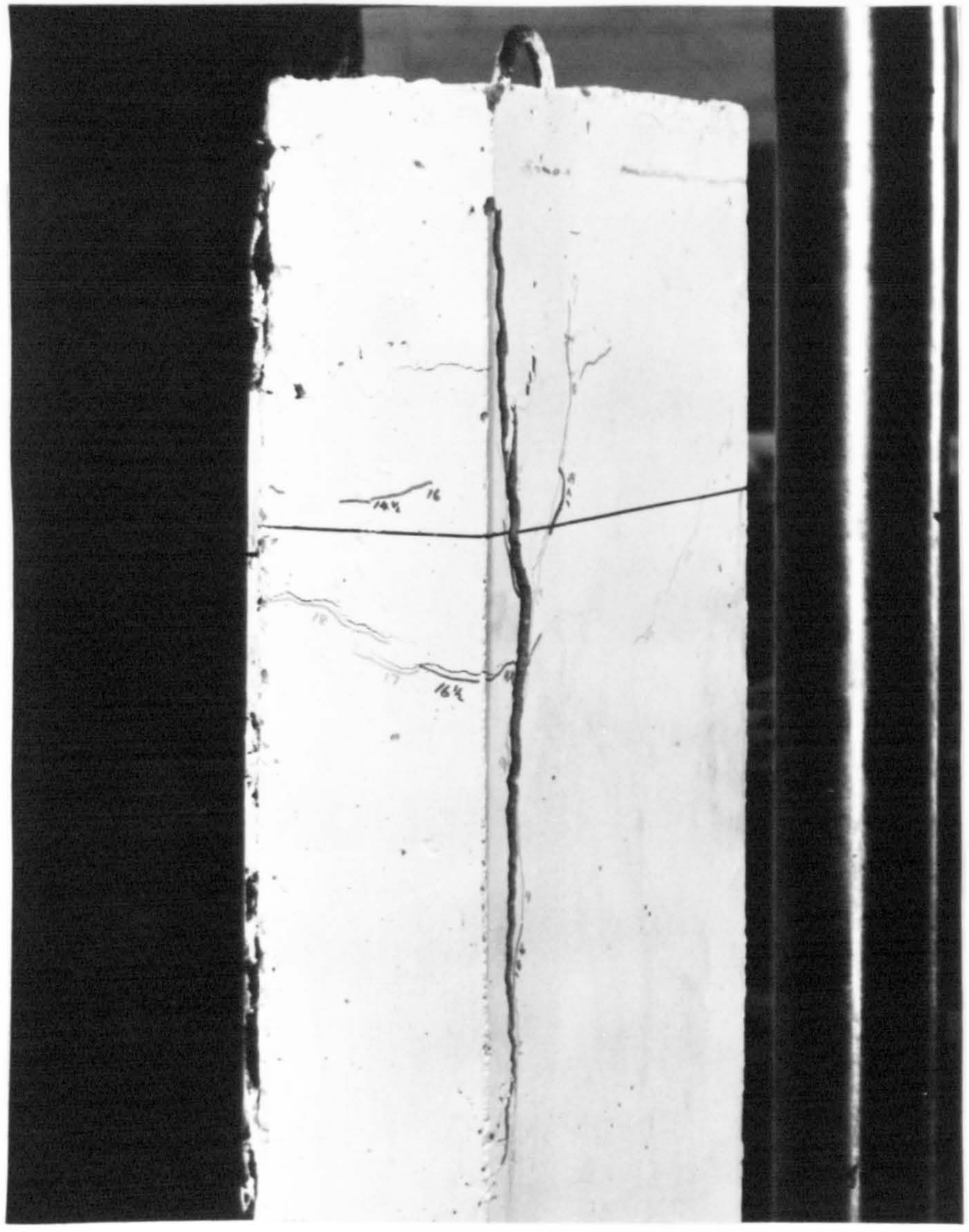

Fig. 5.18 Reinforcement looped around a single stud. Longitudinal split.

Fig. 5.19 Reinforcement looped around a single stud. Alternative failure mode to longitudinal splitting.

Fig. 5.20 Reinforcement looped around a double stud.

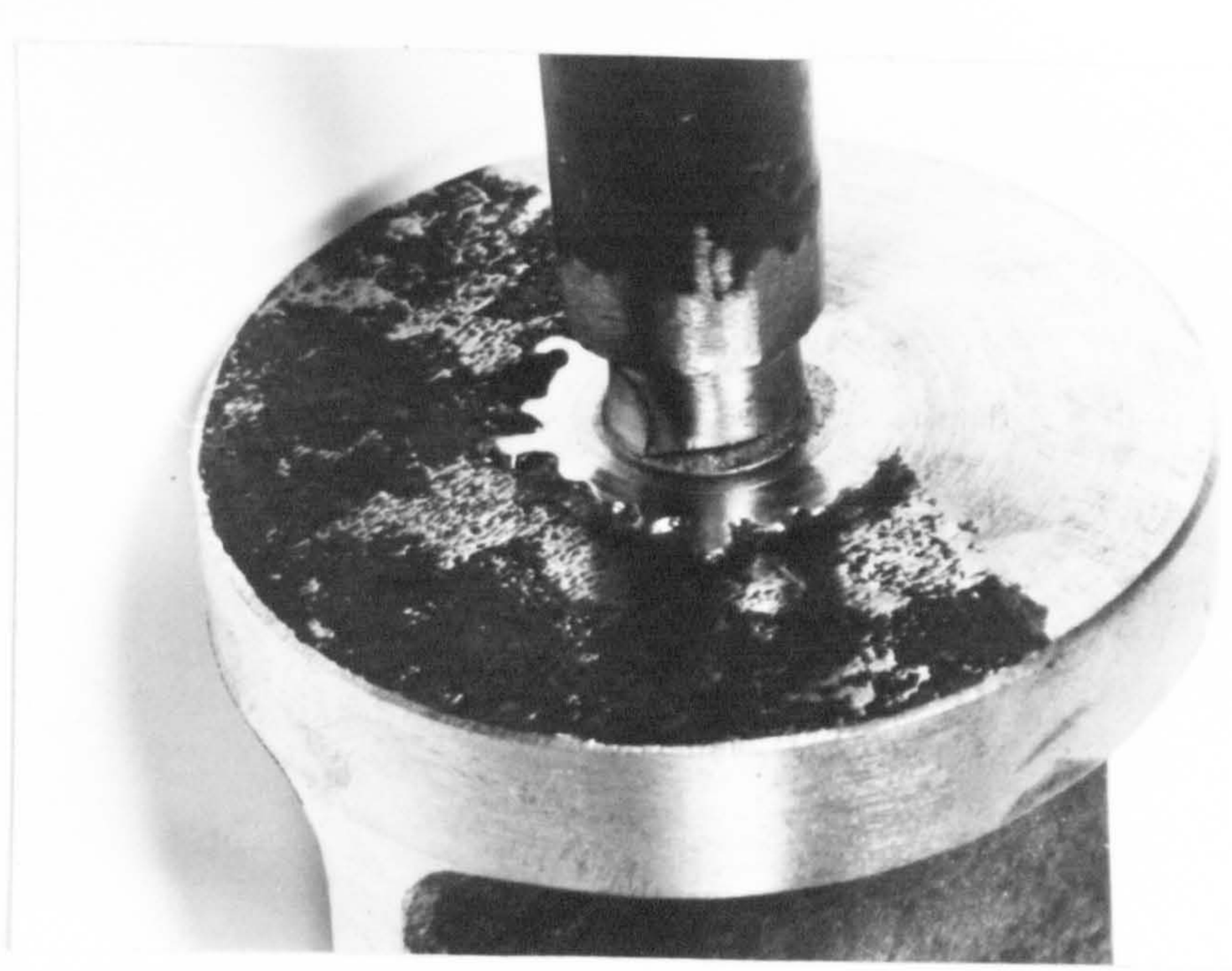

Fig. 5.21 Tensile test on the weld material.

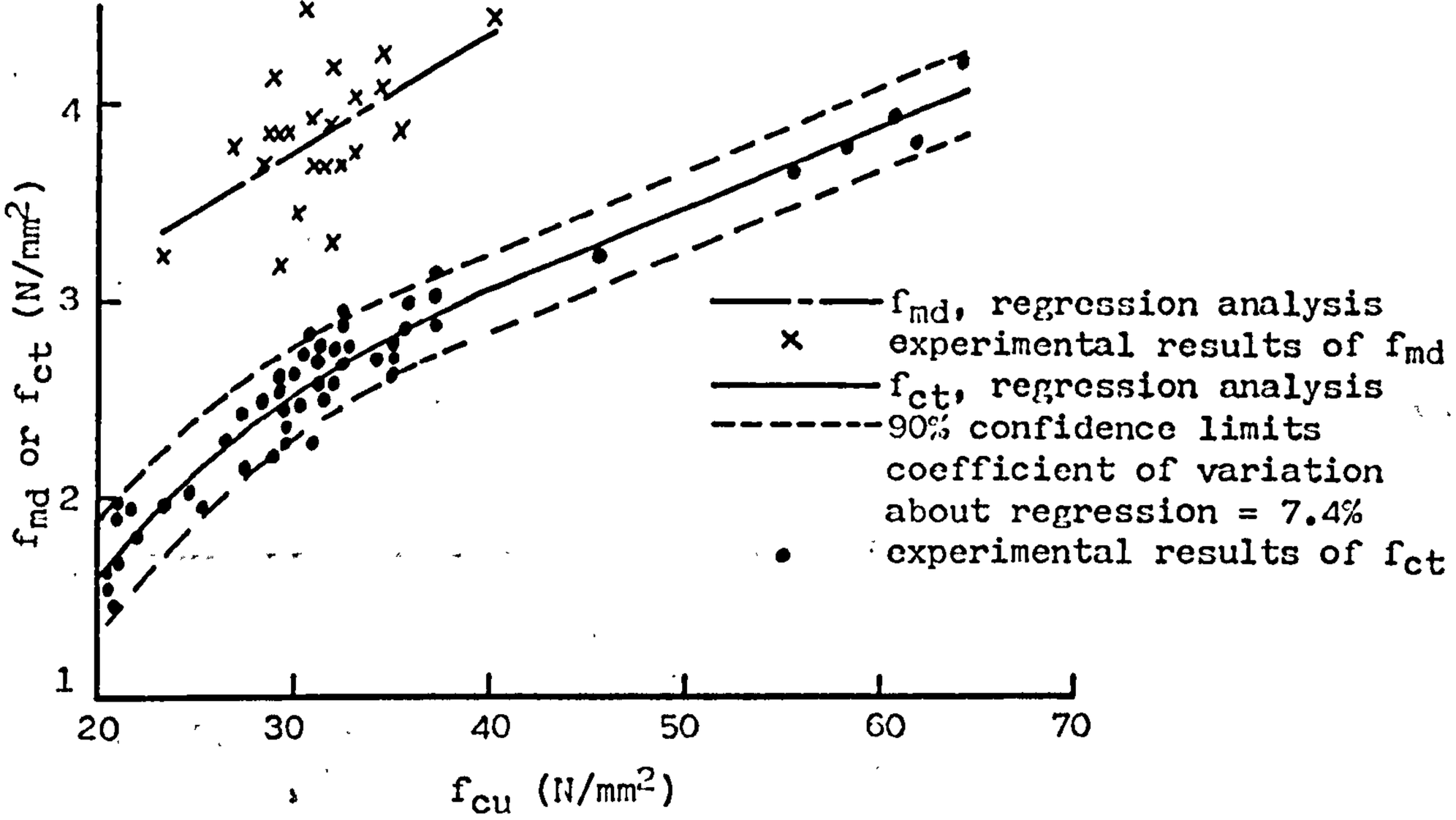

Fig. 5.22 Variation of the tensile strength of the concrete with the cube strength.

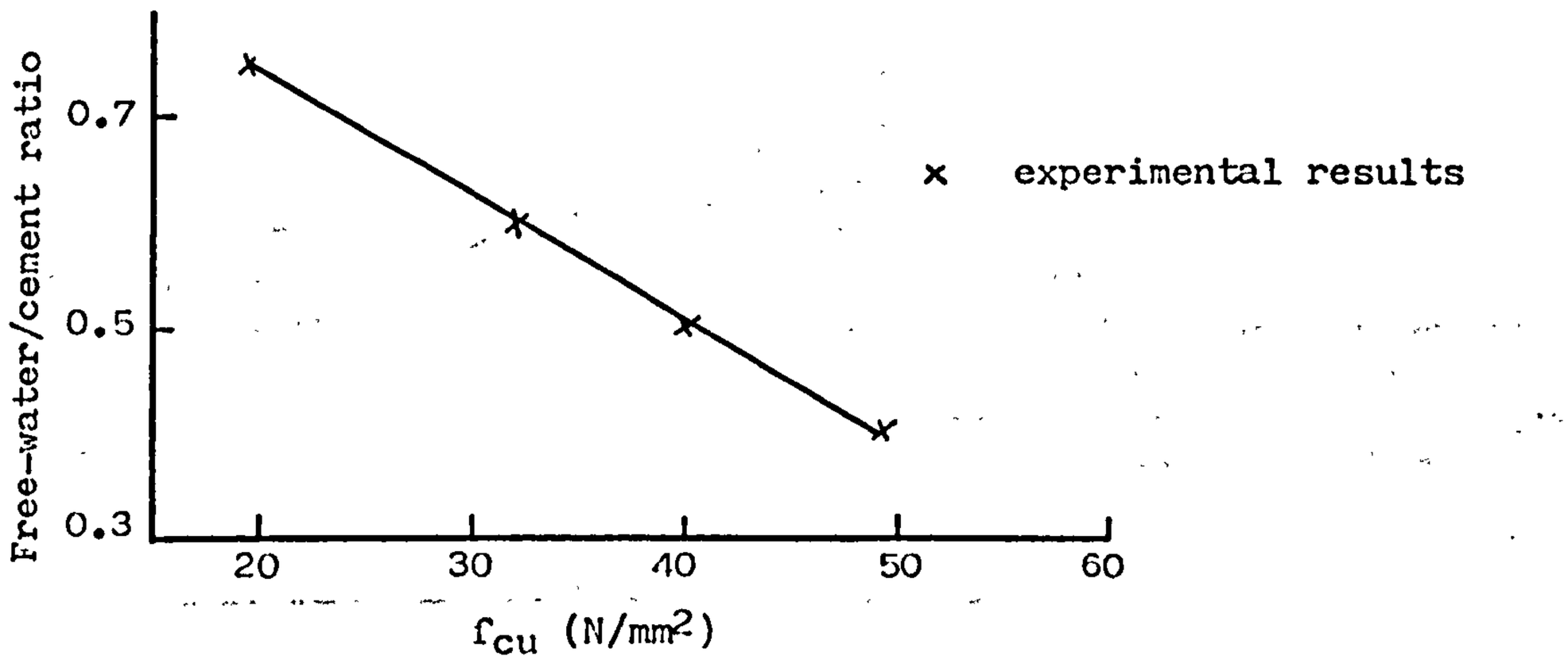

Fig. 5.23 Variation of the free-water/cement ratio with the cube strength.

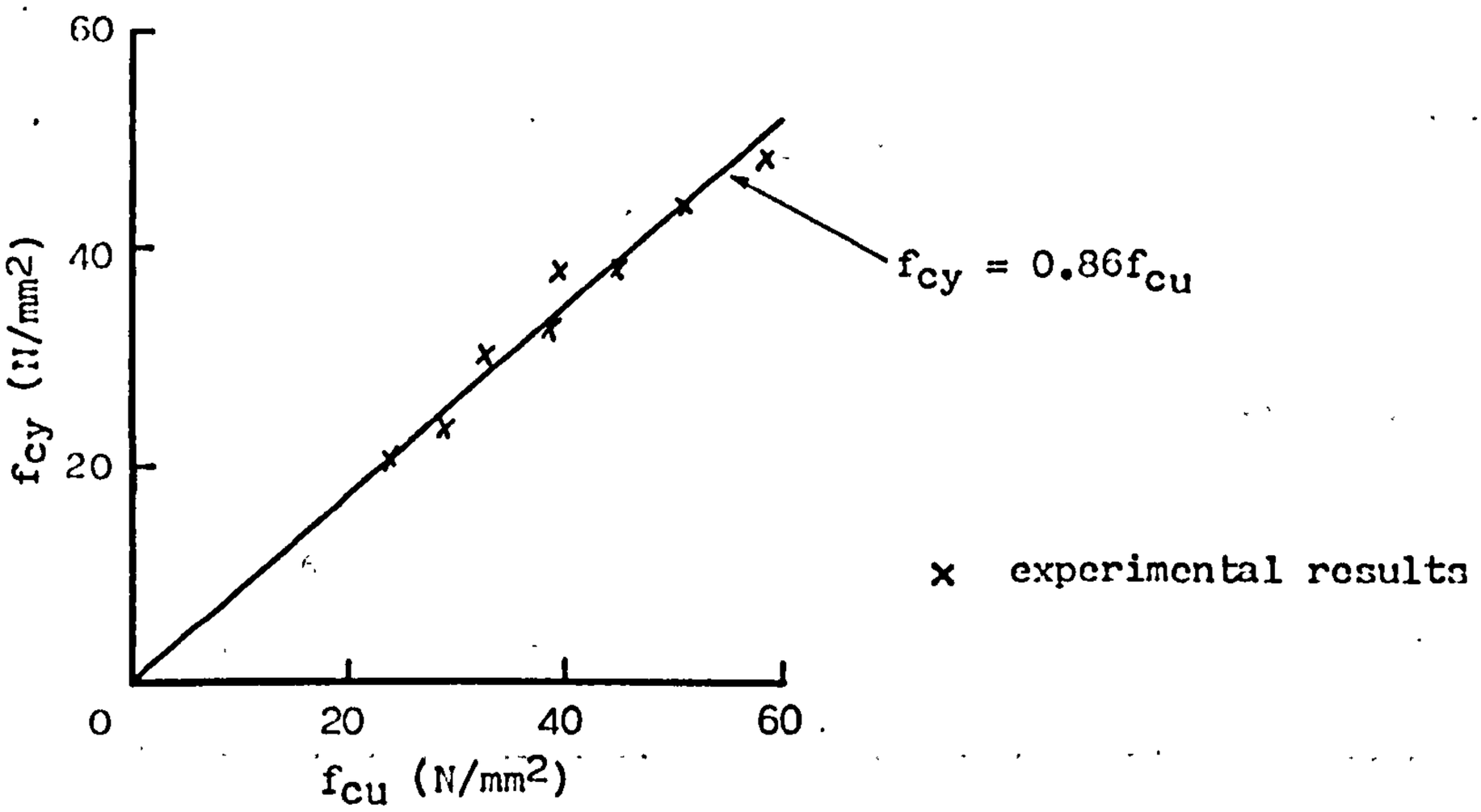

Fig. 5.24 Variation of the cylinder strength with the cube strength.

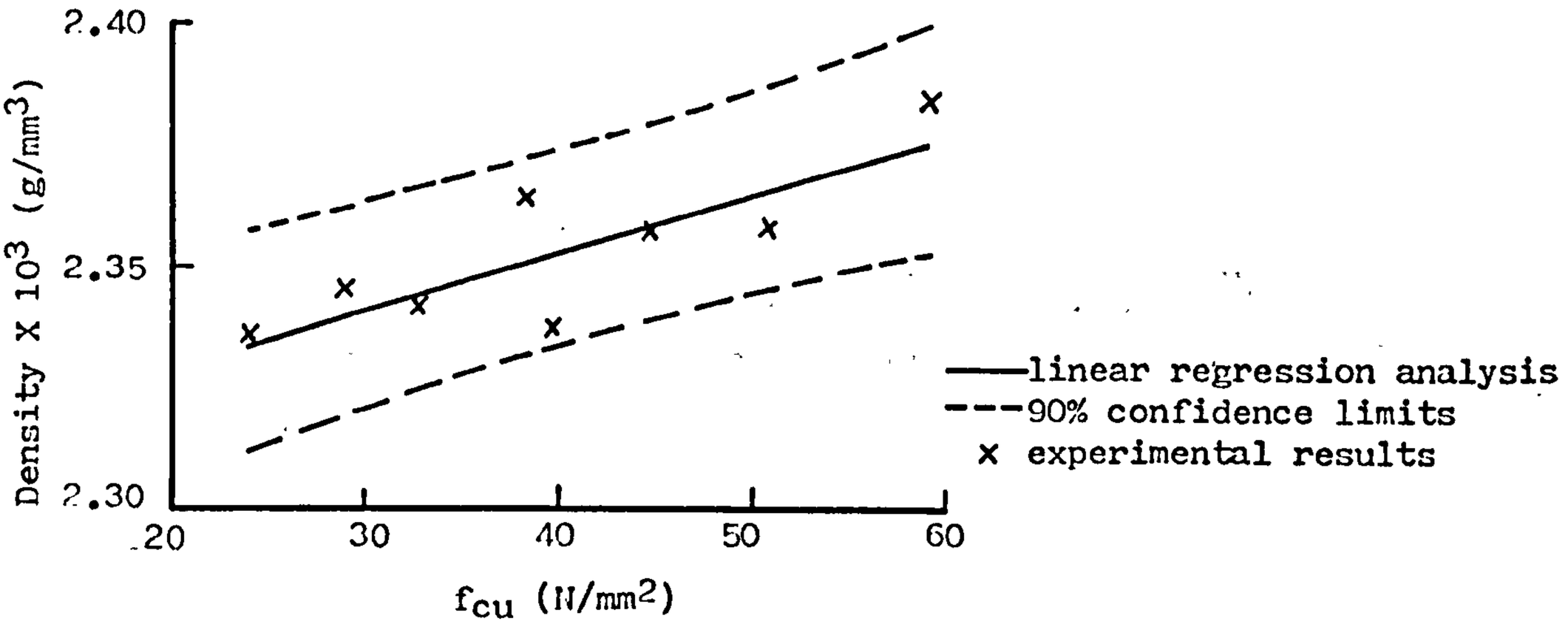

Fig. 5.25 Variation of the density of the saturated concrete with the cube strength.

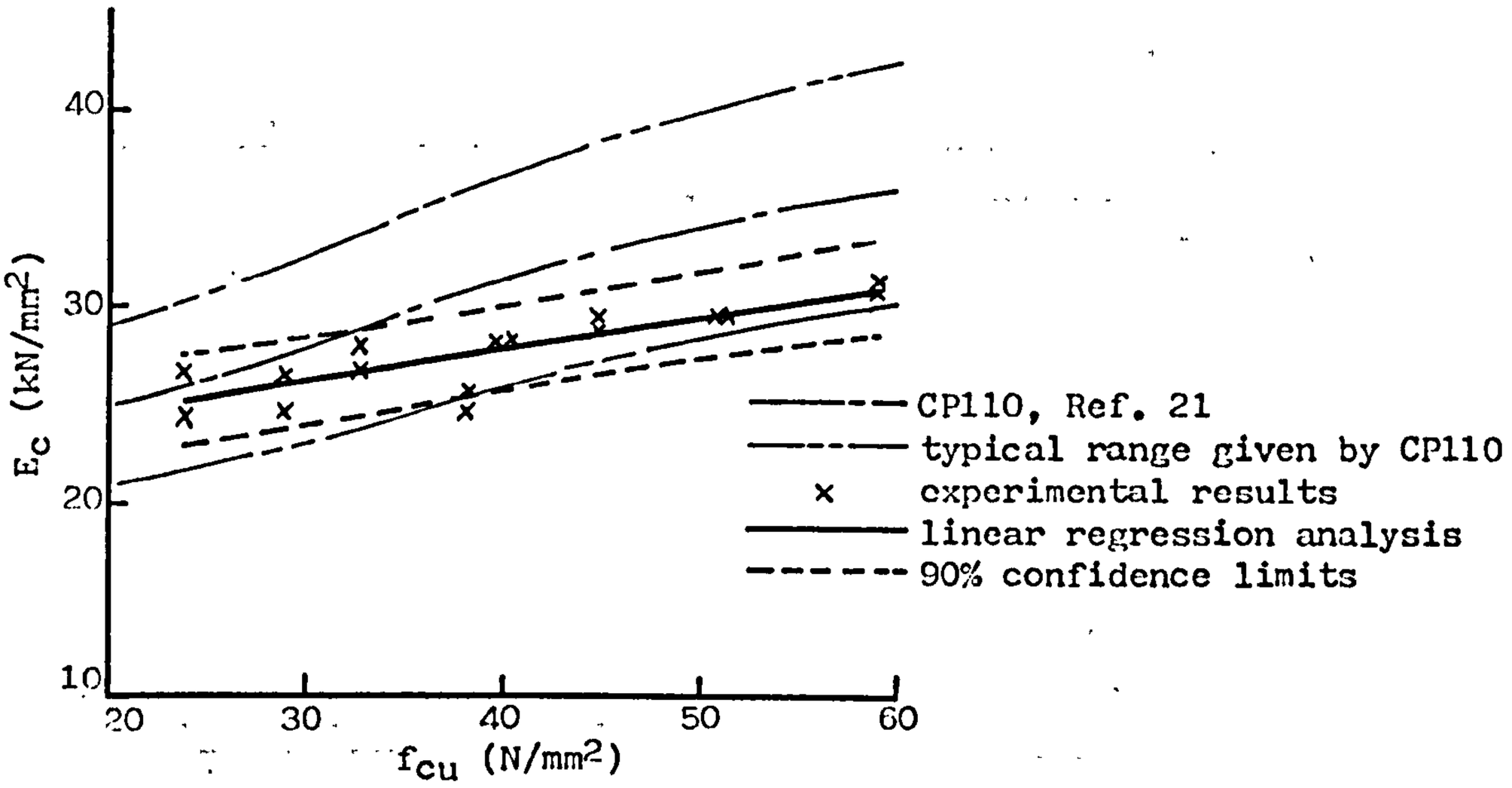

Fig. 5.26 Variation of the modulus of elasticity with the cube strength.

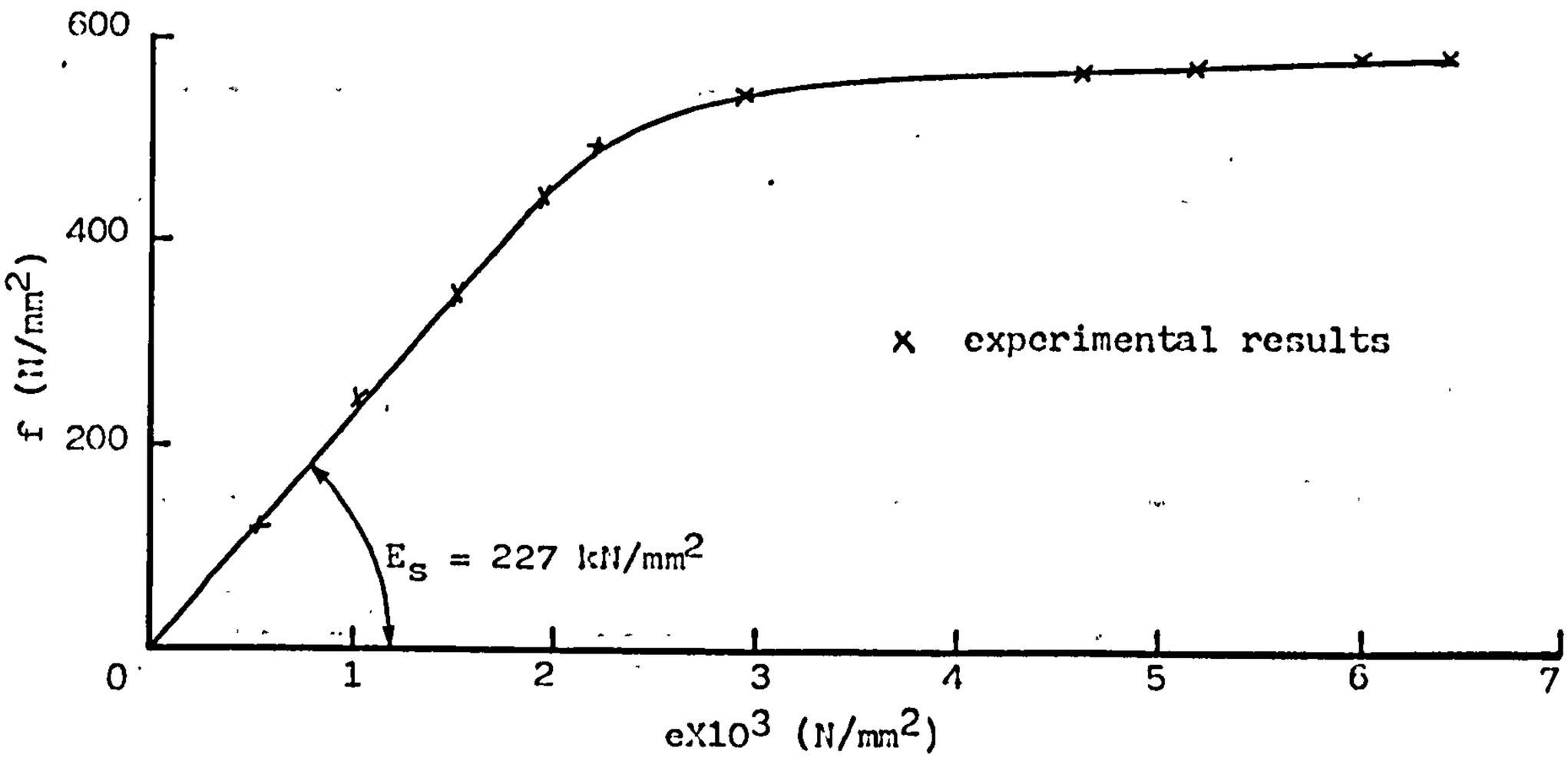

Fig. 5.27 Coupon test of the material from the shank of a stud.

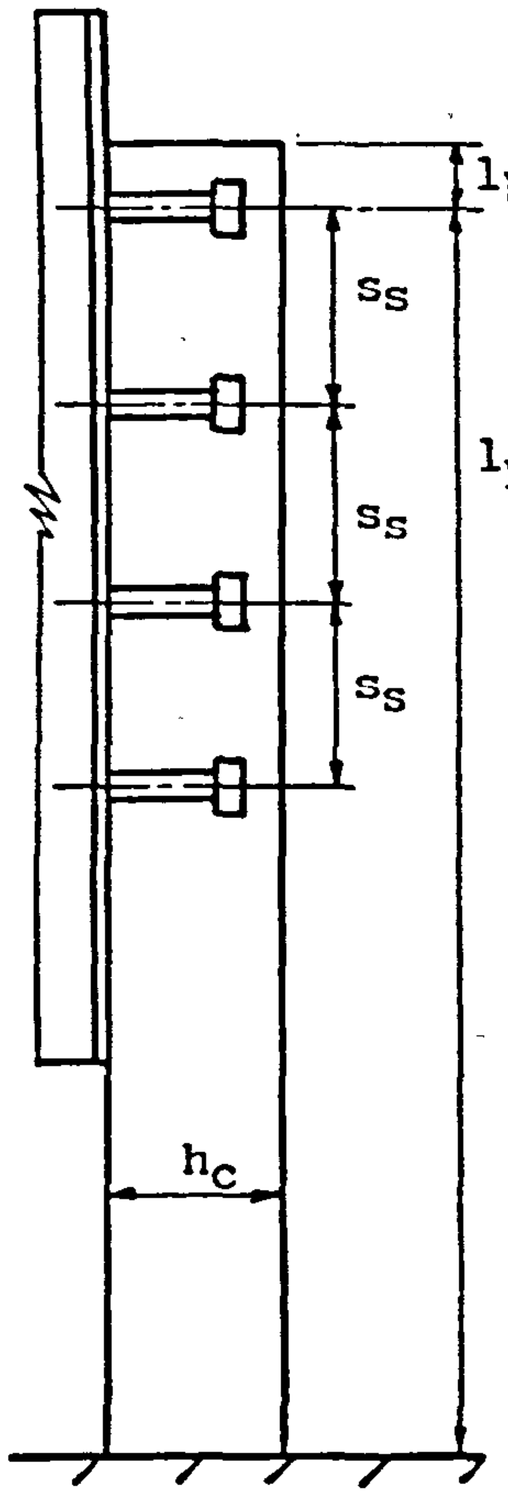

Fig. 5.28 Push specimen with longitudinally spaced studs.

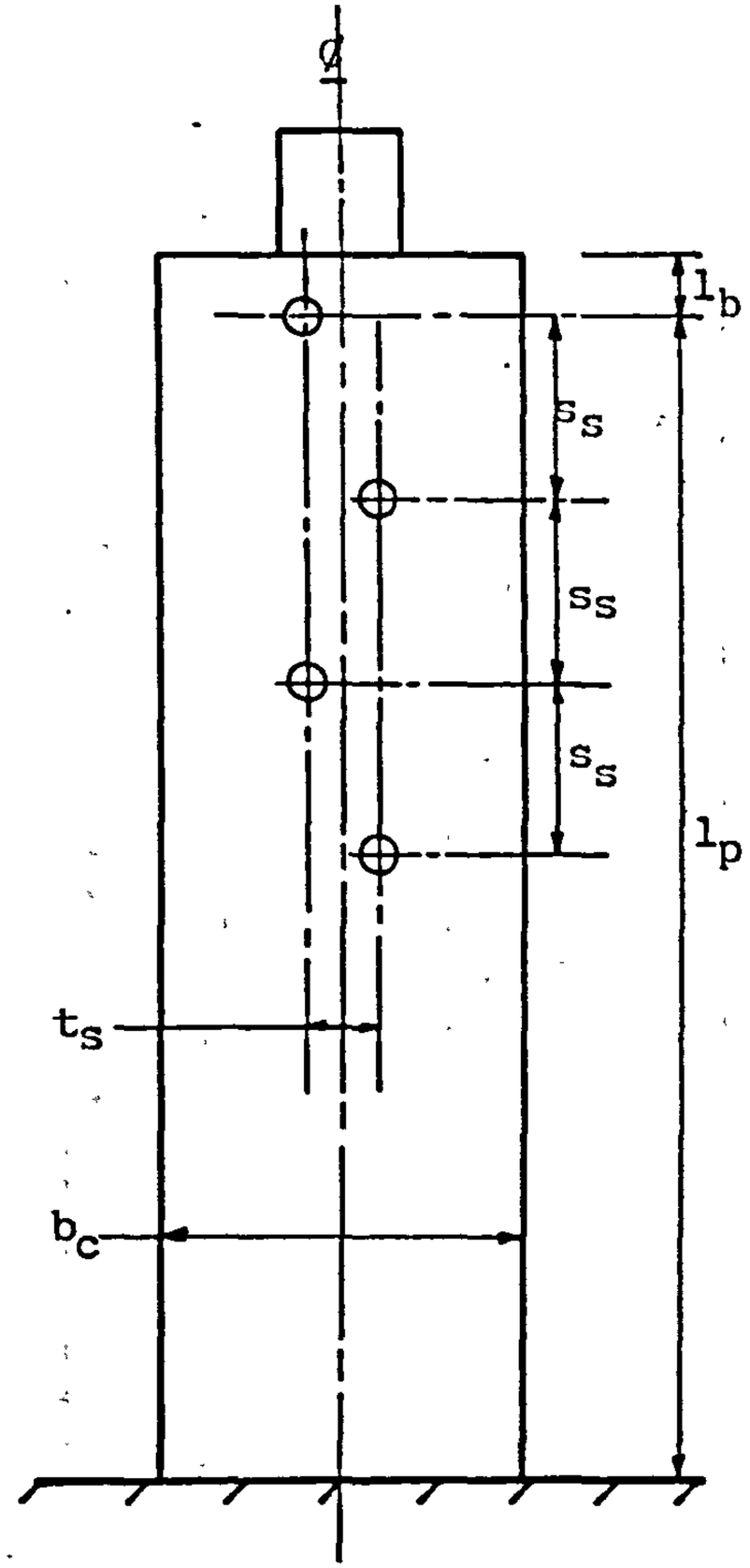

Fig. 5.29 Push specimen with staggered studs.

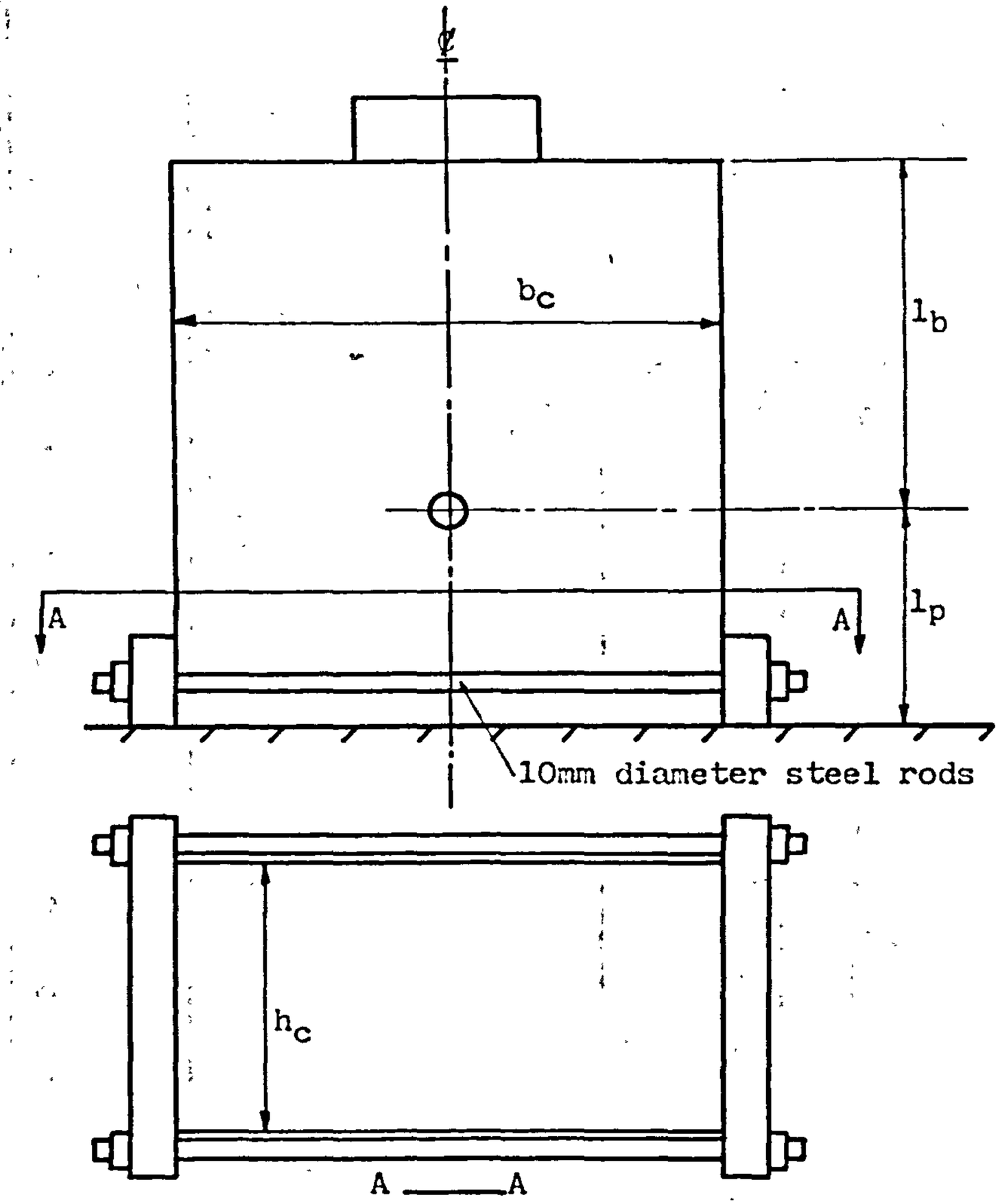

Fig. 5.30 Additional lateral restraint applied to the base of the push specimen.

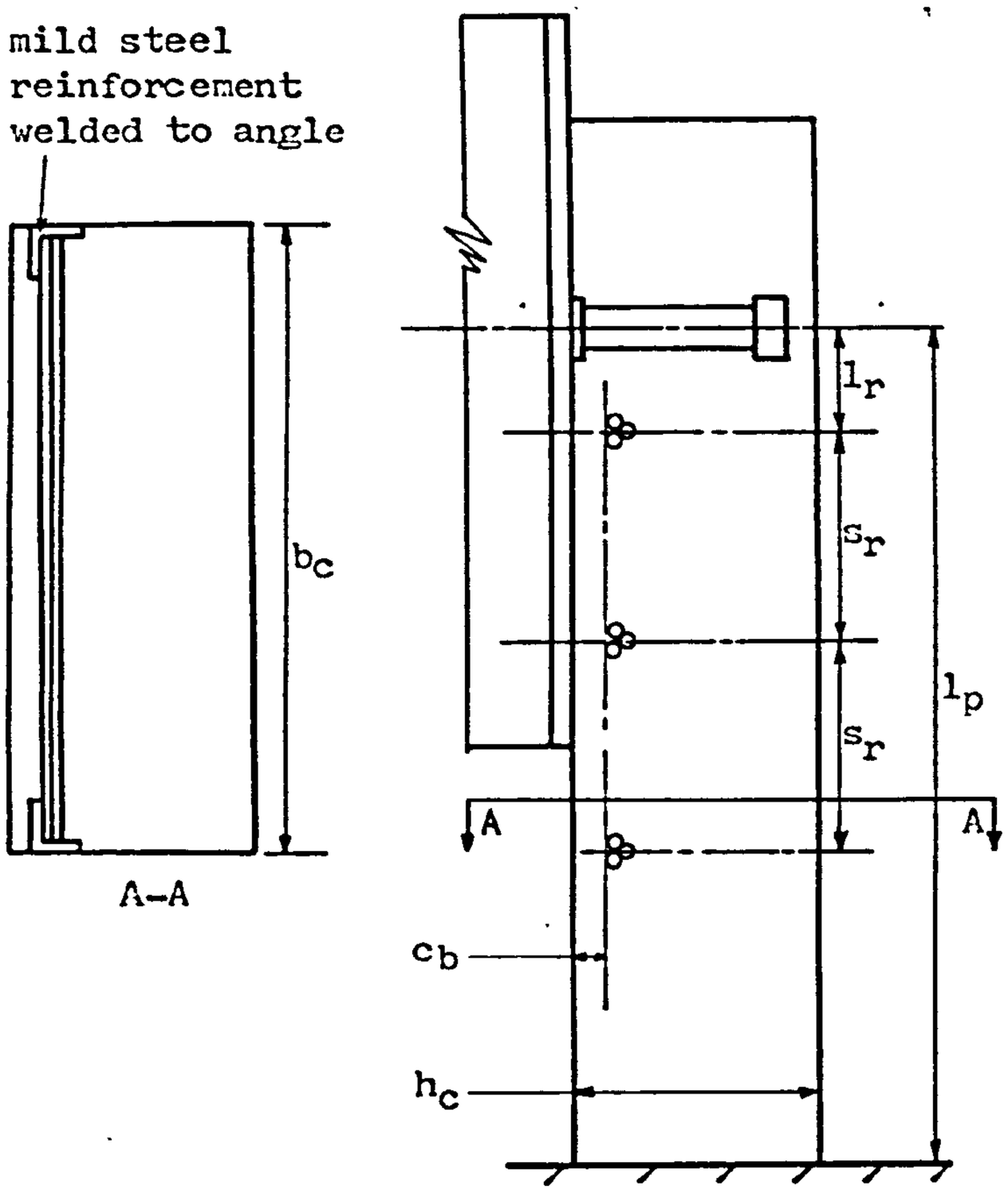

Fig. 5.31 Push specimen with the transverse reinforcement fully anchored.

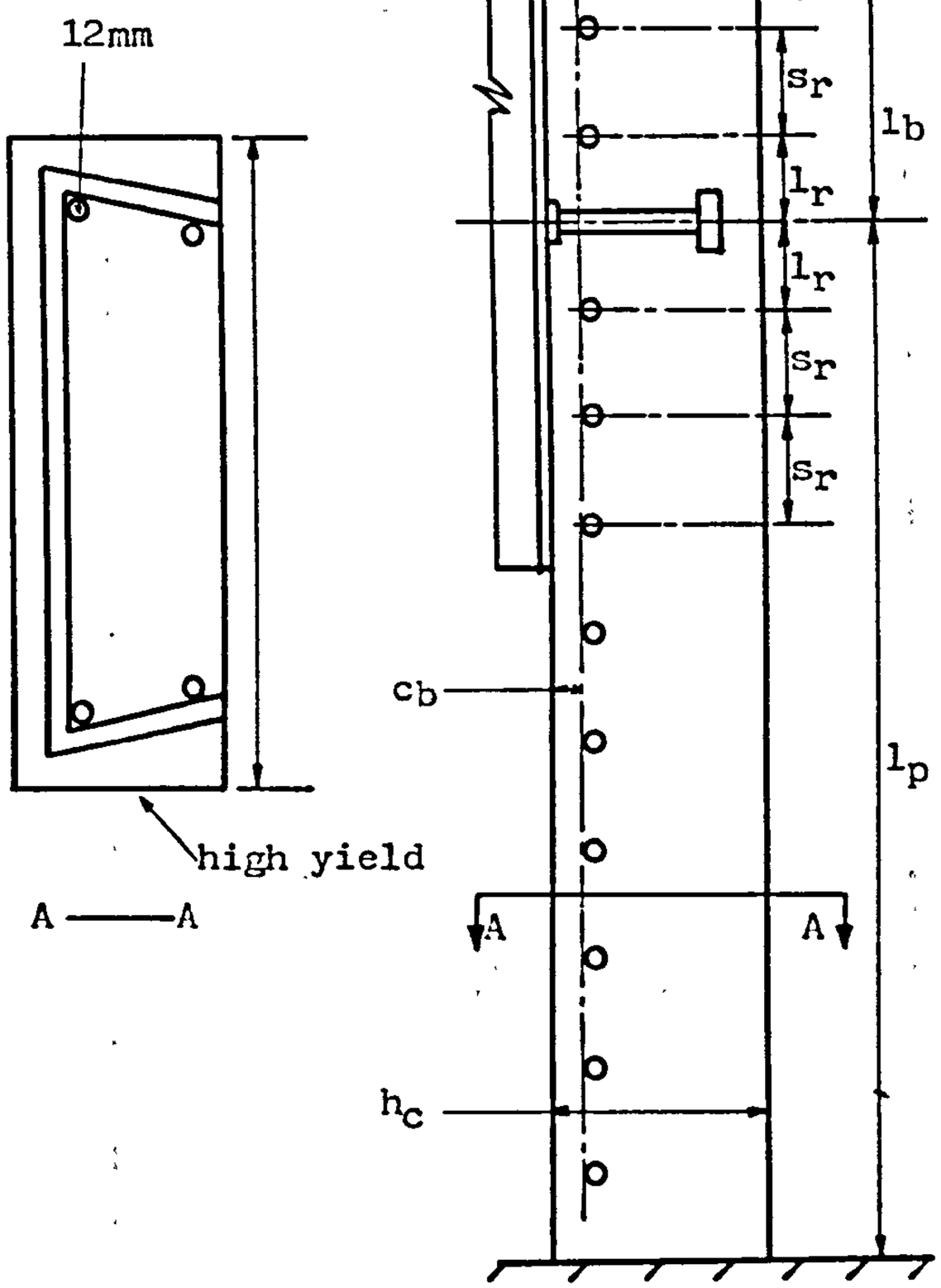

Fig. 5.32 Push specimen with uniformly distributed transverse reinforcement.

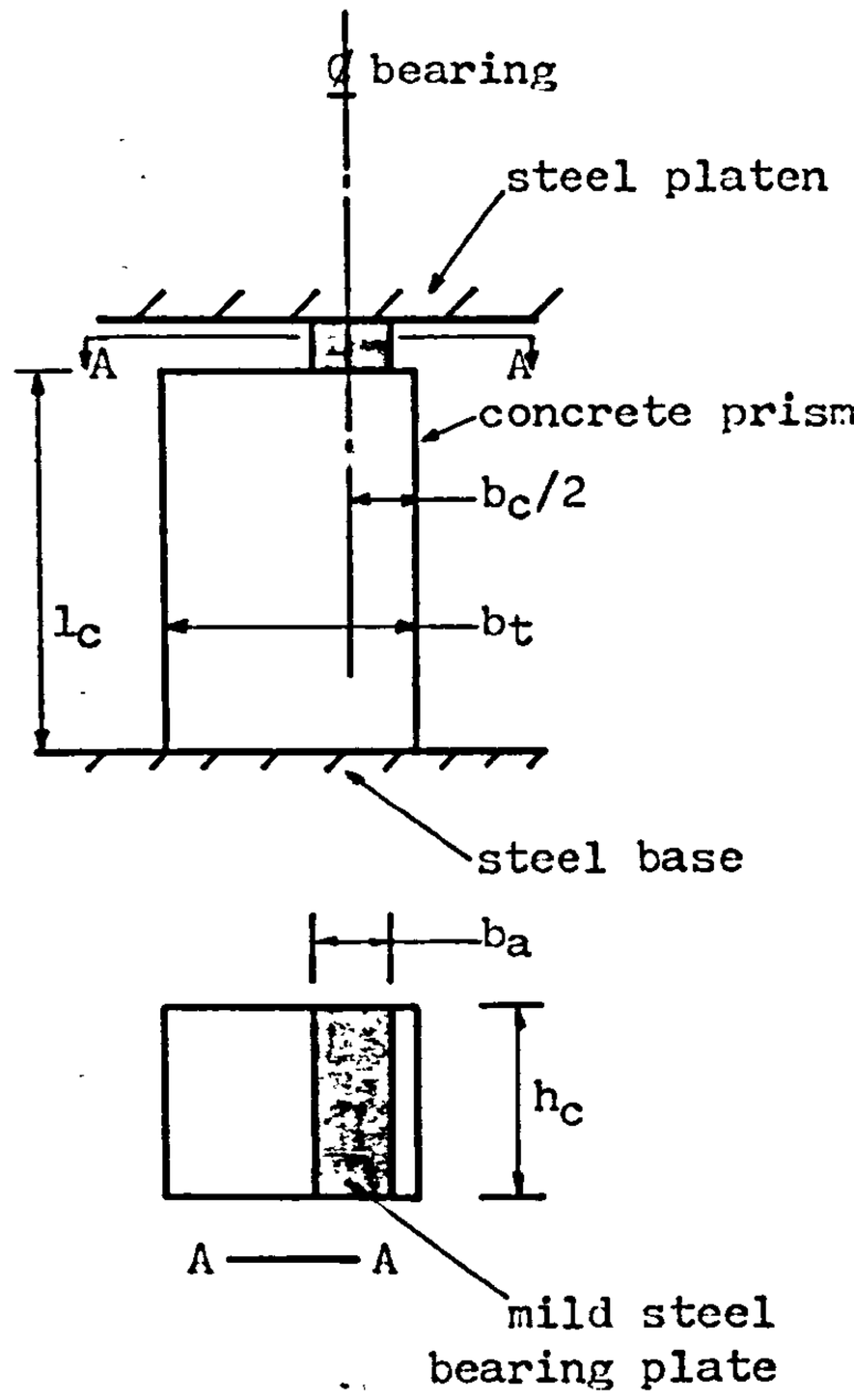

Fig. 5.33 Prism subjected to eccentric strip loads.

Appendix 5.1 Push tests. Tests on 13X65 studs at Warwick University by Burkhardt[62] and Fung and King[63].

Details:
Specimen as in Fig. 1.1. b_c = 300mm. h_c = 150mm. l_p = 250mm. l_b = 210mm. 13X65 studs. Fung and King used concrete with a maximum aggregate size of 10mm whereas Burkhardt used a maximum aggregate size of 19mm. Specimens lightly reinforced according to the Bridge Code[7]. Studs failed along the shank.

Specimen No.	Ref. No.	No. of studs	t_s (mm)	f_{cu} (N/mm^2)	f_{ct} (N/mm^2)	P_e (kN)
RSs7	62	1		47	-	77
RSs8	62	1		44	-	44
RSs9	62	1		42	-	54
RSs10	62	1		50	-	68
RSs11	62	1		43	-	72
RSt1	63	2	39	21	1.9	59
RSt2	63	2	39	21	1.9	59
RSt3	63	2	39	20	1.6	55
RSt4	63	2	39	20	1.6	55
RSt5	63	2	39	21	1.7	57
RSt6	63	2	39	21	1.7	60
RSt7	63	2	39	21	1.9	59
RSt8	63	2	39	21	1.9	56

Chapter Six

FAILURE OF THE SHANK OF THE STUD

6.1 INTRODUCTION

The maximum load that a stud can transmit into a slab which does not split, fail along planes of maximum shear nor allow the stud to pull out, is determined in this chapter.

The finite element model is described in Sect. 6.2. This model is used to determine the distribution of forces about the stud, Sect. 6.3, and the change in the strength of a stud when the parameters of the push test are altered, Sect. 6.4. The results are used to determine the maximum strength of studs, Sect. 6.5.

6.2. FINITE ELEMENT MODEL

6.2.1 The standard push test

6.2.1.1 Dimensions

The proportions of the stud, Fig. 6.1, were based upon the mean dimensions of 13X65 studs, Table 5.1; these proportions also closely resemble those of a 19X100 stud. The length and stiffness of the slab, Fig. 6.2, were arbitrary values.

Each rectangle of the finite element model represents two triangles, as shown in Fig. 6.3. The thickness of the elements in front of the stud were increased uniformly in order to represent the dispersal of the applied force into the concrete. The angle of dispersal was derived from Sect. 7.5.1.1. The shank and the weld collar were assumed to be square.

6.2.1.2 Material properties

A Mode 2 analysis, Sect. 4.3, showed that the concrete at the back of the stud and adjacent to the weld collar cracked at very low loads and that this crack quickly progressed along the shank to the head; the stud was in fact separating from the concrete behind it. These elements were therefore given zero stiffness, Fig. 6.3.

In order to represent the reduction in stiffness due to the high stresses at the base of the shank at failure, the stiffness of the elements below line F - F, Fig. 6.3, was halved.

6.2.1.3 Constraints

The constraints are shown in Fig. 6.3; the nomenclature is given in Fig. 4.2. The specimen was loaded by applying a uniform displacement to the nodes along the boundary B-C. The flange/slab interface, A-B, was free to slide. The base, which was fixed at D, was allowed to expand along D-E.

6.3 ELASTIC DISTRIBUTION OF FORCES

The Mode 1 analysis, Sect. 4.2, was used to analyse the standard specimen, Sect. 6.2.1. The distributions of forces, which were developed when a 100 kN shear force was applied to a 19X100 stud, should only be considered as a qualitative representation of the forces, as the two dimensional Mode 1 analysis is a very crude representation of the three dimensional problem.

The forces which are exerted on the stud, Fig. 6.4, can be considered to consist of: the shear force, the axial force and the bending moment at the base of the stud, the normal force perpendicular to the shank, the frictional force along the front of the shank, and the embedment force applied to the head of the stud.

The axial compressive force which is caused by the lateral restraint imposed upon the base of the concrete slab, Fig. 6.5, is almost equal to the horizontal restraining force at the base of the slab.

The longitudinal displacement of the stud pulls the head of the stud down and rotates it in an anti-clockwise direction, Fig. 6.6, causing larger embedment forces at the back of the head than in the front. These forces, in turn, cause a shear deformation in the concrete, Fig. 6.6. If these forces were large enough, cracking would start at the back of the stud and propagate all the way round, producing a conical type of failure in the concrete, which is often referred to as embedment failure. This phenomenon has been shown experimentally by Ollgaard, Slutter and Fisher[2].

6.3.1 Stud without a weld collar

6.3.1.1 Stud displaced longitudinally

The resultant of the external forces and the distribution of the internal forces are shown in Fig. 6.4. The bending moments and shear forces are at a maximum at the base of the stud and the axial load changes from compression at the base to tension at the head. The frictional force is usually much smaller than the normal force, Fig. 6.7, and so is unlikely to be limited by the coefficient of friction at the shank/concrete interface.

The distribution of the shear forces and bending moments in the finite element analysis, Fig. 6.4, is similar to that of Gogoi's[24] theoretical analysis, Figs. 2.2 and 2.3, about the bottom of the stud. The difference in the variations about the top is mainly because the finite element analysis allows the shank of the stud to separate from the concrete in front of the stud in this region and because of the embedment forces.

6.3.1.2 Stud displaced longitudinally and vertically

The effect of applying a vertical downward displacement of 30% of the longitudinal displacement can be seen by comparing Figs. 6.4 and 6.8. The vertical displacement increases the axial force, tension being positive, and reduces the frictional force; the combined effect is to increase the embedment forces particularly at the back of the stud. The moment at the base is hardly changed as its main contributor, the normal force, is not affected by the vertical displacement. The negative moments are increased by the embedment forces. The reversal in the direction of the frictional force, Fig. 6.7, causes the position of the maximum axial tensile force to change from the top of the stud to the bottom, Fig. 6.9.

6.3.1.3 Failure

A 'beam' analysis has been used to determine the probable causes of failure, although it is realized that the stress distributions are affected by the proximity of the applied loads and stress concentrations caused by abrupt changes in the dimensions.

The maximum flexural tensile stress, Fig. 6.10, occurs at the front of the stud at the shank/flange interface. The effect of the vertical displacement was to increase the axial stress to only 9% of the flexural stress. It would therefore appear that failure of a stud without a weld collar is predominantly a flexural failure.

6.3.2 Stud with a weld collar

6.3.2.1 Stud displaced longitudinally

The effect of the weld collar can be seen by comparing Figs. 6.4 and 6.13. Since most of the normal force is now resisted by the weld collar, its resultant is nearer the flange and hence the bending moment is reduced. The normal stresses, Fig. 6.15, are smaller than those of

a stud without a weld collar because the bearing surface of the weld collar is greater than that of the equivalent height of shank.

6.3.2.2 Stud displaced longitudinally and vertically

The effect, Fig. 6.14, is similar to that of a stud without a weld collar, Sect. 6.3.1.2.

6.3.2.3 Failure

The stresses at the weld-collar/flange interface, Fig. 6.11, and at the weld-collar/shank interface, Fig. 6.12, can be compared with those of a stud without a weld collar, Fig. 6.10. It is apparent that the weld collar substantially reduces the maximum stresses in all cases.

At the weld-collar/flange interface the flexural stresses, shear stresses and axial stresses are smaller because of the larger cross-sectional area of the weld collar. The flexural stresses are also smaller because of the reduction in the moment, Sect. 6.3.2.1.

At the weld-collar/shank interface the flexural stresses and shear stresses are smaller because most of the normal force is resisted below the interface by the weld collar. However, the axial stress is not significantly reduced and is now approximately the same size as the other stresses.

6.4 PARAMETRIC STUDY

The parametric study of Sect. 6.4.1 was conducted by analysing variations of the standard push test, Sect. 6.2.1, using the Mode 2 program, which does not allow the concrete to fail in compression. The effect of compressive failure was determined empirically in Sect. 6.4.2.

The shear connection was assumed to have reached its maximum strength when the maximum stress in the stud reached the ultimate tensile strength

of a 19X100 stud, Table 5.3. The maximum stress always occurred in the failure zone, Fig. 6.3. The concrete was assumed to split when the maximum stress reached 3.9 N/mm^2. Splitting was restricted to the concrete below the line F-F, Fig. 6.3, in order to prevent embedment failure.

6.4.1 Theoretically derived variations

One parameter of the standard push test was altered at a time. The variation in the theoretical strength is given as a proportion of the theoretical strength of the standard push test.

6.4.1.1 Tensile strength of the concrete

The cracking pattern, at the maximum load, when a longitudinal displacement was applied to the standard push-test specimen is shown in Fig. 6.21. The cracks, which started and propagated from the elements immediately above the weld collar, are shown as individual cracks but they probably join to form a series of longitudinal struts which eventually fail by buckling; this method of concrete failure, i.e. spalling, can be seen in Fig. 5.17. A reduction in the tensile strength of the concrete of 72%, Fig. 6.22, increased the amount of cracking but only reduced the maximum load by less than 2%.

6.4.1.2 Material stiffness

As the stiffness of the concrete increases, in relation to the stiffness of the stud, the level of the resultant of the normal force, Fig. 6.4, falls and hence the forces at the interfaces reduce causing the stud to fail at a higher shear load, Fig. 6.16. The variation of the finite element analysis is compared with the empirical variation of Ollgaard, Slutter and Fisher[2], Equ. 2.3, by plotting the variation of the empirical rules about the point $K_e = 1$ and $E_c/E_s = 0.115$. The

variations have a good agreement.

It can be derived from Fig. 6.16 that the 15% reduction in strength of studs in lightweight concrete of a density greater than 1400 kg/m^3, which is required by the Bridge Code[7], becomes unconservative when the density is less than 1940 kg/m^3, if the relationship between the density and stiffness of concrete given by CP110[21] is used.

6.4.1.3 Voids and dense inclusions

A void or an inclusion in the concrete has the same effect as varying the material stiffnesses, Sect. 6.4.1.2, except that the variation is now localized.

A void along the bearing surface of the weld collar, Fig. 6.23, reduced the strength of the standard specimen by 29%. A 10mm inclusion, of the same stiffness as the stud, increased the strength of a 13X65 stud in the standard specimen by 23%, when it was placed at the soffit of the slab, Fig. 6.24, and by only 0.4% when it was placed at the same distance from the shank, but with 15mm cover; a 10mm inclusion increased the strength by 32%. The theoretical results have been compared with the experimental results of studs which failed along the shank, Fig. 6.27; the range is similar. The experimental results, Fig. 6.27, include those of Appendix 5.1 and those of Table 3.1 in which the slab was wider than 200mm, since it will be shown in Chapter 7 that these were unlikely to split.

It would appear that the strength is highly dependent upon the properties of the concrete in the immediate vicinity of the weld collar; bad compaction and changes in the position of the individual aggregate particles can alter the strength substantially. This may explain why the range of Burkhardt's[62] results, 70% to 122% of the mean, is much greater than those of Fung and King[63], 94% to 105%, in Appendix 5.1.

Burkhardt used a maximum aggregate size of 19mm whereas Fung and King used a maximum aggregate size of 10mm. The difficulty of compacting 19mm aggregates around the weld collars of 13X65 studs may have caused the lower range of Burkhardt's results whereas the larger aggregate size would cause the higher range.

6.4.1.4 Height of the shank

The variation found in the finite element analysis, Fig. 6.17, compares reasonably well with the empirically derived rules of the Draft European Recommendations[23], considering that the proportional change is small and hence would be difficult to determine experimentally. The lower strengths of Slutter and Driscoll[3], at low values of h_{sh}/d_s, is probably because their specimens failed due to embedment failure whereas the finite element analysis does not allow this to occur. The Bridge Code[7] assumes a difference in strength between a 19X75 and a 19X100 stud of 13%, which agrees well with the 10% difference given by the finite element analysis.

6.4.1.5 Height of the weld collar

The theoretical variation, Fig. 6.18, is compared with the experimental results in Sect. 6.4.2.2. The extent of cracking of a stud without a weld collar at the maximum load, Fig. 6.25, is less than that of the standard specimen, Fig. 6.2 1, partly because of the lower strength and partly because the weld collar acts as a crack inducer by causing high stress concentrations. The effect of this on the distribution of the normal force about the weld collar is shown in Fig. 6.15.

The optimum height of the weld collar of the standard stud, Fig. 6.1, i.e. the height at which failure occurs simultaneously at the two interfaces, can be calculated from Fig. 6.18. The strength of the

weld-collar/flange interface is proportional to $0.59A_w f'_{su}$, where 0.59 is K_w at $h_w/d_s = 0$, Fig. 6.18, A_w = Area of weld collar and f'_{su} is the ultimate tensile strength of the weld material. The strength of the shank/weld-collar interface is proportional to $K_w A_s f'_{su}$. Since $f'_{su}=1.13f_{su}$, Sect. 5.3.2.2, the interfaces fail simultaneously when $K_w = 1.19$ i.e. $h_w = 0.35d_s$.

6.4.1.6 Length of the slab

The theoretical strength increases as the length of the slab reduces, Fig. 6.19, because the axial compressive load, caused by the lateral restraint at the base, Sect. 6.3, also increases, Fig. 6.31, and hence reduces the tensile stresses at the interfaces. Furthermore, the deformation of the concrete reduces because of the proximity of the base and hence becomes apparently stiffer.

It may be more appropriate to assume that the base is fully fixed, Fig. 6.19, as the slab is unlikely to rotate about D, Fig. 6.3, when the stud is close to the base. The variations converge when $l_p > 20d_s$.

When the base of a push-test specimen is allowed to slide, the slab rotates about the studs forming compressive forces across the flange/slab interface above the stud. These forces are balanced by an axial tensile force at the base of the stud which acts over the interfaces of the studs causing the strength to reduce. The theoretical axial compressive force in a push test, in which $l_p = 45d_s$ and the base was partly restrained, was 9% of the shear load and when the base was allowed to slide, the force changed to an axial tensile force of 3% of the shear load; the effect of which was to reduce the shear strength by 11%. Mainstone and Menzie[10] showed experimentally that the strengths of studs tested in slabs which were free to slide were consistently about 10% below the strengths given in CP117[8].

6.4.1.7 Axial loads

The variation in strength when an axial displacement as well as a longitudinal displacement is applied is shown in Fig. 6.32, The effect of tensile cracking is shown by the difference between the Mode 1 and Mode 2 analyses. The sudden reduction in the strength between the points A and B is caused by the complete disintegration of the concrete around the weld collar, Fig. 6.26, and hence the variation follows the theoretical variation when a void is assumed to be adjacent to the bearing surface of the weld collar. The load at which the concrete starts to disintegrate, point A, is dependent upon the tensile strength of the concrete, Fig. 6.29.

If it is assumed that the longitudinal cracks which occur around the weld collar, Fig. 6.21, eliminate the frictional force at the weld collar, Fig. 6.14, then the axial force can be considered to be almost uniform along the shank, in contrast to the normal force which reduces rapidly. The axial force has therefore an increasingly greater effect than the normal force on the shank/weld-collar interface as the height of the weld collar increases. This is confirmed by the theoretical initial rate of reduction in strength, the slope at D, Fig. 6.32, which increases as the height of the weld collar increases, Fig. 6.28.

The theoretical variations for the standard specimen with and without a weld collar, Figs. 6.29 and 6.30, form a lower bound to the empirical rules of McMackin, Slutter and Fisher[13], which are used in the Draft European Recommendations[23], and to the design rules of the Bridge Code[7]. McMackin's rules were derived from tests on studs without weld collars for which they appear to give a slightly better correlation with the finite element analysis. The Bridge Code, which only considers the strength of the shank of the stud, assumes that its strength reduces according to Von Mises yield criterion, as recommended by Van Dalen[25].

6.4.2 Empirically derived variations

As the maximum shear strength of a stud shear connector, P_{sh}, is assumed to occur when the shank reaches its ultimate strength, f_{su}, it will be assumed that P_{sh} is proportional to the strength of the shank, $A_s f_{su}$, and therefore the strength of a stud in a push specimen is given by by

$$P_{sh} = A_s f_{su} K_c K_f K_h K_w K_l K_a \qquad (6.1)$$

where the theoretical variations of K_c, K_h, K_w, K_l and K_a have been determined in Sect. 6.4.1 and K_f is the variation due to the compressive strength of the concrete.

6.4.2.1 Compressive strength of the concrete

The variation caused by changes in the compressive strength of the concrete, K_f, was determined from the experimental results of Tables 5.8 and 5.11 in which the depth of the failure zone, h_f, was measured, by assuming $P_{sh} = P_e$ in Equ. 6.1. The empirical variation, line A-A in Fig. 6.20, has a coefficient of variation of 7.5% which is close to the statistically derived coefficient of variation of the experimental error, Sect. 3.4.3.1, of 7.9%. An analysis of all the results of the tests which failed along the shank, Tables 5.8 and 5.11 and those of Fung and King in Appendix 5.1, gave the line B-B when the height of the weld collar was assumed to be $0.25d_s$ and the line C-C when the height of the weld collar was assumed to be the mean height of the measured failure zones, $0.33d_s$. The results of Fung and King were included because they used the same type of aggregates and cement and hence their concrete had the same material variations as in Sect. 5.3. The theoretical variation, A-A, agrees closely with the empirical variation of Ollgaard[2] et al, which has been plotted through the intercept of the lines A-A and C-C, and it is probably conservative to extrapolate it downwards as it falls below the line C-C.

The failure mechanism is similar to that caused by variations in the material stiffness, Sect. 6.4.1.2. When the concrete fails its stiffness reduces causing the resultant of the normal force to rise and hence increases the stresses at the stud interfaces. Slabs of weak concrete will therefore start to fail at lower loads than those of stronger concrete and hence the maximum load will be less.

6.4.2.2 Height of the weld collar

The theoretical variation caused by changes in the height of the weld collar, K_w, is compared with the experimental variation in Fig. 6.18. The experimental values of K_w were determined from the test results of Tables 5.8 and 5.11, in which the depth of the failure zone was measured, and specimen USs9, Table 5.9, by assuming $P_{sh} = P_e$ in Equ. 6.1 and deriving K_f from line C-C in Fig. 6.20. This is a feasible method of comparison since the line C-C was not derived from the individual heights of the failure zones. The variations have a reasonable agreement; the scatter may be partly due to the difficulty in measuring the height of the failure zone.

6.5 MAXIMUM STRENGTH

The maximum strength of a stud in a push test, Equ. 6.1, is compared with empirically derived rules in Sect. 6.5.1 and is used to determine tentative design rules in Sect. 6.5.2.

6.5.1 Strength of a stud in a push test

6.5.1.1 An upper bound to the maximum strength

The following properties may be considered to define an upper bound to the strength of a stud in a push test.

The base of the slab is fully fixed; $K_a = 1$ in Fig. 6.29.

The height of the weld collar is equal to or greater than the optimum height of $0.35d_s$, Sect. 6.4.1.5; $K_w = 1.19$ in Fig. 6.18.

The stiffness of the concrete varies according to the upper range given by CP110[21], Fig. 5.26.

The strength and stiffness of the stud are the same as those used in this research project; $f_{su} = 620$ N/mm^2, Table 5.3, and $E_s = 227$ kN/mm^2, Fig. 5.27.

The stud is placed at a distance of $20d_s$ from the base; $K_l = 1$ in Fig. 6.19.

6.5.1.2 A lower bound to the maximum strength

The following properties may be considered to define a lower bound to the strength of a stud in a push test.

The base of the slab is allowed to slide and hence the shear connection is 11% weaker than in a slab which is prevented from sliding, Sect. 6.4.1.6; $K_a = 0.89$. There is not a weld collar; $K_w = 0.59$.

The ultimate tensile strength of the stud material is 500 N/mm^2; this is the characteristic strength as given by the Bridge Code[7]. The failure strength is therefore 13% greater, Sect. 5.3.2.2.

The stiffness of the stud is the same as those used in this research project; $E_s = 227$ kN/mm^2, Fig. 5.27.

The stiffness of the concrete varies according to the lower range given by CP110[21], Fig. 5.26.

The stud is placed at a distance of $20d_s$ from the base; $K_l = 1$ in Fig. 6.19.

6.5.1.3 A comparison with empirically derived rules

The upper and lower bounds, which were derived in the previous sections, have been compared with empirically derived rules for the

strength of 19X100 studs, Fig. 2.1. The bounds clearly encompass the empirical rules.

6.5.2 Design rules

6.5.2.1 Derivation of rules

As the behaviour of the studs in composite beams is not known, the following properties and assumptions may be considered only to be a guide in determining the maximum strength of studs in beams.

There is no axial load at the base of the stud; $K_a = 0.93$ in Fig. 6.29.

Since the change in strength with the length of the slab, K_l, is caused by the induced axial loads, Sect. 6.4.1.6, the assumption that the axial load is zero means the strength is now independent of the length of the slab. Furthermore, since $K_a = 0.93$ was derived from a specimen in which $l_p = 20d_s$, $K_l = 1$ in Equ. 6.1.

The height of the weld collar is $0.25d_s$, which is the mean of several measurements, Table 5.1; $K_w = 1$ in Fig. 6.19.

The maximum strength of a stud in a beam is therefore given by

$$P_{sh} = 0.93A_s f_{su} K_e K_f K_h \qquad (6.2)$$

6.5.2.2 Comparison with design rules

The strength of a stud in a beam, Equ. 6.2, is compared in Fig. 2.1 with the present design rules for the strength of 19X100 studs, for the case when $f_{su} = 620$ N/mm^2, the strength of the studs used in this research project, and for the case when $f_{su} = 500$ N/mm^2, the characteristic strength of studs as stipulated by the Bridge Code[7]. It was assumed that the stiffness of the concrete varied according to the mean as given by CP110[21], Fig. 5.26, and that the stiffness of the stud

material was 220 kN/mm^2. There is a reasonable agreement between the strengths.

The Bridge Code[7] requires that the strength is reduced by 15% when the studs are embedded in lightweight concrete. However, the variation due to the stiffness of the concrete, K_c, automatically allows for the reduction in strength for studs embedded in lightweight concrete.

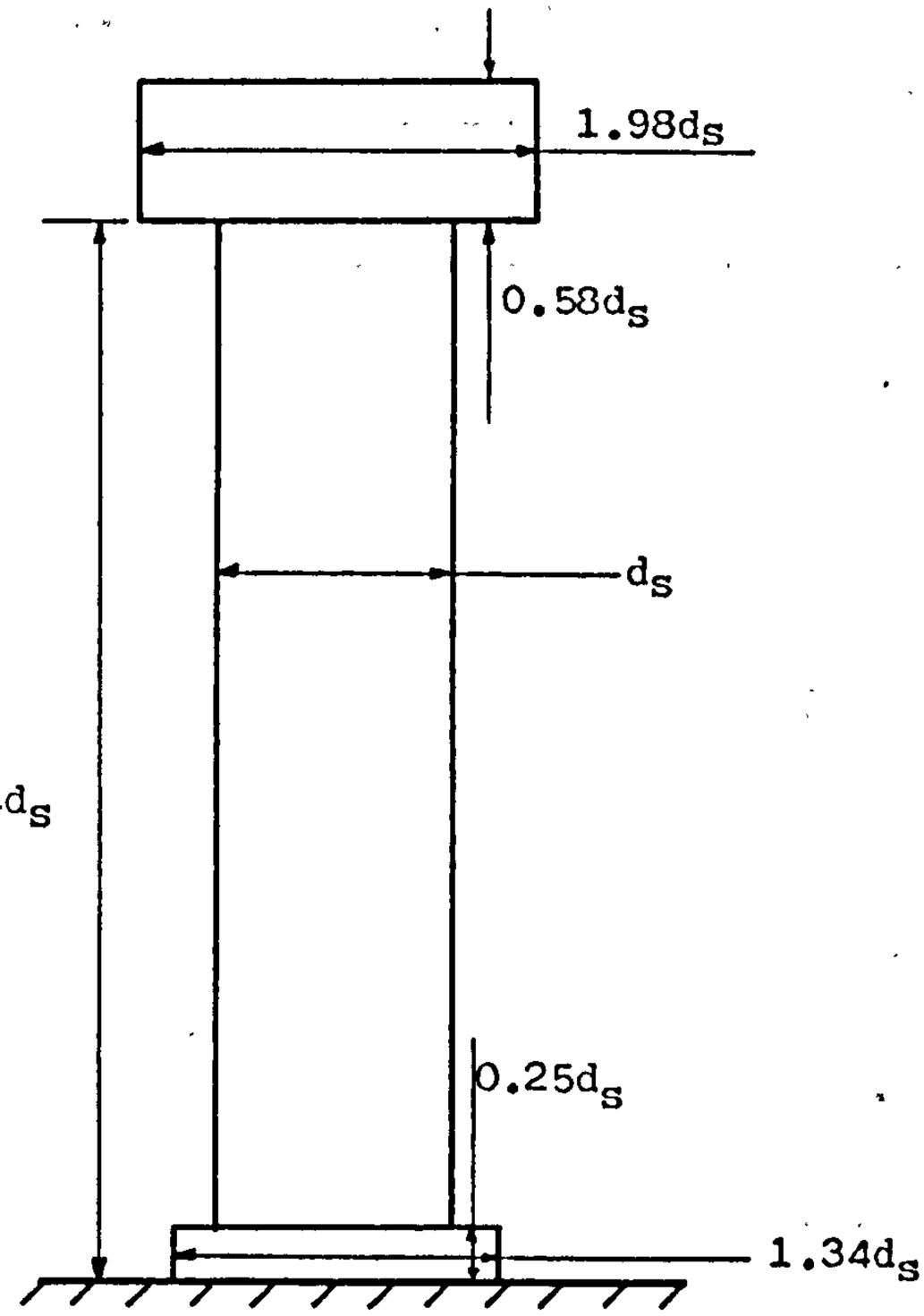

Fig. 6.1 Dimensions of the standard stud.

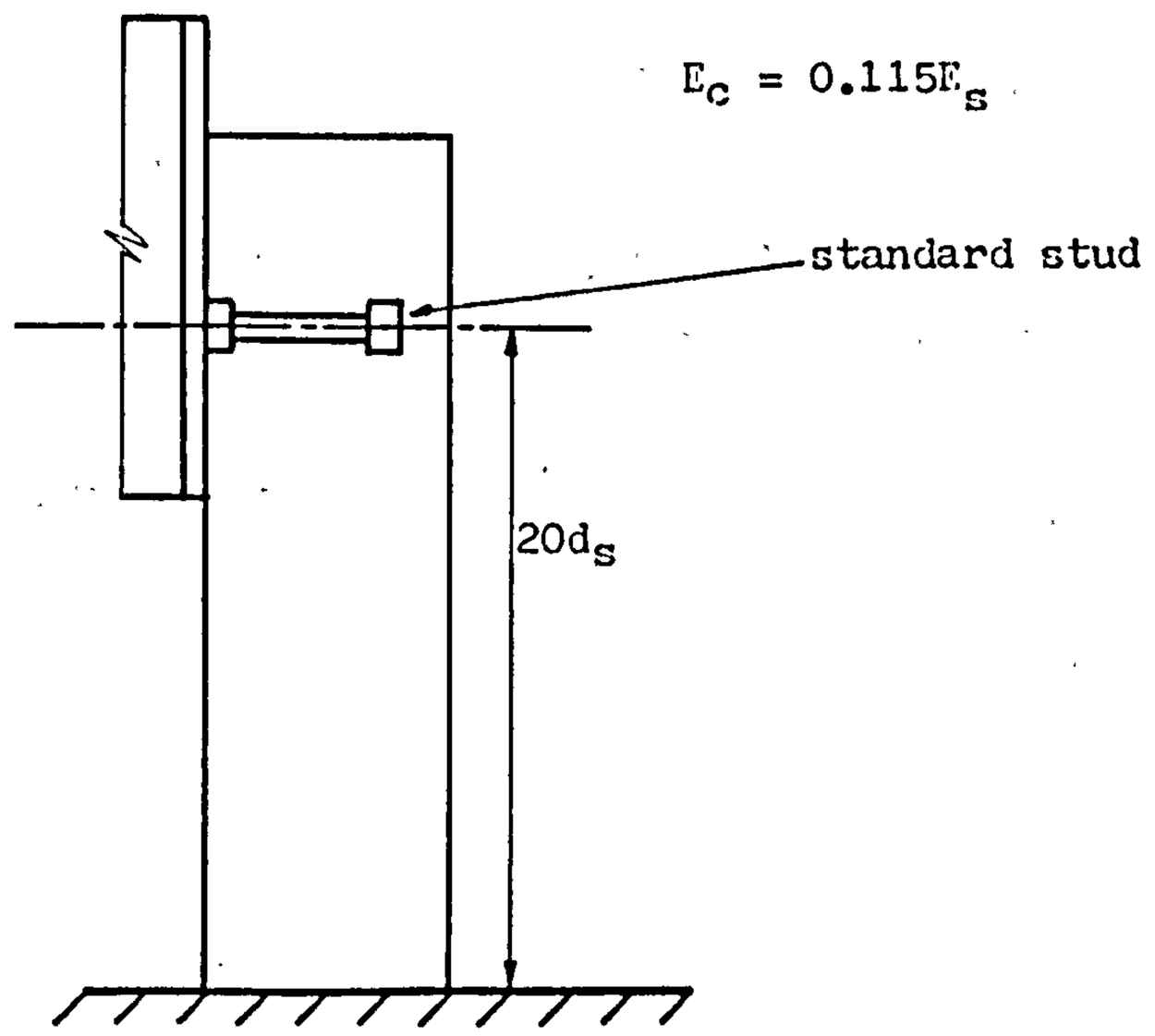

Fig. 6.2 Properties of the standard push specimen.

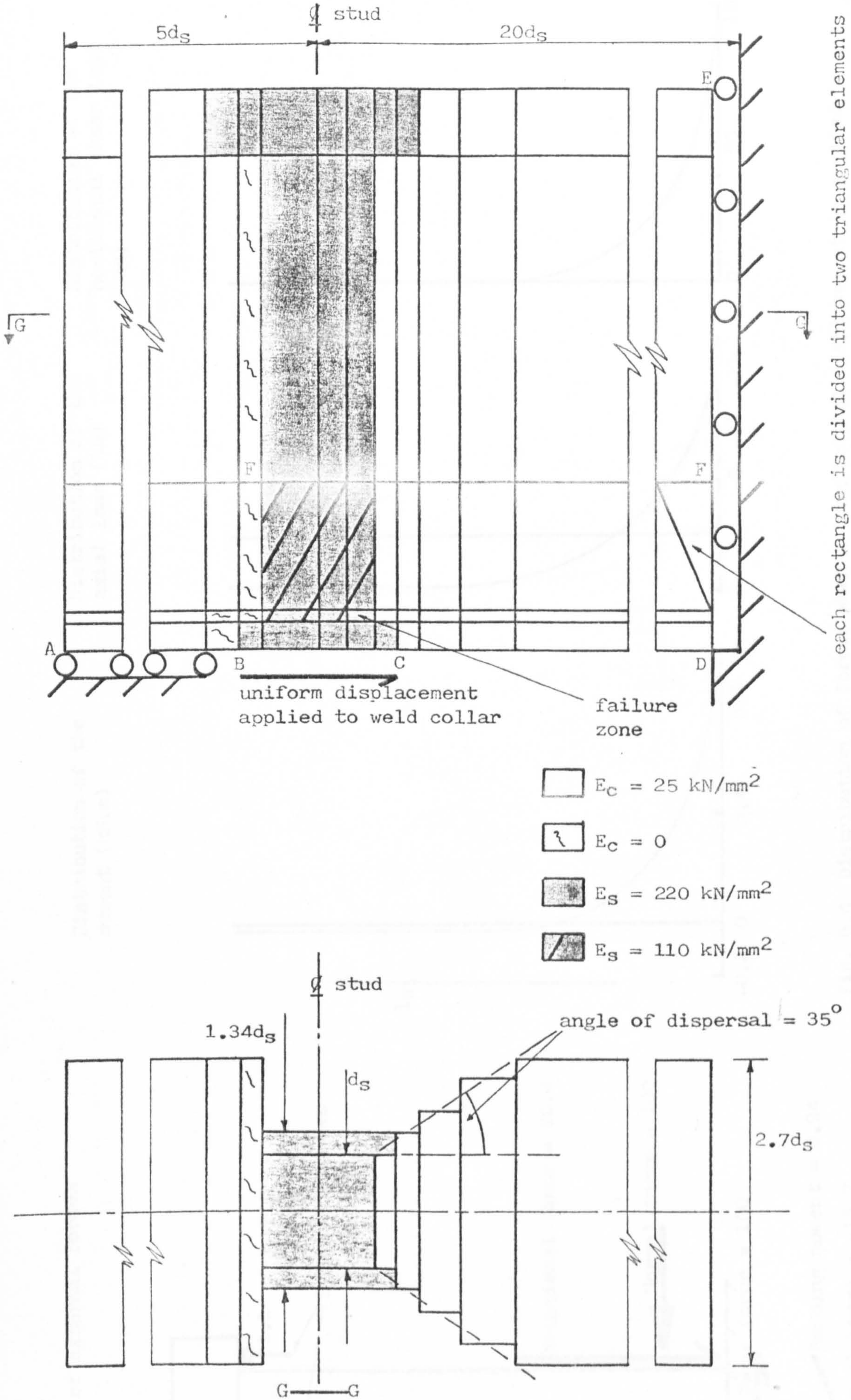

Fig. 6.3 Finite element model of the standard push test.

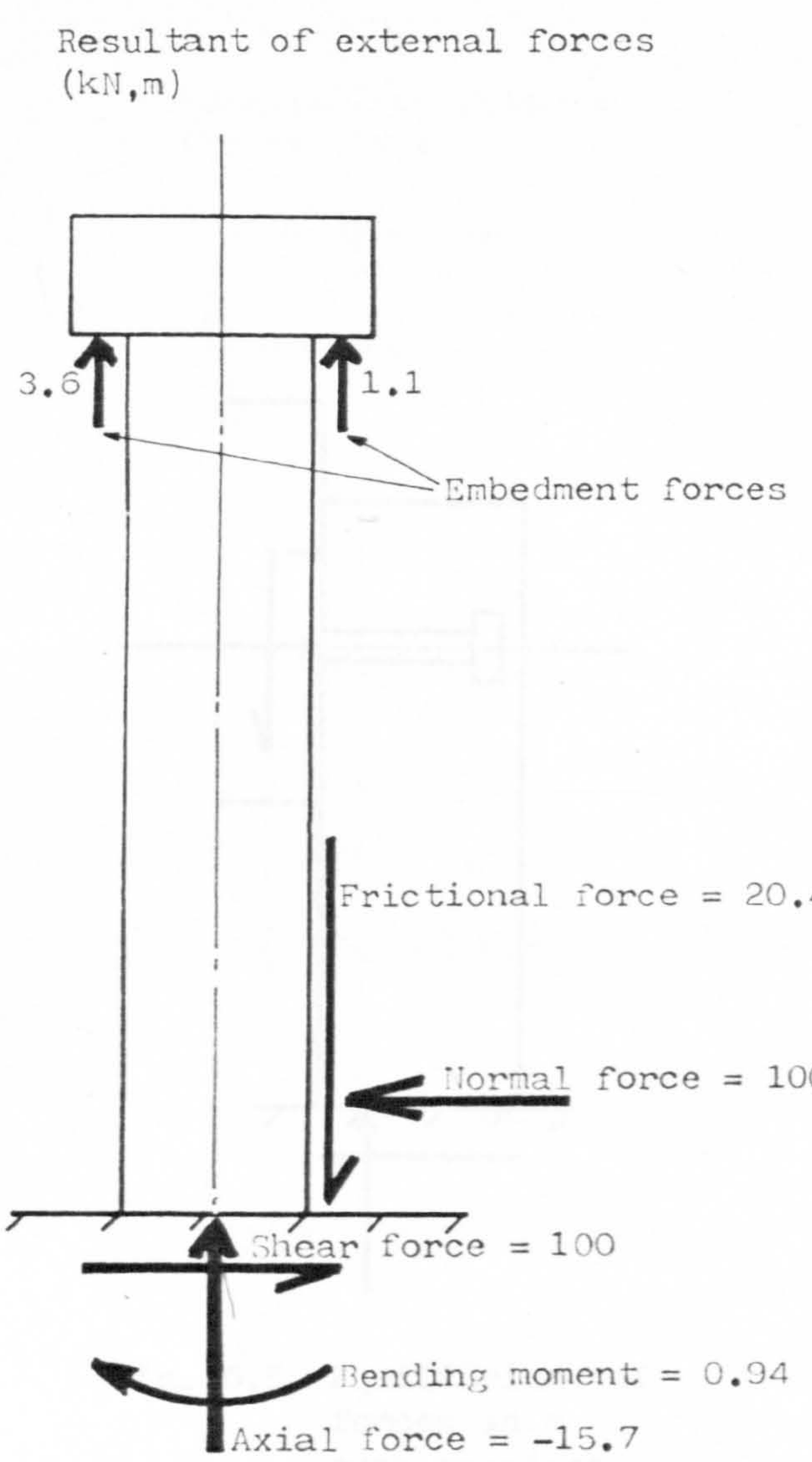

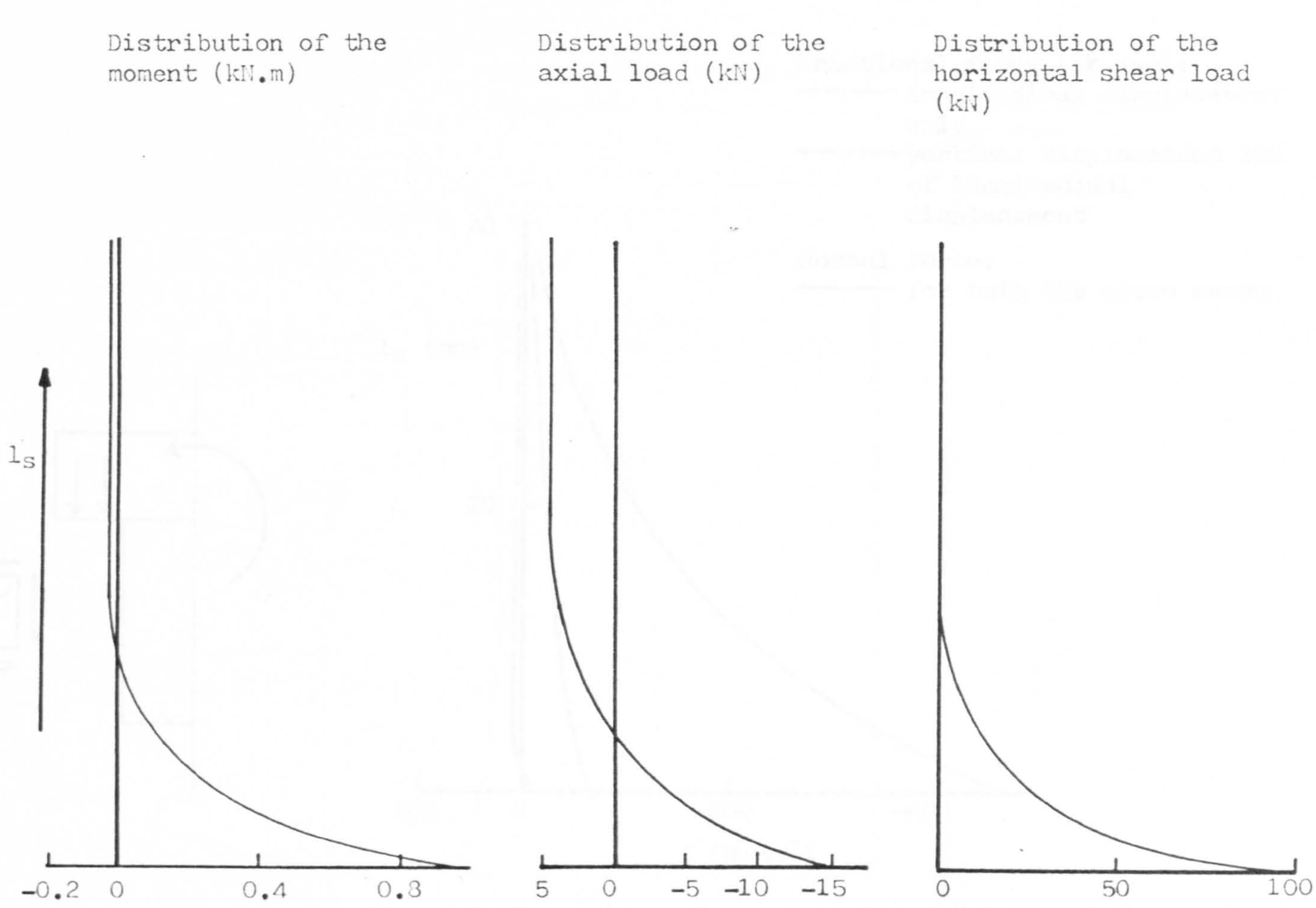

Fig. 6.4 Distribution of forces when a longitudinal displacement is applied to the base of a stud without a weld collar.

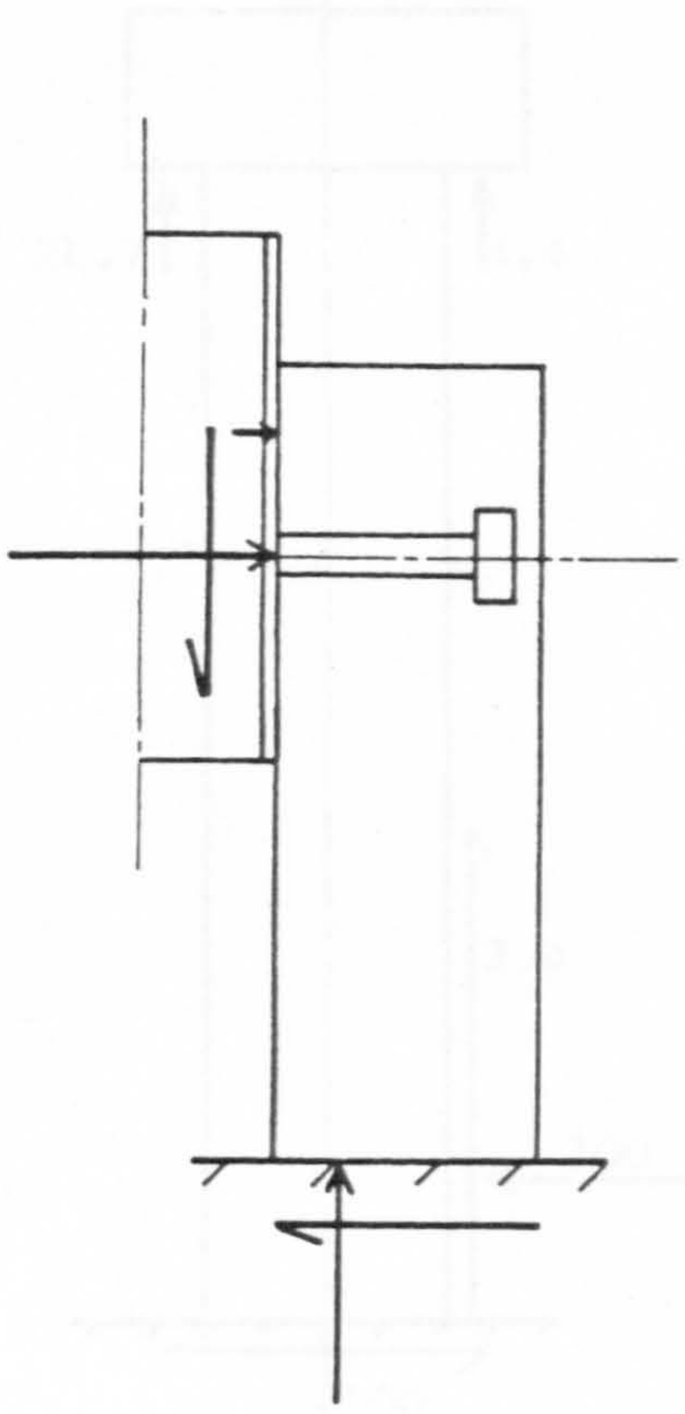

Fig. 6.5 Equilibrium of forces in a push specimen.

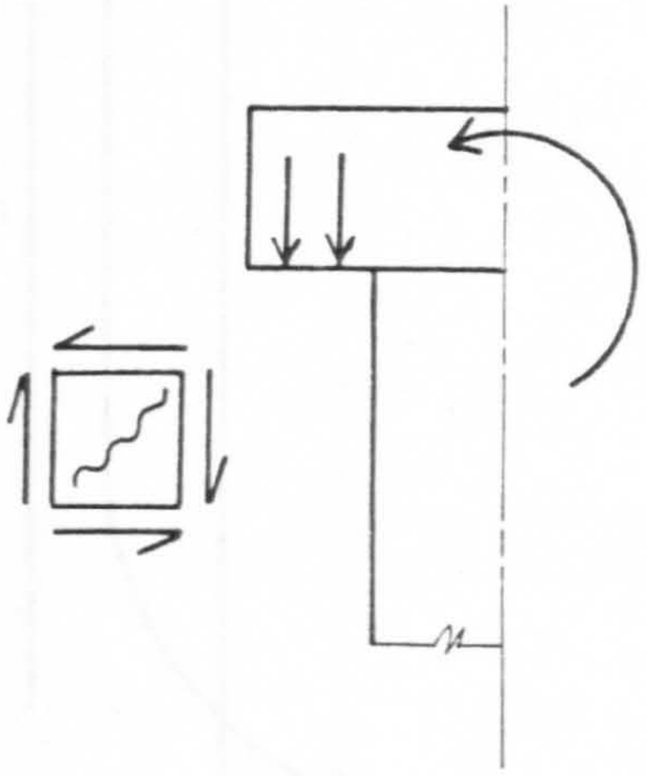

Fig. 6.6 Embedment failure.

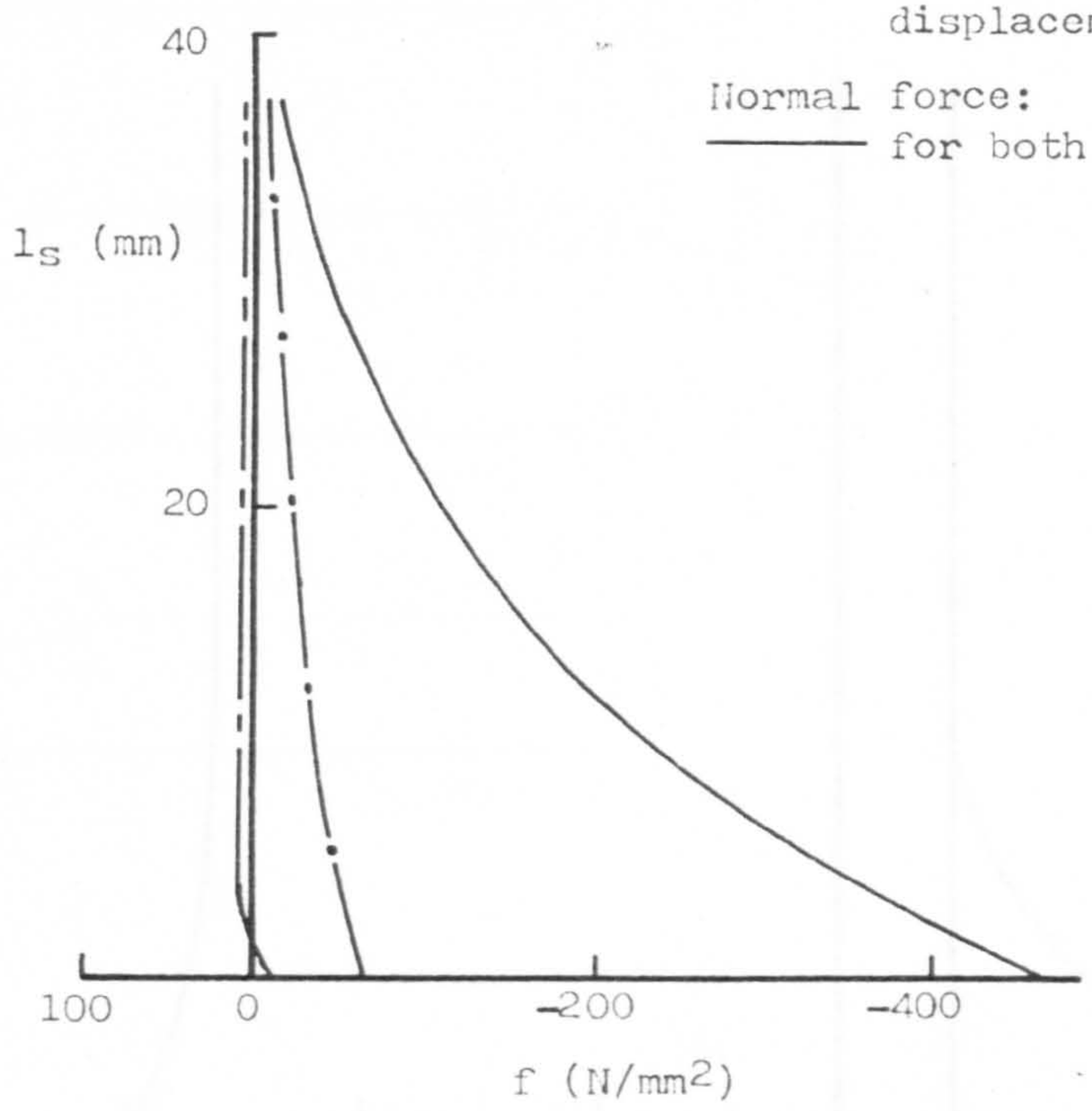

Frictional force (↓ +ve):
——·—— longitudinal displacement only
——-—— vertical displacement 30% of longitudinal displacement

Normal force:
——— for both the above cases

Fig. 6.7 Comparison of the normal and frictional force along the shank of a stud without a weld collar.

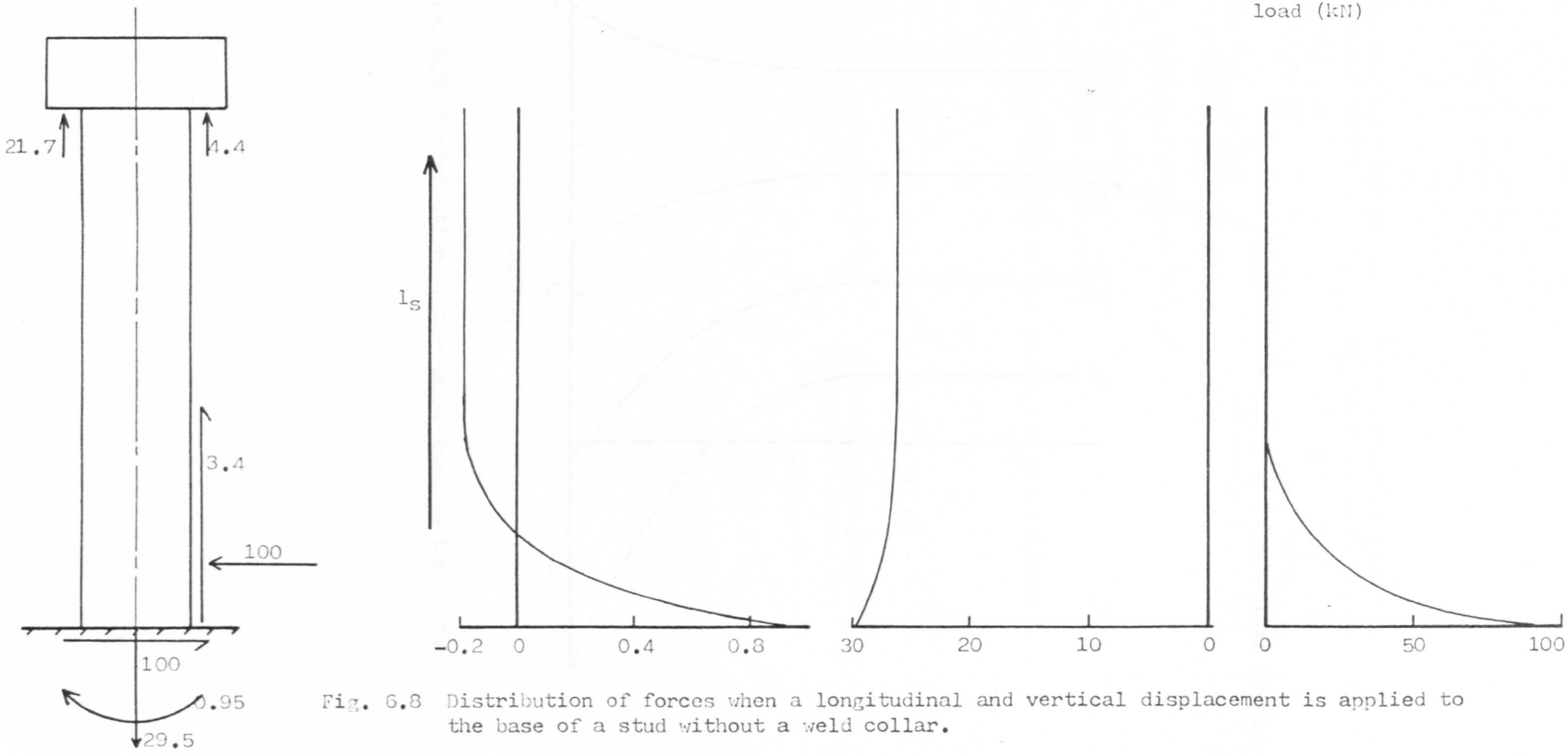

Fig. 6.8 Distribution of forces when a longitudinal and vertical displacement is applied to the base of a stud without a weld collar.

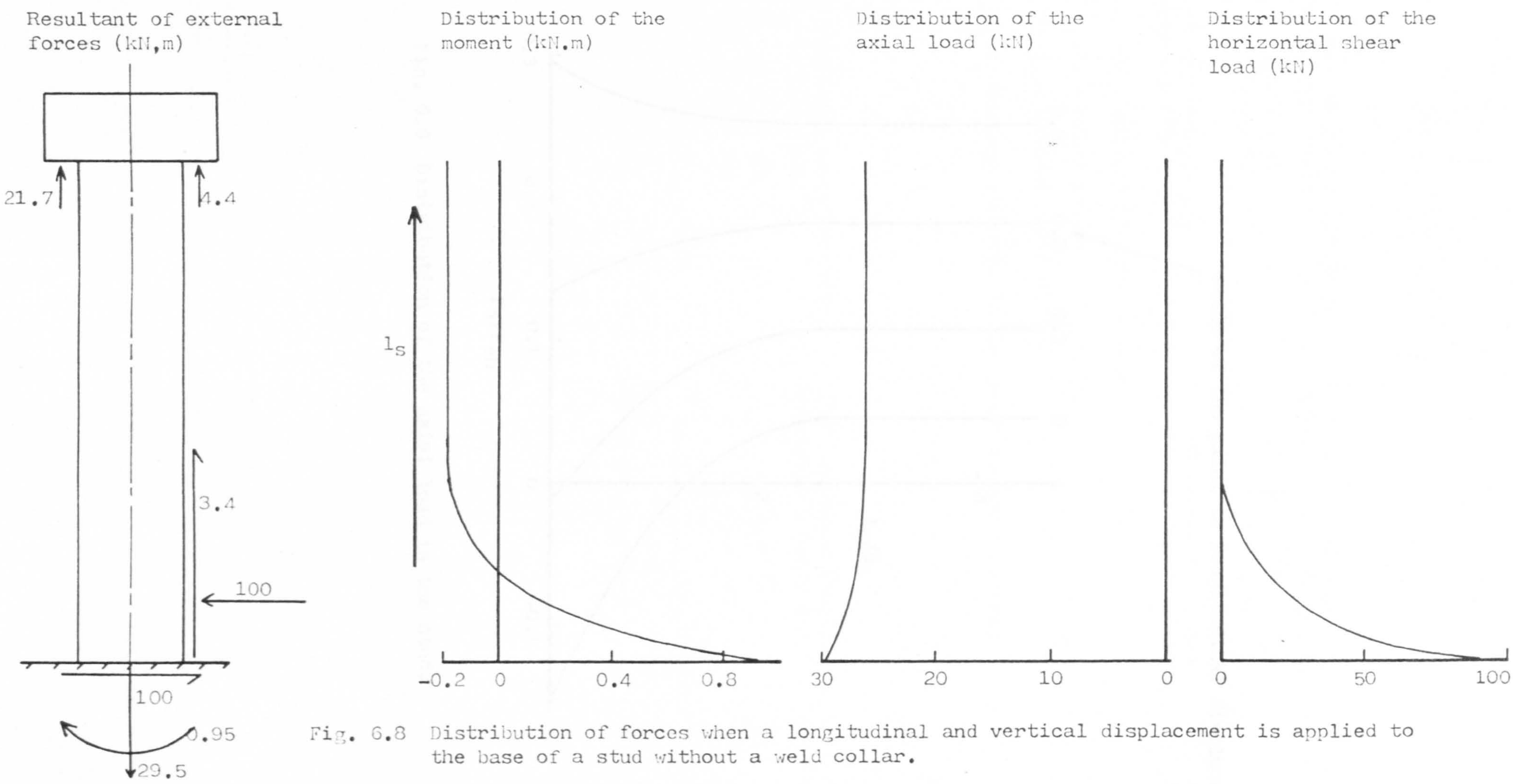

Fig. 6.8 Distribution of forces when a longitudinal and vertical displacement is applied to the base of a stud without a weld collar.

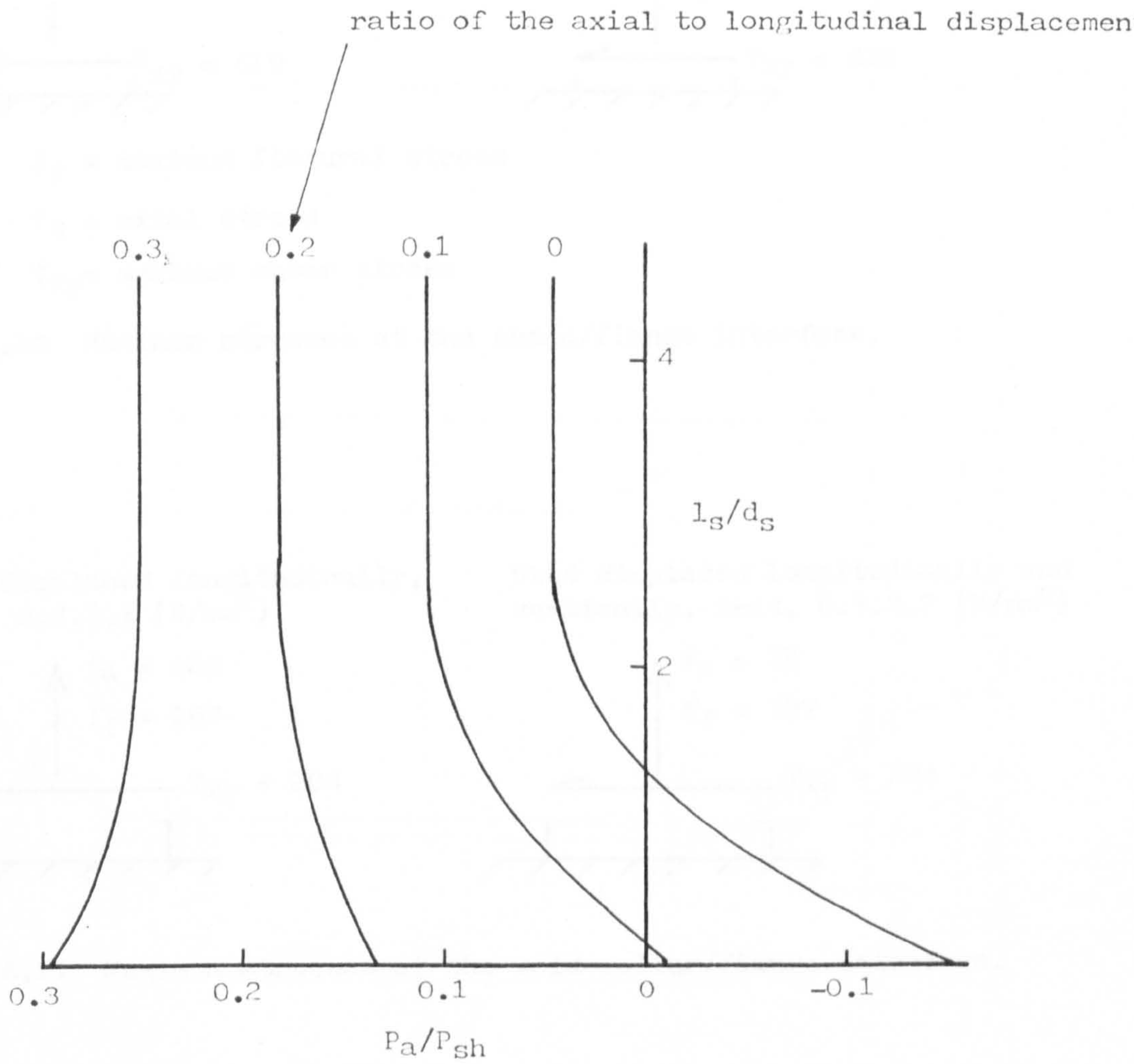

Fig. 6.9 Distribution of the axial load in the stud.

Stud displaced longitudinally, Sect. 6.3.1.1 (N/mm^2)

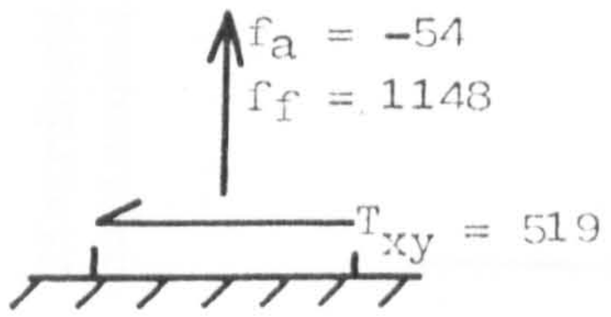

Stud displaced longitudinally and vertically, Sect. 6.3.1.2 (N/mm^2)

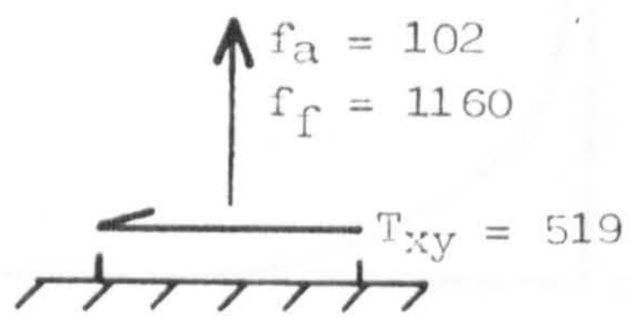

where f_f = maximum flexural stress

f_a = axial stress

T_{xy} = maximum shear stress

Fig. 6.10 Maximum stresses at the shank/flange interface.

Stud displaced longitudinally, Sect. 6.3.2.1 (N/mm^2)

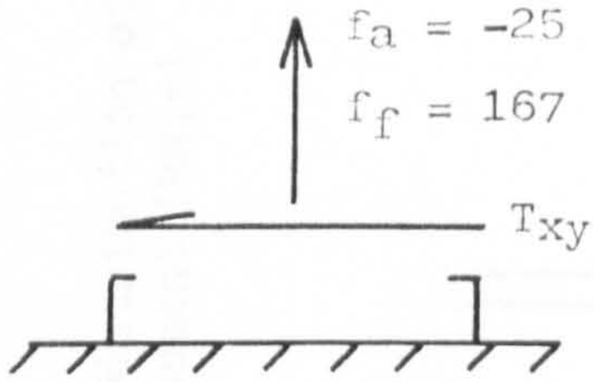

Stud displaced longitudinally and vertically, Sect. 6.3.2.2 (N/mm^2)

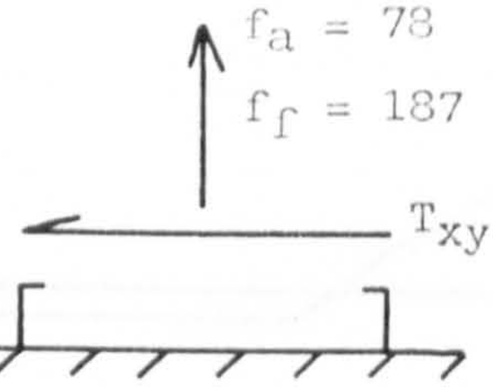

Fig. 6.11 Maximum stresses at the weld-collar/flange interface.

Stud displaced longitudinally, Sect. 6.3.2.1 (N/mm^2)

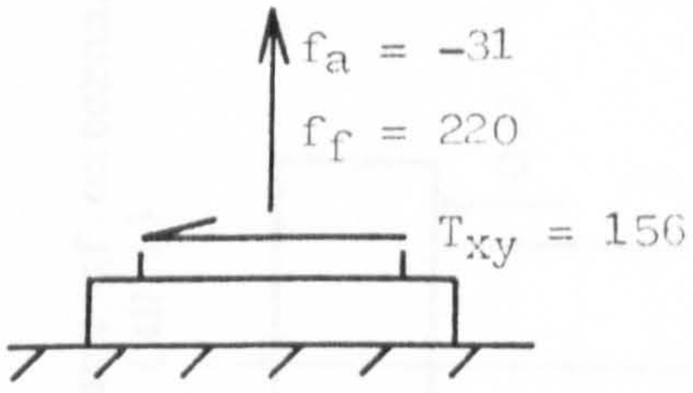

Stud displaced longitudinally and vertically, Sect. 6.3.2.2 (N/mm^2)

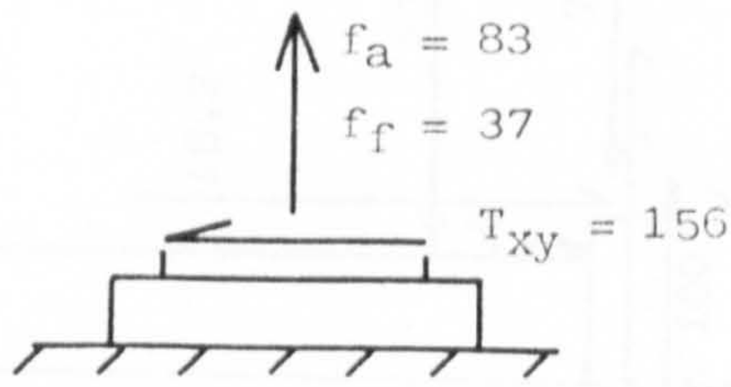

Fig. 6.12 Maximum stresses at the shank/weld-collar interface.

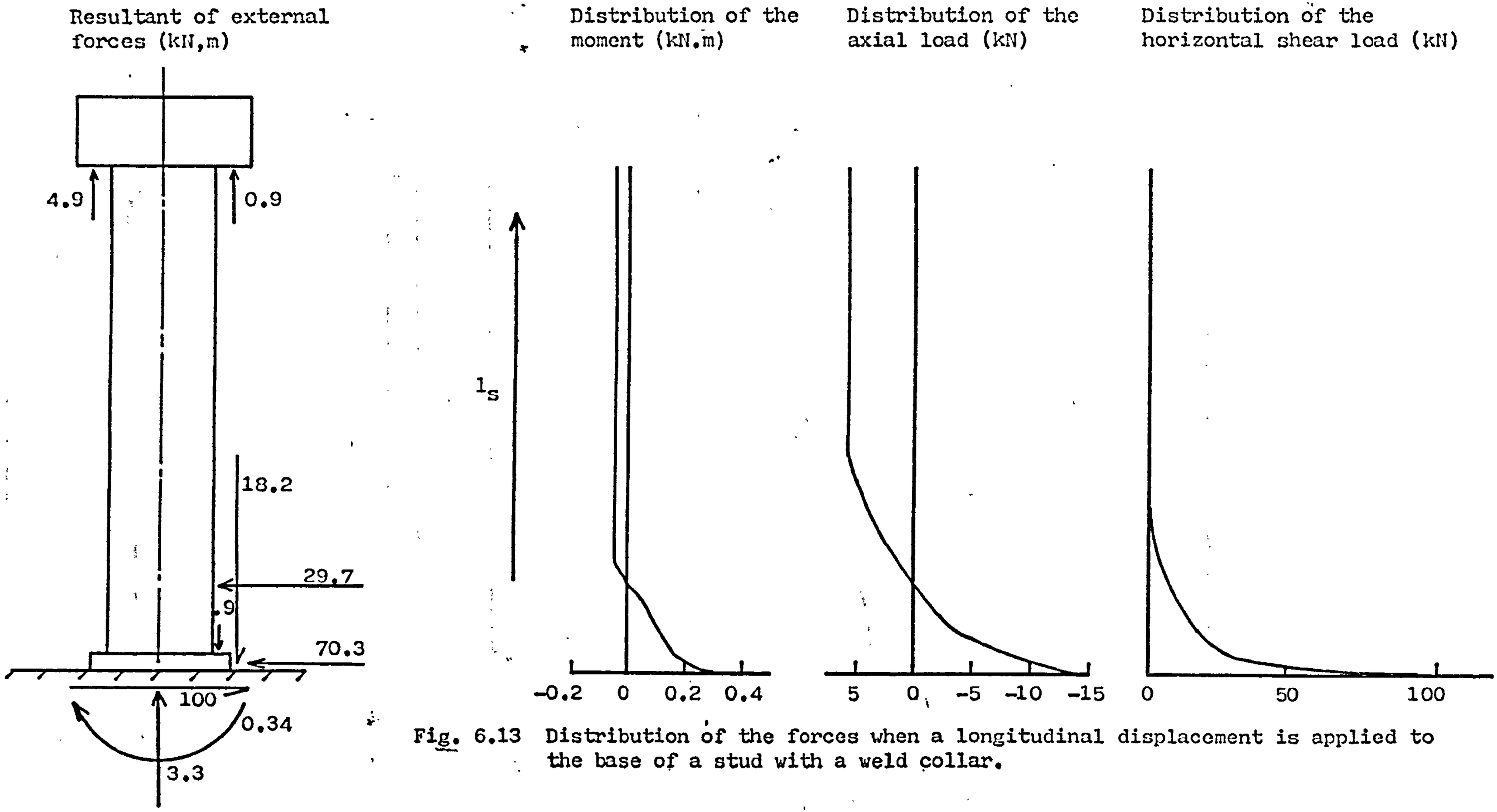

Fig. 6.13 Distribution of the forces when a longitudinal displacement is applied to the base of a stud with a weld collar.

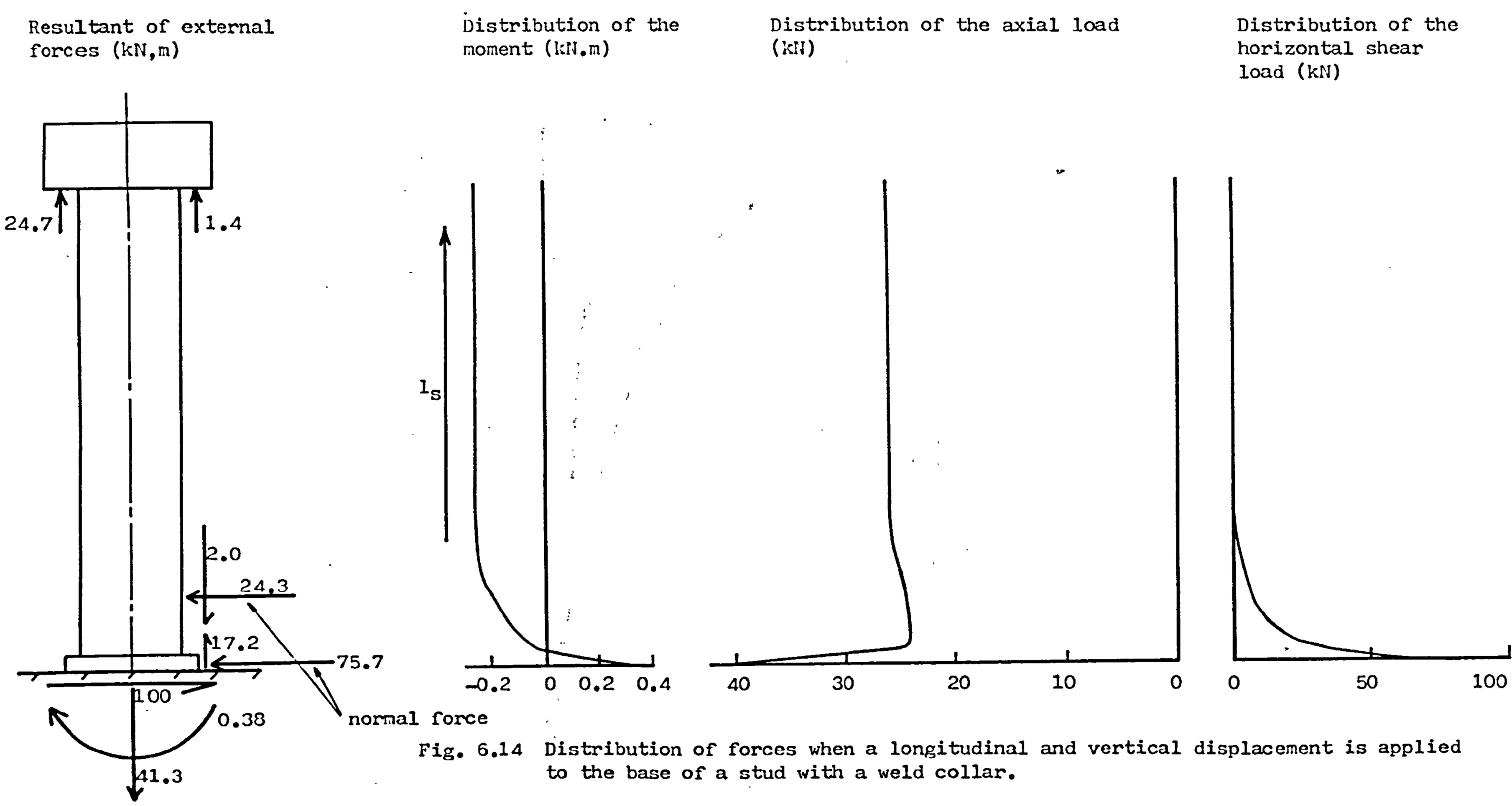

Fig. 6.14 Distribution of forces when a longitudinal and vertical displacement is applied to the base of a stud with a weld collar.

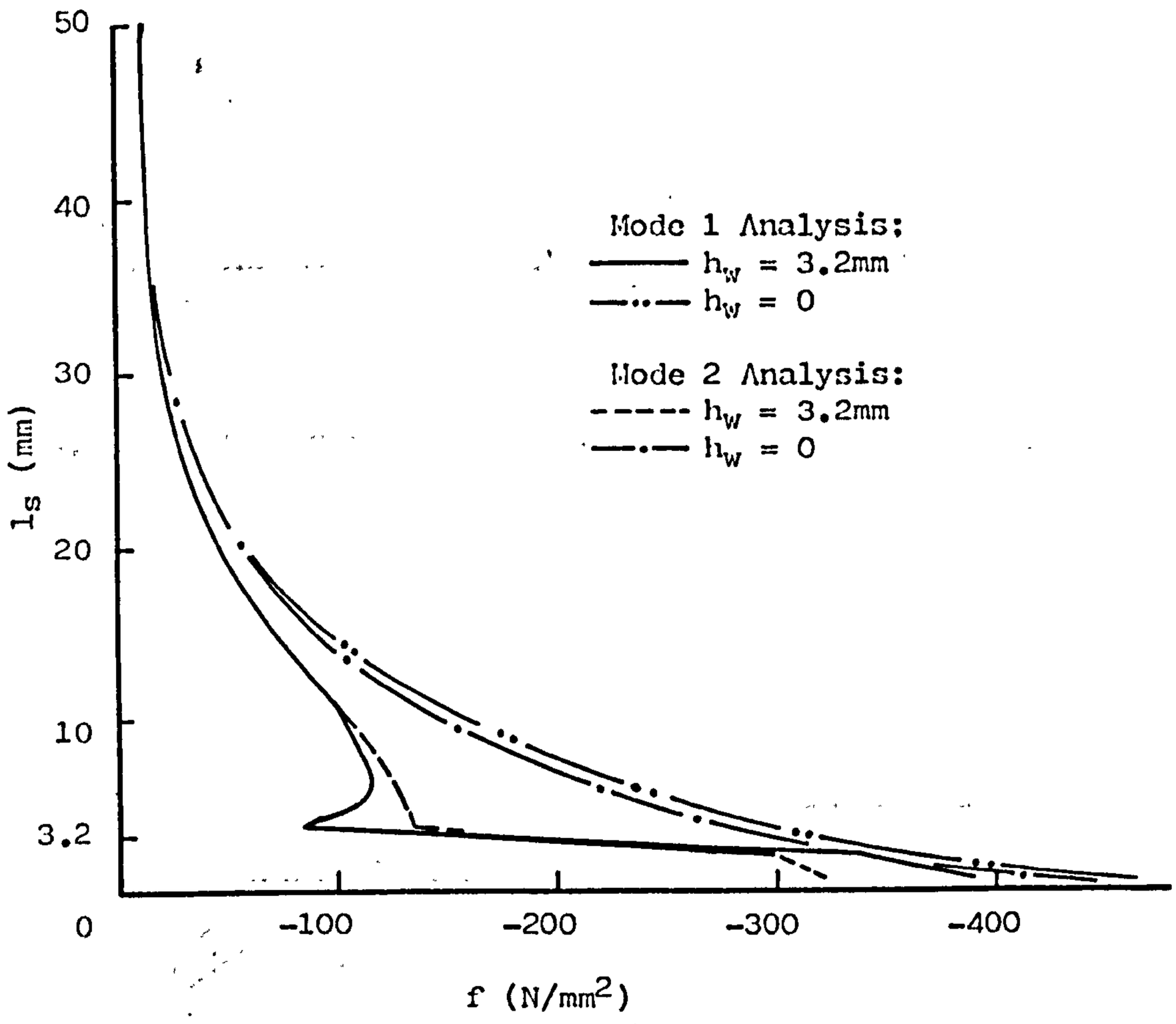

Fig. 6.15 Distribution of the normal force.

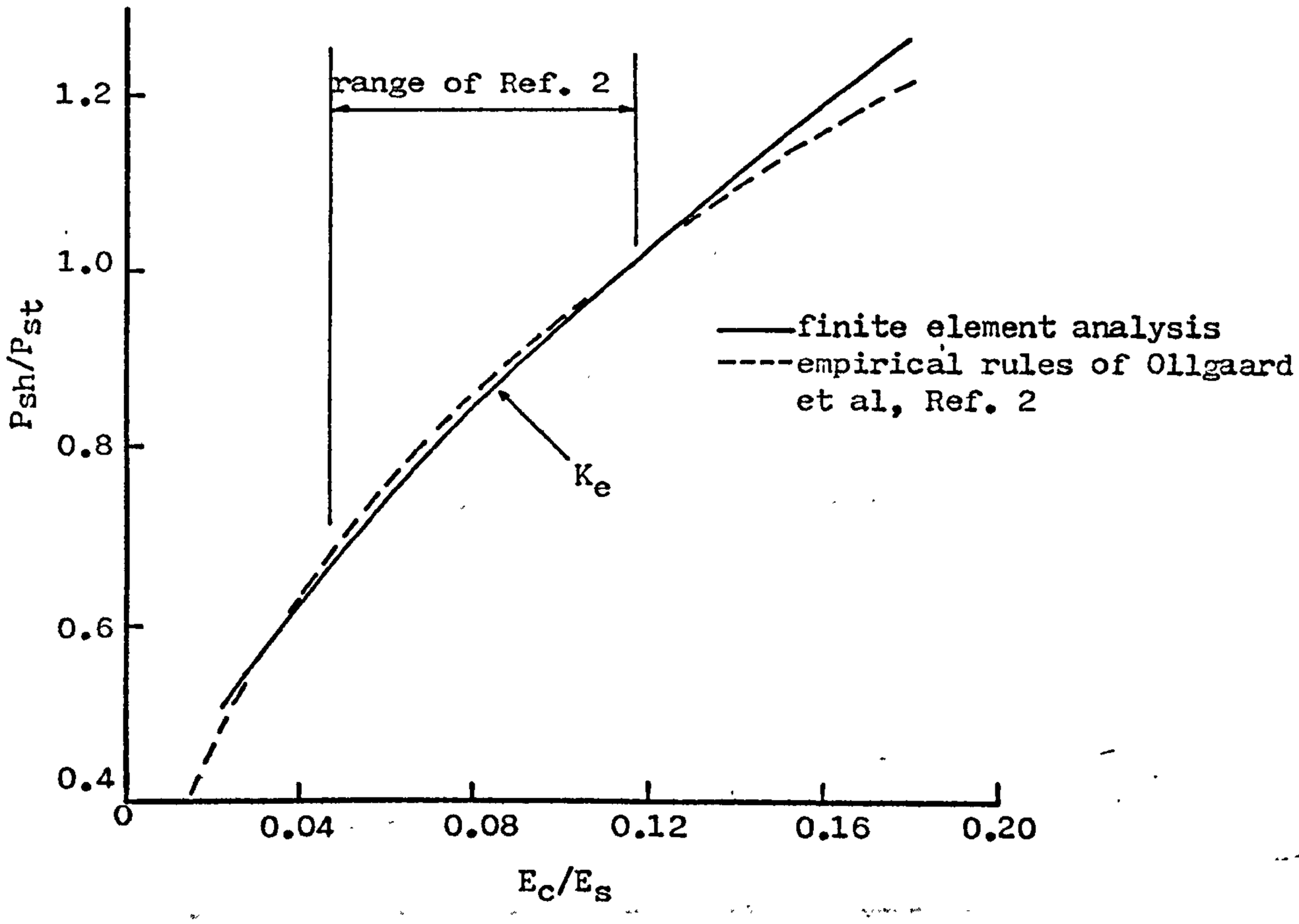

Fig. 6.16 Variation of the shear strength with material stiffness.

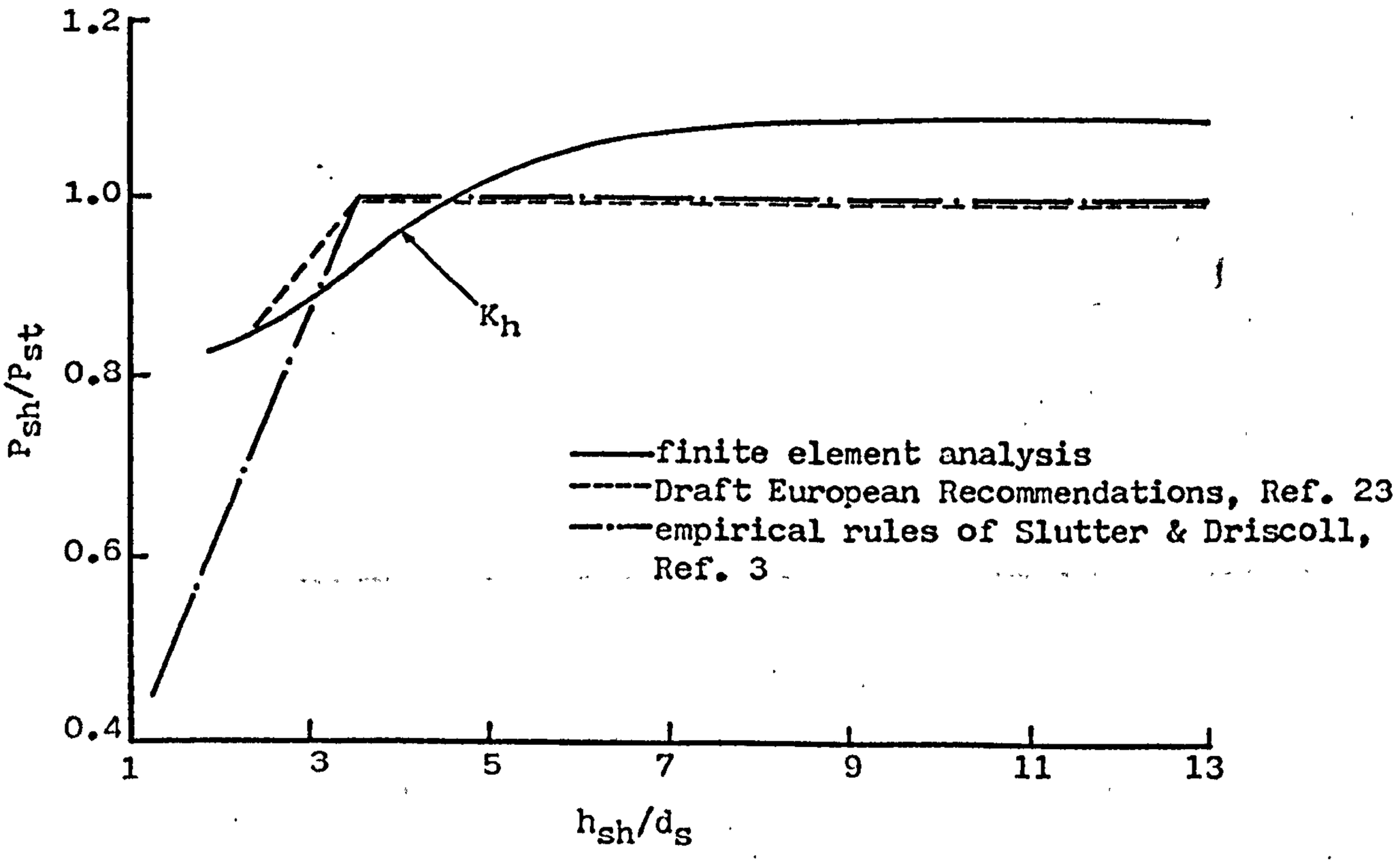

Fig. 6.17 Variation of the shear strength with the height of the stud.

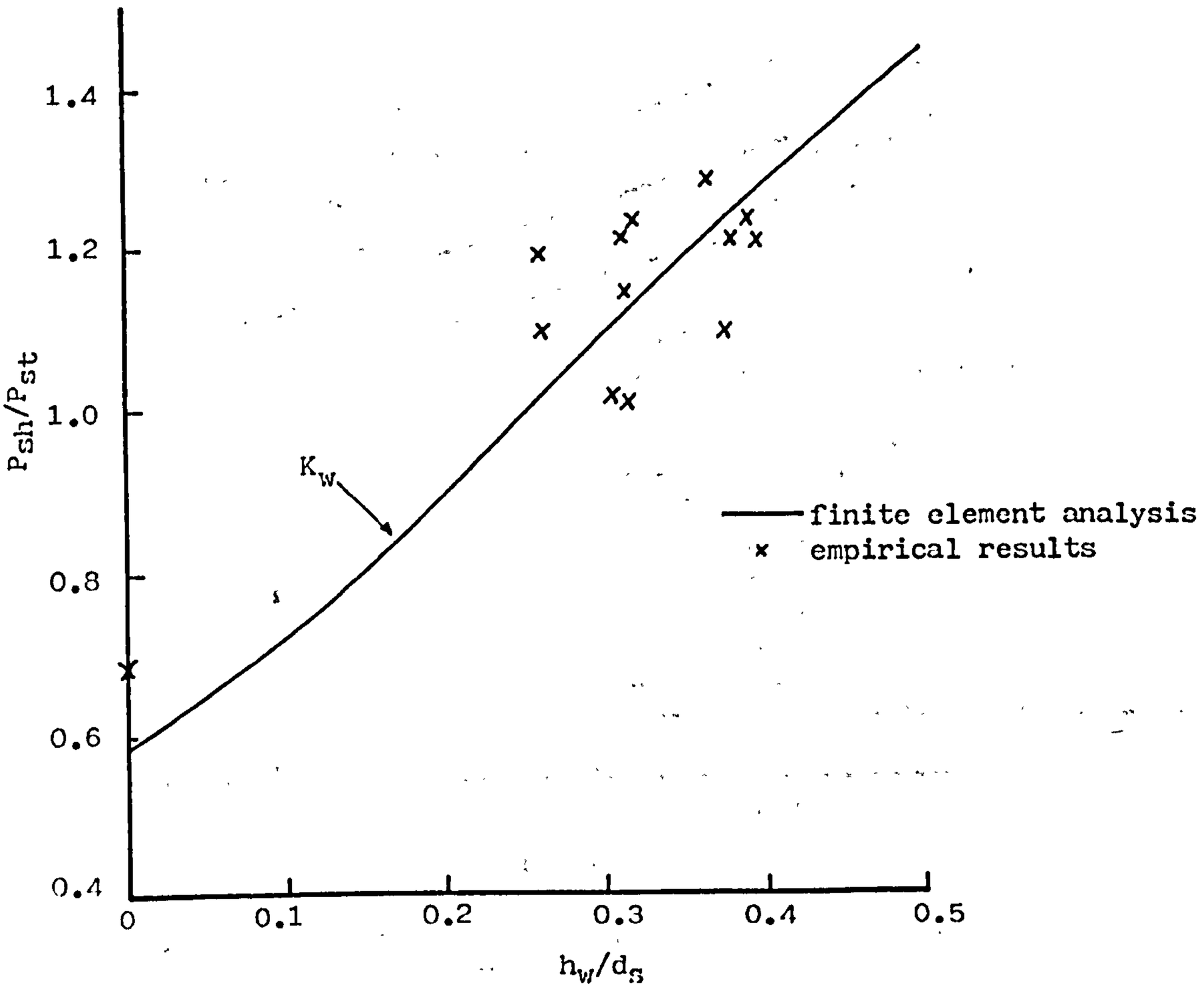

Fig. 6.18 Variation of the shear strength with the height of the weld collar.

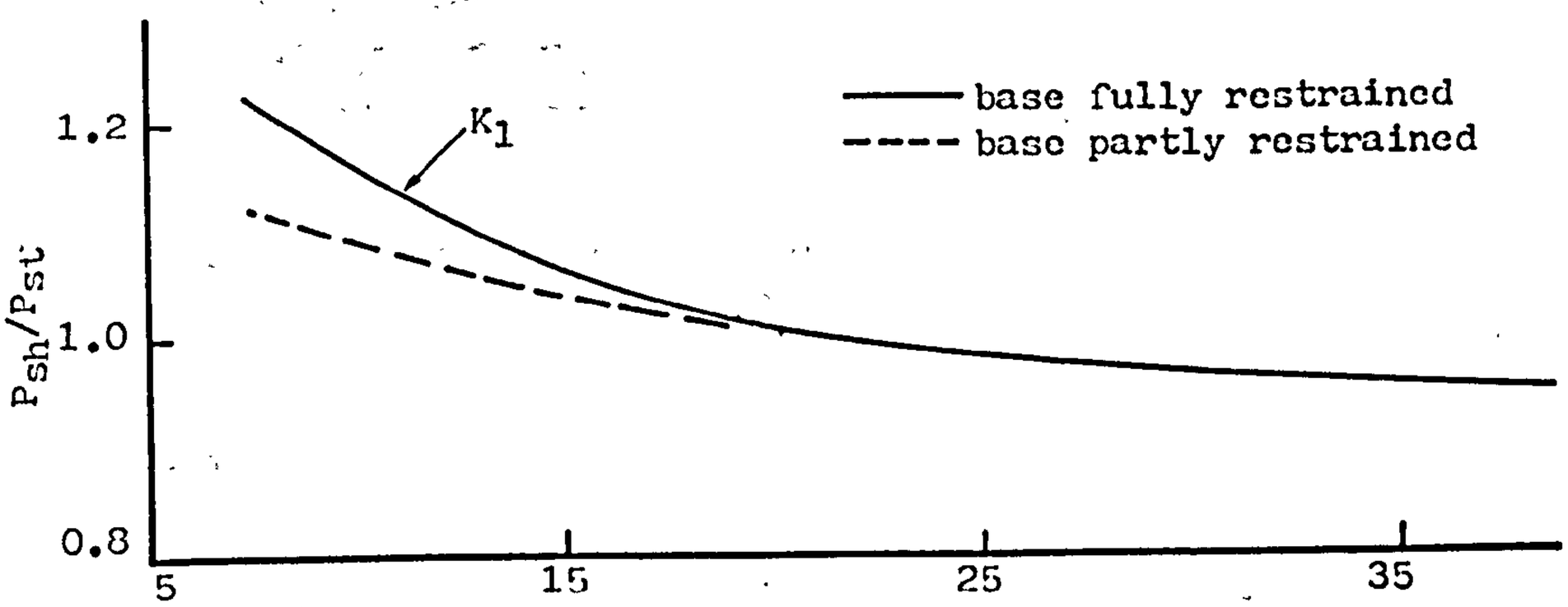

Fig. 6.19 Variation of the shear strength with the length of the slab.

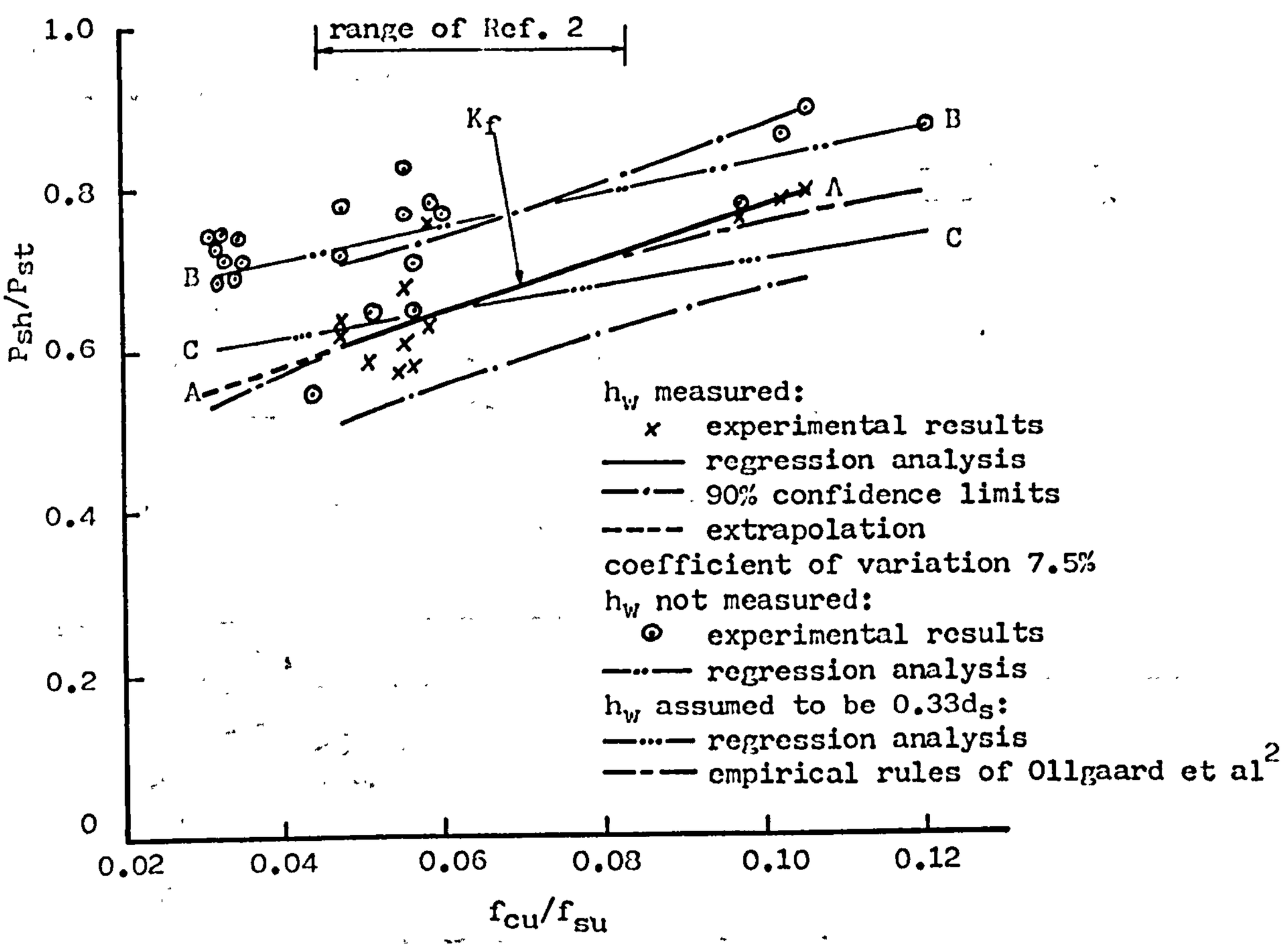

Fig. 6.20 Variation of the shear strength with the material strengths.

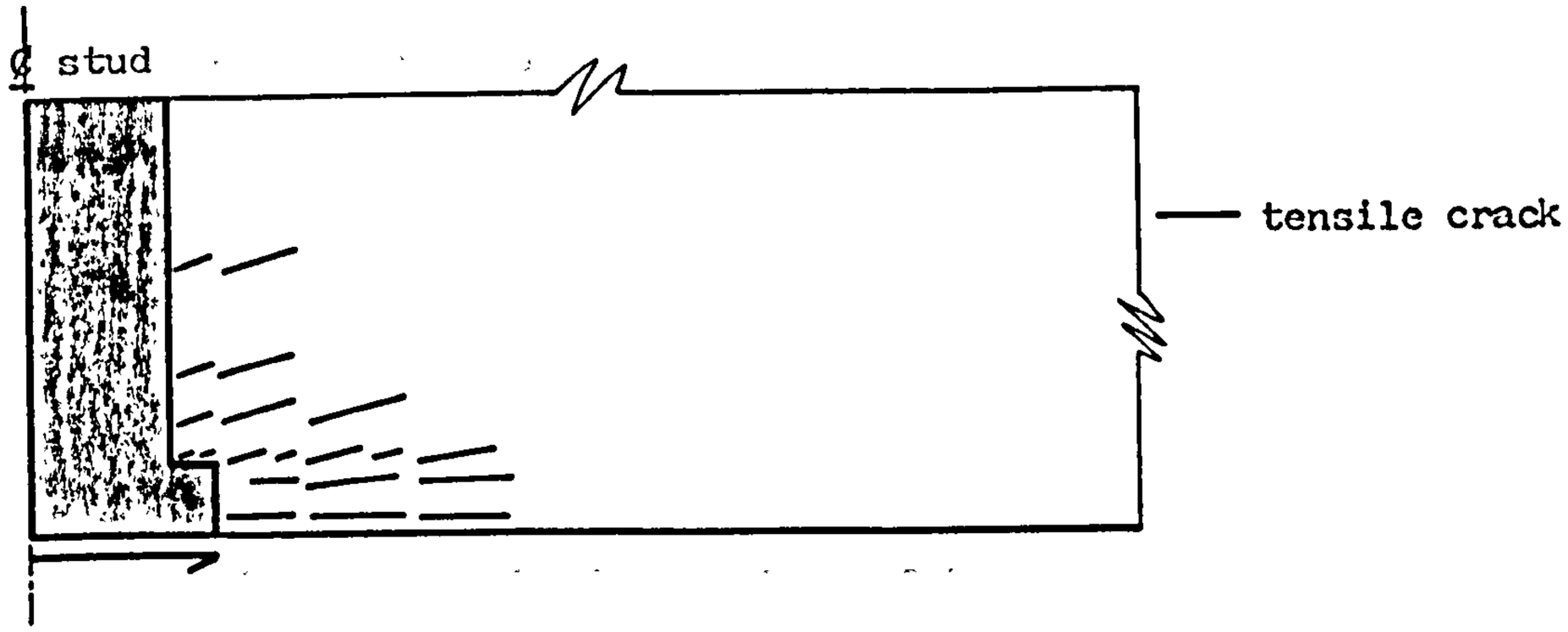

Fig. 6.21 Cracking pattern of the standard push test at the maximum load (f_{ct} = 3.9N/mm^2).

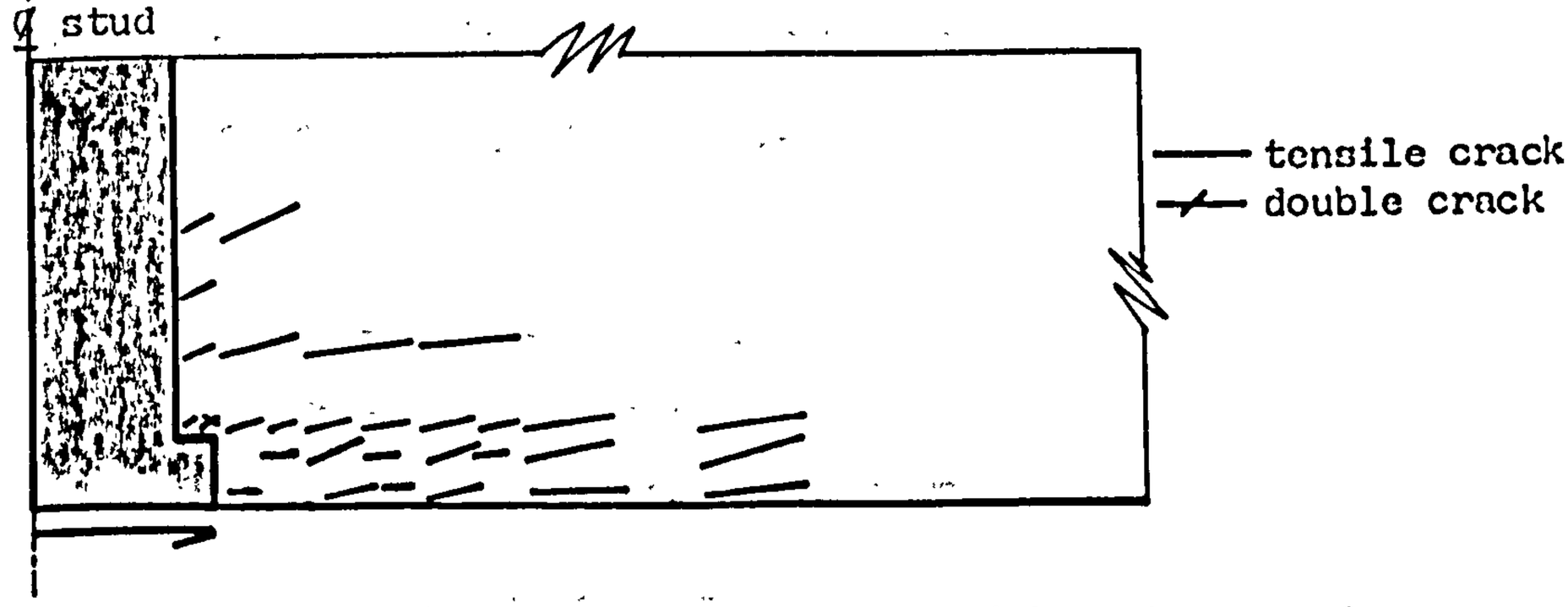

Fig. 6.22 Cracking pattern of a slab, with weak concrete, at the maximum load (f_{ct} = 1N/mm^2).

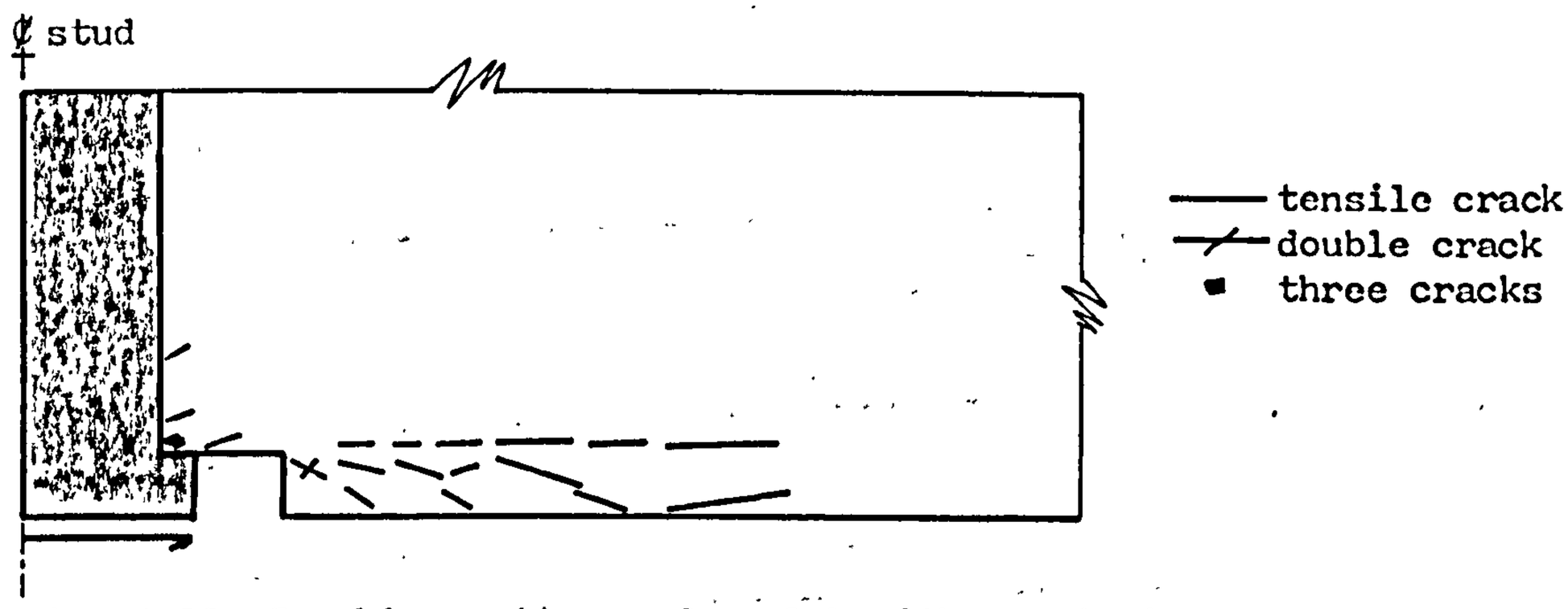

Fig. 6.23 Cracking pattern of a slab, with a void in front of the weld collar, at the maximum load (f_{ct} = 3.9N/mm^2).

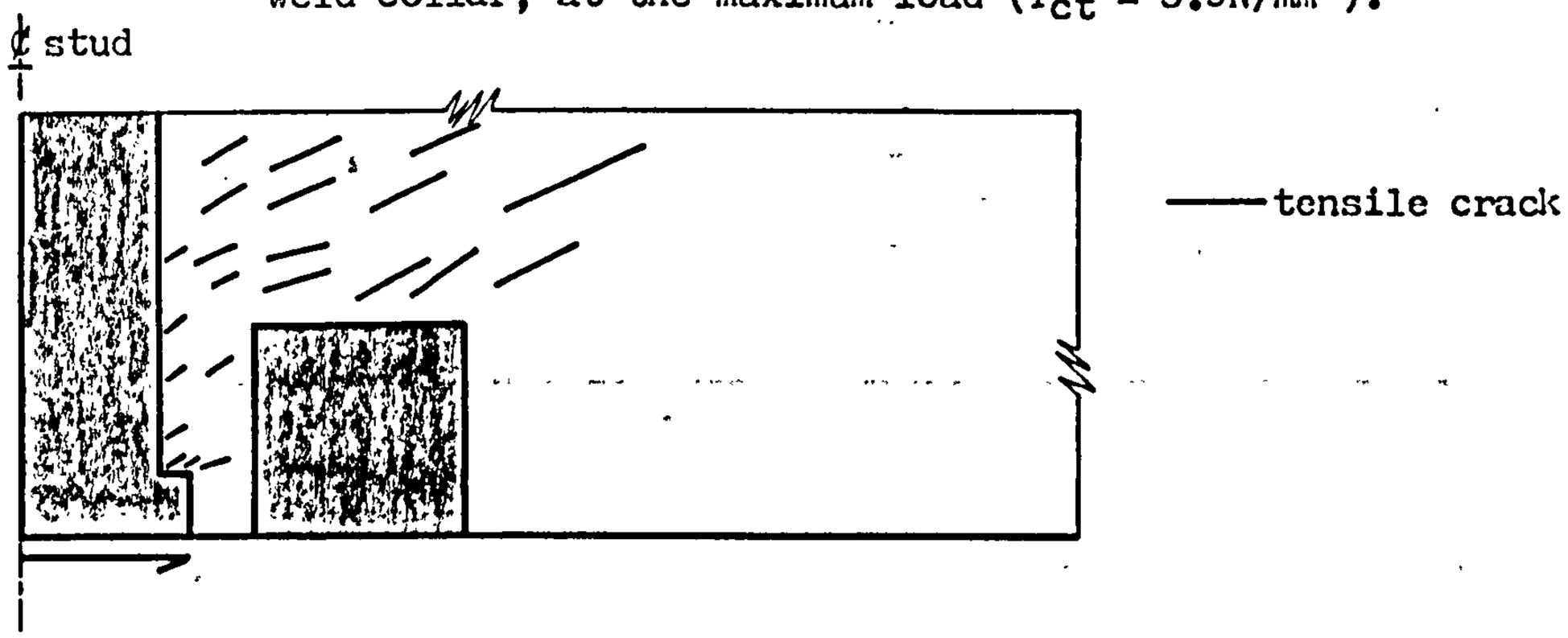

Fig. 6.24 Cracking pattern of a slab, with an inclusion in front of the weld collar, at the maximum load (f_{ct} = 3.9N/mm^2).

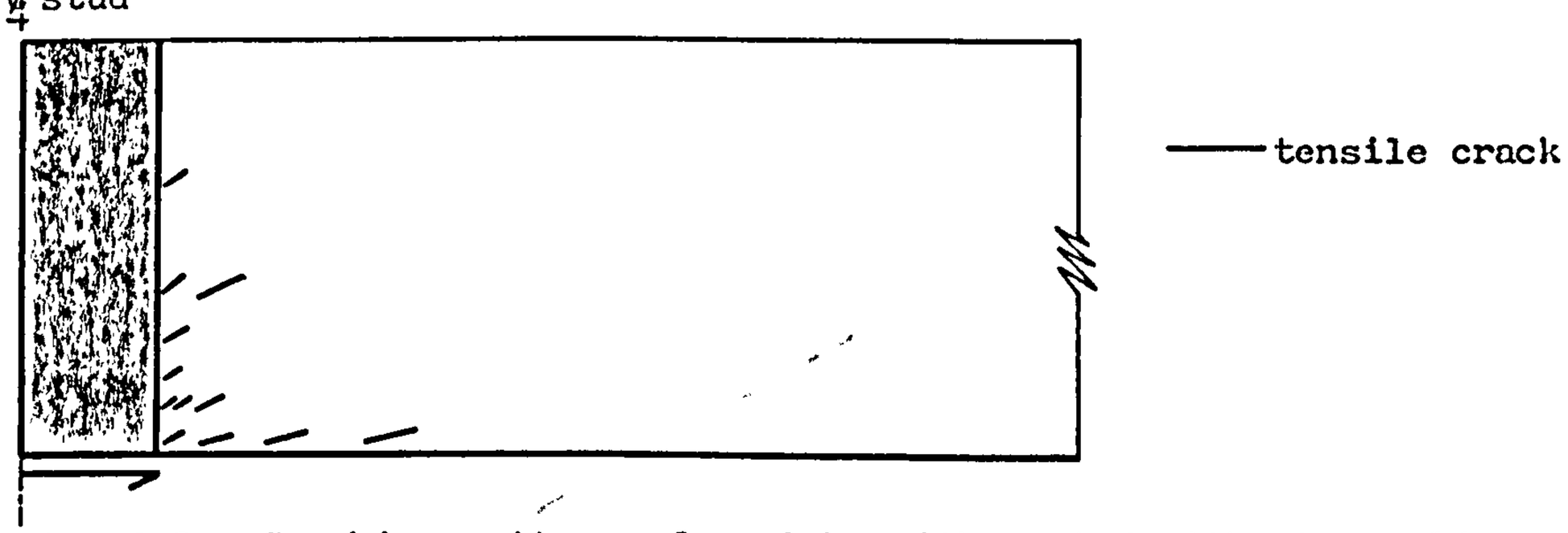

Fig. 6.25 Cracking pattern of a slab, with a stud without a weld collar, at the maximum load (f_{ct} = 3.9N/mm^2).

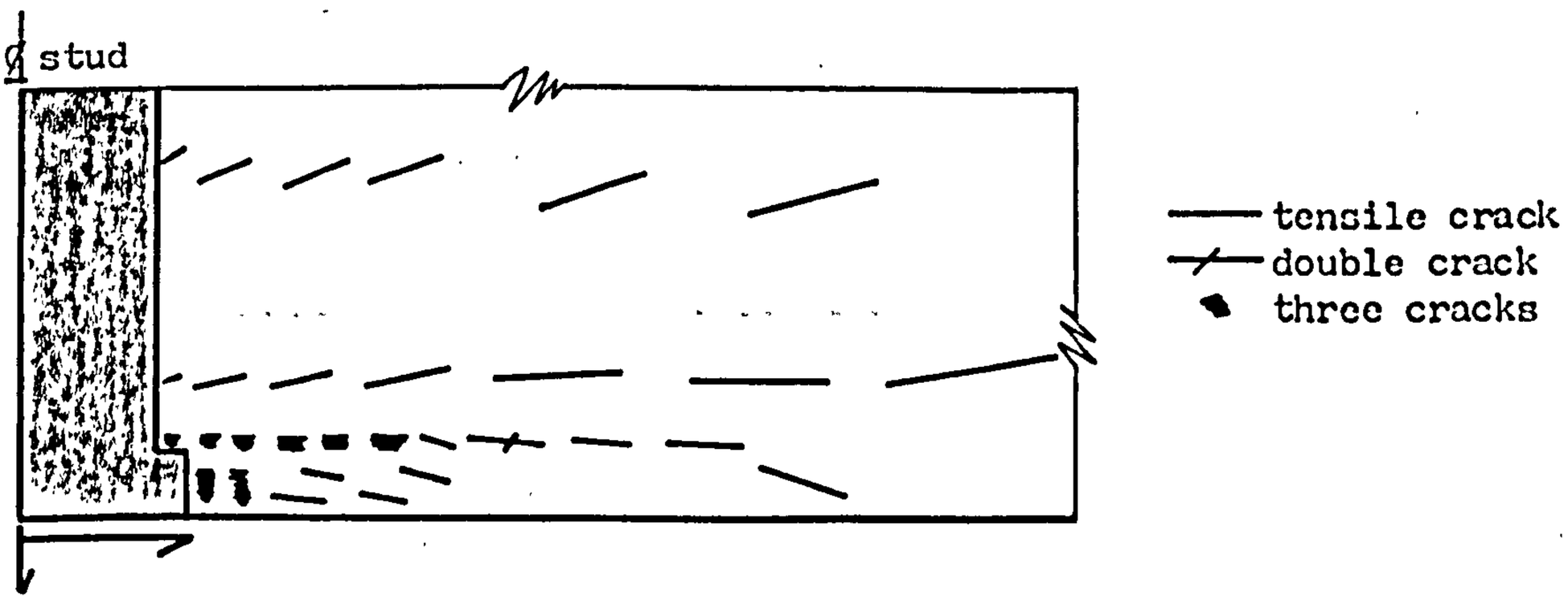

Fig. 6.26 Cracking pattern of a slab, in which the stud is displaced longitudinally and vertically, at the maximum load (f_{ct} = 3.9N/mm^2).

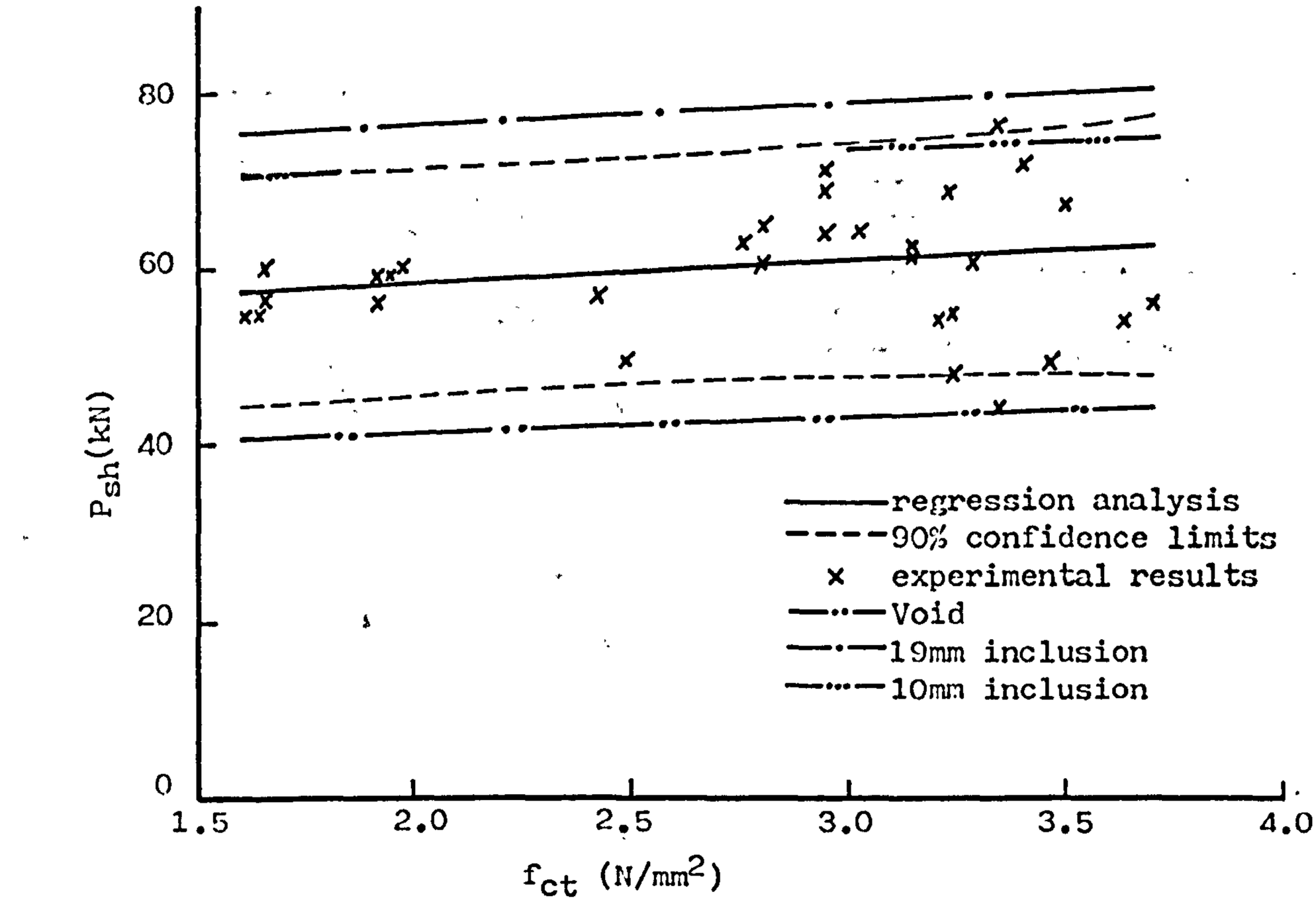

Fig. 6.27 The effect of voids and inclusions on the maximum strengths of 13X65 studs.

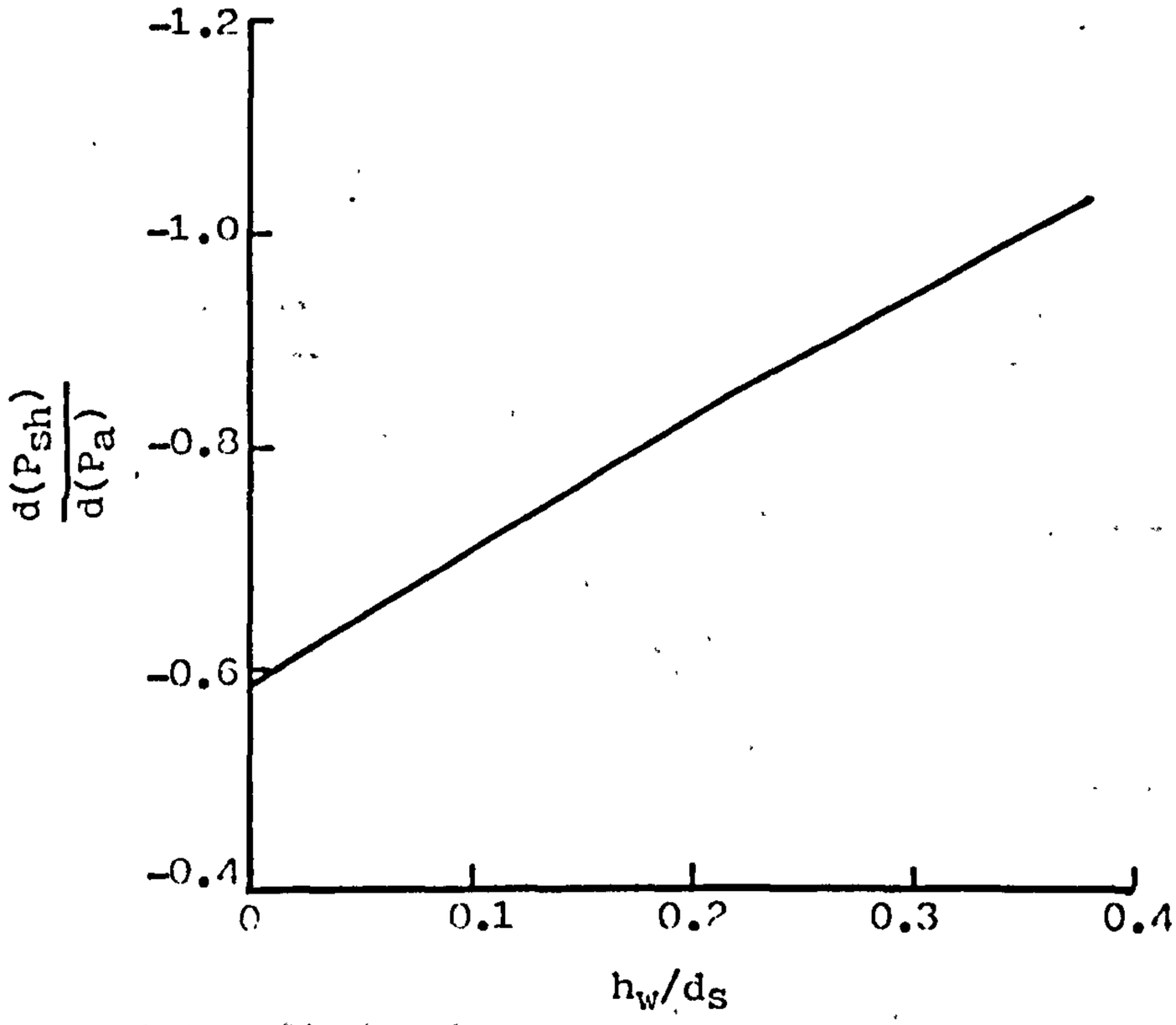

Fig. 6.28 Initial change in the shear strength when an axial load is applied to the stud.

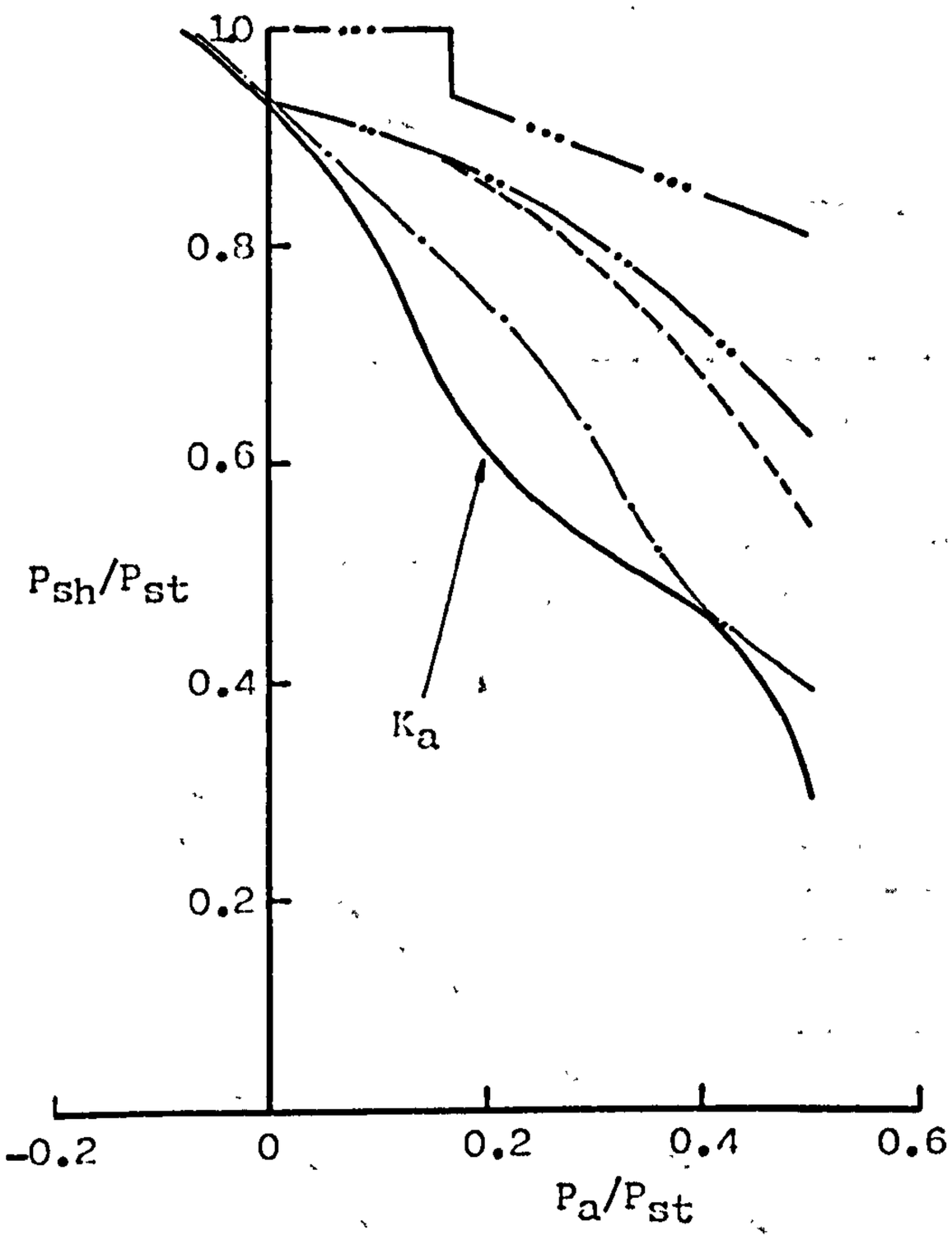

Fig. 6.29 Variation of the shear atrength with the axial load in the stud ($h_w = 0.25d_s$)

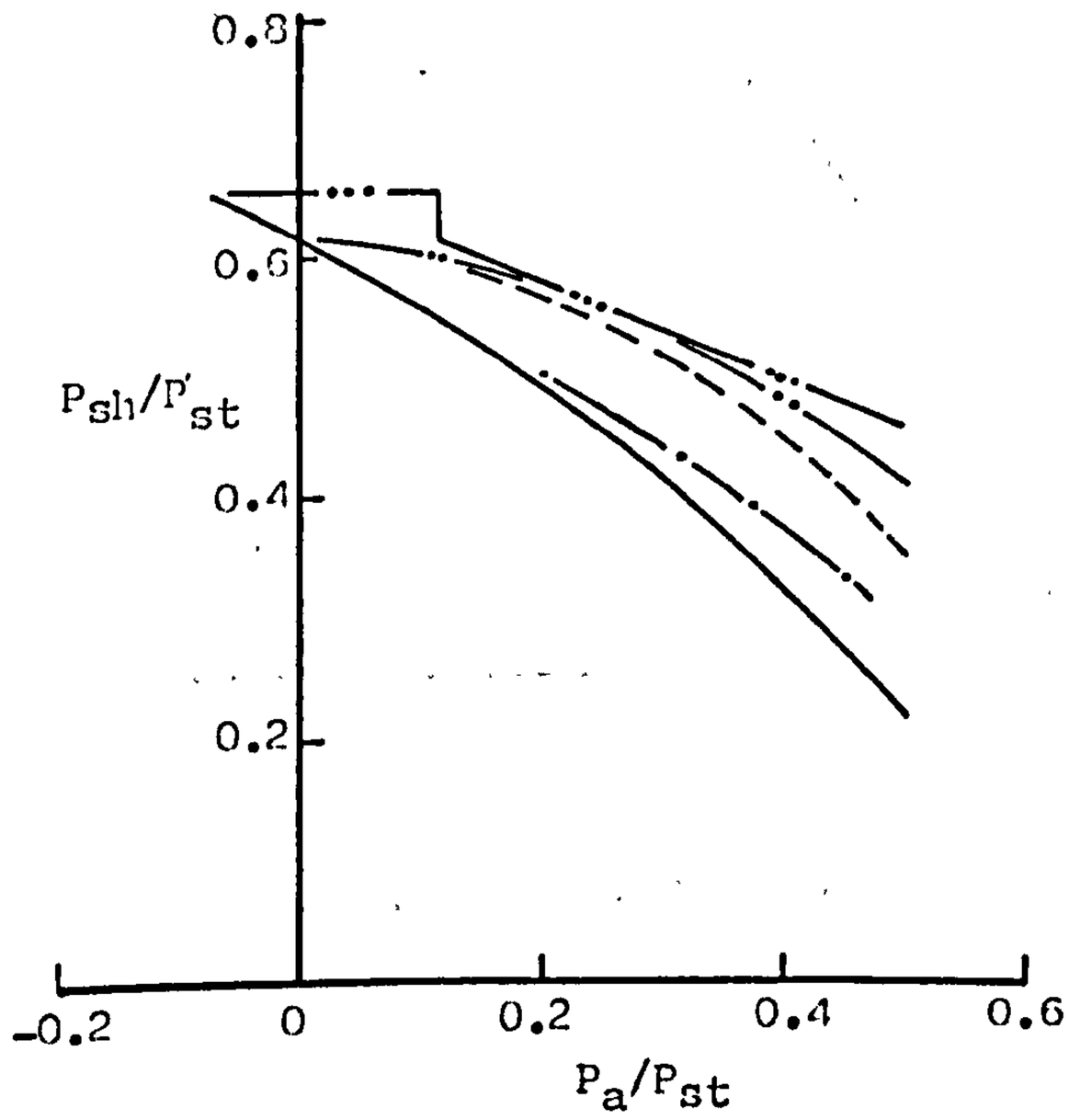

Fig. 6.30 Variation of the shear strength with the axial load in a stud without a weld collar.

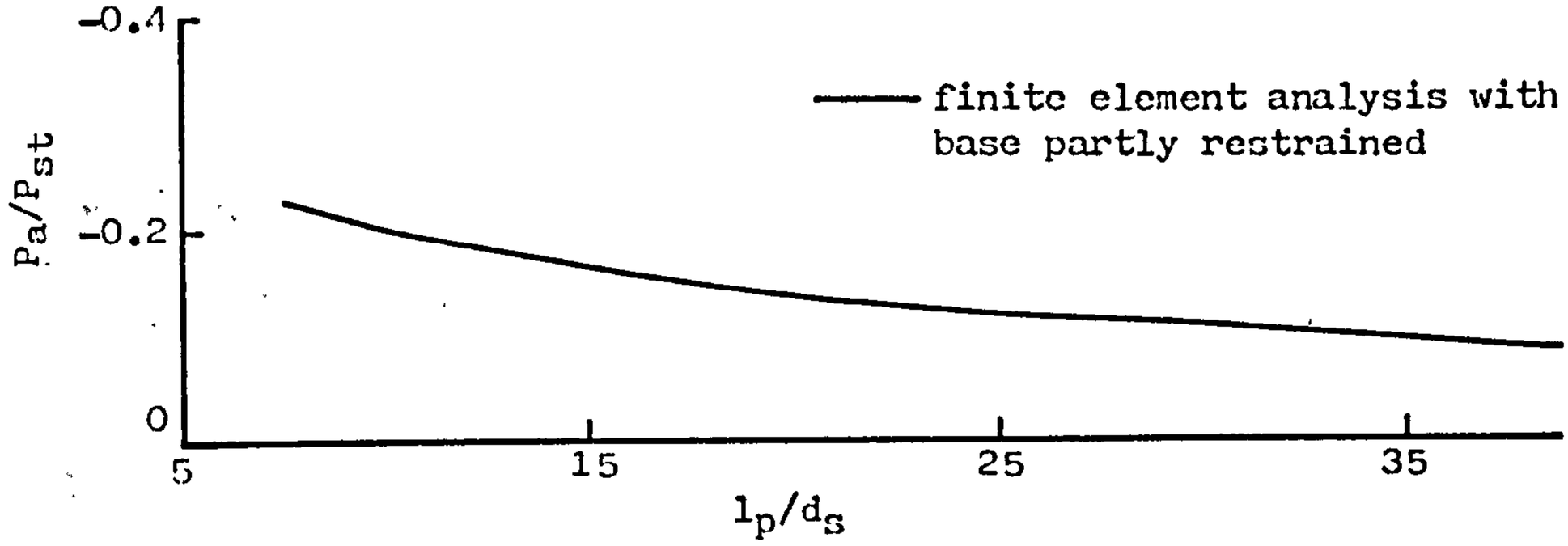

Fig. 6.31 Variation of the axial load at the base of the stud with the length of the slab.

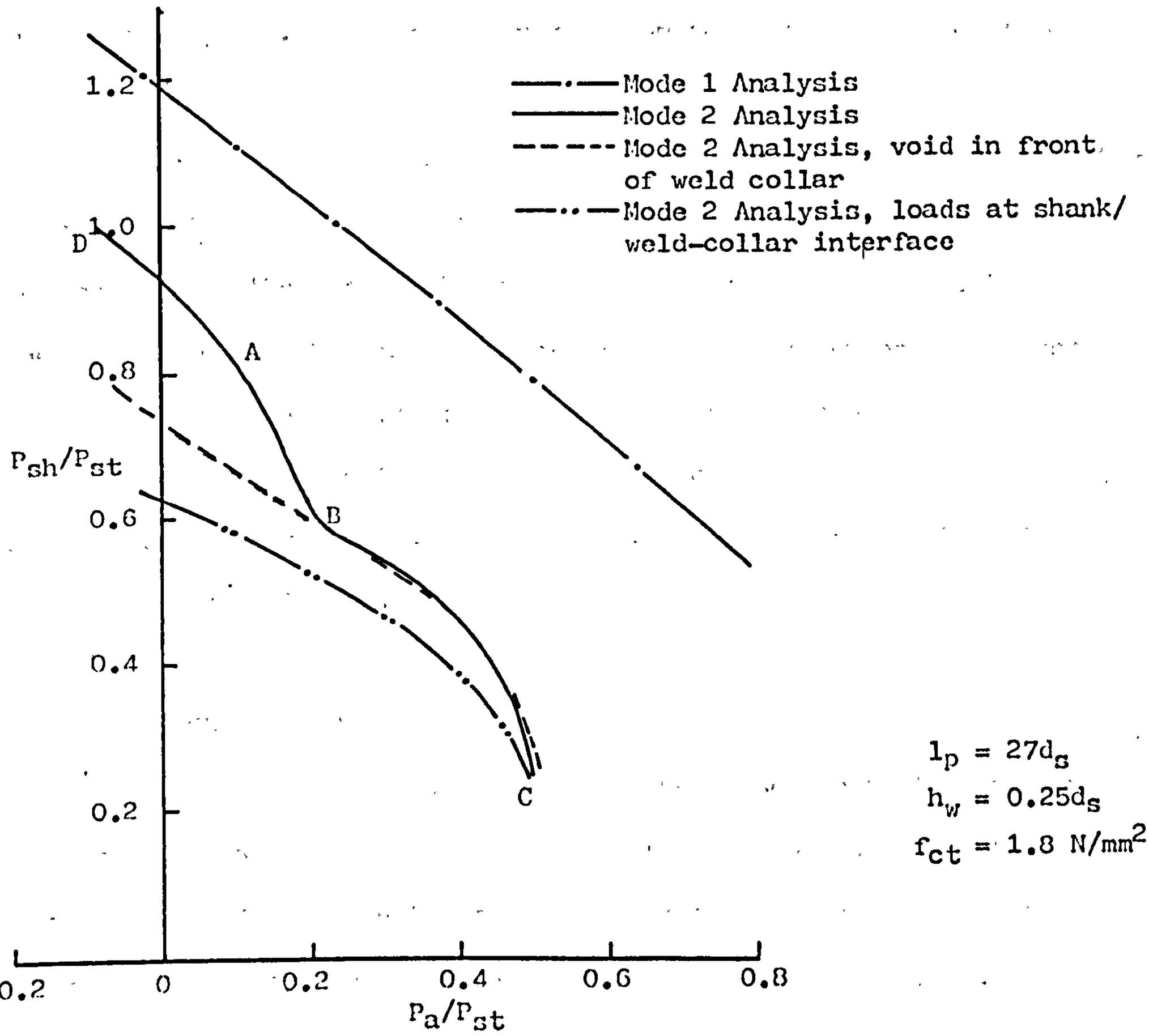

Fig. 6.32 Failure envelope for the shear and axial loads in a stud.

Chapter Seven

SPLITTING OF CONCRETE SLABS

7.1 INTRODUCTION

Splitting occurs in push tests, Sect. 5.4.1, in composite L-beams[33], Fig. 5.16, and has been observed in composite T-beams by Davies[28], Chapman[16], Adekola[64] and Barnard[65]. Davies' empirical rules for transverse reinforcement, Equ. 2.10, were derived from the splitting strength of concrete slabs.

In order to determine the splitting strength of composite beams, the simpler problem of concrete prisms subjected to concentrated loads was analysed first; the finite element model is described in Sect. 7.2, the propagation of the tensile cracks and the distribution of stresses are described in Sect. 7.3, and the load at which a concrete prism first splits is determined empirically in Sect. 7.4 and theoretically in Sect. 7.5. The results are used in Sect. 7.6 to determine the splitting strength of composite slabs.

7.2 FINITE ELEMENT MODEL

The finite element computer programs were used to analyse specimens in which the load was applied uniformly over the full depth of the concrete, Fig. 4.17. The theoretical assumptions which are made in an analysis of this type of specimen are discussed in Sect. 4.4.6.3.

A typical finite element model is shown in Fig. 7.1; the nomenclature is given in Fig. 4.2. Each element was divided into two triangles as shown. The specimen was loaded by applying a uniform displacement to the nodes over a width equal to that of the applied load.

7.3 MODE 2 FINITE ELEMENT ANALYSIS

A Mode 2 Analysis, Sect. 4.3, was used to obtain a qualitative representation of the distribution of the tensile cracks, Sect. 7.3.1, and their effect on the stress distribution, Sect. 7.3.2. The load was applied either to the surface of the prism, Fig. 7.3, or within the specimen, Fig. 7.2.

7.3.1 The distribution of the tensile cracks

The distribution of the tensile cracks at the load at which splitting occurred is shown in Figs. 7.2 to 7.4. When the load was applied to the surface of the prism, the cracks formed in two regions, Fig. 7.3. In the region of large lateral tensile stresses and very small shear stresses, the cracks formed in line with the applied load and therefore joined to form a continuous crack which is often referred to as a split. In the region of small lateral tensile stresses and very large shear stresses, the cracks were inclined to the line of the applied load; these are referred to as shear cracks.

The application of a load within a prism, Fig. 7.2, caused large longitudinal tensile forces which formed the 'lateral' crack. The application of a longitudinal force to the prism, which was equal to ten times the concentrated force, suppressed the formation of the lateral and shear cracks, Fig. 7.4.

The split, lateral cracks and shear cracks are shown in Figs. 5.1 and 5.2.

7.3.2 The distribution of the lateral stresses

When a concentrated load was applied to the surface of a prism, Fig. 7.3, the dispersal of the force caused lateral tensile forces which were balanced by the large lateral compressive forces adjacent to the load, Fig. 7.5.

When the load was applied within a prism, Fig. 7.2, a lateral compressive force was also induced behind the load, Fig. 7.6. As the lateral crack was formed, the lateral compressive force behind the load reduced, Fig. 7.6, until, at the point at which splitting was about to start, the lateral force behind the load became tensile so that the prism split in front of and behind the load, Figs. 5.1, 5.2 and 5.14.

7.4 AN EMPIRICAL ANALYSIS OF SPLITTING

The strength of concrete prisms subjected to patch loads was determined from an analysis of Niyogi's experimental results[58]. Niyogi applied concentric strip loads, Fig. 4.17, concentric patch loads, Fig. 7.23, and eccentric patch loads, Fig. 7.24, to prisms of varying dimensions. The procedure used in the tests was similar to that of determining the cube strength of concrete.

7.4.1 An empirical analysis of concentric strip loads

Some of the empirical analyses are shown in Fig. 7.25. The strength of the prism is dependent upon the length of the specimen and the width of the applied load and since the linear regressions appeared to have a common intercept at $b_a/b_c = 0.0625$ and $K_{sp} = 1.47$ the results were plotted through this intercept in Fig. 7.11. The scatter about these empirical rules, Fig. 7.11, is shown in Fig. 7.26; the mean is 1, as P_e and P_u were derived from the same population, the slope is not significant and the coefficient of variation is similar to that of split tensile tests, Fig. 5.22. The empirical rules were derived from experiments in which $0.0625 < b_a/b_c < 0.5$.

7.4.2 An empirical analysis of concentric patch loads

7.4.2.1 Hypothetical failure load

Let P_Y be the splitting load of a hypothetical strip of width b_a and depth h_c, Fig. 7.30, and P_Z be the splitting load of a hypothetical strip of width h_a and depth b_c, where b_a/b_c is less than h_a/h_c and therefore P_Y is less than P_Z. It will be assumed that the inverse of the strength of a prism which is subjected to a concentric patch load is the sum of the inverse of the strengths of the prism when subjected to the hypothetical strip loads i.e.

$$\frac{1}{P_u} = \frac{1}{P_Y} + \frac{1}{P_Z} \qquad (7.1)$$

7.4.2.2 Comparison of the hypothetical failure load with experimental results

Niyogi's experimental results from cubes subjected to concentric patch loads are compared in Fig. 7.27 with the hypothetical failure loads, which were derived from the empirical strengths of his specimens which were subjected to strip loads, $l_c/b_c = 1$ in Fig. 7.11. The mean, Fig. 7.27, is 1.01, the regression is not significant and the coefficient of variation is close to that obtained from concentric strip loads, Fig. 7.26.

Wheen and Rogers[68] tested concrete prisms which were subjected to concentrated loads that were applied through the anchor plates of post tensioned members. They had realized that the base constraint could have a large effect on the strength and so reduced it to a minimum in their tests. Their results have therefore been compared with the hypothetical load in Fig. 7.28 by deriving the failure loads of the hypothetical strips from the results of a finite element analysis, $l_c/b_c = 10$ in Fig. 7.11, the derivation of which is given in Sect. 7.5.1.1. The mean, Fig. 7.28,

is 1.02, the regression is not significant and the coefficient of variation is close to that obtained from concentric strip loads, Fig. 7.26.

Williams' experimental results[59] for prisms of length b_c and $2.33b_c$ are compared in Fig. 7.29 with the hypothetical failure loads, which were derived from the empirical strengths of Niyogi's strip loads, Fig. 7.11. The mean is 0.93, the regression is not significant and the scatter is much larger than can be attributed to the measurements of the split tensile strength.

The hypothetical failure load, Equ. 7.1, gives a reasonable prediction of the strength of a patch load, which disperses the force in three dimensions, from the strength of concentric strip loads, which disperse the force in two dimensions, when $0.016 < A_p/A_c < 0.33$; the mode of failure probably changes from being predominantly tensile to compressive beyond this range, Figs. 7.27 and 7.29. The results have been validated experimentally for $0.063 < b_a/b_c < 0.5$, where $b_a/b_c < h_a/h_c$, Fig. 7.30.

7.4.2.3 Comparison of the hypothetical failure load with empirical results

The bearing strength at the hypothetical failure loads for concentric patch loads are plotted in Fig. 7.34 for the cases when $l_c = b_c$ and $l_c = 10b_c$ in Fig. 7.11. The derivation of the latter is discussed in Sect. 7.5.1.1. It is assumed that $f_{cu} = 13f_{ct}$. The variations agree reasonably well with Williams' empirical rules[59], however Guyon's rules[69] appear to underestimate the change in the strength.

7.4.3 An empirical analysis of eccentric patch loads

The failure load, Equ. 7.1, underestimated the strength for eccentric patch loads, Fig. 7.24, when applied to Niyogi's experimental results for uni-axial and bi-axial eccentric loads on cubes, Fig. 7.31.

The mean is 1.15, the regression is not significant. Niyogi[58] had also noted this increase in strength.

7.4.3.1 Eccentric strip loads

The increase in the strength of prisms subjected to eccentric strip loads, Fig. 5.33, over those of concentric strip loads, Fig. 4.17, was determined experimentally, Sect. 5.7, for specimens in which $b_a/b_c=0.12$ and $l_c > 2b_c$. The experimental results, Fig. 7.32, were plotted in terms of the theoretical strength of a strip load, Equ.7.3 or Fig. 7.11, acting over a prism of width b_c, Fig. 5.33; to eliminate any error in determining the tensile strength of the concrete all the results were factored by P_{sp}/P_e of specimen UC1 since this specimen was concentrically loaded.

7.4.3.2 Eccentric patch loads

In order to allow for eccentric loads, Equ. 7.1 becomes

$$\frac{1}{P_u} = \frac{1}{K_Y P_Y} + \frac{1}{K_Z P_Z} \qquad (7.2)$$

The factor K_Y allows for the increase in the strength of the hypothetical strip of width b_a/b_c, Fig. 7.30, and K_Z the increase in the strength of the hypothetical strip of width h_a/h_c, i.e. $b_c/b_t = h_c/h_t$ in Fig. 7.32. It is possible that the variation in Fig. 7.32 is only applicable when $b_a/b_c = 0.12$, because this value remained constant in the experimental tests, however, the application of this variation in Equ. 7.2 gave a better correlation between the experimental and empirical results, Fig. 7.33, than that of Equ. 7.1, Fig. 7.31. The mean, Fig. 7.33, is 1.04, the regression is not significant and the scatter similar to that obtained from concentric strip loads, Fig. 7.26.

7.5 MODE 1 FINITE ELEMENT ANALYSIS

A Mode 1 Analysis, Sect. 4.2, was used to determine the load at which splitting first occurred in prisms subjected to strip loads.

7.5.1 Concentric strip loads applied to the surface of a prism

The finite element model is shown in Fig. 7.1.

7.5.1.1 Distribution of the lateral tensile stresses along the line of action of the applied load

The length of the splitting zone, l_z in Fig. 7.5, is equal to $1.75b_c$. The position of the maximum lateral tensile stress, l_m in Fig. 7.5, is dependent upon the width of the applied load, Fig. 7.9. The variation of the total lateral tensile force as a proportion of the applied load, K_d, is shown in Fig. 7.10. The parameter K_d can be considered to represent half the tangent of the angle of dispersal of the concentrated load into the prism. The variation of the mean lateral stress over the splitting zone as a proportion of the maximum lateral stress, K_s, is shown in Fig. 7.10. The parameter K_s can be considered to represent the shape of the distribution.

The load at which splitting starts, P_{sp}, is therefore

$$P_{sp} = 1.75 b_c h_c f_t K_{sp} \qquad (7.3)$$

where $K_{sp} = K_s/K_d$

The variation is shown in Fig. 7.11.

7.5.1.2 Distribution of the lateral tensile stresses along the edge of the applied load

Along planes parallel to the line of action of the applied load, the length of the splitting zone, l_z, and the shape of the distribution, K_s, remain constant, but the lateral force, K_d, reduces as l_t increases, Fig. 7.5. Therefore, the maximum lateral stress along the edge, which is inversely proportional to the magnitude of the line C-C in Fig. 7.12, is

usually smaller than along the line of action of the applied load, line A–A. However, the maximum lateral stress along the edge is greater than along the line of action of the applied load when $b_a/b_c > 0.58$ because the higher stresses at the edge of a uniformly displaced patch, Fig. 7.13, have a greater effect when the dispersal of the force is small.

A comparison of the strength of the prism along the line of action of the applied load, line A–A in Fig. 7.12, and along the edge of the applied load, line B–B, shows that shear failure occurs when $b_a/b_c > 0.41$. The difference between the lateral stress, line C–C, and the principal stress, line B–B, along the edge of the applied load is due to the high shear stresses in this failure zone. The strength of a prism is therefore given by the lower bound to the curves A–A and B–B. The formation of two longitudinal cracks along the planes of maximum shear, when the width of the specimen is reduced, has been shown experimentally by Plum[67]; the cracking pattern is similar to that in Fig. 5.2.

7.5.1.3 Comparison with experimental results

The theoretical variations of K_s, K_d, K_{sp} and l_m, Figs. 7.9 to 7.11, agree reasonably well with those of a photo-elastic analysis which were used by Leonhardt[66] in his design recommendations for the anchorage zone of post tensioned members.

The effect of the base restraint on the distribution of the lateral stresses, Fig. 7.8, causes the strength to increase as the length of the specimen reduces, as shown by the empirical analysis of Niyogi's results[58], Fig. 7.11. The theoretical distribution remained constant when l_c was greater than $3b_c$. It was assumed in the empirical analysis that the tensile strength of the concrete, f_t in Equ. 7.3, was equal to the split tensile strength, because the mechanism of failure in the split cylinder

test, Sect. 4.4.5.2, is similar to that of a strip load on a prism.

Williams' empirical rule[59], Fig. 7.12, which was derived from the analysis of patch loads on concrete prisms, would appear to underestimate the strength of prisms subjected to strip loads.

7.5.1.4 The effect of compressive failure

The Mode 1 Analysis of concentric strip loads on unreinforced prisms, Fig. 7.11, is compared in Fig. 4.16 with a Mode 3 Analysis, which allowed for tensile and compressive failure, by assuming that $f_{cu} = 13f_{ct}$. Failure is dominated by the compressive strength of the concrete as opposed to the tensile strength at low values of b_a/b_c, where the length of the splitting zone, $1.75b_c$, is large in comparison with the width of the applied load and hence the lateral tensile stresses are relatively small in comparison with the bearing stress, and at high values of b_a/b_c, where the dispersal of the force is small, K_d in Fig. 7.10, and hence the lateral tensile stresses are small in comparison with the bearing stress. The two failure modes are interrelated because the split or shear cracks reduce the lateral restraint to the concrete under the load and hence reduce its compressive failure strength.

Prisms which are prevented from separating along a split by lateral reinforcement will always fail because of the compressive failure of the concrete under the load which is induced by the reduction of the lateral restraint due to the split.

7.5.2 Double strip loads applied to the surface of a prism

The finite element model is shown in Fig. 7.14. The load per strip load at which the prism failed, P_{sp} in Fig. 7.15, was plotted in terms of the failure load of an individual patch, P_{sg}, which was derived from Equ. 7.3. When $b_c = b_t$, both strip loads lie along the centre line

of the prism, Fig. 7.14, and hence the failure load is equal to that of a single strip i.e. $P_{sp} = 0.5P_{sg}$. The case when $b_c = 0.5b_t$ is equivalent to two individual prisms of width b_c and hence the failure load of the prism is almost equal to the sum of the failure loads of the strips i.e. $P_{sp} \longrightarrow P_{sg}$. The theoretical strength of the prism, Equ. 7.3, when subjected to a strip load of width b_d, Fig. 7.14, is plotted in Fig. 7.15. It would appear that the double strip load can be considered to act as a single load when $b_c/b_t > 0.65$ and that $P_{sp} > P_{sg}$ when $b_c/b_t < 0.75$.

7.5.3 Longitudinal spacing of strip loads

The distribution of the lateral stresses in a slab which is subjected to longitudinally spaced strip loads consists of the local distribution between the strip loads, Fig. 7.16, plus the global distribution, Fig. 7.17, which is the mean lateral stress between the strip loads. The distribution in Fig. 7.16 is a superimposition of the individual stress distributions, Fig. 7.6. When a uniform longitudinal shear flow is applied to a slab, which is equivalent to a concentrated load on a beam, the global distribution, Fig. 7.17, consists of a region (A) of high lateral tensile stresses which is adjacent to the point of shear reversal, a region (B) of zero lateral stress, and a region (C) of predominantly high lateral compressive stresses.

7.5.3.1 The region of zero mean lateral stresses

In Region B, the lateral stresses in front of and behind the load, Fig. 7.6, are unaffected by the ends of the shear span and hence the distribution of the lateral compressive and tensile stresses is uniform, which causes the global stress to be zero. The lateral tensile stress is reduced by the superimposition of the lateral compressive stresses and hence the splitting strength of the slab increases as the spacing of the

studs is reduced and the width of the slab increased, Fig. 7.18. The increase in the maximum shear flow is shown in Fig. 7.19.

Since the beneficial effect of the lateral compressive stress behind the load is dependent upon the cracking behind the load, Fig. 7.6, which is dependent upon the longitudinal compressive load, Sect. 7.3.1, which is dependent upon the position of the load in the slab and the dispersal of the load into the slab, a conservative design would be to assume that the maximum strip load that can be applied to a slab is the load at which the slab splits when subjected to a single strip load, Equ. 7.3.

7.5.3.2 The region of a discontinuity in the shear flow

A uniform shear flow was simulated by applying equal loads to the nodes along the centre line of a prism in which the X-grid was uniformly spaced, Fig. 7.1. The global distribution of the lateral stresses, Fig. 7.20, consists of two regions. In Region D, the lateral tensile stresses in front of a load are reduced by the superimposition of the lateral compressive stresses behind the loads which are closer to the discontinuity, also the total lateral compressive force reduces whilst the total lateral tensile force increases as the discontinuity is approached. This causes a peak stress to be reached in front of the discontinuity, where the lateral compressive forces are zero. The effect of the very large lateral compressive forces in front of a load, Fig. 7.5, on the splitting strength of a slab can be ignored as they extend over a very short length. The stresses in Region E, Fig. 7.20, consist of the superimposition of the lateral tensile forces in front of the loads.

The lateral tensile force which is induced by a concentrated load, P, is equal to $K_d P$, Sect. 7.5.1.1. Therefore, the maximum mean lateral stress, between applied loads, f_m, in a region of zero lateral compressive force is given by

$$f_m = K_d q \tag{7.4}$$

If l_z/s_s is large then the superimposition of the lateral tensile stresses in Region D, Fig. 7.20, will cause the distribution to be uniform and hence the peak stress will be equal to $K_d q$. It would appear, Fig. 7.20, that $K_d = 0.22$; the coarse grid system made the point shear loads appear as patches of width $0.1b_c$, Fig. 7.10. The lateral global force, L_g, on either side of a discontinuity, Fig. 7.20, is the same, extends over a distance of $1.4b_c$ from the discontinuity and is given by

$$L_g = 0.25K_d P b_c/s_s \tag{7.5}$$

When a shear force is acting away from a discontinuity, the distribution of the lateral compressive forces in the region of zero shear flow is the same as the distribution of the lateral tensile forces, Fig. 7.22. The maximum stress can therefore be calculated at a sudden change in the shear flow; for example, $f_m = K_d(q_1-q_2)$ at point A in Fig. 7.35 and $f_m = K_d(q_2+q_3)$ at point B. This analysis is only applicable when the shear flow is uniform and the slab extends a distance of $1.4b_c$ on either side of the change in the shear flow. It is therefore not applicable at the ends of a slab, Fig. 7.17, where the lateral forces cannot develop fully. The overall stress distribution in this region consists of the superimposition of individual stress distributions which lie between those of a load applied to the surface of a prism, Fig. 7.5, and those of a fully embedded load, Fig. 7.6.

7.5.3.3 The region of a reversal in the shear flow

The lateral tensile stresses in Region A, Fig. 7.17, can be considered to be uniform when $b_c/s_s \geqslant 7$, Fig. 7.21. The distribution, Fig. 7.21, is affected by the distance of the concentrated load from the

point of shear reversal, Fig. 7.7, and by the longitudinal spacing of the loads, Fig. 7.21. As the position of the load approaches the point of shear reversal, Fig. 7.7, the lateral tensile stresses become more uniform and as the longitudinal spacing reduces, the distribution becomes more uniform because of the superimposition of the stresses.

When the studs are closely spaced, the global distribution of the lateral stresses, Fig. 7.22, consists of the superimposition of the stresses due to the loads on either side of the point of shear reversal, Fig. 7.20, and hence when the shear flows are opposite, equal and uniform, the global lateral force, L_g, on both sides of the point of shear reversal and the maximum tensile stress, f_m, are given by

$$L_g = K_d P b_c / s_s \qquad (7.6)$$

$$f_m = 2K_d q \qquad (7.7)$$

The difference between the distribution of the mean lateral tensile stress and the global stress, Fig. 7.22, is due to the beneficial effect of the lateral compressive stresses behind the loads.

The accumulation of the lateral tensile stresses at the point of shear reversal reduces the strength of the slab, the effect of which is shown in Fig. 7.18.

7.6 ANALYSIS OF THE SPLITTING STRENGTH OF COMPOSITE SLABS

The empirical analysis, Sect. 7.4, the finite element analysis, Sect. 7.5, and the push tests, Sect. 5.4.1, are used to determine the load that a stud has to exert in order to cause the slab to split.

The splitting strength of the slab of a push test was proportional to the split tensile strength of the concrete, Fig. 7.3 6.

7.6.1 The effective height of a stud

The results of the analysis of patch loads are not directly applicable to studs because the longitudinal displacement of the shank of a stud is not uniform and hence the distribution of the bearing stresses, Fig. 6.15, is not the same as that of a patch load, Fig. 7.13. The experimental results have therefore been used to determine the size of an equivalent patch load which causes the same failure load as the stud. The width of the patch load is assumed to be equal to the diameter of the shank of the stud; it is therefore only required to determine the equivalent length of the patch i.e. the effective height of the stud.

7.6.1.1 An analysis of slabs with single studs

The push tests, Sect. 5.4.1.1, were analysed as concentric patch loads, Fig. 7.37, by using Equs. 7.1 and 7.3 with the restrictions given in Sect. 7.4.2.2.

The failure load, P_u in Equ. 7.1, was equal to $2P_e$, Table 5.4. The strength of the equivalent strip, Fig. 7.30, of width h_a was determined from $P_Z = 1.75h_c b_c f_{ct} K_{sp}$. Since the dispersal of the force in the Z direction is dependent upon the axial load in the stud, $K_d = \frac{1}{2}(P_a/P_{sh})$, Sect. 7.5.1.1, where P_a/P_{sh} was determined from Figs. 6.19 and 6.31. This value of K_d was used to determine h_a/h_c from Fig. 7.10 and therefore K_{sp} in Fig. 7.11, using the Mode 1 Analysis as l_c/h_c was large. The strength of the equivalent strip of width b_a, Fig. 7.30, was determined from $P_Y = 1.75b_c h_c f_{ct} K_{sp}$, where K_{sp} was determined, from the empirical variations of Fig. 7.11, for d_s/b_c. Equation 7.1 was therefore solved to determine h_a, Fig. 7.30, which is equal to twice the effective height of a stud.

7.6.1.2 An analysis of slabs with longitudinally spaced studs

The push tests of Sect. 5.4.1.2 were first analysed on the Mode 1 program in order to determine the distribution of the shear forces on the studs; the finite element model was similar to Fig. 5.28. These forces were then applied as patch loads to a Mode 1 analysis of the plan of the slab, as described in Sect. 7.5.3.2,the dimensions and properties of which are given in Table 5.5. The effective height of a stud was therefore equal to the depth of the patch load which gave the same failure load as the experimental load. No allowance was made for the dispersal of the force in three dimensions as the initial Mode 1 analysis showed that the axial forces were much smaller than those induced in slabs with single studs.

7.6.1.3 The effective height

The mean of the experimentally derived effective heights, Fig. 7.38, is $1.87d_s$, the regression is not significant and the coefficient of variation, 16.6%, is much greater than that which can be attributed to determining the split tensile strength of the concrete, Fig. 5.22. Part of the scatter may be attributed to the variation in the depth of the weld collar. The experimental loads, Fig. 7.38, were plotted in terms of their theoretical shank failure loads, Equ. 6.1.

The effect of allowing for the dispersal of the force in three dimensions, Sect. 7.6.1.1, was to reduce the effective height by approximately 17%.

7.6.2 Slabs with a single stud

The maximum load that a stud can apply to a slab, P_{sp}, can be derived from Equ. 7.3, when there is no axial load at the base of the stud, since $h_c = 1.87d_s$.

$$P_{sp} = 3.28 b_c d_s f_{ct} K_{sp} \qquad (7.8)$$

The distribution of the lateral tensile stresses along a longitudinal plane through the axis of the stud is the same as the distribution of the normal force, Fig. 6.15, because K_d, K_s and l_z are constant along planes parallel to the soffit of the slab. These lateral tensile forces near the soffit of the slab must be balanced by lateral compressive forces near the top, a fact which was deduced and measured experimentally by Davies[28].

7.6.3 Slabs with double studs

The experimental loads at which double studs caused slabs to split are plotted in Fig. 7.15 as a proportion of double the theoretical splitting load of a single stud. The method of determining the theoretical strength is described in Sect. 7.6.1.1. The total width, b_t, of the specimens in Table 5.14, which were eccentrically loaded, was assumed in Fig. 7.15 to be twice the distance from the centre line of the studs to the nearest edge of the slab. The total width of Teraszkiewicz's specimens[41] was assumed to be equal to the width of the haunch and the tensile strength of his concrete was assumed to have the same relationship with the cube strength as shown in Fig. 5.22. The experimental variations are similar to the theoretical variations, Fig. 7.15, which were determined in Sect. 7.5.2, however, they do not show the theoretical reduction in strength for low values of b_c/b_t. The experimental results from Table 5.14 are higher than the theoretical results probably because of the eccentricity of loading, the effect of which is discussed in Sect. 7.4.3.

The hypothesis that double studs can be analysed as a single patch load, Sect. 7.5.2, has been proved experimentally for all practical values of b_c/b_t, Fig. 7.15. The theory could probably be extended to include

groups of studs, in which there are more than two longitudinal rows, which would be analysed as longitudinally distributed patches of a width equal to the maximum lateral extremities of the studs, b_d in Fig. 7.14.

7.6.4 Longitudinally spaced studs

7.6.4.1 Discontinuity of the shear flow

The strengths from push tests with longitudinally spaced studs, Table 5.5, and staggered studs, Table 5.7, have been compared with the theoretical strengths of Equ. 7.4 in Fig. 7.39. The effective width of the staggered studs was assumed to be equal to $(t_s + d_s)$, Sect 7.6.3. The line in Fig. 7.39 was plotted through the mean of the results, point B, and through the theoretical strength of a single stud, Equ. 7.8, point A. The variation is probably not linear but does indicate that the lateral tensile stress distribution can be considered to be uniform, and hence Equ. 7.4 is applicable, when $b_c/s_s > 4$, i.e. P_e/P_{sp} is greater than 1, which is confirmed by the theoretical analysis of Fig. 7.21.

A composite T-beam can therefore be defined as a beam in which the lateral stress distribution at a change in the shear flow can be considered to be uniform i.e. $s_s < b_c/4$. The converse is applicable to L-beams.

7.6.4.2 Reversal in the shear flow in composite T-beams

The theoretical analysis, Equ. 7.7, assumed that the shear flow was uniform between the loads on a beam and changed abruptly at the load. However, experimental tests by Chapman and Balakrishnan[35] showed that the shear flow was not uniform between loads and reduced gradually at the loads. The effect of the latter would be to increase the splitting strength of a slab.

Davies[28] tested composite T-beams with varying amounts of transverse reinforcement. The application of Equ. 7.7 to his most lightly reinforced beam showed that splitting occurred at approximately half the load at

which it first became visible. The shear flow was determined by assuming that the beam was elastic and did not slip across the flange/slab interface.

When a single stationary concentrated load is applied to a composite T-beam with transverse reinforcement the split is probably restricted to a small length adjacent to the load, because the maximum stress reduces rapidly from its peak, Fig. 7.22, and hence the longitudinal shear strength and ultimate strength of the beam are only slightly reduced. The load at which splitting occurs, as derived from Equ. 7.4, is therefore a lower bound to the ultimate strength of a beam. However, if the concentrated load was moved along the length of the beam the peak stress would act over a much larger length and it may be expected that the ultimate load would tend towards the load at which splitting first occurred.

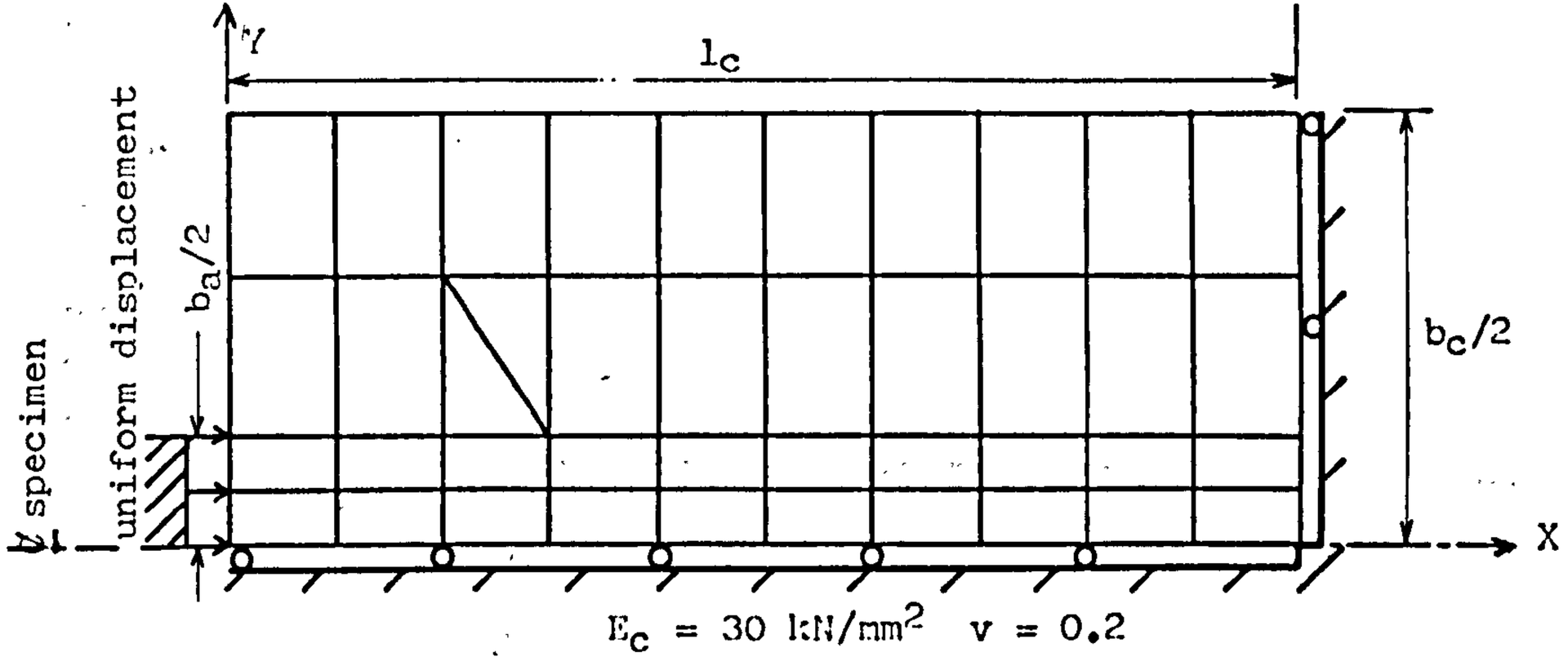

Fig. 7.1 Finite element model of a strip load on a concrete prism.

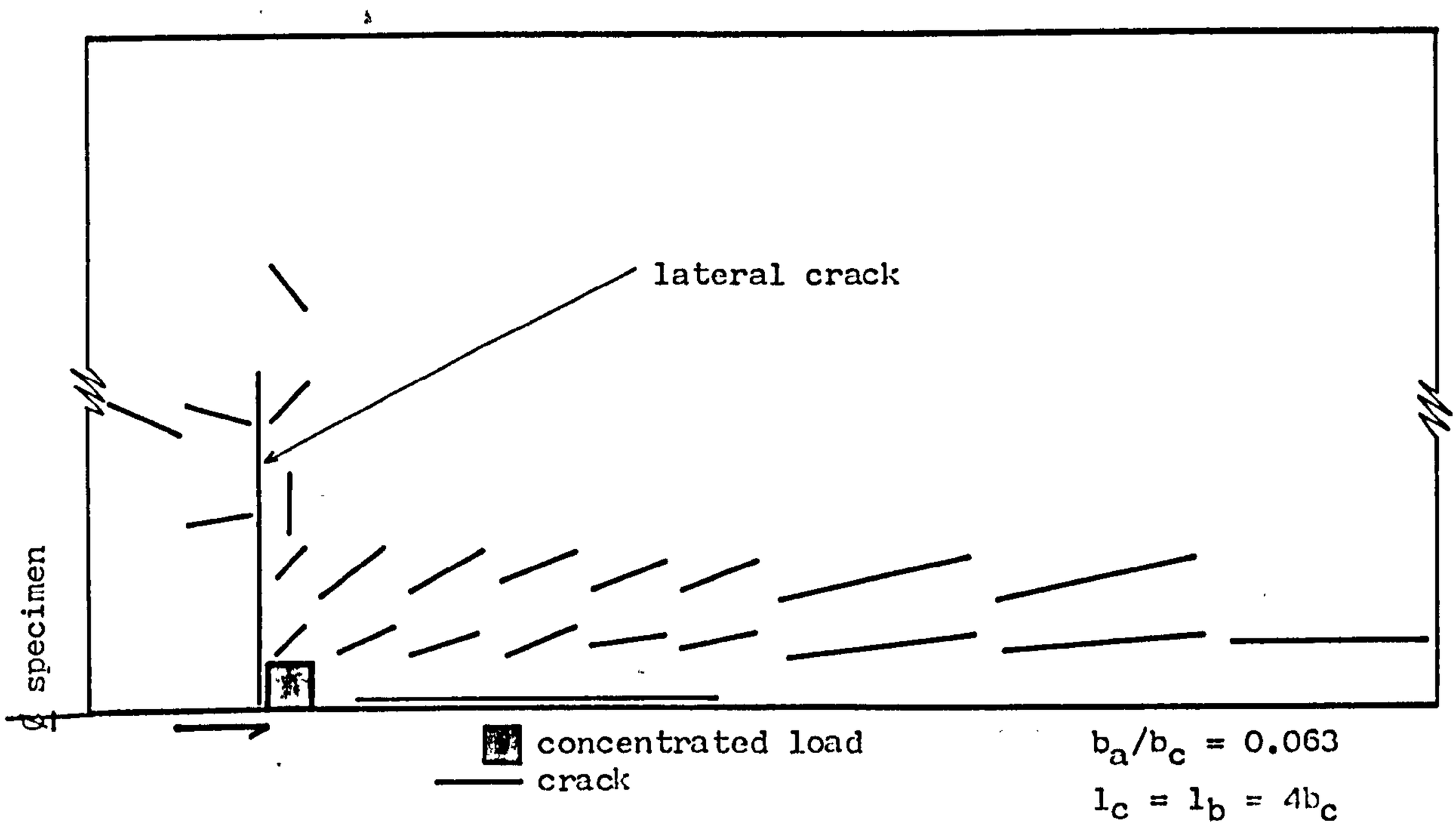

Fig. 7.2 Cracking pattern when a load is applied within a prism.

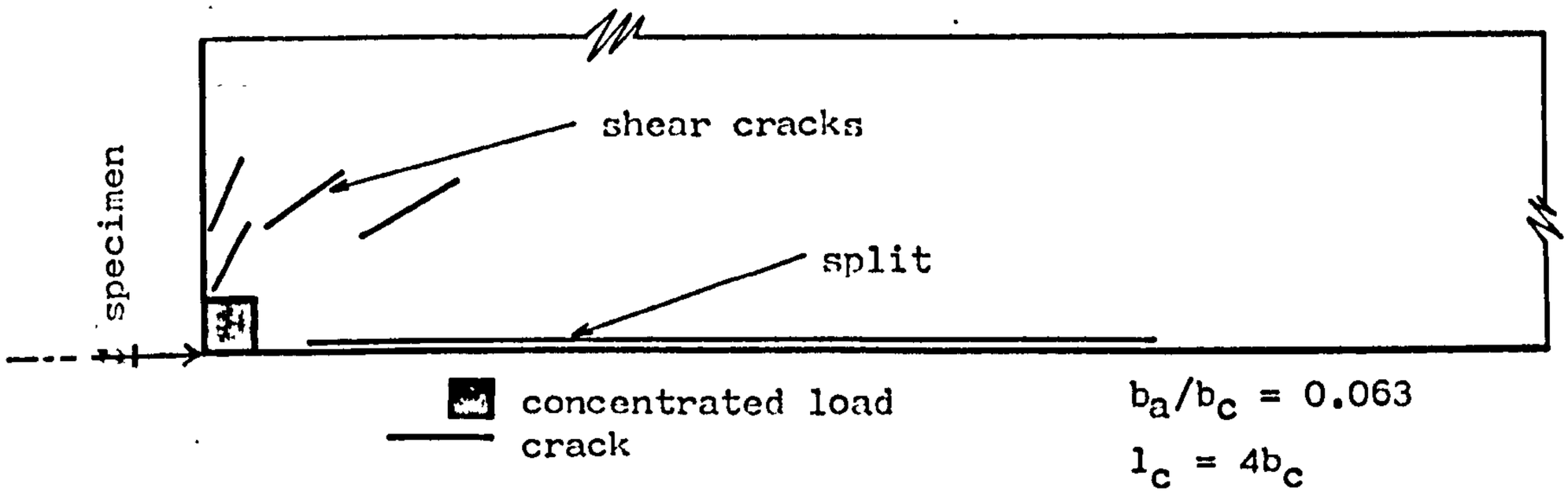

Fig. 7.3 Cracking pattern when the load is applied to the surface of the prism.

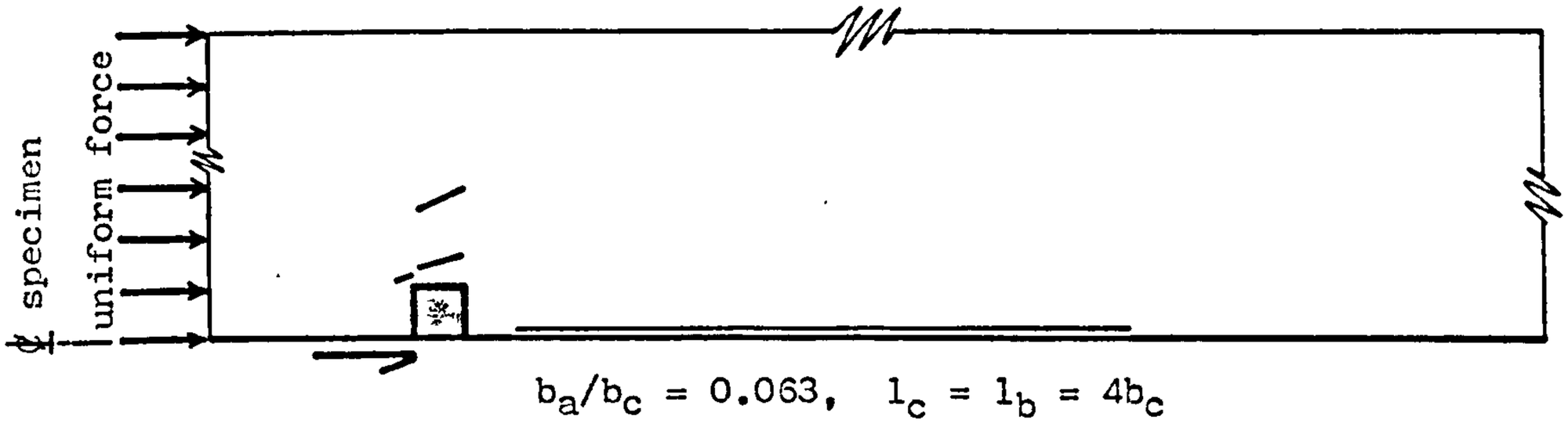

Fig. 7.4 Cracking pattern when a uniform force is applied behind the concentrated load.

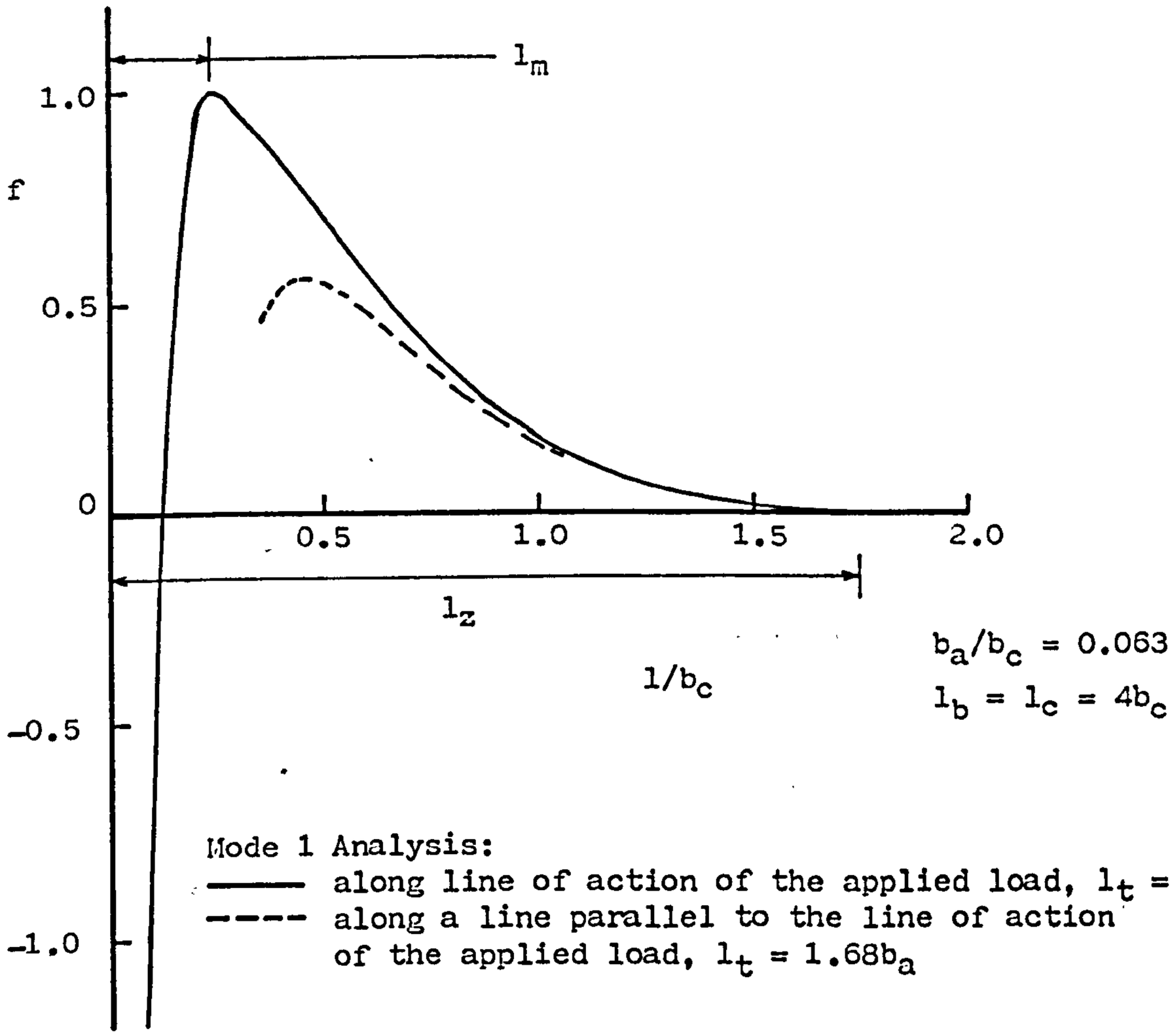

Fig. 7.5 Distribution of the lateral stresses when the load is applied to the surface of a prism.

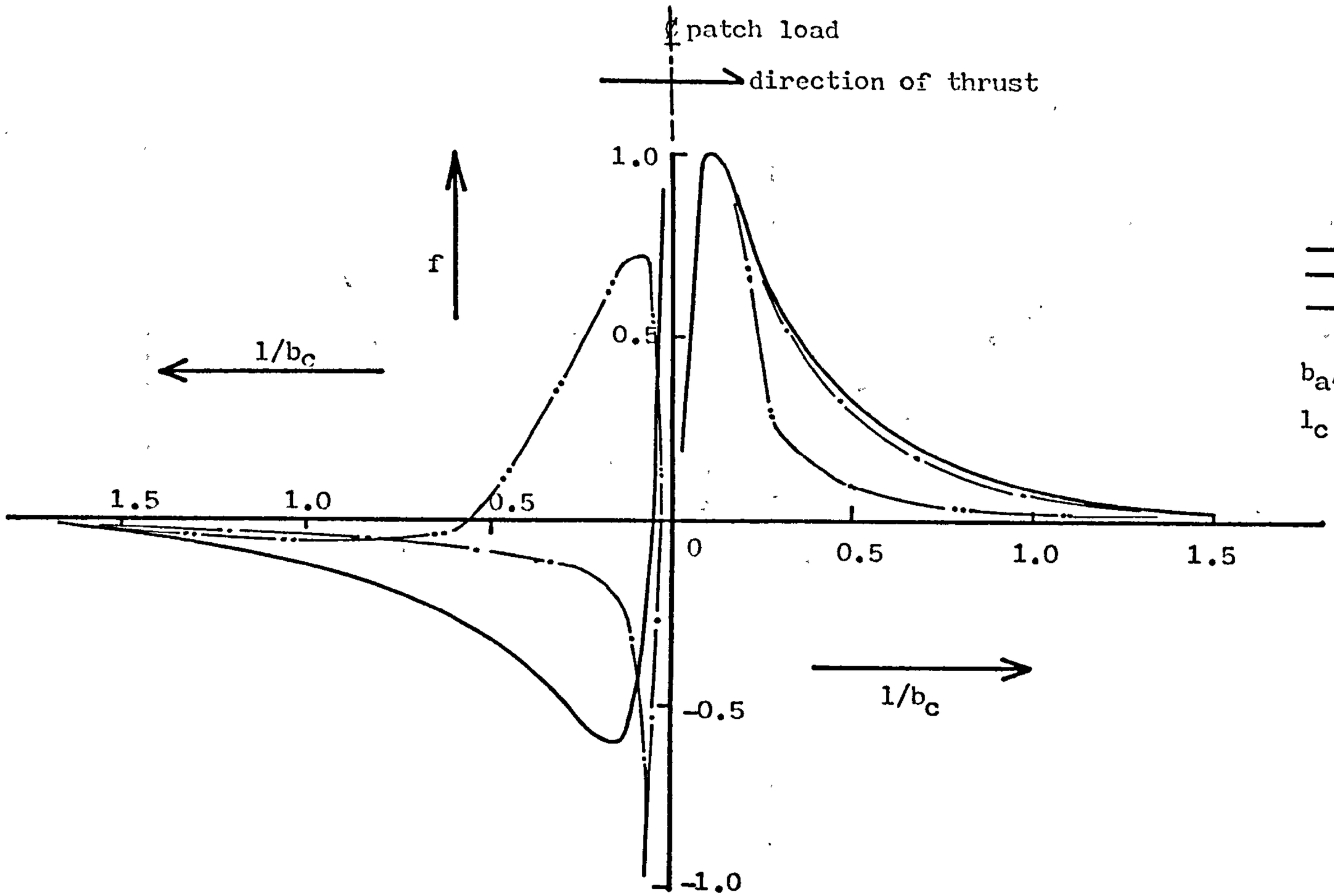

Fig. 7.6 Distribution of the lateral stresses when the load is applied within a prism.

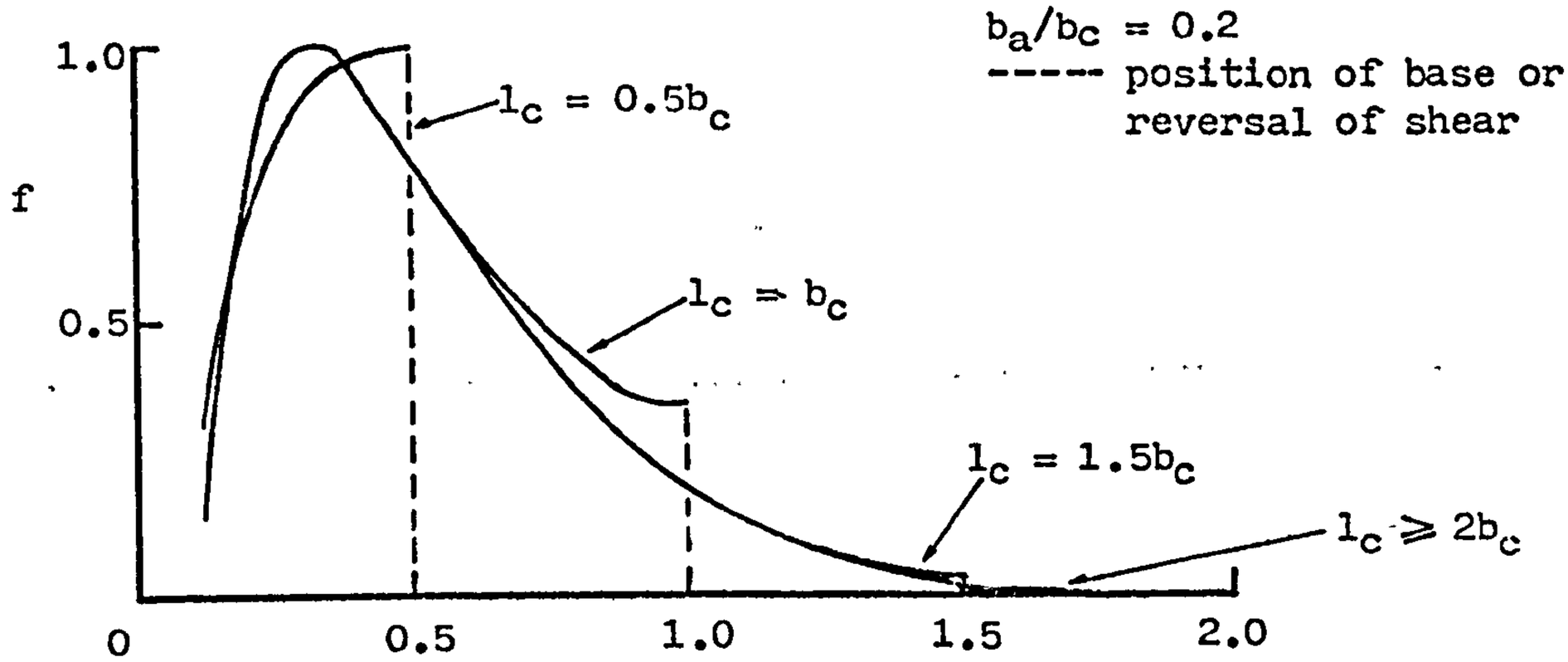

Fig. 7.7 Variation of the distribution of the lateral stresses with the length of the prism when the base is free to expand laterally.

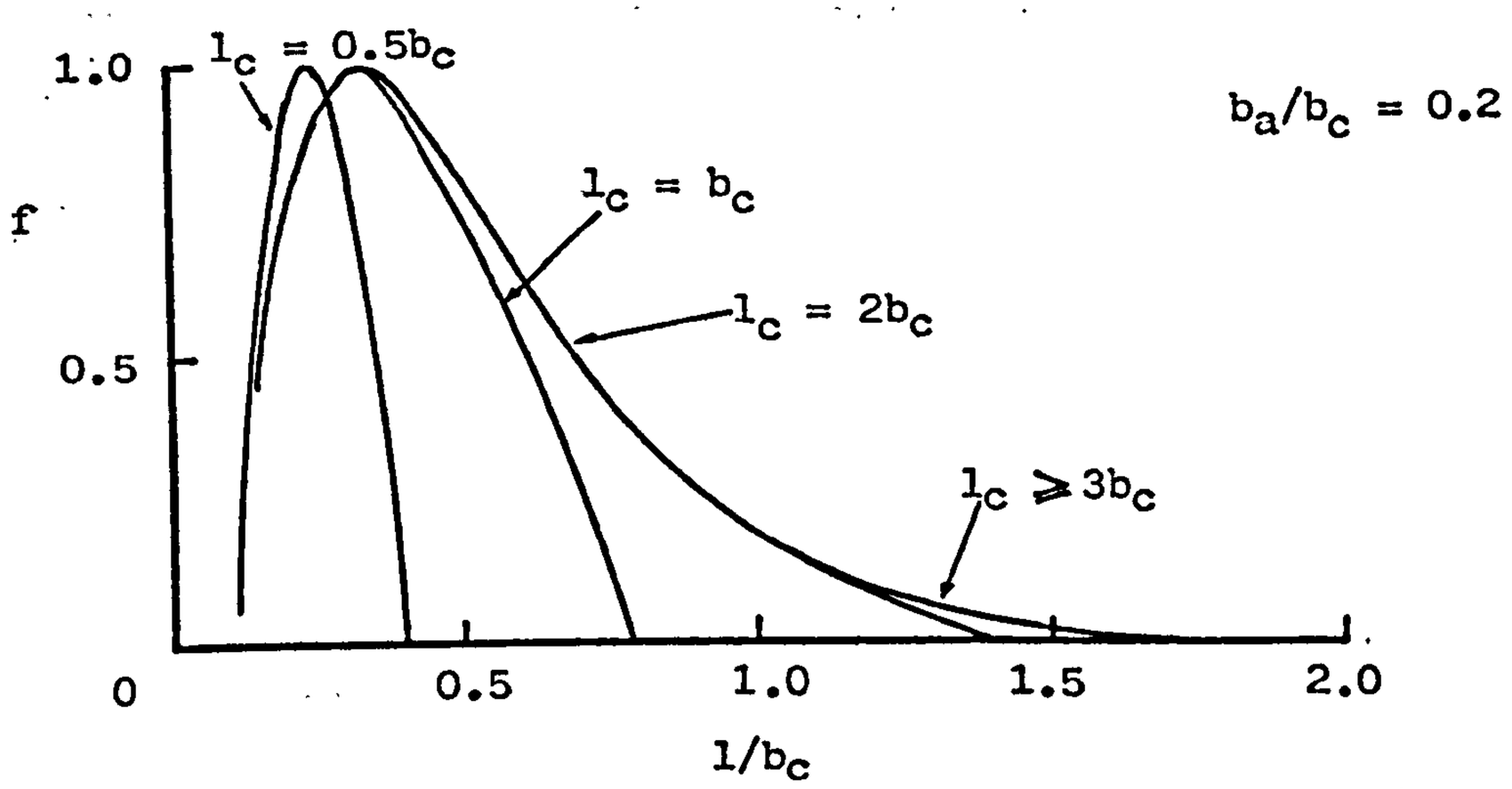

Fig. 7.8 Variation of the distribution of the lateral stresses with the length of the prism when the base is fully restrained.

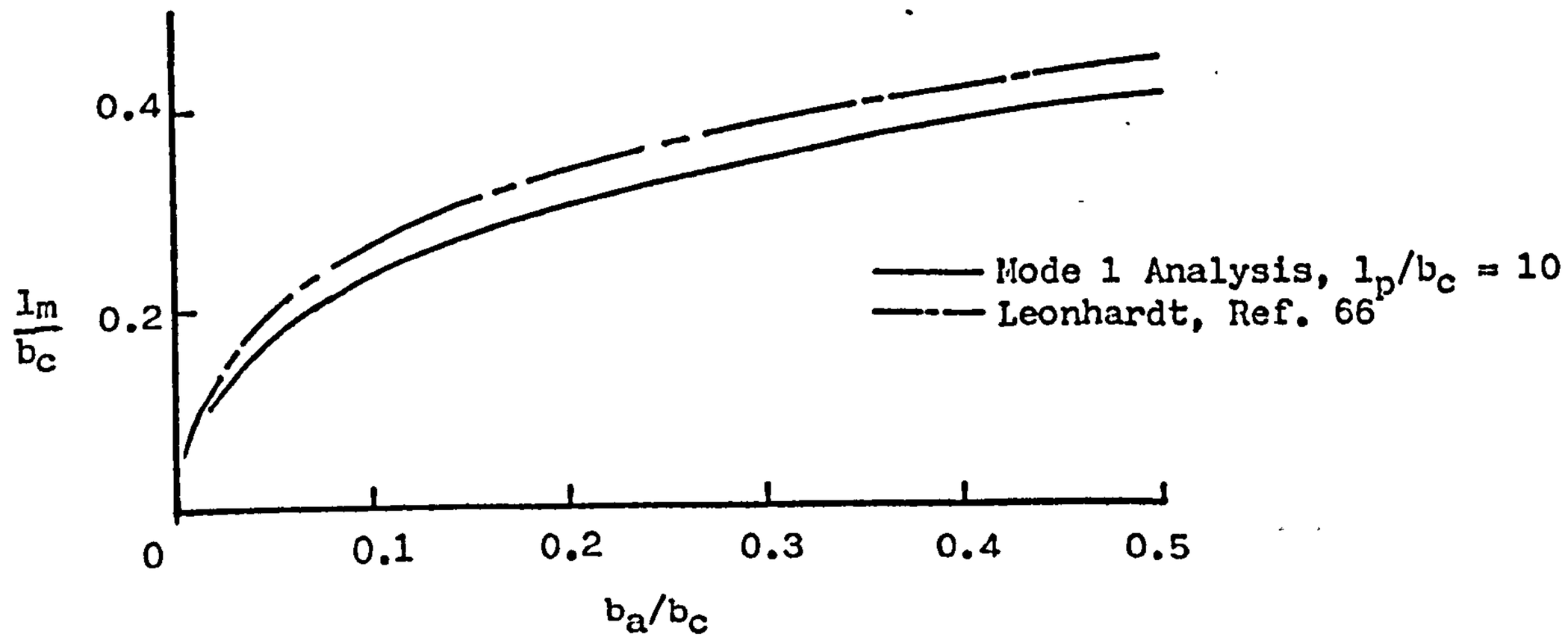

Fig. 7.9 Position of the maximum lateral tensile stress.

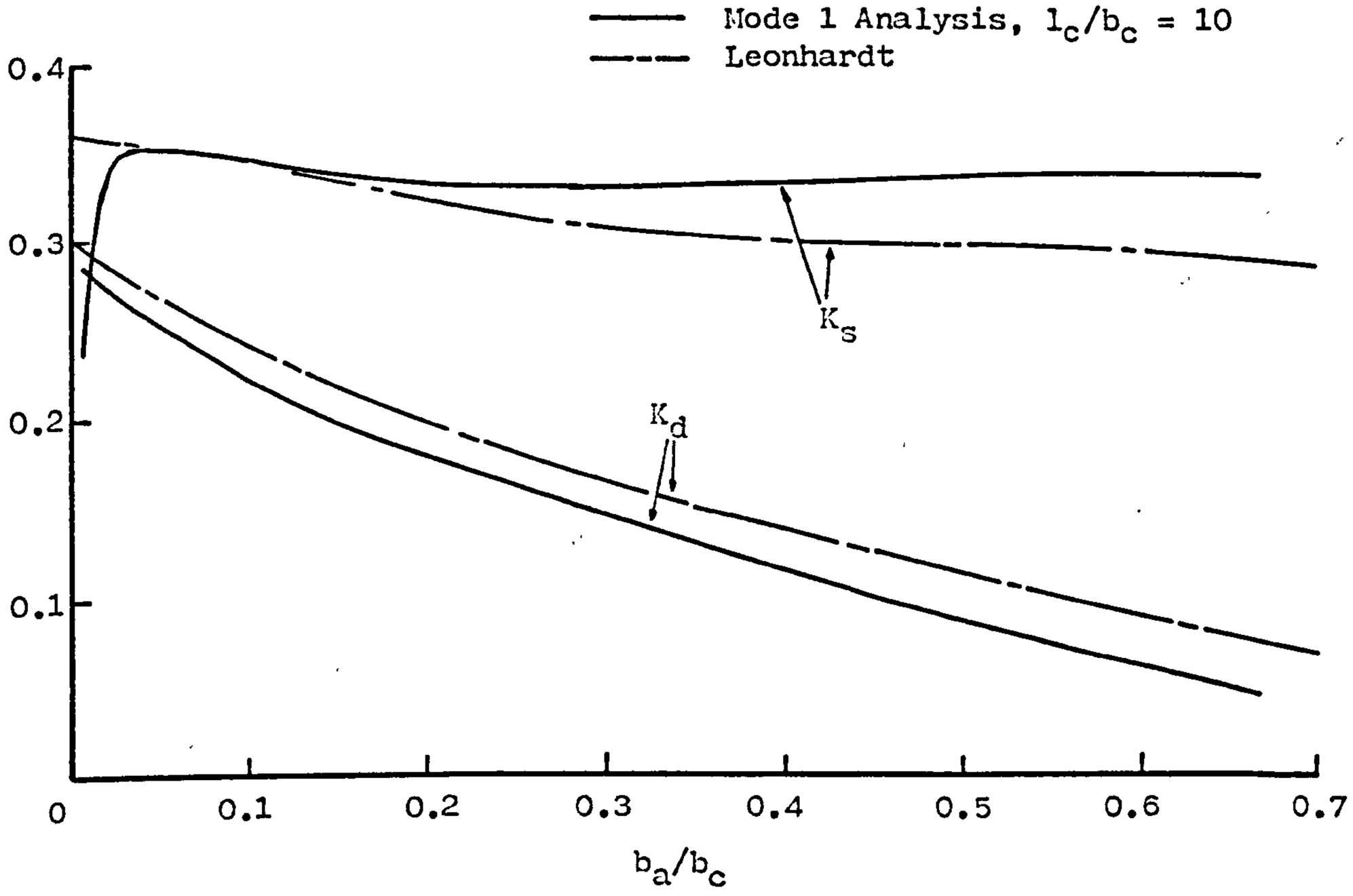

Fig. 7.10 Variation of K_d and K_s.

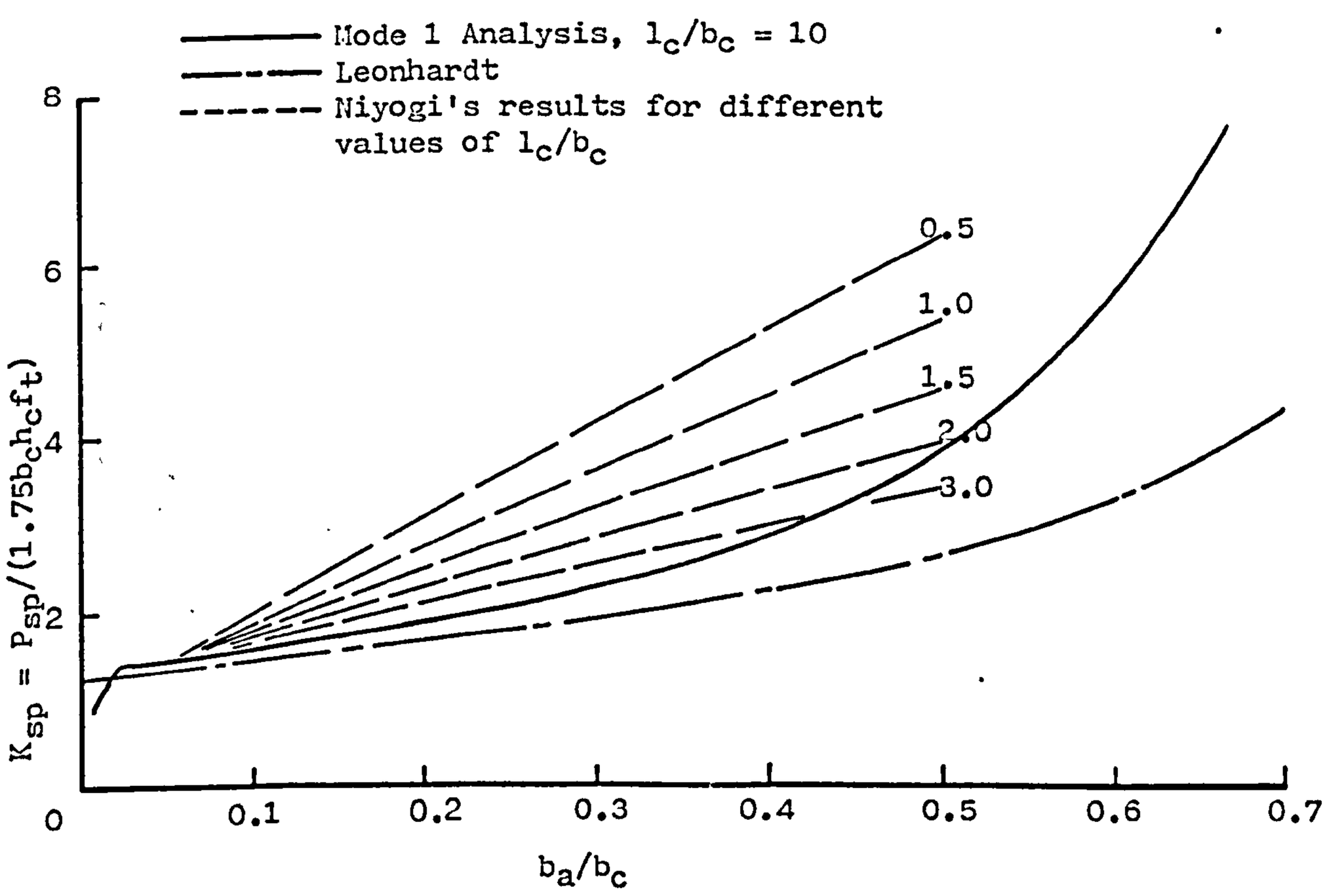

Fig. 7.11 Variation of K_{sp}.

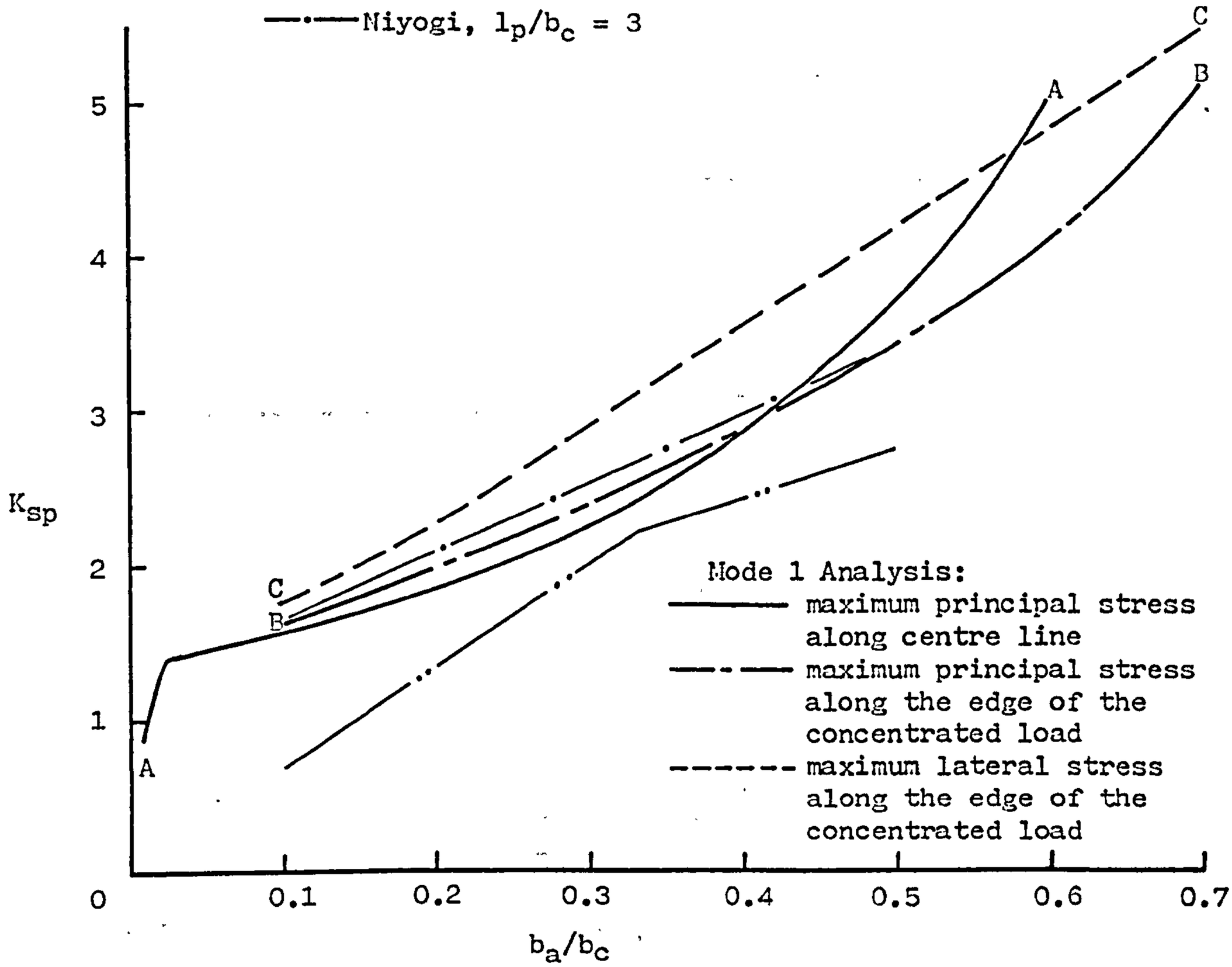

Fig. 7.12 Lower bound to K_{sp}.

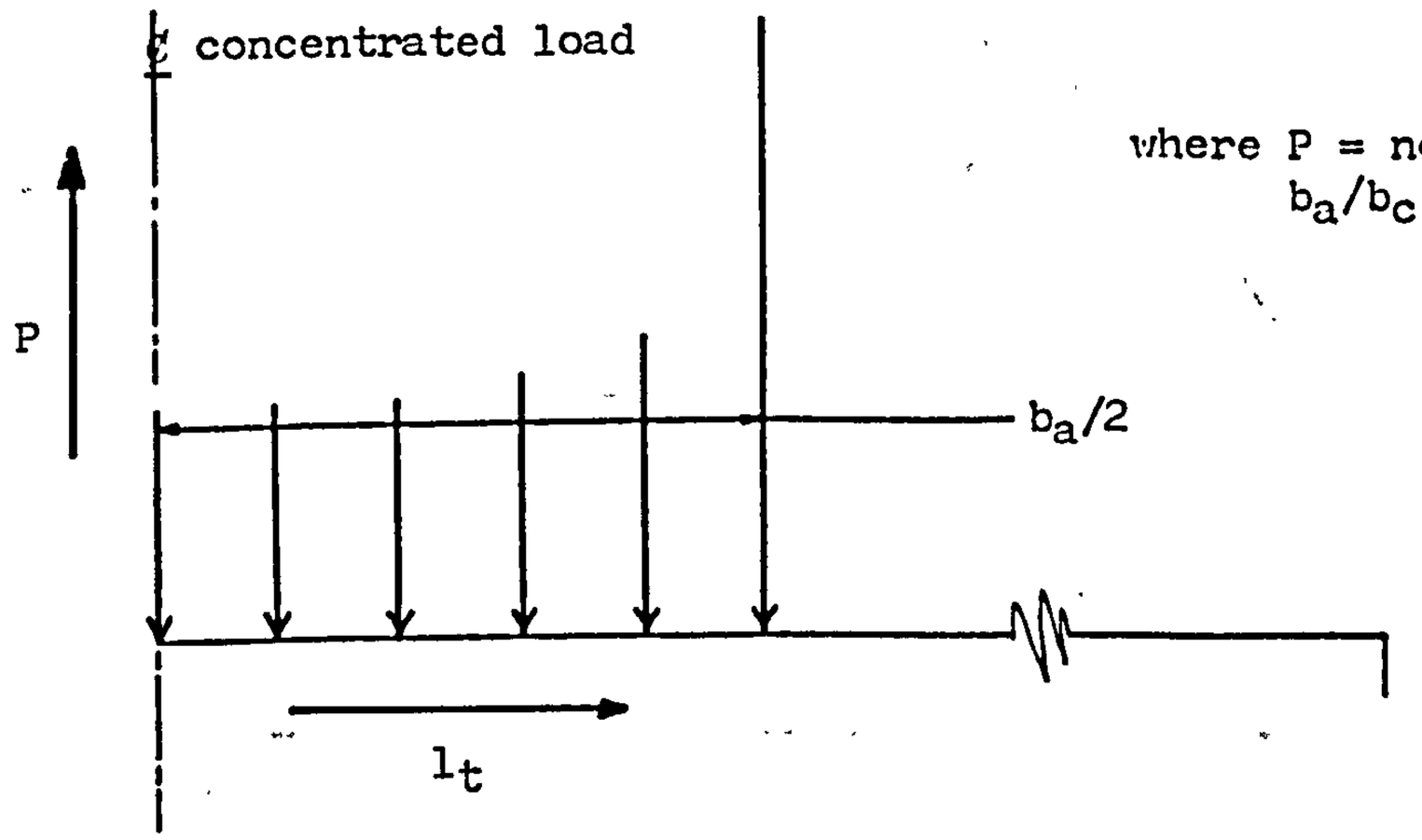

Fig. 7.13 Distribution of the nodal forces when a uniform displacement is applied to the prism.

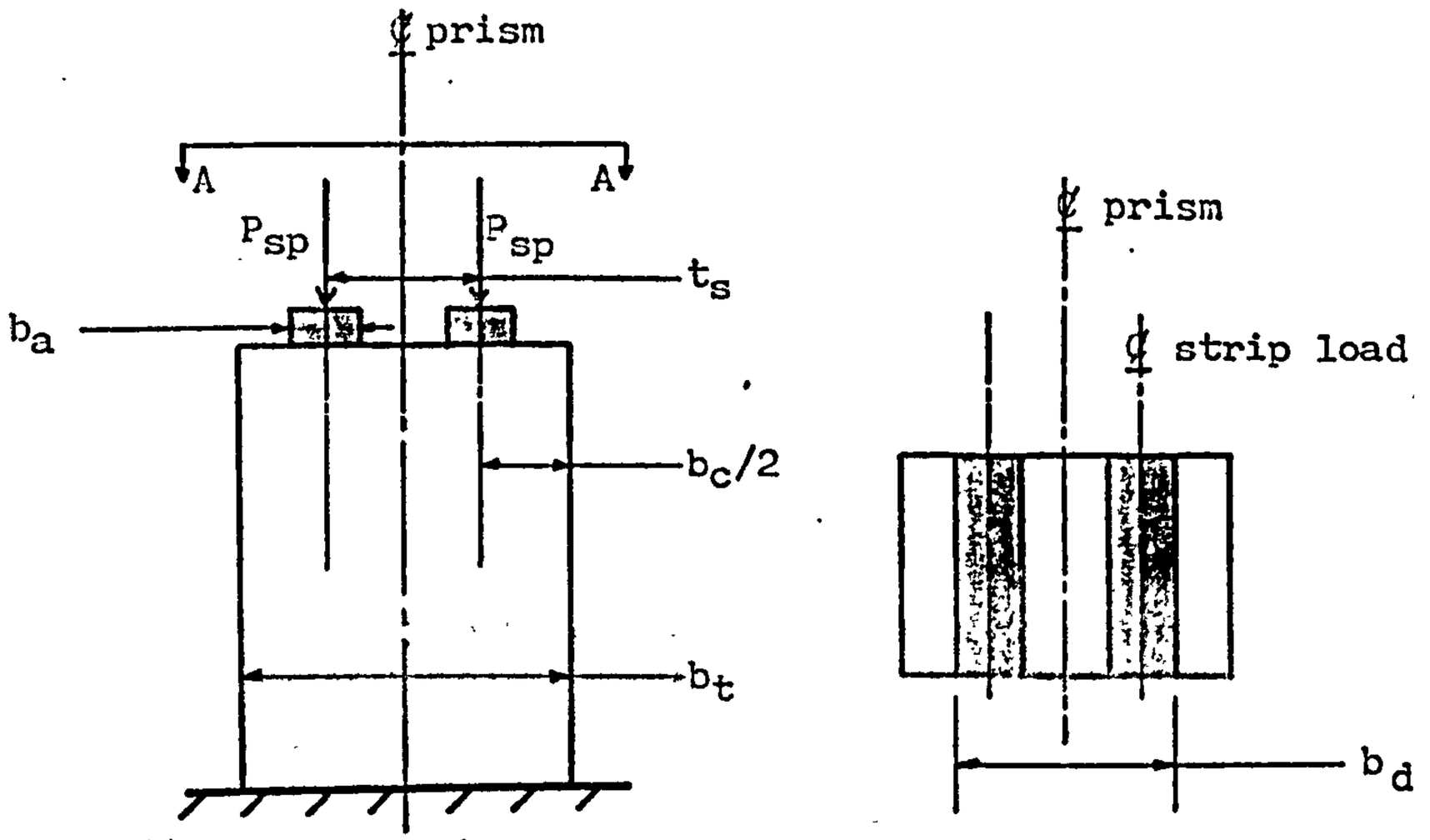

Fig. 7.14 Prism subjected to a double strip load.

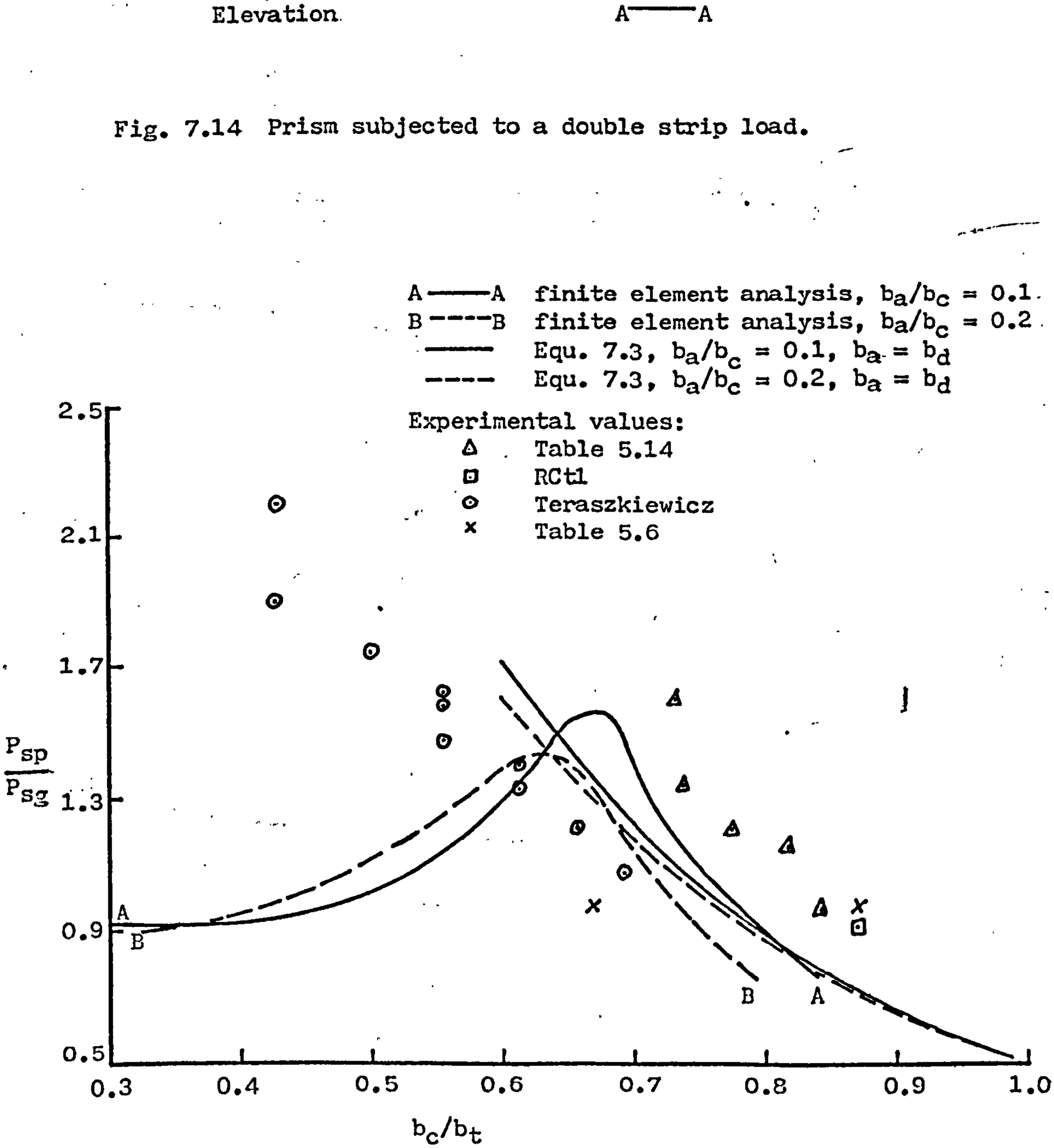

Fig. 7.15 Theoretical and experimental variation in the splitting strength of slabs subjected to double strip loads.

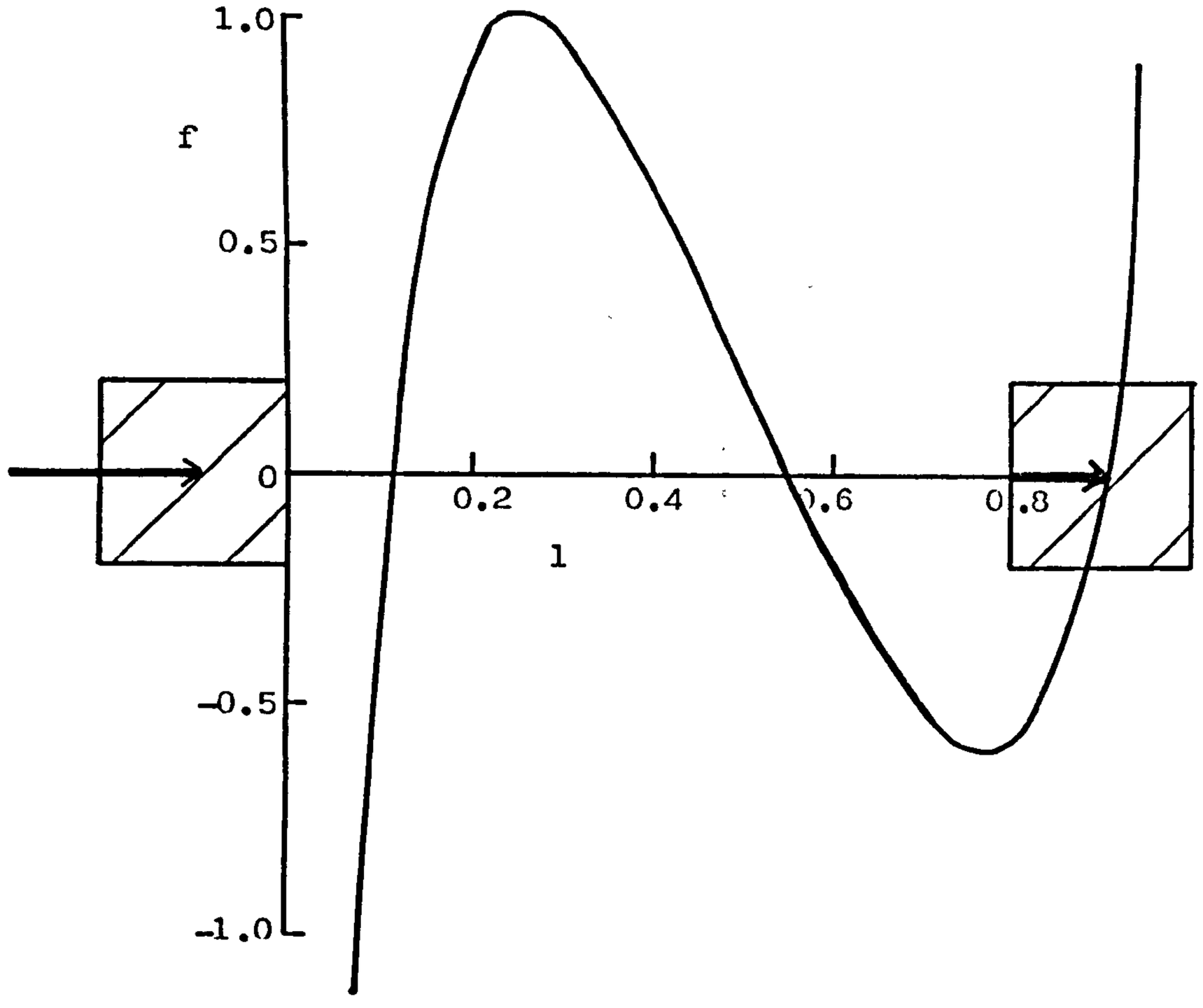

Fig. 7.16 Local distribution of the lateral stresses in a slab.

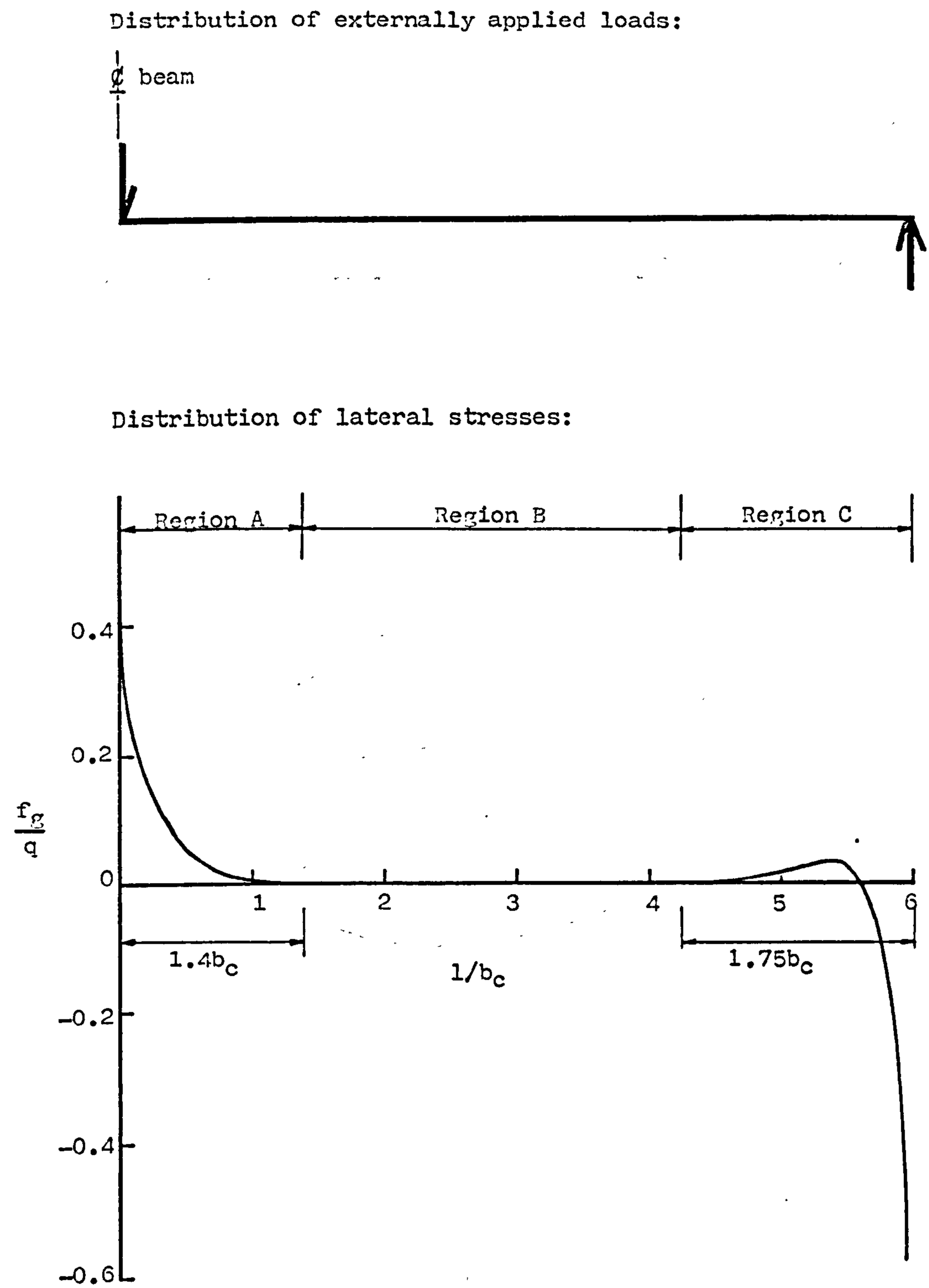

Fig. 7.17 Global distribution of the lateral stresses in a beam in which there is a uniform longitudinal shear flow.

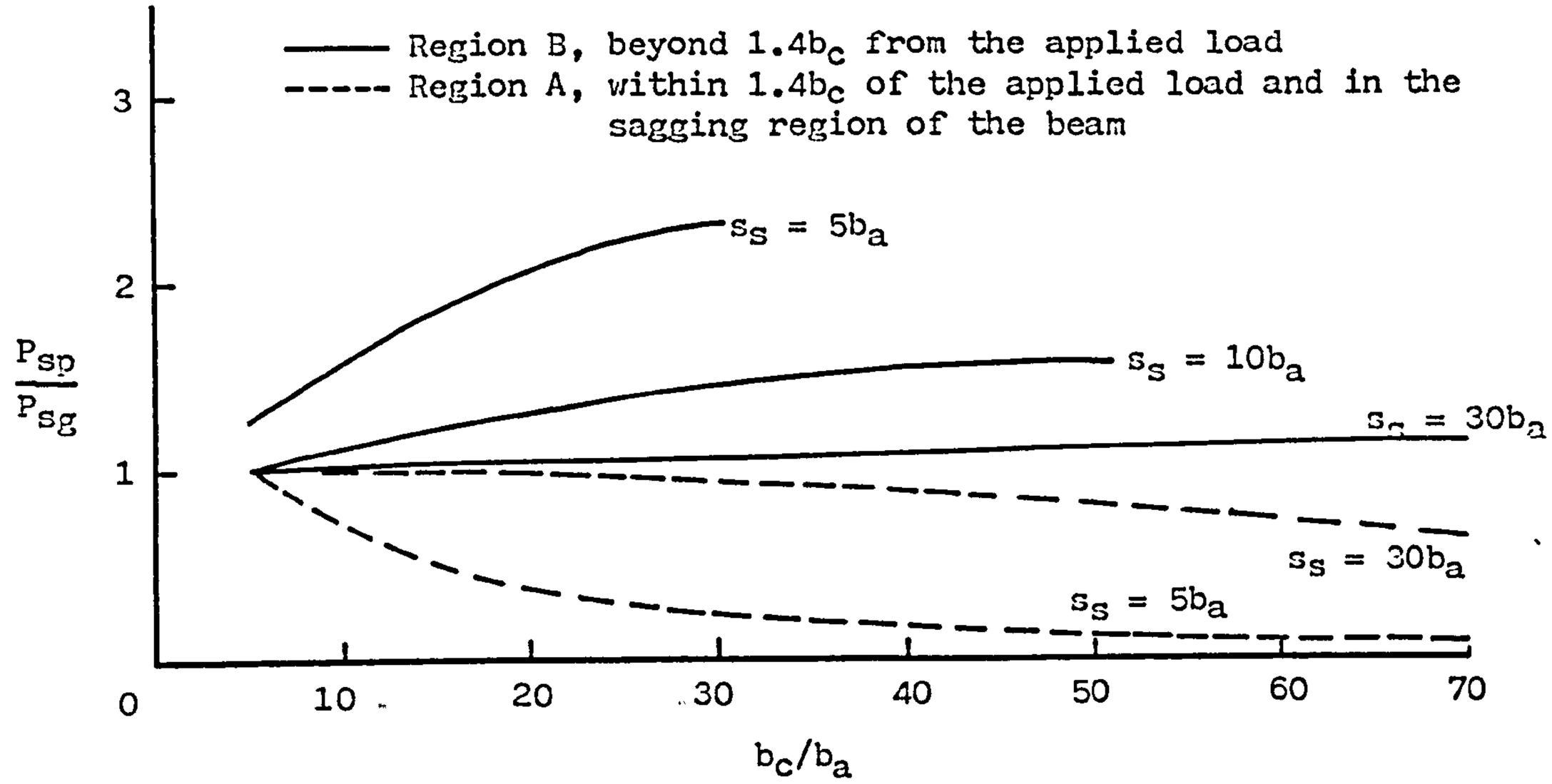

Fig. 7.18 Variation of the splitting strength due to the longitudinal overlap of the lateral stresses.

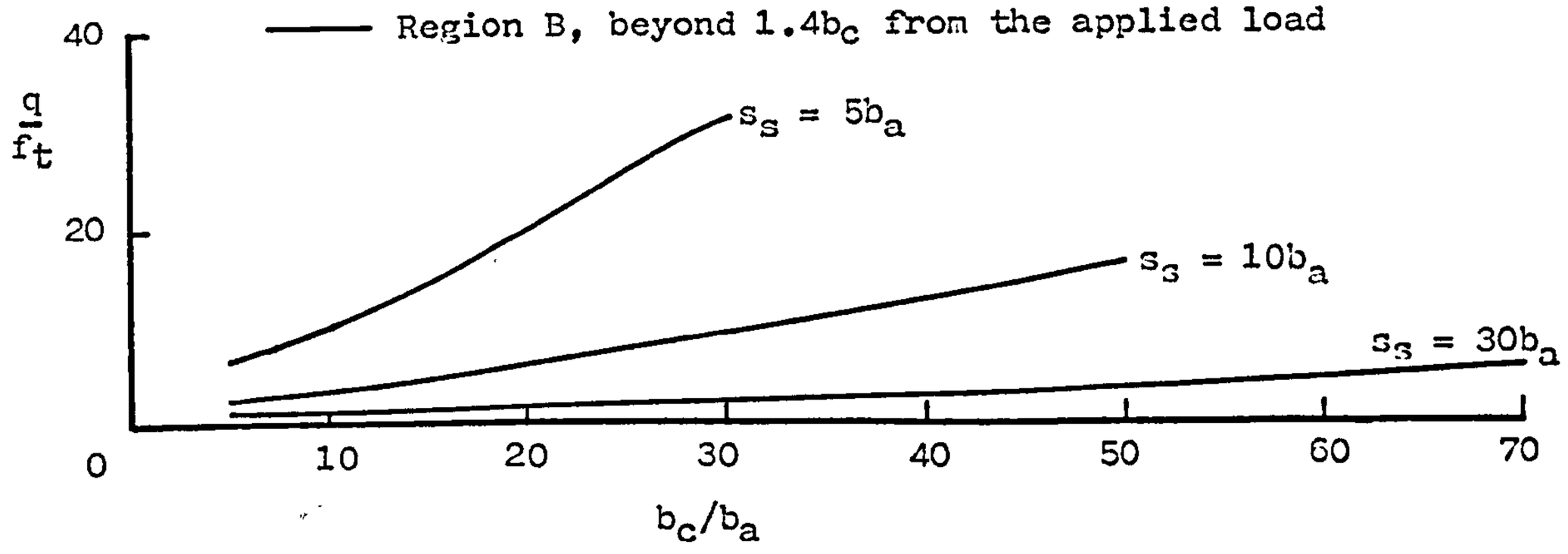

Fig. 7.19 Variation in the maximum shear flow.

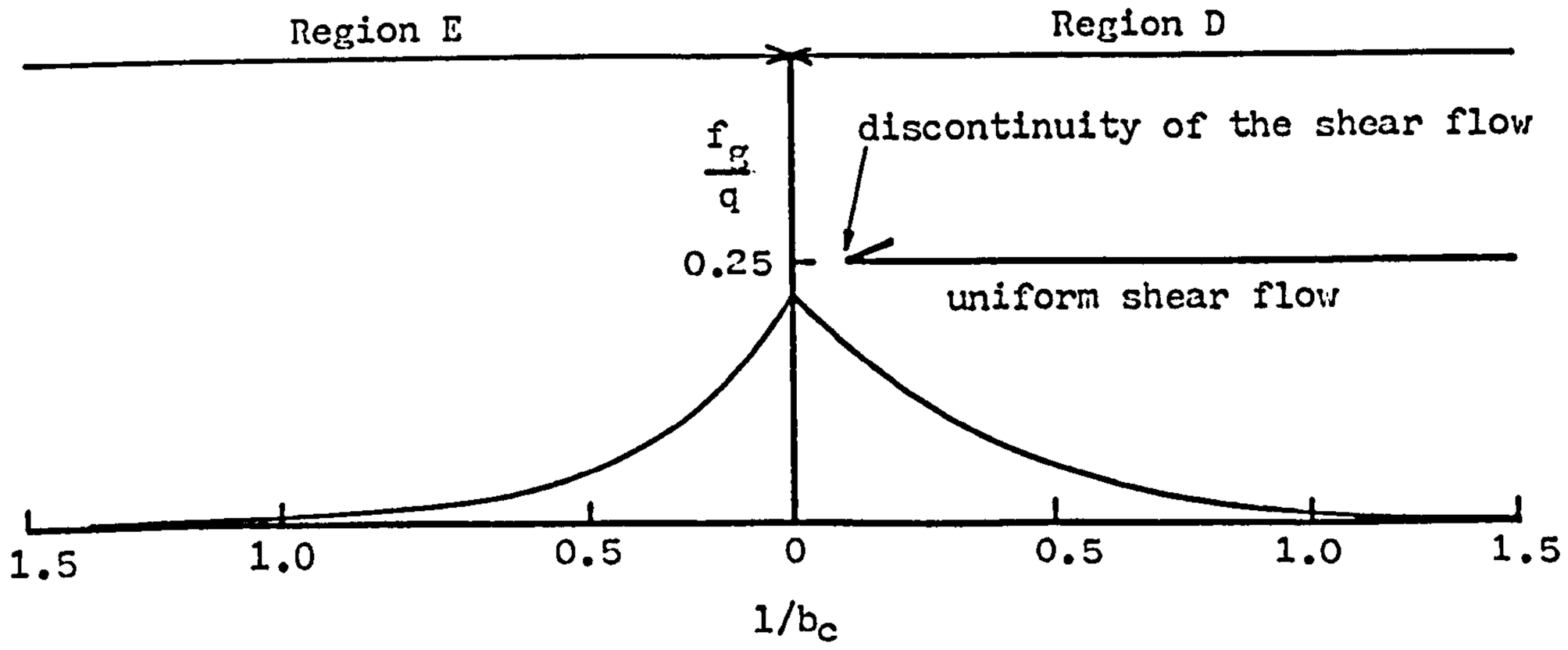

Fig. 7.20 Global distribution of the lateral stresses in the region of a discontinuity in the shear flow.

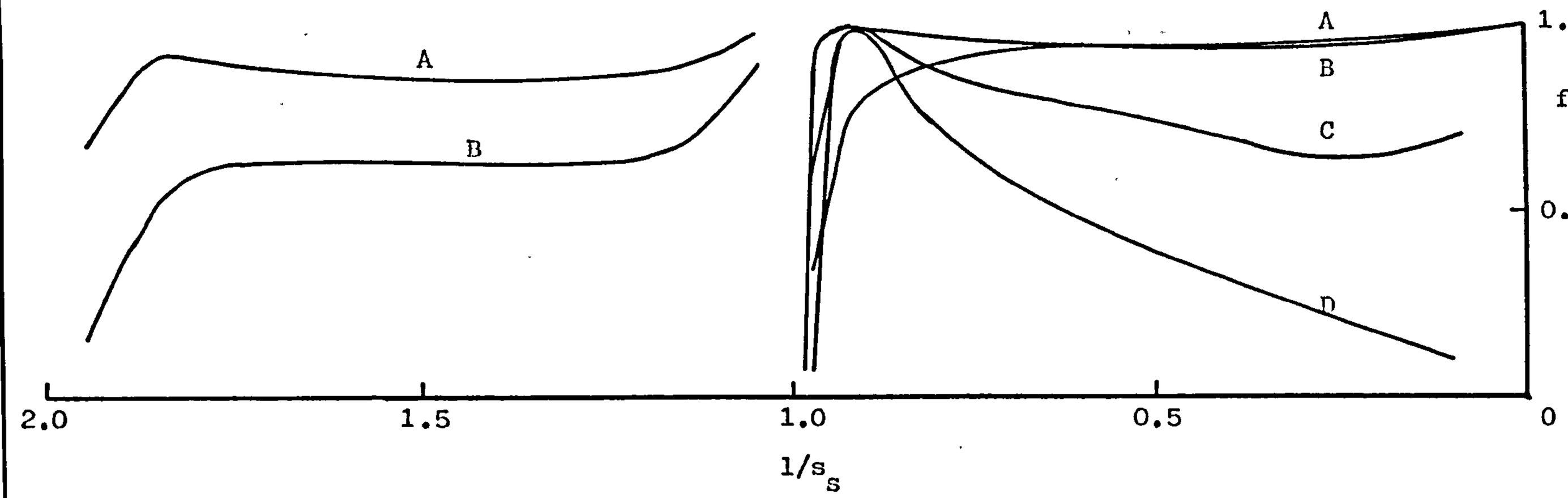

Details:

curve	b_c/b_a	b_c/s_s
A	70	14
B	35	7
C	70	2.3
D	35	1.2

Fig. 7.21 Local distribution of the lateral tensile stresses in the region of the reversal in the shear flow of a simply supported beam loaded at mid-span.

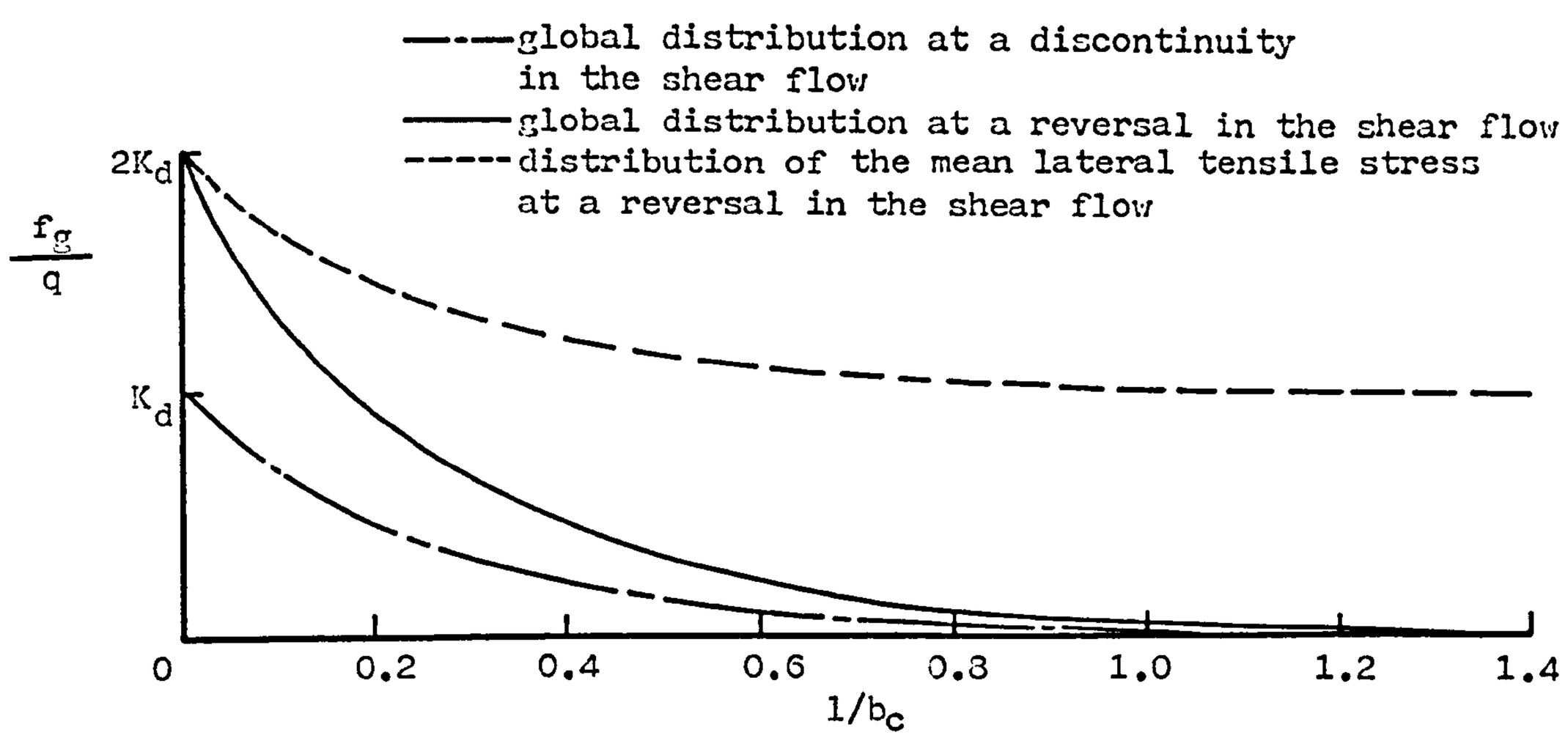

Fig. 7.22 Distribution of the lateral stresses in the region of a change in the uniform shear flow.

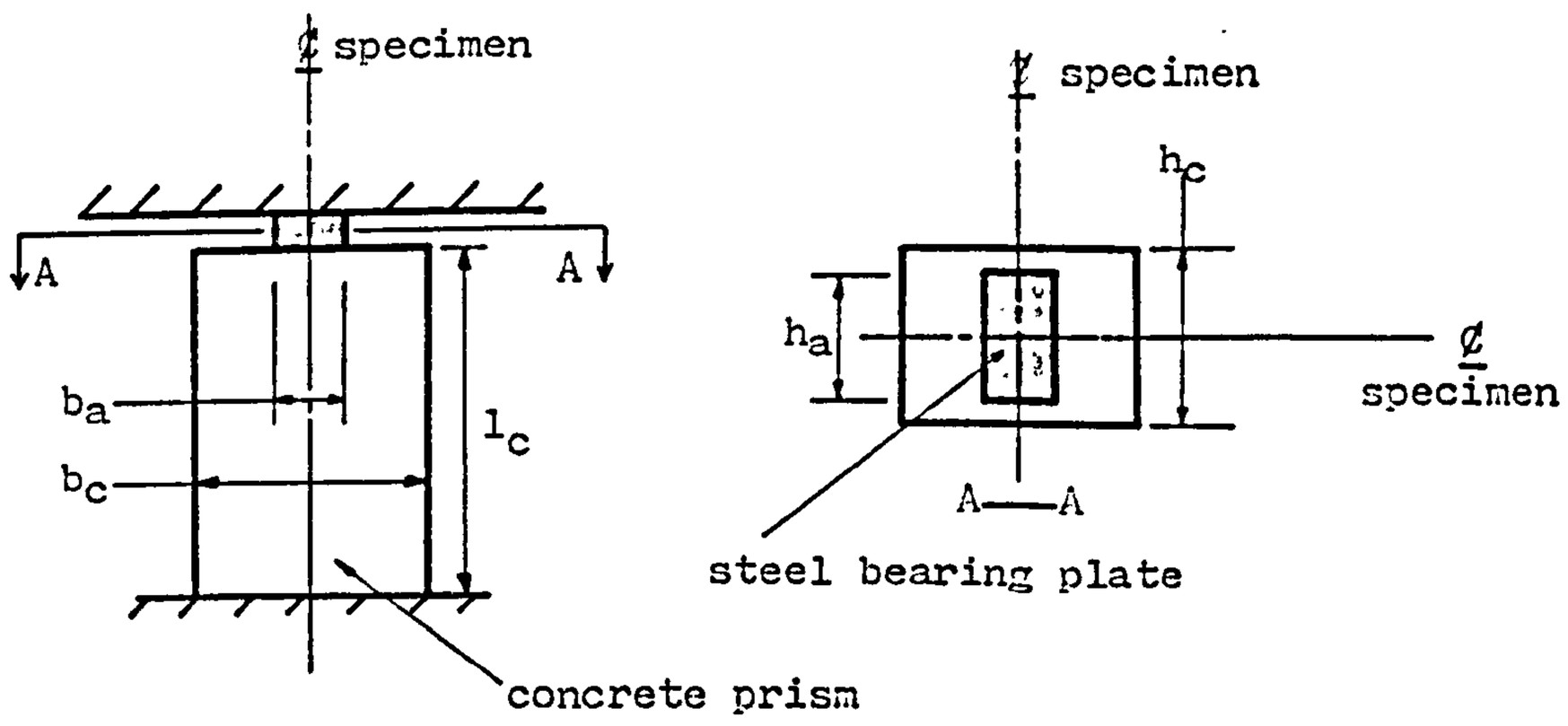

Fig. 7.23 Prism subjected to a concentric patch load.

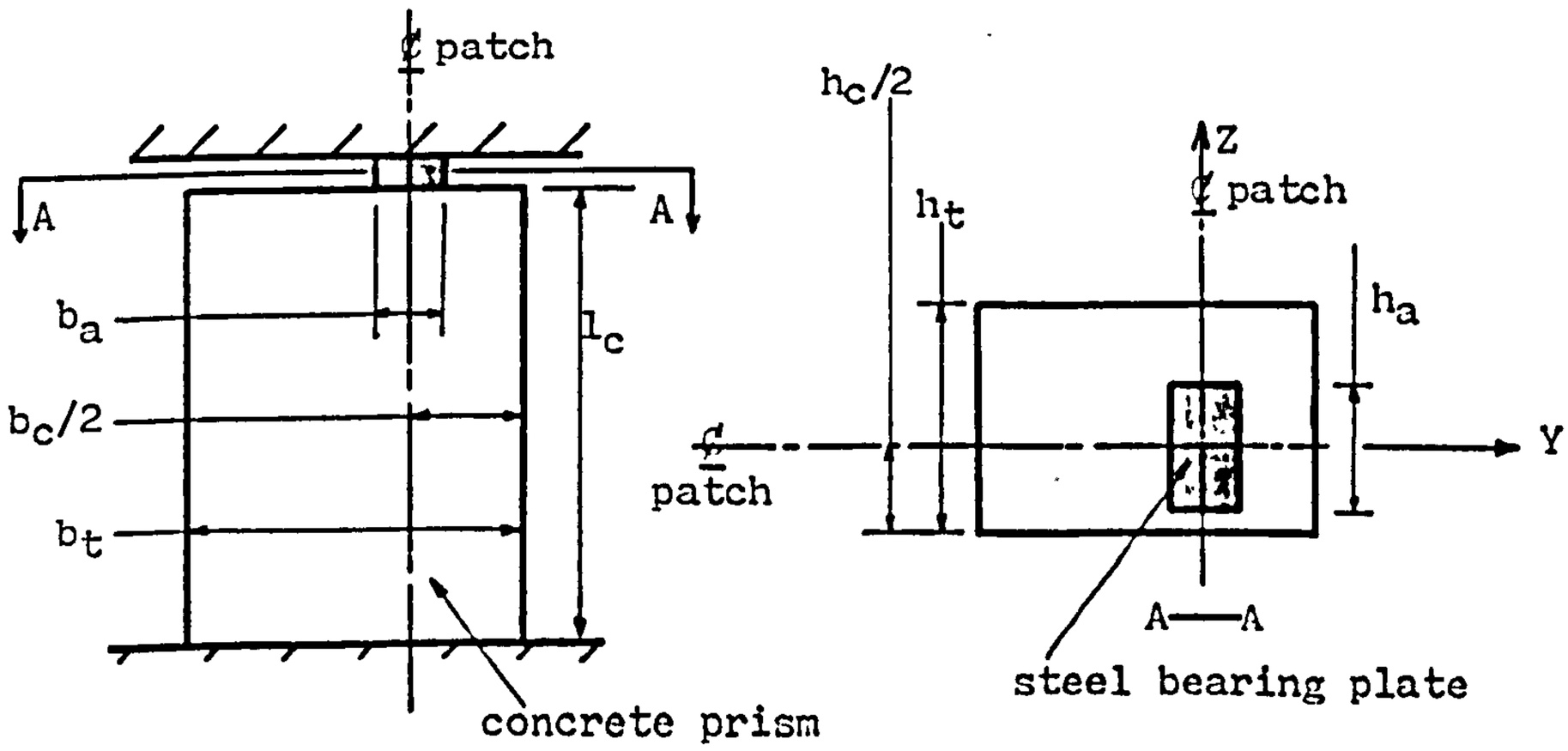

Fig. 7.24 Prism subjected to an eccentric patch load.

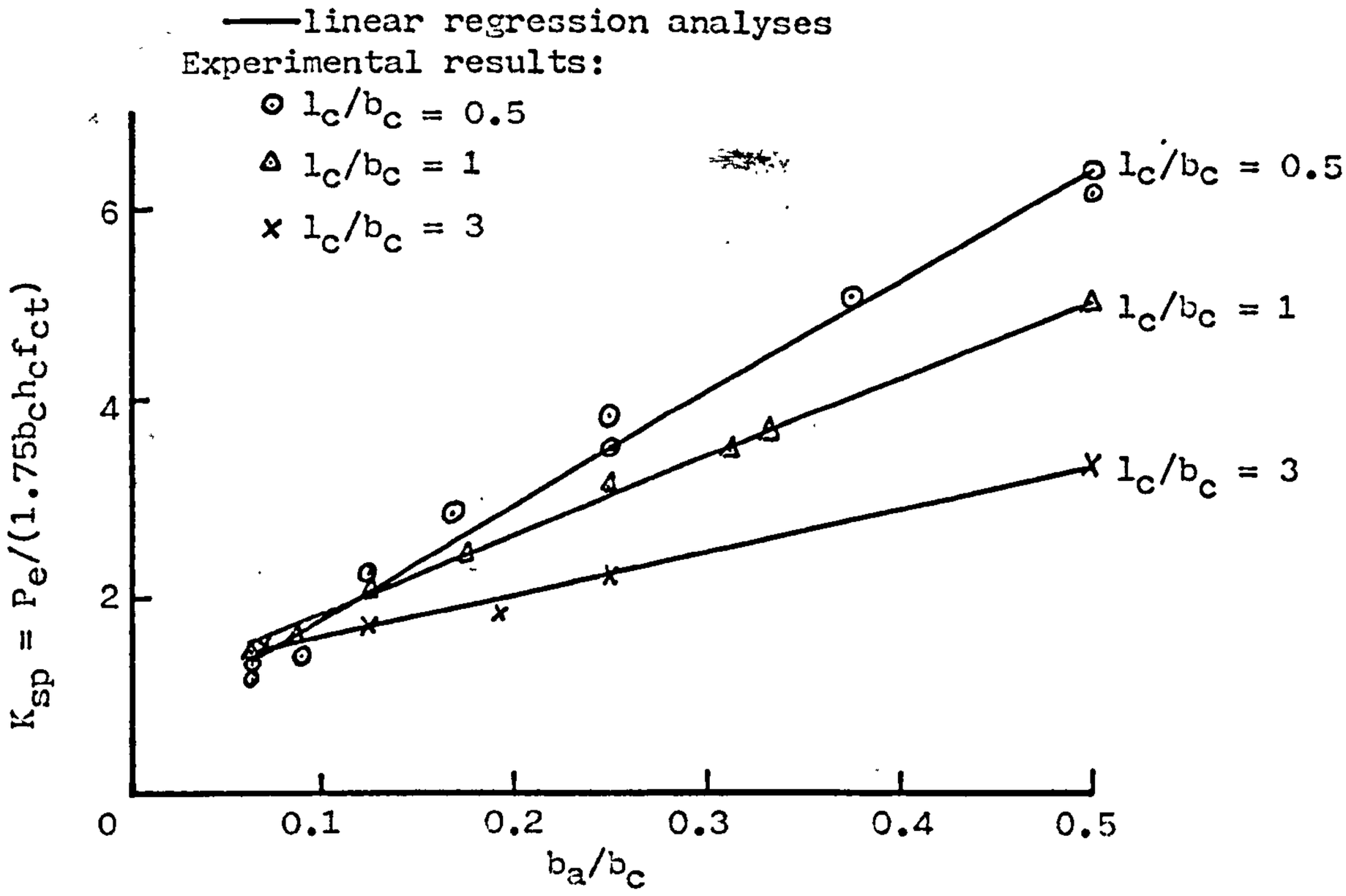

Fig. 7.25 Empirical analysis of the splitting strength of prisms subjected to concentric strip loads.

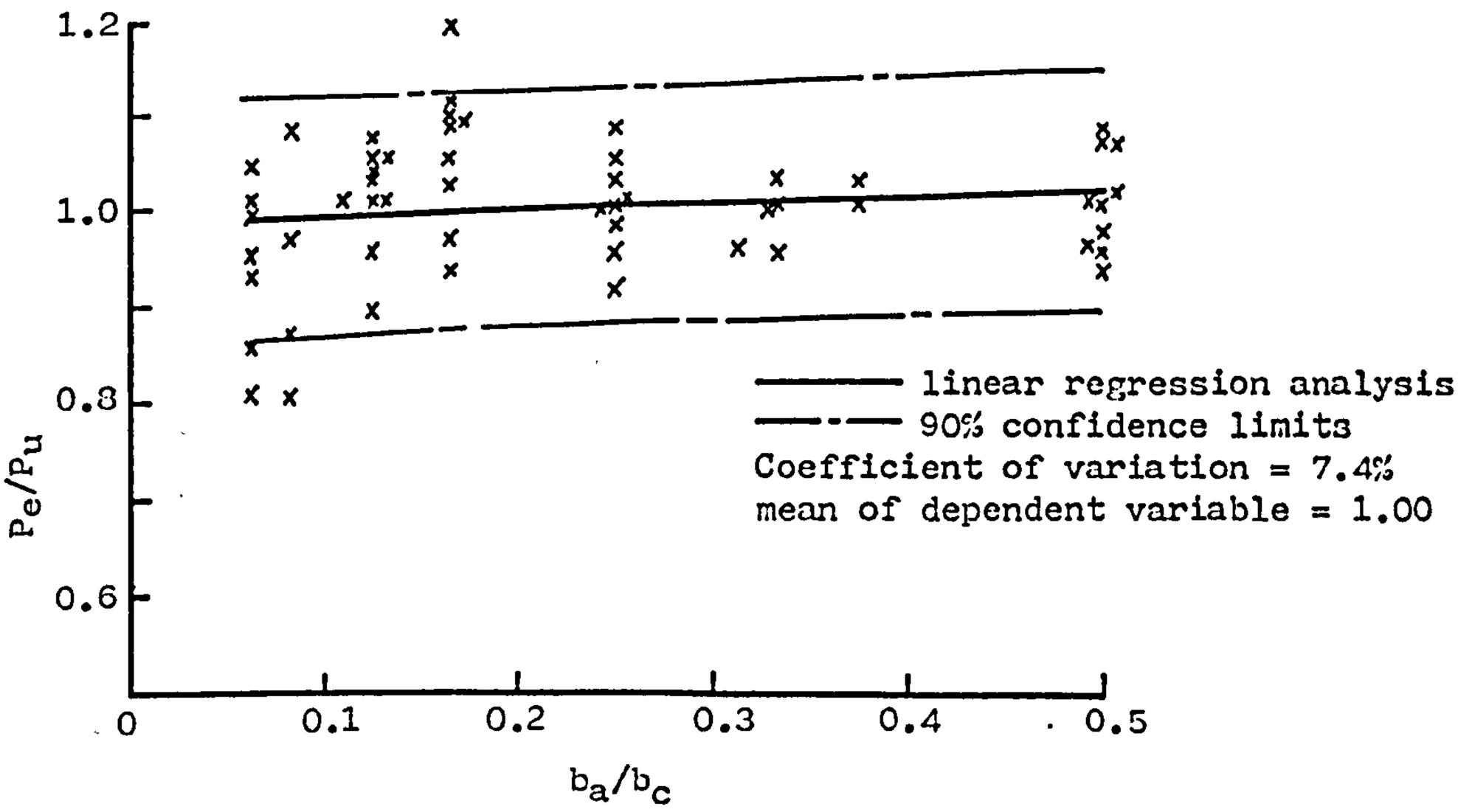

Fig. 7.26 Scatter of the empirical analysis of concentric strip loads.

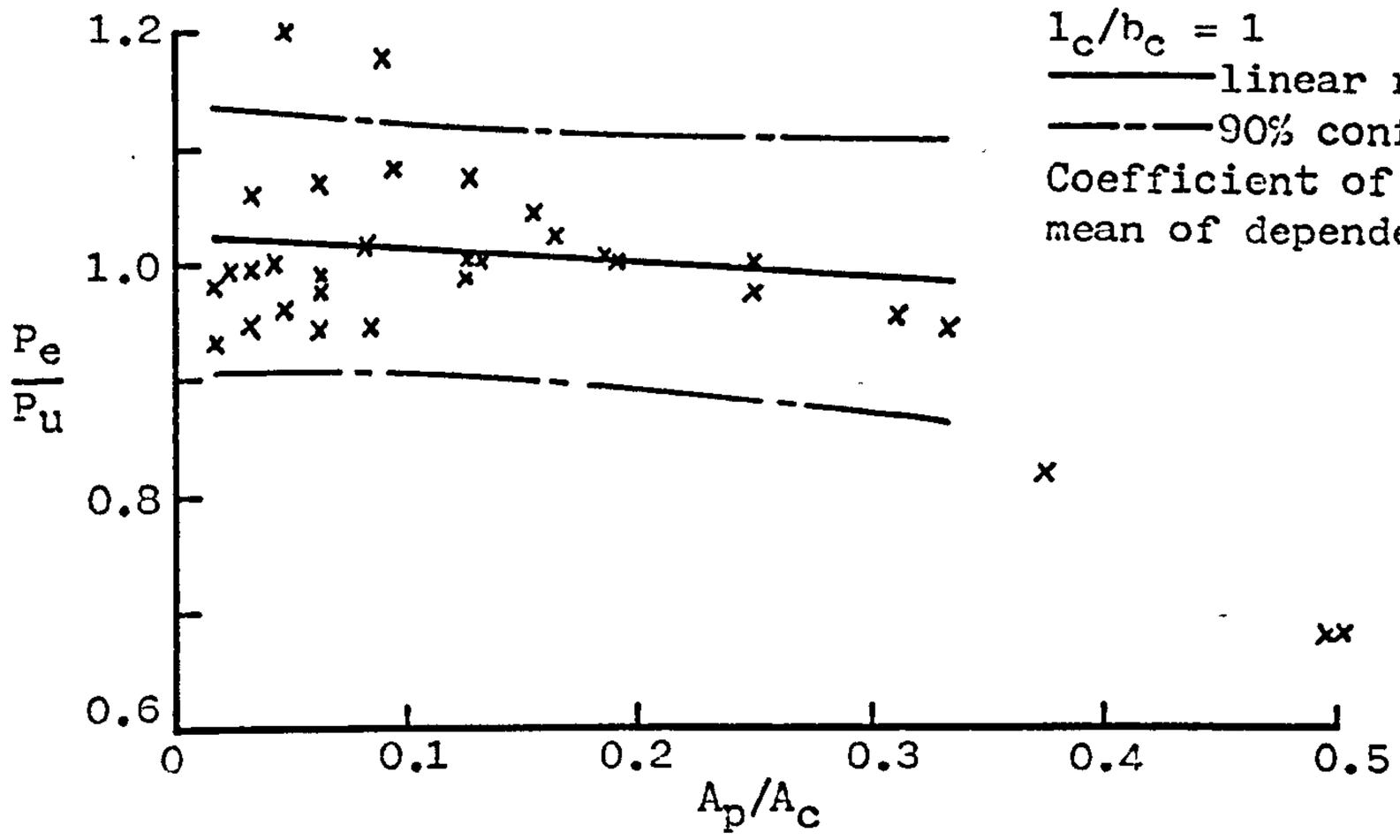

Fig. 7.27 Comparison of Niyogi's experimental results with the design rules for concentric patch loads.

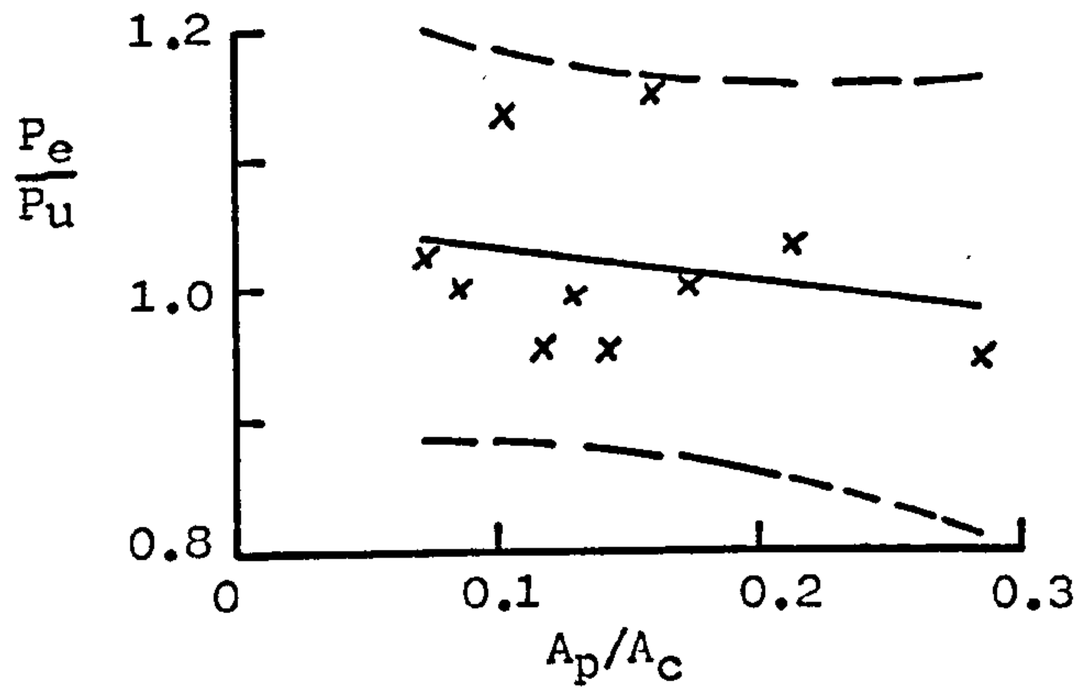

Fig. 7.28 Comparison of Wheen and Rogers' experimental results with the design rules for concentric patch loads.

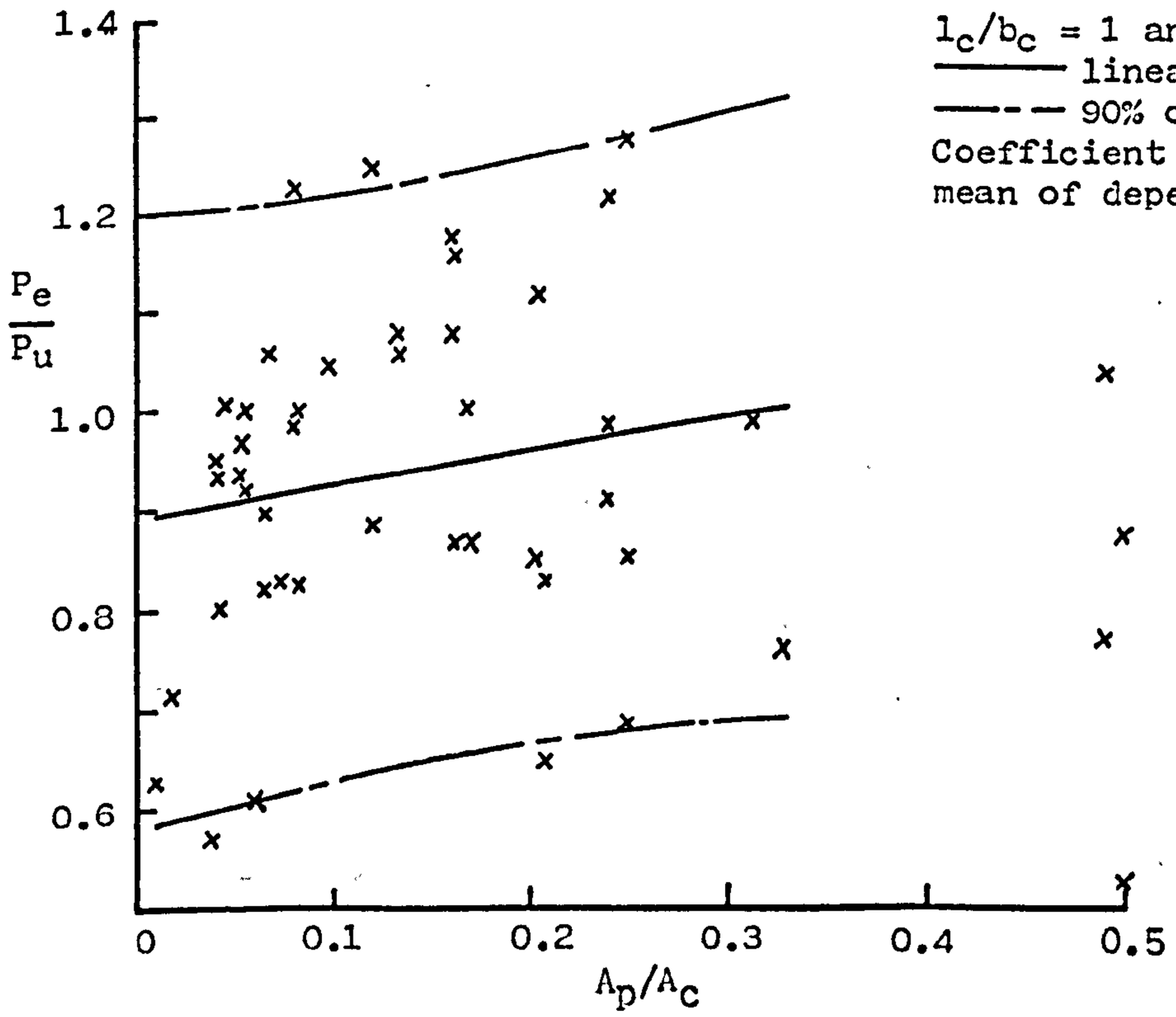

Fig. 7.29 Comparison of Williams' experimental results with the design rules for concentric patch loads.

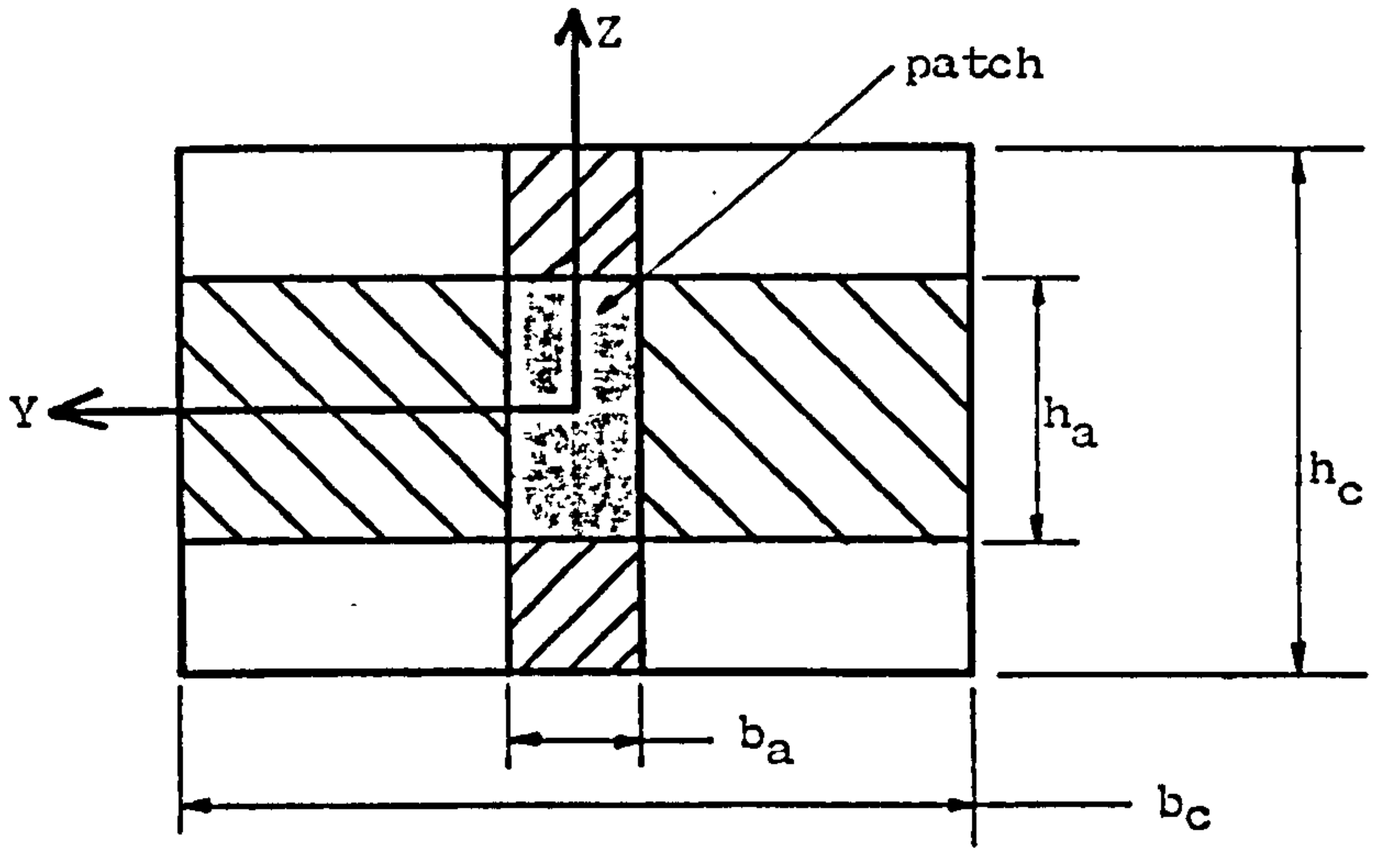

Fig. 7.30 Hypothetical strip loads.

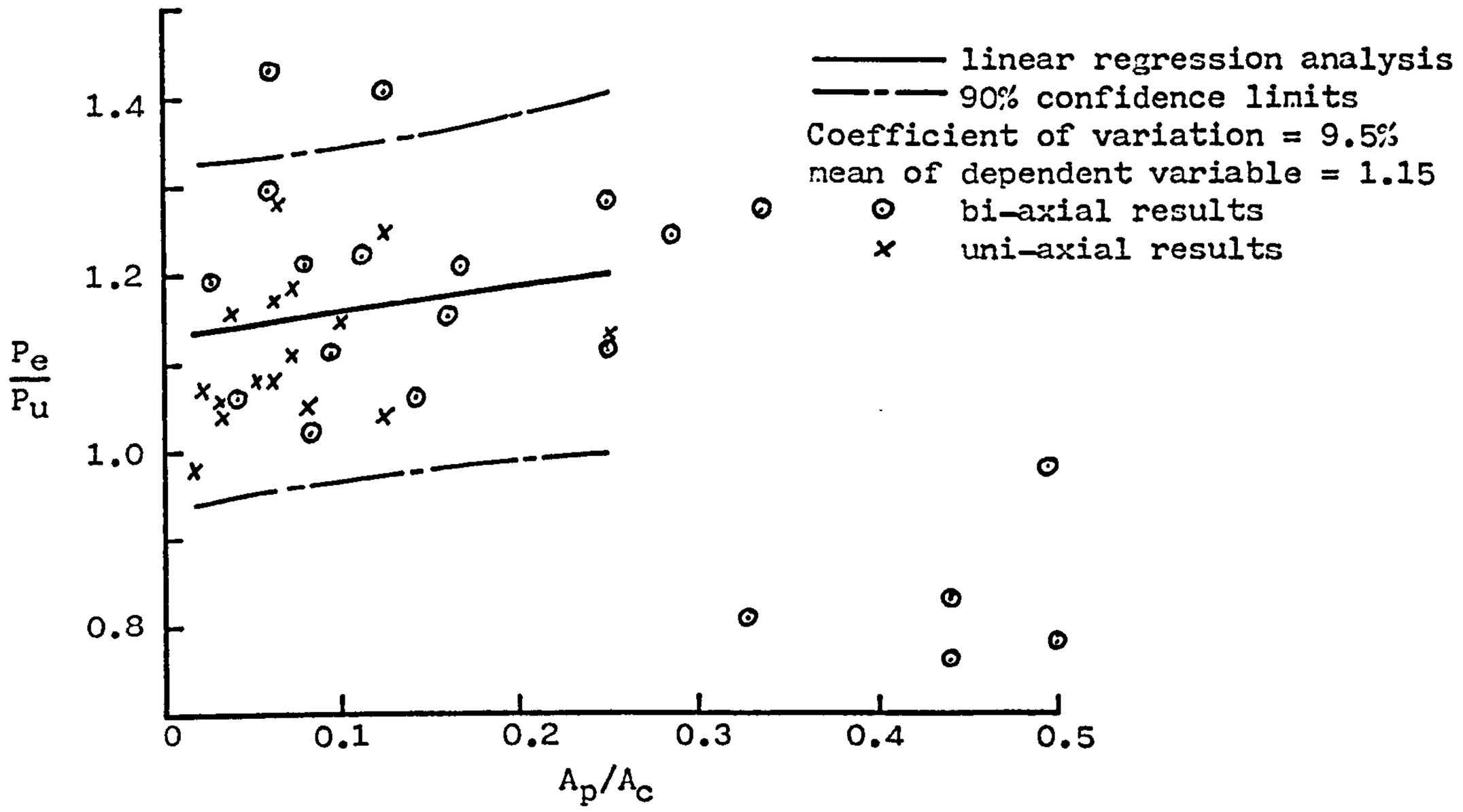

Fig. 7.31 Comparison of Niyogi's experimental results for eccentric patch loads with the design rules for concentric patch loads.

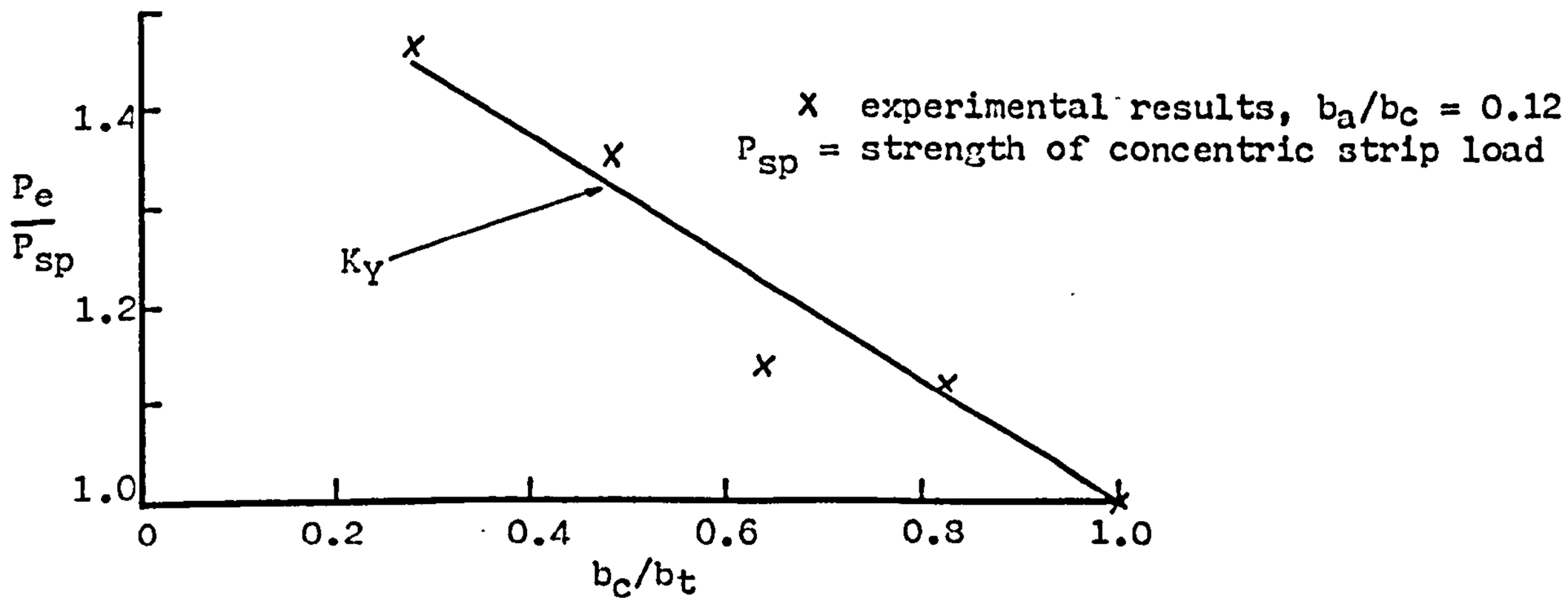

Fig. 7.32 Increase in the splitting strength due to the eccentricity of loading.

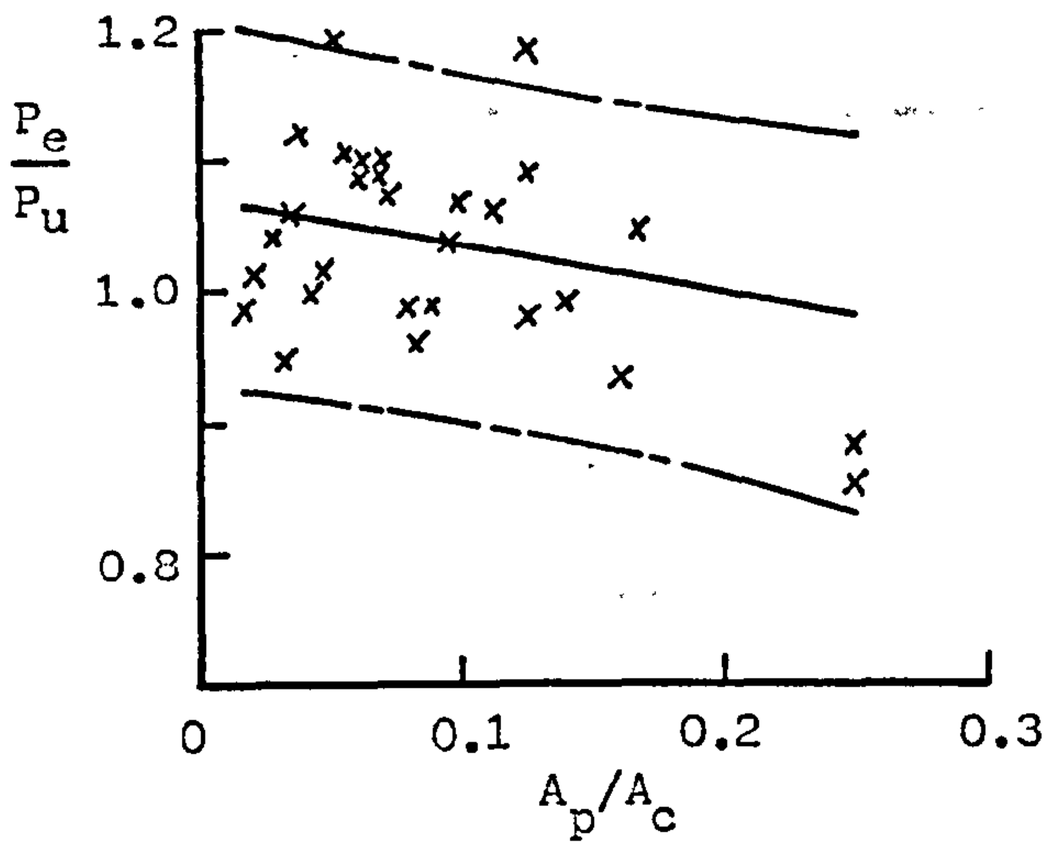

Fig. 7.33 Comparison of Niyogi's experimental results for eccentric patch loads with the design rules for eccentric patch loads.

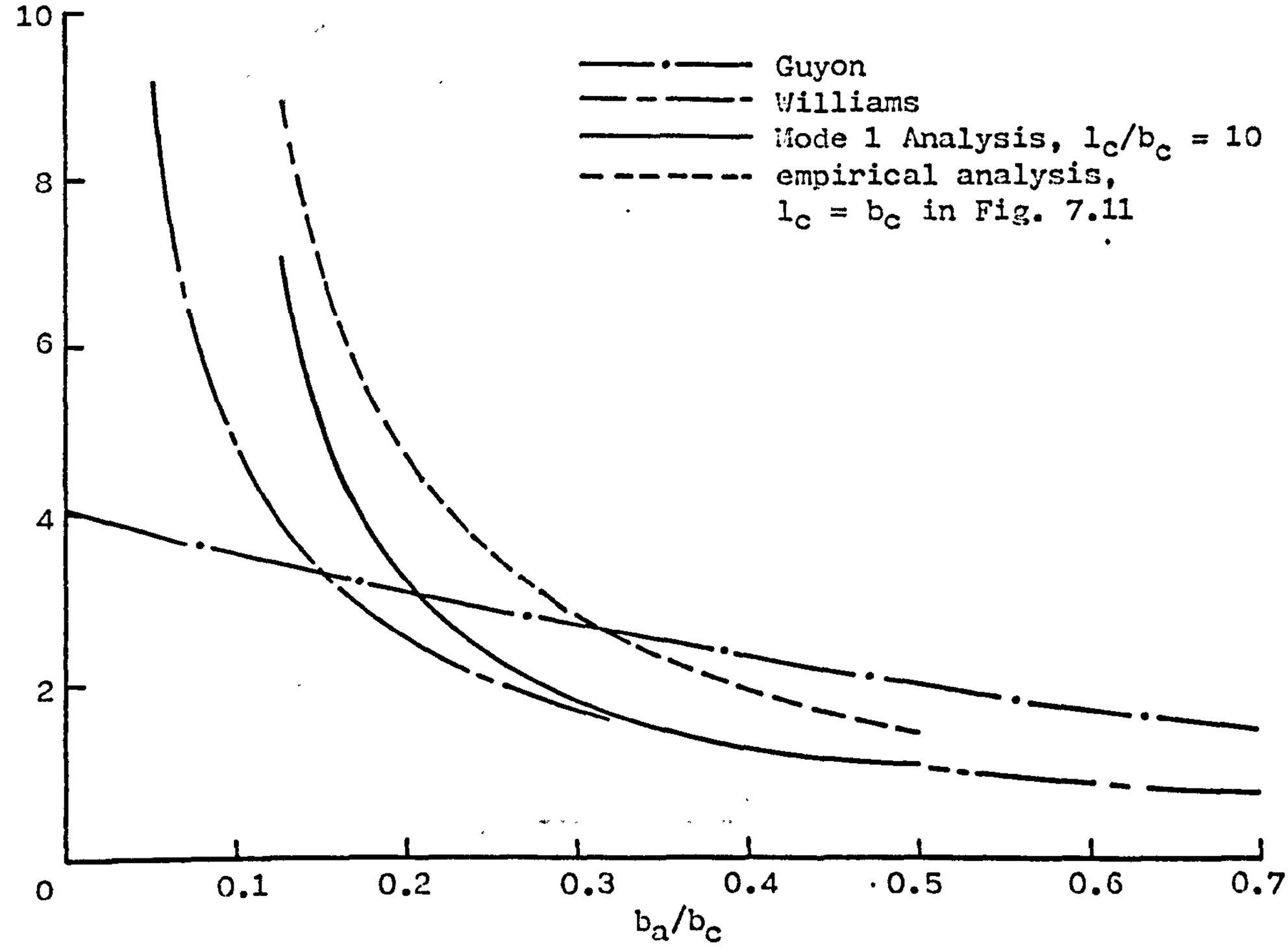

Fig. 7.34 Bearing strength of concentric patch loads.

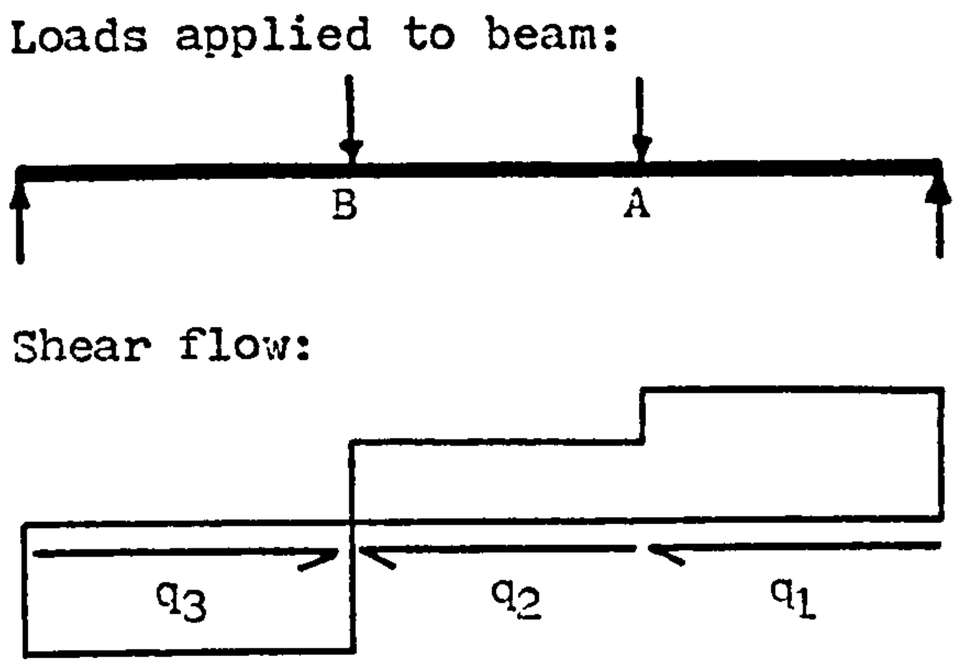

Fig. 7.35 Example of the distribution of the shear flow.

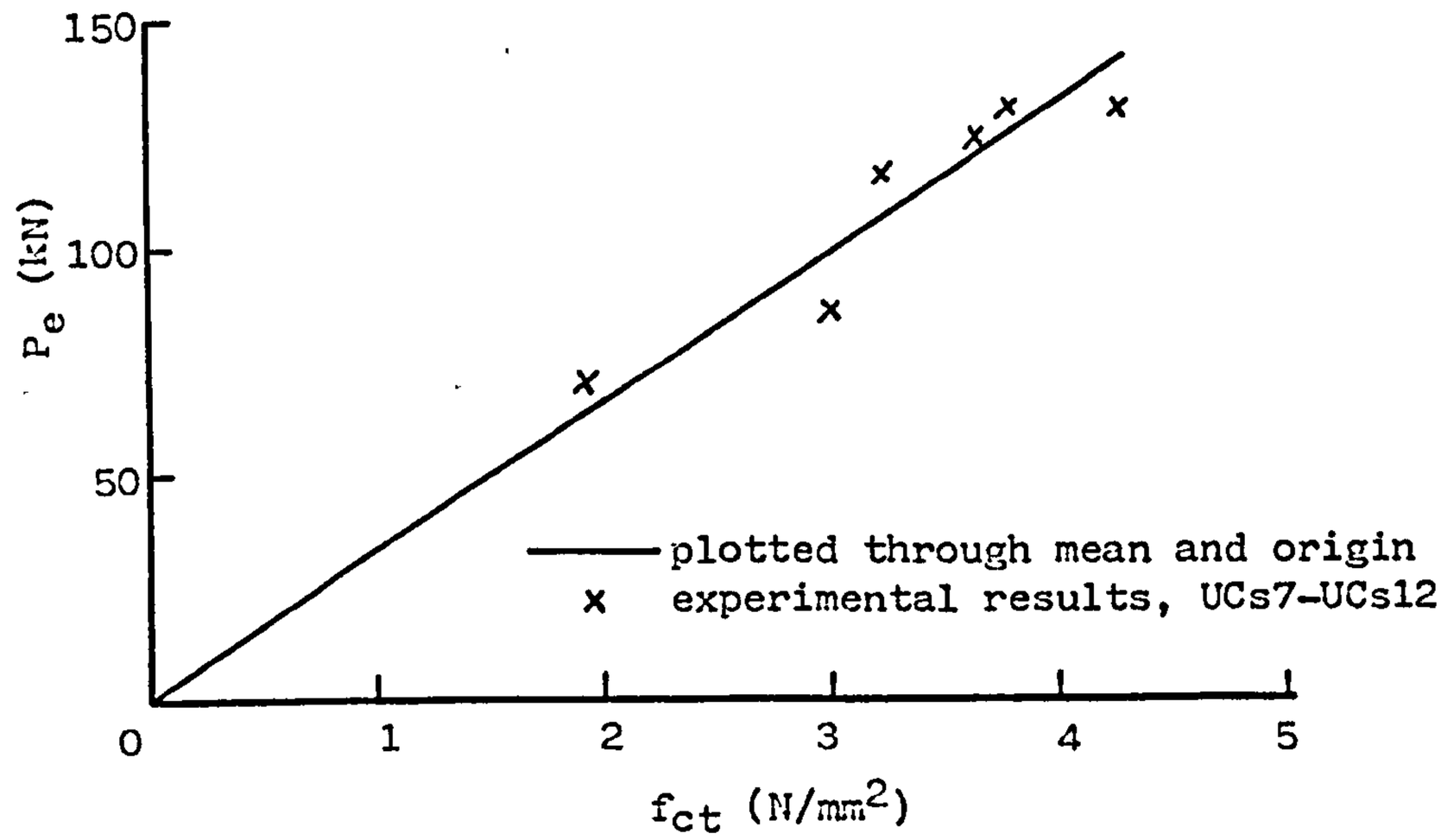

Fig. 7.36 Variation of the splitting strength of push specimens with the tensile strength of the concrete.

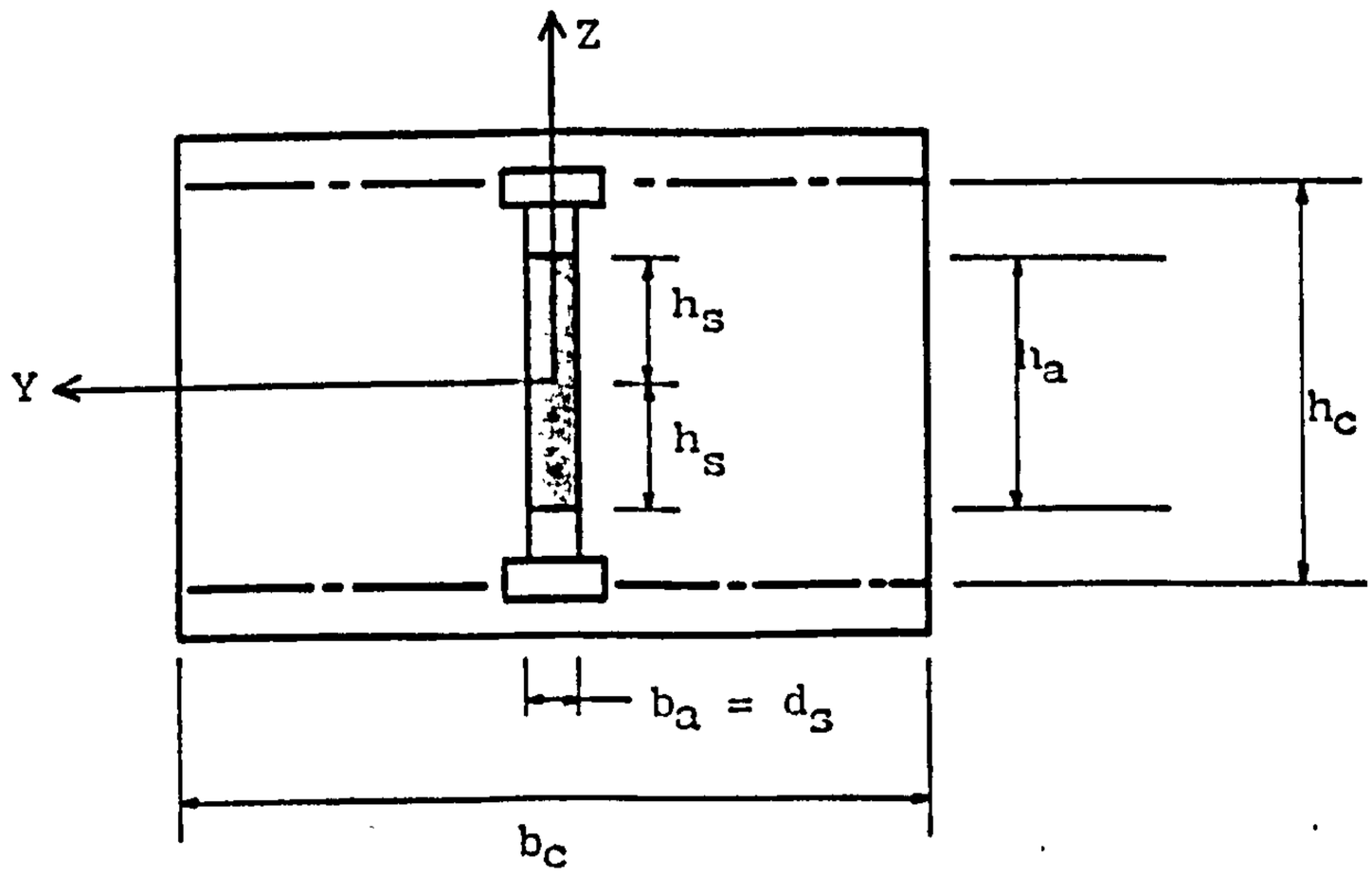

Fig. 7.37 A theoretical analysis of the splitting strength of push tests with single studs.

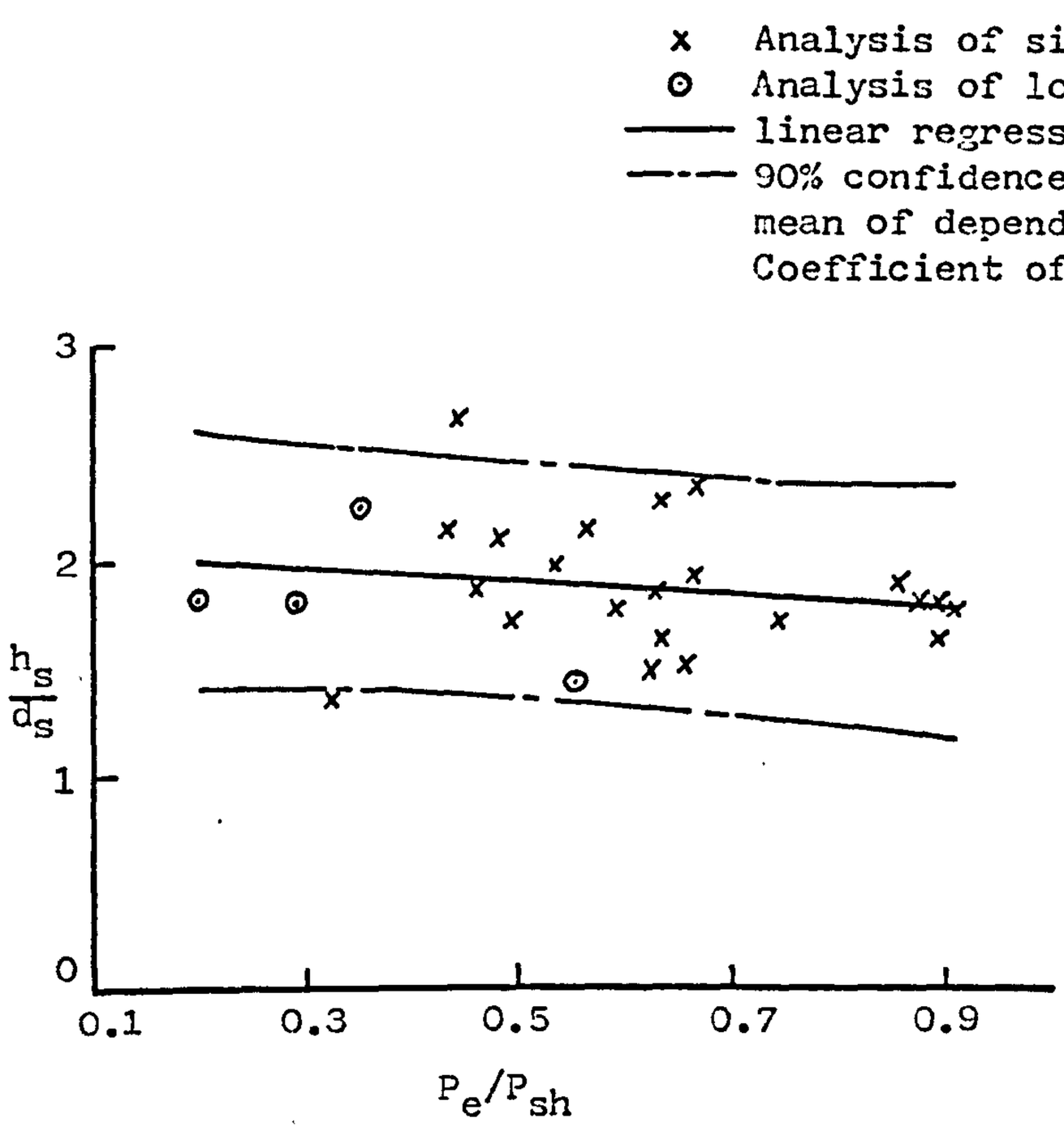

Fig. 7.38 Effective height of a stud.

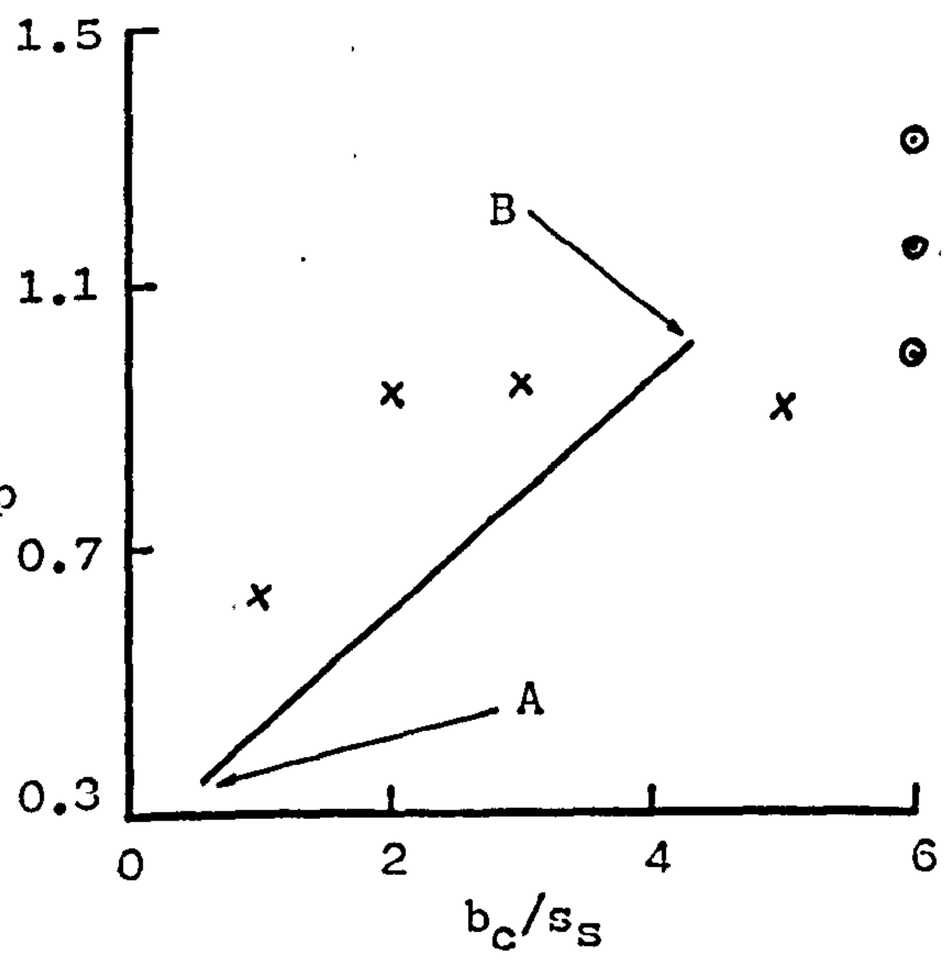

Fig. 7.39 Variation of the splitting strength of push tests in which the studs were longitudinally spaced.

Chapter Eight

THE EFFECT OF LATERAL RESTRAINTS

8.1 INTRODUCTION

A Mode 3 Analysis, Sect. 4.4, was used to determine the variation of the shank failure load of a stud and the splitting strength of a slab when active and passive lateral restraints were imposed on a slab. The theoretical results are compared with experimental results in Sect. 8.3 in order to determine design rules, Sect. 8.4. The finite element model was the same as that described in Sects. 7.2 and 4.4.6.3.

8.2 MODE 3 FINITE ELEMENT ANALYSIS

8.2.1 The progression of the failure of the concrete

The nomenclature is described in Fig. 4.5.

8.2.1.1 Laterally unreinforced specimens

The extent of the failure of the concrete at the maximum load and at the failure load, which is the load at which the theoretical resistance of the concrete slab against the applied load reduced to zero, is shown in Fig. 8.1. The concrete first disintegrated along the shear plane and the load continued to increase until the concrete below the patch started to disintegrate. The experimental failure of the slab, Fig. 5.17, can be considered to be an accumulation of the theoretical two dimensional failures, Figs. 8.1 and 6.21.

8.2.1.2 Laterally reinforced specimens

The transverse reinforcement, Fig. 8.2, was uniformly spaced. The failure of the concrete progressed in the same way as in an unreinforced

slab, Fig. 8.1. The axial stress in the reinforcement remained low until the maximum load was reached when the concrete below the patch started to disintegrate. The load was then transferred directly through the cone of the concrete beneath the patch to the transverse reinforcement and hence the axial load in the reinforcement increased very rapidly. The strength of laterally reinforced specimens may therefore be expected to reduce gradually as the reinforcement yields; the rate of reduction would depend on the strength of the reinforcement.

8.2.2 Variation in the transverse reinforcement

The effect of the transverse reinforcement on the bearing strength at the maximum load is shown in Fig. 8.3. The bearing strength for the slab without transverse reinforcement, f_b', which has been shown to be dependent upon the width of the applied load in Fig. 4.16, was increased in proportion to the increase in the transformed area of the prism, A_m/A_c. It would appear that the maximum strength is dependent upon the total lateral stiffness of the reinforced prism; the difference in the theoretical results, Λ in Fig. 8.3, was probably because the reinforcement was placed at discrete positions in the finite element analysis.

The axial strain in the reinforcement at the maximum load was approximately twice the tensile strain of failure of the concrete, Sect. 4.4.5.2. Therefore, at the maximum load the reinforcement requires only a relatively short anchorage length, however, it may be required to increase the anchorage length as the reduction in the strength after failure, Sect. 8.2.1.2, is dependent upon the strength of the transverse reinforcement.

8.2.3 Variation in laterally applied forces

The theoretical effect of applying an external uniform lateral

tensile force to a laterally reinforced and unreinforced prism is shown in Fig. 8.4. The lateral force was maintained at a constant proportion of the applied longitudinal load during the finite element analysis. The strengths were plotted as a proportion of the theoretical strength of the prism without external lateral forces, P'. The lateral force was plotted in terms of the stress which it applied to the concrete, f_1, which was determined from the transformed section, and as a proportion of the assumed tensile strength of the concrete, f_t.

The reduction in the strength of the prism without external lateral forces is initially directly proportional to the external lateral stress which is applied to the concrete, line A-A, and reaches a lower bound, line B-B, which is independent of the external lateral force. The bearing stress at the lower bound was equal to the theoretical strength of a laterally unrestrained element of concrete, f_{ce}, and therefore the proportional reduction in the strength at the lower bound is given by f_{ce}/f_b from Fig. 4.16 and is therefore also dependent upon the dimensions of the applied load. When the load is dispersed in three dimensions, the lower bound, which can be derived from Fig. 7.34, can be as little as one seventh of P'.

8.3 THE ANALYSIS OF THE PUSH TESTS

8.3.1 Variation in the strength of the transverse reinforcement

The transverse reinforcement in the push tests, Table 5.10, was welded to angles, Sect. 5.5.1, so that the full tensile strength could be achieved if required. All the specimens split at the maximum load and failed when the shank of the stud broke. The shear strengths, Fig. 8.5, were plotted in terms of the theoretical splitting strength, Sect. 7.6.1.1, and the yield strengths of the transverse reinforcement within the splitting zones were plotted as a proportion of the total lateral tensile force

which is equal to $P_e K_d$, Sect. 7.5.1.1.

The maximum strengths did not increase beyond the splitting strengths even when the yield strength of the transverse reinforcement was more than four times the induced lateral tensile force. It would therefore appear that placing transverse reinforcement across the splitting zone in order to maintain equilibrium after splitting has occurred, as postulated by Leonhardt[66], cannot increase the strength above that of the splitting strength because the concrete crushes as soon as splitting occurs when the strain in the reinforcement is much smaller than its yield strain.

8.3.2 Variation in the stiffness of the transverse reinforcement

The variation between the experimental failure loads and the stiffness of the transverse reinforcement is shown in Fig. 8.6. The experimental failure loads were plotted as a proportion of the theoretical splitting loads, Sect. 7.6.1.1; the results from Table 5.11, in which the shank of the stud failed at the maximum load, are therefore a lower bound to the increase in the splitting strength of the slab. In determining the proportion of the transverse reinforcement it was assumed that the reinforcement acted within the splitting zone of the slab, the area within a distance of $1.87d_s$ from the soffit and $1.75b_c$ from the stud, even when the reinforcement was placed outside this zone as in Specimens RSs5 and RSs6. When there was only a single group of reinforcement, Table 5.10, it was assumed that it acted over a length $2l_r$, Fig. 5.31, which therefore gives an overestimate of the amount of transverse reinforcement. The theoretical variation, Fig. 8.6, was obtained by assuming that the splitting strength increased in proportion to the increase in the area of the transformed section, Sect. 8.2.2.

The assumption that the reinforcement acted within the splitting zone appears to give a conservative estimate of the increase in the

strength, Fig. 8.6; further experimental work is required to determine the effective depth over which the reinforcement acts and its variation with the cover to the transverse reinforcement.

8.3.3 Lateral compressive forces

The application of an external lateral compressive force to the slab, Fig. 5.30, increased the load at which the concrete failed by 12% and increased the load at which the shank failed by 19%, Table 5.9. The results, which can only be considered as qualitative as the lateral force was not measured, show that the strength of the stud and the strength of the slab are both affected by lateral forces.

8.4 DESIGN RULES

8.4.1 The strength of the stud

It was shown in Sect. 6.4.2.1 that the strength of the shank is dependent upon the compressive strength of the concrete. Since lateral tensile forces reduce the compressive strength, Sect. 8.2.3, and since the compressive forces are very large, Fig. 6.15, a conservative design would be to assume that the shank failure load, P_u, reduced at the same rate as the compressive strength, line A-A in Fig. 8.4.

$$P_u = P_{sh}(1-(f_g/f_{ct})) \qquad (8.1)$$

where P_{sh} is derived from Equs. 6.1 or 6.2 and f_g is the global lateral tensile stress between studs. It will be shown in Sect. 10.3 that the lower bound to the strength is dependent upon the slip. It may be more appropriate to assume that the compressive strength of the concrete is reduced by the factor $(1-f_l/f_t)$ and hence to reduce the factor K_f in Fig. 6.20. However, this has to be validated experimentally.

The converse of the above is applicable to lateral compressive

forces, however, it would be a conservative design to ignore this increase.

8.4.2 The strength of the slab

The change in the splitting strength of the slab is directly proportional to the lateral stress in the splitting zone which is induced by the external lateral forces. Hence the strength, P_u, is given by

$$P_u = P_{sp}(1-(f_l/f_{ct}))(A_m/A_{sp}) \qquad (8.2)$$

where P_{sp} is determined from Equs. 7.4 or 7.8; A_{sp} is the area of the splitting zone and A_m is the transformed area of the splitting zone. The above equation applies to lateral tensile and compressive forces.

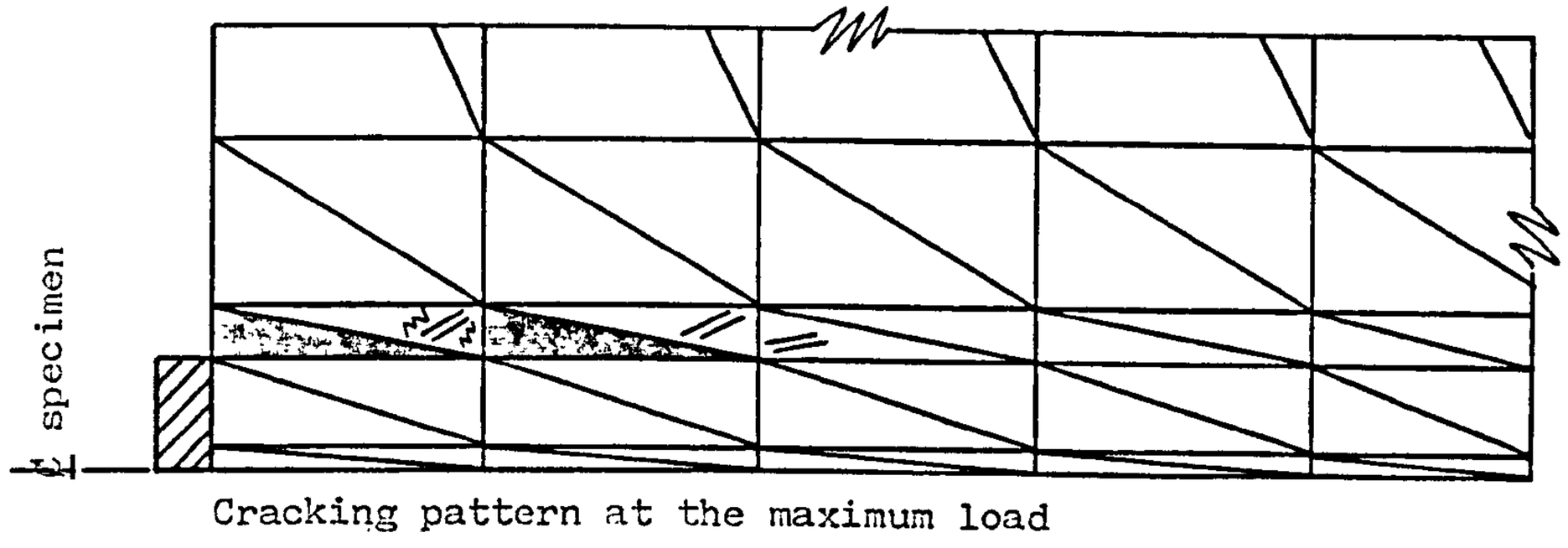

Cracking pattern at the maximum load

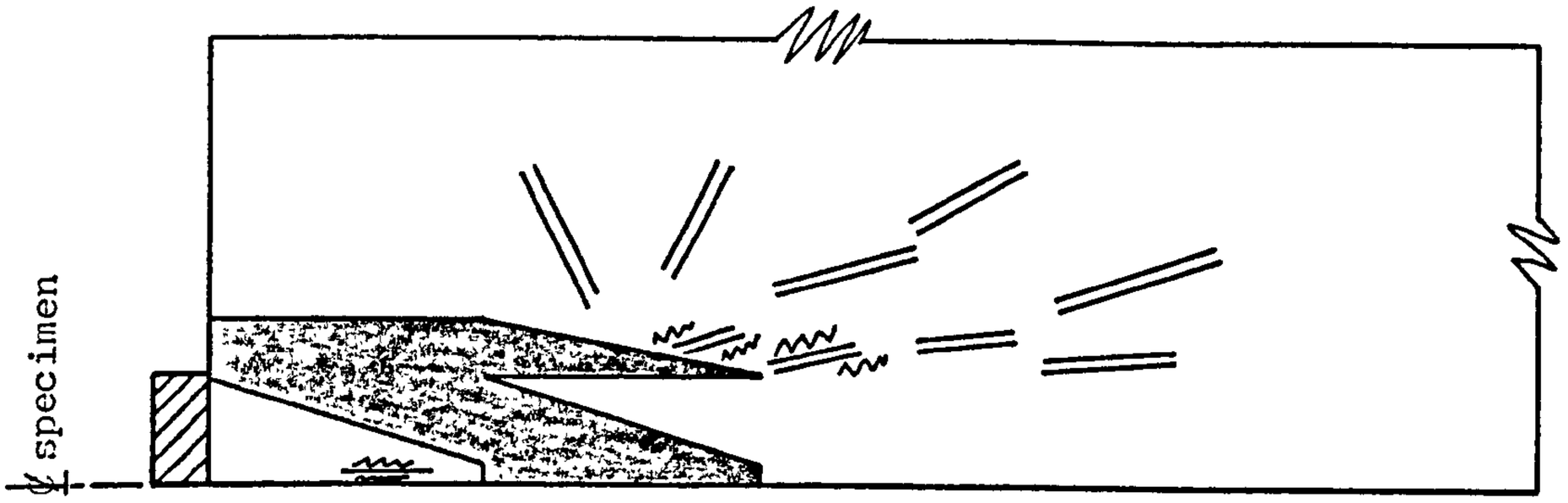

Cracking pattern at failure

$b_a/b_c = 0.017$

$l_c/b_c = 2$

Fig. 8.1 Propagation of the concrete failure in an unreinforced prism subjected to a strip load.

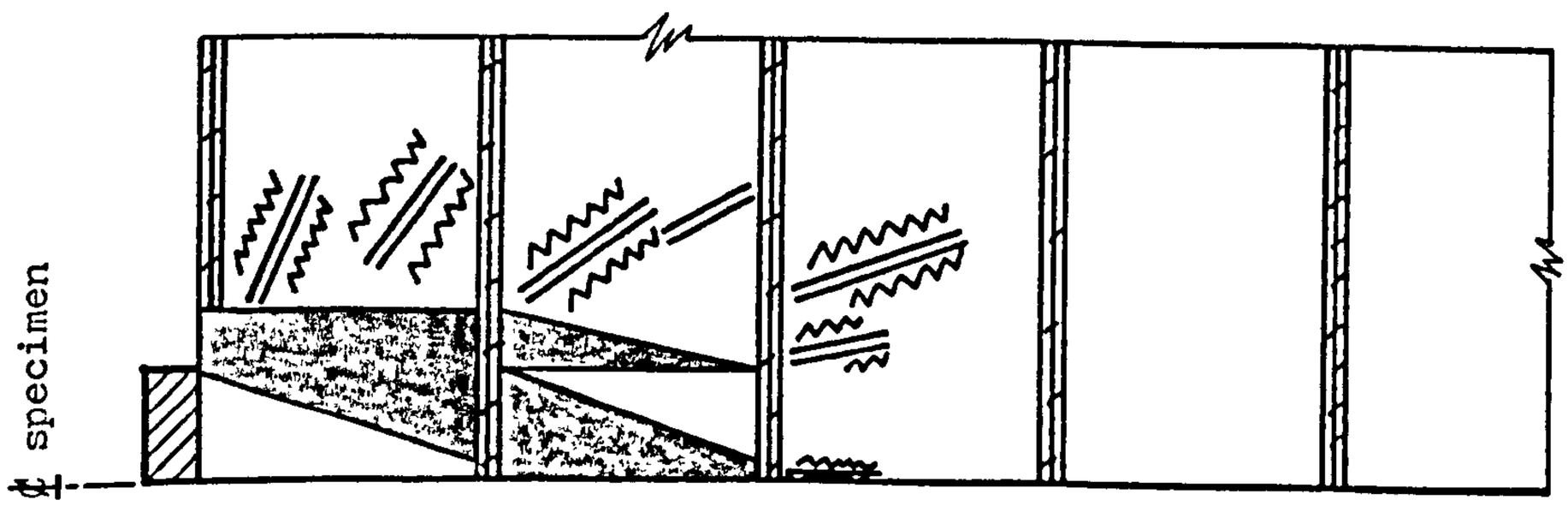

transverse reinforcement, $E_s = 200 kN/mm^2$, $v_s = 0.3$

$f_{rt} = 6$, $l_c/b = 2$, $b_a/b_c = 0.017$

Fig. 8.2 Distribution of the concrete failure in a reinforced prism subjected to a strip load.

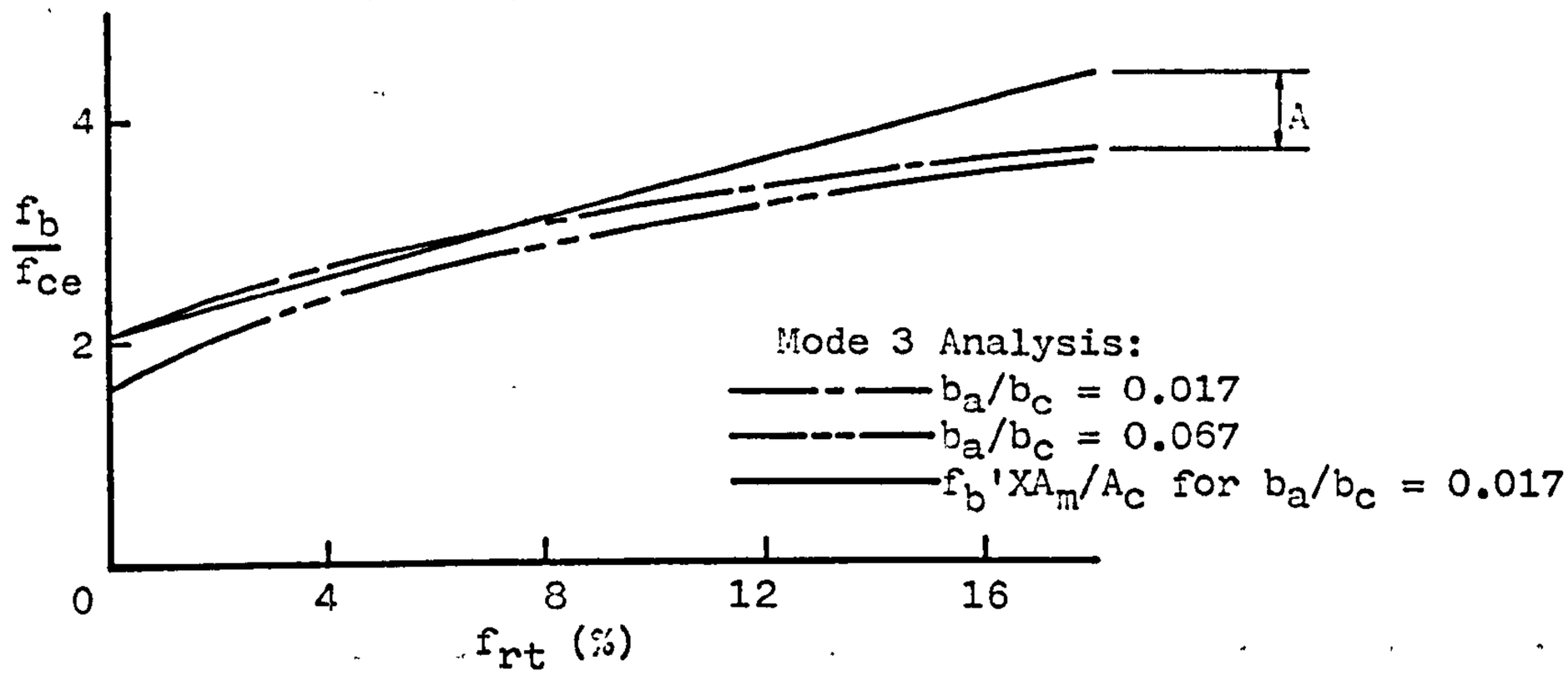

Fig. 8.3 Theoretical variation of the bearing strength with the transverse reinforcement.

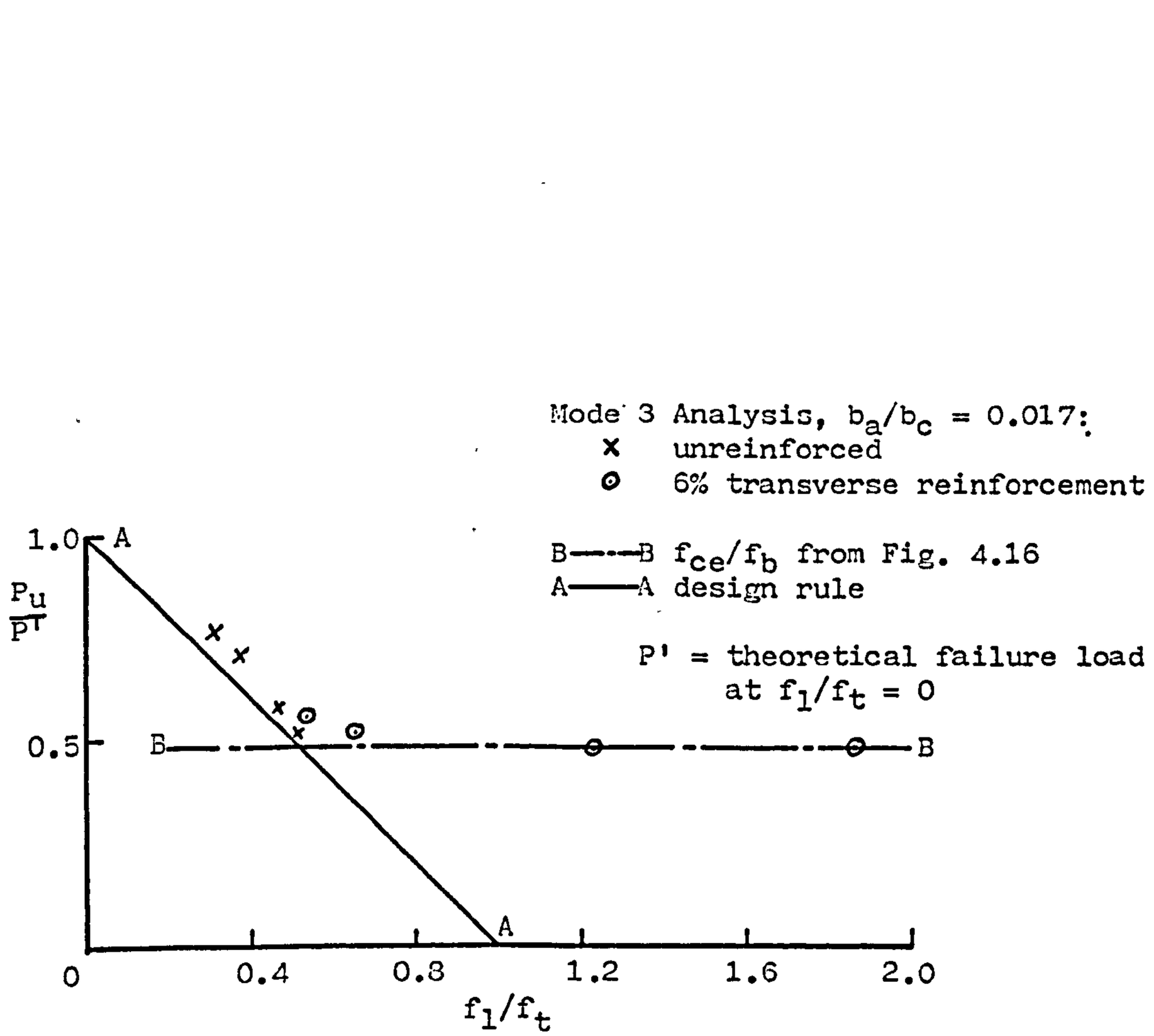

Fig. 8.4 Theoretical variation of the strength of the slab with laterally applied forces.

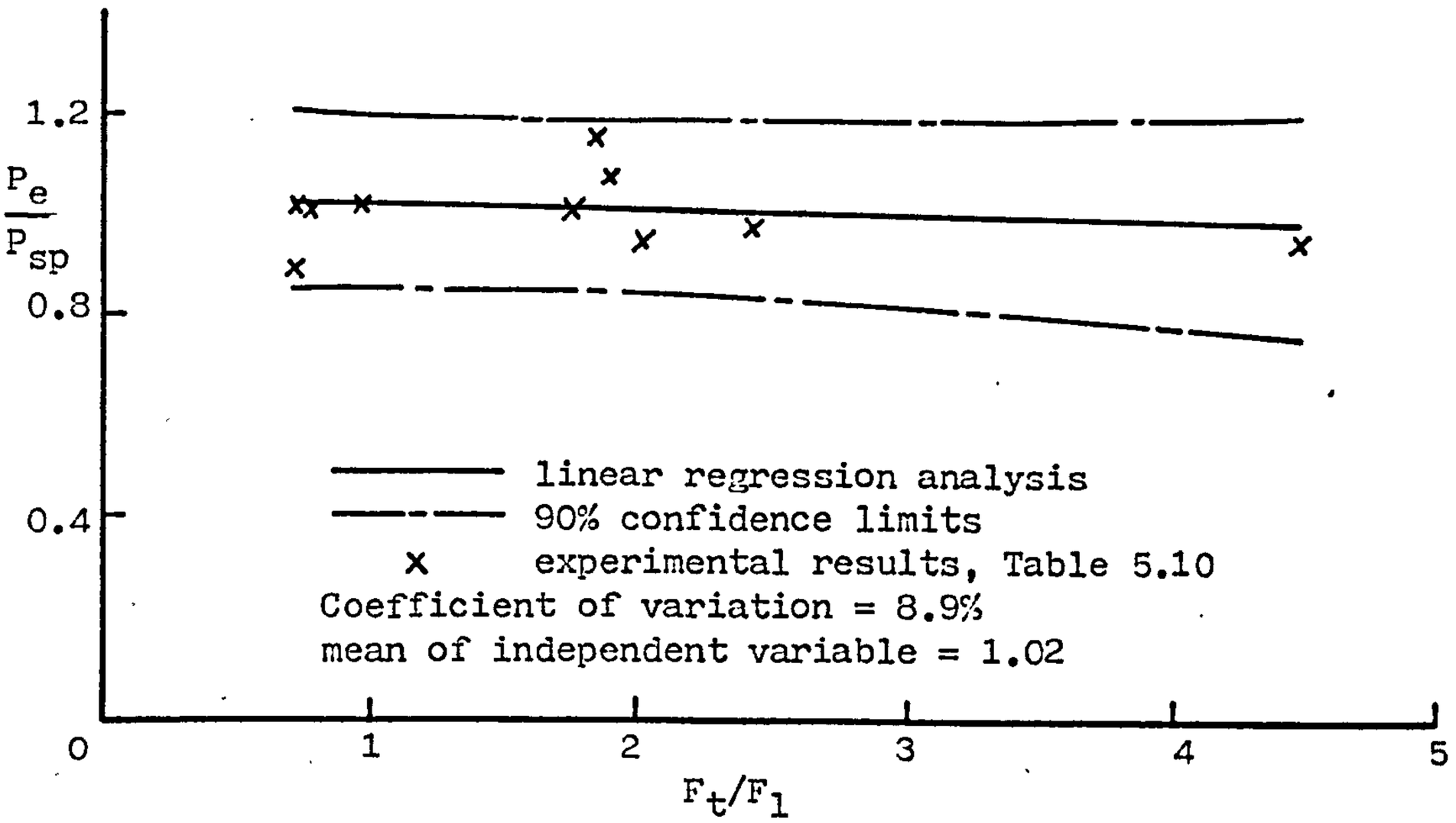

Fig. 8.5 Variation of the splitting strength of push tests with the strength of the transverse reinforcement.

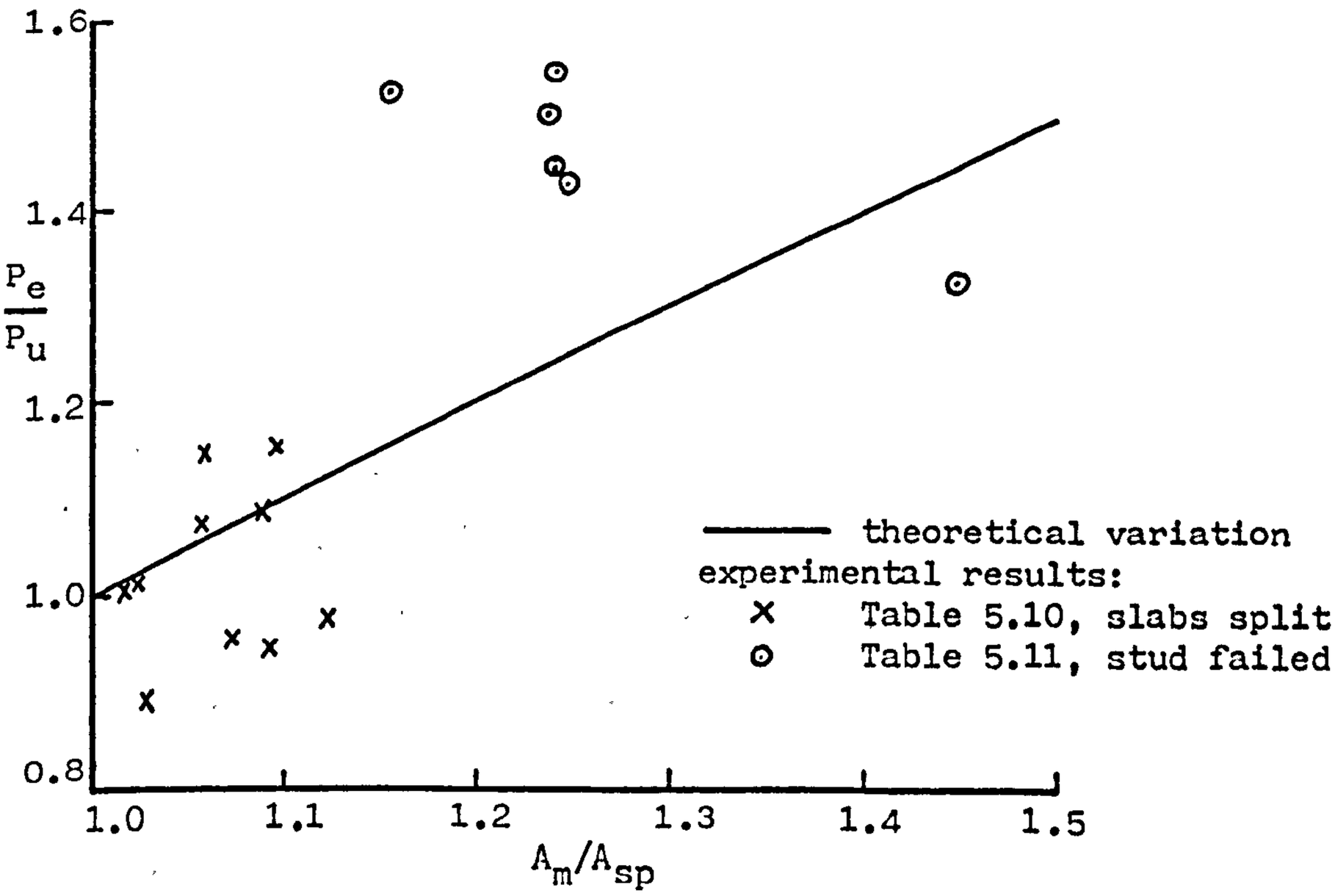

Fig. 8.6 Variation of the strength of push tests with the stiffness of the transverse reinforcement.

Chapter Nine

REINFORCEMENT LOOPED AROUND A SINGLE STUD

9.1 INTRODUCTION

When studs are placed close to the edge of a slab the transverse reinforcement can be fully anchored by looping the reinforcement around the studs, Fig. 3.2.

The design rules[7] for the transverse reinforcement, which were derived by Johnson[31] from the experimental work of Mattock[29,30] and results of tests on composite beams, are only applicable to shear planes in which the amount of transverse reinforcement is relatively small. The push tests have therefore been compared with Mattock's experimental work, Sect. 9.2, in order to determine whether the design rules[7] are applicable when the reinforcement is looped around the stud. A Mode 3 Analysis was used to determine the variation in the strength of the slab and the stud, Sect. 9.3, when the amount and position of the transverse reinforcement was altered; the results were used in Sect. 9.4 to determine design rules.

9.2 COMPARISON WITH MATTOCK'S EXPERIMENTAL WORK

9.2.1 Mattock's experimental work

The specimen, Fig. 9.1, was of a uniform depth, h_c, and the length of the shear plane was the same as the width of the specimen, b_c. Mattock tested specimens in which the shear plane was either initially cracked or uncracked. The results are given in terms of the mean shear stress across the shear plane at the maximum load, $v_{cu} = P_c/b_c h_c$, and the mean yield strength of the transverse reinforcement which crossed the shear plane, $pf_y = F_{sh}/b_c h_c$. The mean stresses in the shear plane are shown

in Fig. 9.7; pf_y is the compressive force on the concrete which is exerted by the reinforcement.

9.2.1.1 Empirical analyses

The results of Mattock's tests in which the shear plane was initially uncracked, Fig. 9.3, were used to construct the failure envelope, Fig. 9.2, from which was derived the line A-A in Fig. 9.3. When $pf_y < 5$ N/mm^2 failure occurred in planes subjected to shear and tension, quadrant A in Fig. 9.2, and when $pf_y > 5$ N/mm^2 failure occurred in planes subjected to shear and compression, quadrant B.

The design rules in the Bridge Code[7] were developed from the strengths of Mattock's specimens in which the shear plane was initially cracked, line E-E in Fig. 9.3. The derivation of these design rules has been discussed in Sect. 2.3.

9.2.1.2 Theoretical analyses

If it is assumed that the lateral force that is exerted by the transverse reinforcement on the shear plane, Fig. 9.7, can be ignored prior to cracking, then the angle at which the specimen first cracks, a_b in Fig. 9.9, can be determined from the construction of the Mohr's circle in Fig. 9.4. It was noted by Mattock[29] that a series of diagonal cracks formed struts of concrete across the shear plane. The distribution of the stresses within these struts is shown in Fig. 9.9. It was assumed that the shear force could be transferred across the crack by the granular interlock and that the stress normal to the crack was either zero or compressive; the latter case has not been considered any further as the problem would then revert to that of an uncracked specimen. The strength of the transverse reinforcement that is required to maintain equilibrium when a specimen has cracked, Fig. 9.9, can therefore be determined from

the construction of the Mohr's circle, Circle 1 in Fig. 9.5, from which

$$pf_y = 0.85v_{cu} \qquad (9.1)$$

If the crack occurred at 45^o, Circle 2, then it would be required that $pf_y = v_{cu}$. The theoretical results give in general a lower bound to the experimental results, Fig. 9.3.

An alternative method of analysis would be to assume that failure occurred when the tensile strength of the concrete was reached. The strength of the transverse reinforcement can therefore be determined from the construction of the Mohr's circle in Fig. 9.6.

$$pf_y = v_{cu}^2/(v_{cu}+f_t)-f_t \qquad (9.2)$$

The result, line D-D in Fig. 9.3, has been compared with that from Mattock's failure envelope, line A-A, by assuming $f_t = 2.4\ N/mm^2$, Fig. 9.2. The variations have a close agreement when the concrete fails in shear and tension, Sect. 9.2.1.1, and diverge when the concrete fails in shear and compression, because Equ. 9.2 does not allow for the compressive failure of the concrete.

9.2.2 Push tests

The specimens, Fig. 3.2 had one stud. In order to determine the stress distributions the problem was idealised to the configuration of Fig. 9.10. The area of the shear plane, A_{sh}, is not known. The mean stresses in the shear plane are shown in Fig. 9.8.

9.2.2.1 Empirical analyses

The variation in strength, line A'-A' in Fig. 9.3, was determined from Mattock's failure envelope, Fig. 9.2, by the construction of the Mohr's circles in Fig. 9.15; failure always occurred in planes subjected

to shear and tension, quadrant A in Fig. 9.15.

The transverse reinforcement was the only variable that was deliberately altered in Specimens LS1 to LS5 and LS13, Table 5.13. The stresses in these specimens are plotted in Fig. 9.11. If it is assumed that point A, F_{sh} = 60 kN, is equivalent to f_t = 2.4 N/mm^2, Fig. 9.2, then A_{sh} = 25,000mm^2 and hence the strength of the push-test specimens can be plotted in Fig. 9.3. The variation is similar to that determined from Mattock's failure envelope, line A'-A', for low values of pf_y.

9.2.2.2 Theoretical analyses

The theoretical analyses of Mattock's specimens, Sect. 9.2.1.2, was applied to the mean stresses in the push tests, Fig. 9.8. The angle at which a crack first occurred was 45^o, Fig. 9.12, and the strength of the reinforcement that was required to maintain equilibrium, Fig. 9.13, was equal to twice the shear strength, line B'-B' in Fig. 9.3.

$$pf_y = 2v_{cu} \tag{9.3}$$

When the tensile strength of the concrete determined failure, Fig. 9.14, the variation in strength was given by line D'-D', Fig. 9.3.

$$pf_y = v_{cu}^2/f_t - f_t \tag{9.4}$$

The variation has a good agreement with the experimental results of the push tests and the empirical results, line A'-A', because failure was shown to be predominantly a shear/tension failure, Sect. 9.2.2.1; the effects of which are allowed for in Equ. 9.4.

9.2.3 Comparison of results

The experimental, empirical and theoretical results are compared in Fig. 9.3. In all cases, whether the strength of the reinforcement

was determined from the angle of the initial crack or the tensile strength of the concrete or the failure envelope derived from Mattock's results, the push tests required approximately twice as much reinforcement as Mattock's specimens to withstand the same shear force, because the longitudinal compressive force present in Mattock's specimens was not present in the push tests, Figs. 9.7 and 9.8. The design rule in the Bridge Code[7] which was based upon Equ. 2.11, line E-E, also overestimates the strength of the shear connection. Mattock's work is therefore not directly applicable to push tests in which the reinforcement is looped around the stud.

9.3 MODE 3 FINITE ELEMENT ANALYSIS

9.3.1 Shank failure

The finite element model in Fig. 9.16 was used to study the effect of varying the position of the transverse reinforcement, distances l_t and s_c, on the shank failure load of a stud, Equ. 6.1. The model was analysed on the Mode 3 program, Sect. 4.4, the properties of the concrete are described in Sect. 4.4.6, the nomenclature for the constraints is given in Fig. 4.2 and the grid system was similar to that of Fig. 6.3.

The loads at which the maximum principal stress in the steel exceeded the ultimate tensile strength of the stud and the loads at which the concrete between the applied displacement and the shank of the stud, Fig. 9.16, first disintegrated are plotted in Fig. 9.17 for various levels of reinforcement and for two lengths of the shear plane. It is theoretically possible for the shank failure load of the stud to be exceeded when the reinforcement is concentrated at the base of the stud.

9.3.2 Slab failure

The finite element model is shown in Fig. 9.18. The properties of the concrete are described in Sect. 4.4.6 and the nomenclature for the restraints are given in Fig. 4.2. The patch was displaced longitudinally and the concrete was assumed to have split previously along the line of action of the applied load.

The distributions of the failure of the concrete when the concrete began to disintegrate and when the reinforcement is assumed to have reached its yield strength are shown in Figs. 9.18 and 9.19. The concrete first disintegrated along the plane of maximum shear and then along the bearing surface of the reinforcement. Prior to the concrete failing, the axial force in the reinforcement behind the applied load, F_b in Fig. 9.10, was tensile whilst the axial force in front, F_f, was compressive. As the concrete failed, F_f became tensile. The extent of the redistribution of the forces depended upon the amount of reinforcement; for example, at the load at which the concrete began to disintegrate, $F_f = 0.65F_b$ when $A_r/A_{sh} = 0.13$ and $F_f = 1.02F_b$ when $A_r/A_{sh} = 0.27$.

The mean bearing stress at the patch when the concrete first failed in tension, when the reinforcement yielded and when the concrete began to disintegrate are shown in Fig. 9.20 for various amounts of reinforcement. The results are compared with the strength of laterally reinforced concrete prisms, Sect. 8.2.1.2. The reinforcement is required to maintain equilibrium as soon as the concrete cracks because the specimen is not symmetrical. Therefore the strength of the shear connection is dependent upon the strength of the reinforcement and the shear strength of the slab.

The load at which the reinforcement fails, P_{yr} in Fig. 9.21, and the slab fails in shear, P_{sr} in Fig. 9.22, can be given in terms of the shank failure load, P_{sh}, if it is assumed that the point A in Fig. 9.20 is equivalent to P_{sh}.

9.4 ANALYSIS OF PUSH TESTS

9.4.1 Slab failure

The strengths of specimens LS1 to LS5 and LS13, in which the amount of reinforcement was varied, are plotted in Fig. 9.23 in terms of the theoretical shank failure load, Equ. 6.1. The results have been compared with the theoretical strengths, P_{yr} in Fig. 9.21 and P_{sr} in Fig. 9.22 by assuming that $A_{sh} = 0.5s_c^2$ and $f_{ce} = f_{cy}$. The experimental strengths at low proportions of reinforcement are greater than the theoretical strengths because these specimens failed due to splitting.

9.4.2 Shank failure

The strengths of the push-test specimens in Table 5.13 were compared with the theoretical splitting strength of the slab, Equ. 7.2, and the theoretical slab strength, the lower value of P_{yr} and P_{sr}. When $P_e > P_{sp}$ and P_e was less than the theoretical slab strength, Specimens LS4, LS5 and LS10 to LS13, it was assumed that the strength was determined by the strength of the stud. The results are plotted in Fig. 9.17 in terms of the theoretical shank failure load, Equ. 6.1; it was assumed that $l_t = c_b + h_r/2$. The design rule, which was plotted as a lower bound to the experimental results excluding Specimen LS5, has the same variation as line A-A, as $s_c = 3d_s$ in the push tests, and assumes an upper bound at P_{sh}.

9.4.3 Bearing failure

When s_c was changed from $3d_s$ to $4.5d_s$, Fig. 9.17, the concrete failed earlier because of the reduction in the lateral restraint imposed upon the concrete, at position A in Fig. 9.10, by the shank and the reinforcement. Until further experimental and theoretical evidence is available it would be good design practice to ensure that

$$h_r \geqslant 0.39(s_c - d_s), \qquad (9.5)$$

since this is the minimum depth of reinforcement in the specimens in which $P_e > P_{sp}$, Specimens LS10 to LS12.

If it is assumed that $F_b = F_f$, Fig. 9.10, when the reinforcement yields, then the mean bearing stress within the loop, position B, is equal to $F_{sh}/s_c h_r$. If it is assumed that Specimen LS5 failed prematurely, Figs. 9.3, 9.17 and 9.23, because the concrete failed within the loop then until further evidence is available it would be good design practice to ensure that

$$h_r \geqslant F_{sh}/3.5 f_{cu} s_c \qquad (9.6)$$

which was derived from the maximum experimental bearing stress, Specimen LS4.

9.4.4 Comparison of results

The experimental strengths, the results in Table 5.13 excluding LS5, are compared with the theoretical strengths in Fig. 9.24. The theoretical strength was the lesser of the stud strength, Fig. 9.17, and the slab strength. The slab strength was determined from P_{sp}, P_{sy} and P_{sr}, which were derived from Equ. 7.2, Figs.9.21 and 9.22, bearing in mind that the minimum strength of the slab is P_{sp}. The theoretical rules appear to give a lower bound to the strength; the mean of the dependent variable is 1.12 and the coefficient of variation 10.6%.

The variation in Figs. 9.21 and 9.22 were derived from a theoretical analysis in which $s_c = 3d_s$. It may be expected that A_{sh} is proportional to $h_r s_c$, however, the assumption that A_{sh} was proportional to s_c^2, Sect. 9.4.1, means that the reinforcement, derived from Figs. 9.21 and 9.22, increases more rapidly than is required when s_c increases. Therefore the variations in Figs. 9.21 and 9.22 are probably conservative when $s_c \geqslant 3d_s$.

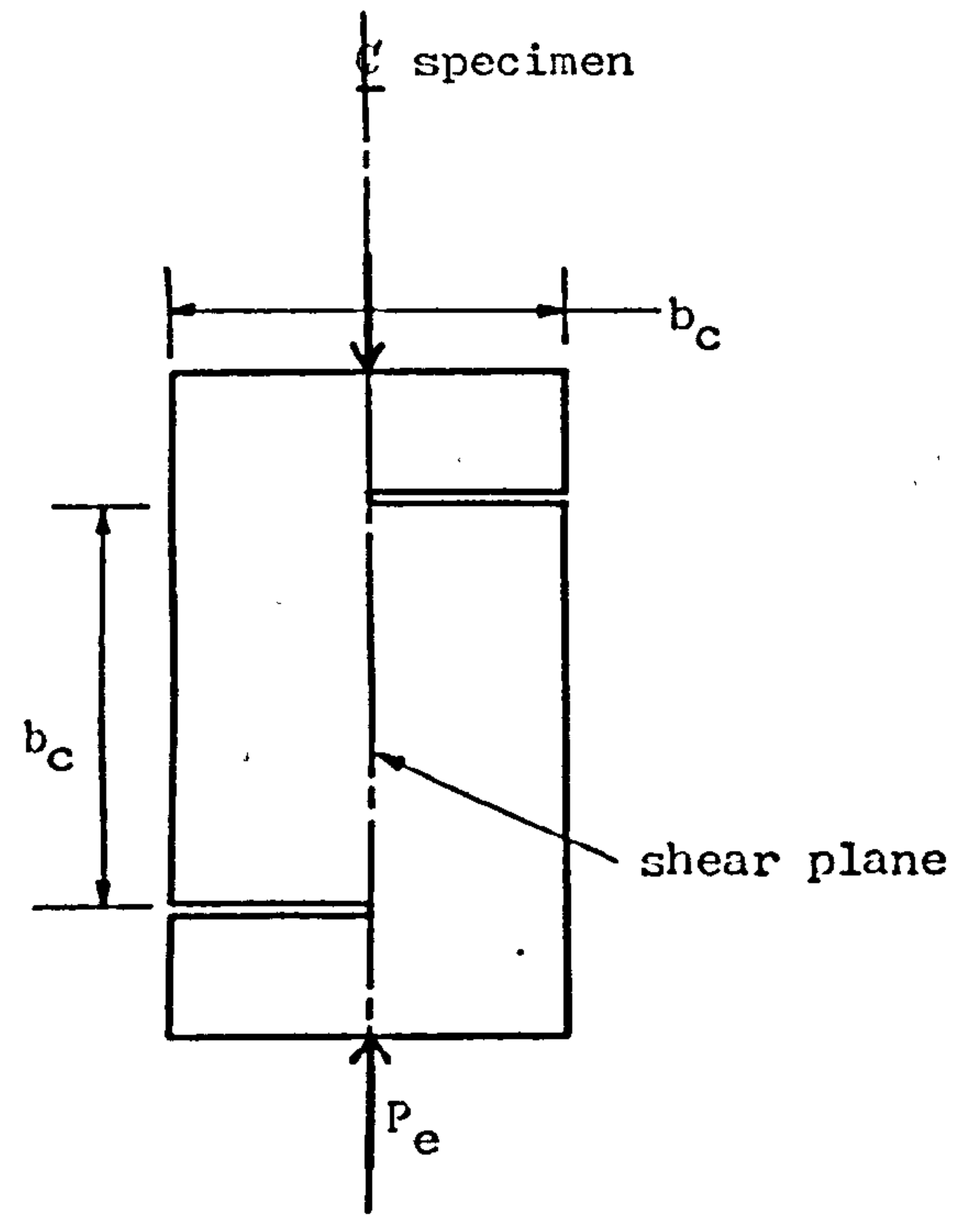

Fig. 9.1 Mattock's test specimen.

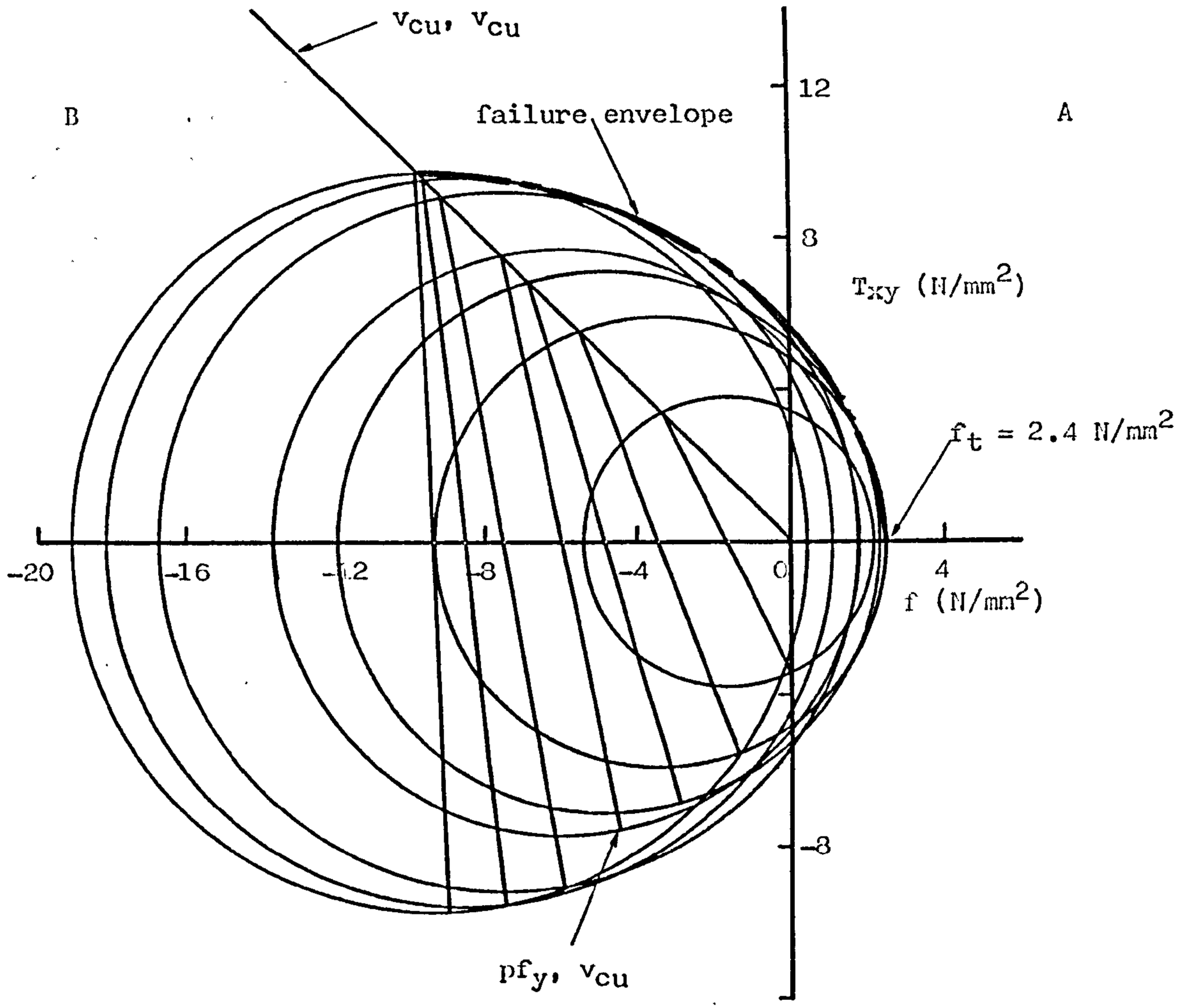

Fig. 9.2 Mohr's circles of the stresses at failure from Mattock and Hawkins' experiments on uncracked shear planes.

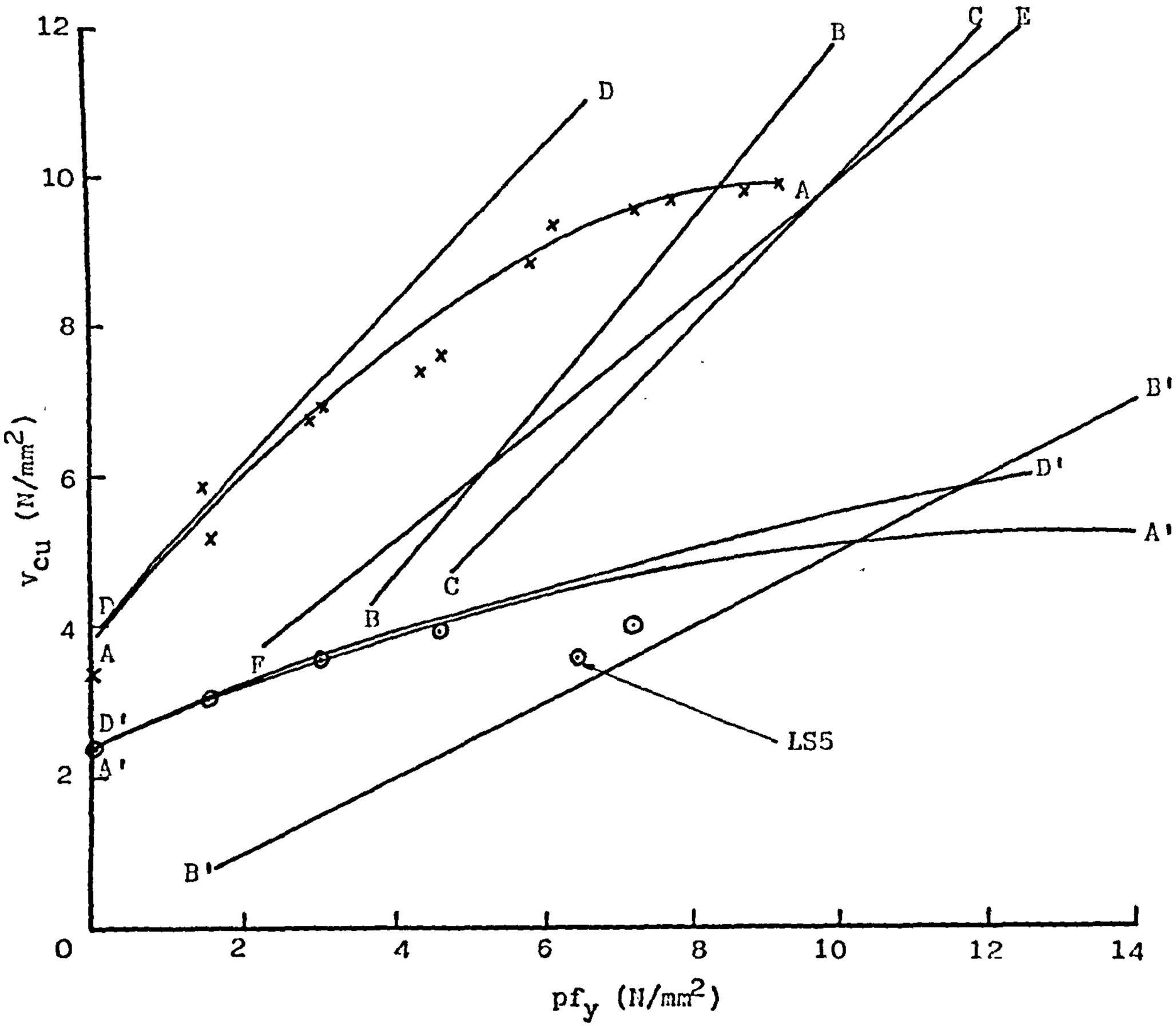

Mattock's specimen:
- × experimental results
- A——A derived from Mattock's failure envelope
- B——B $pf_y = 0.85v_{cu}$
- C——C $pf_y = v_{cu}$
- D——D $pf_y = v_{cu}^2/(v_{cu} + f_t) - f_t$
- E——E Equ. 2.11

Push tests:
- ⊙ experimental results
- A'——A' derived from Mattock's failure envelope
- B'——B' $pf_y = 2v_{cu}$
- D'——D' $pf_y = v_{cu}^2/f_t - f_t$

Fig. 9.3 Variation of the shear strength with the strength of the transverse reinforcement.

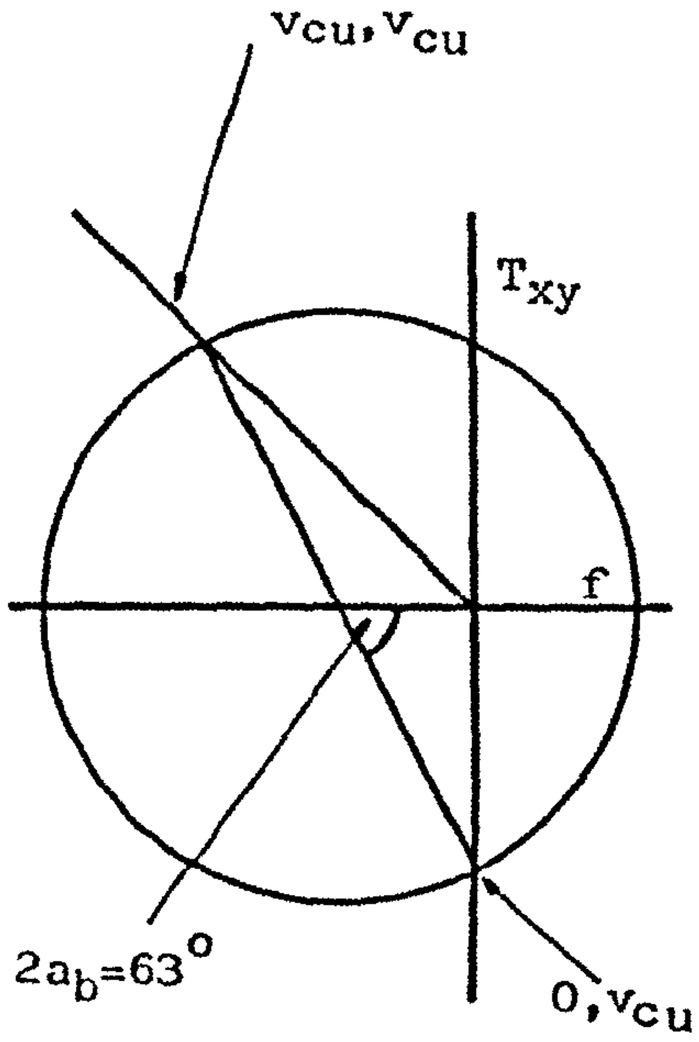

Fig. 9.4 Mattock's specimen. Angle of crack.

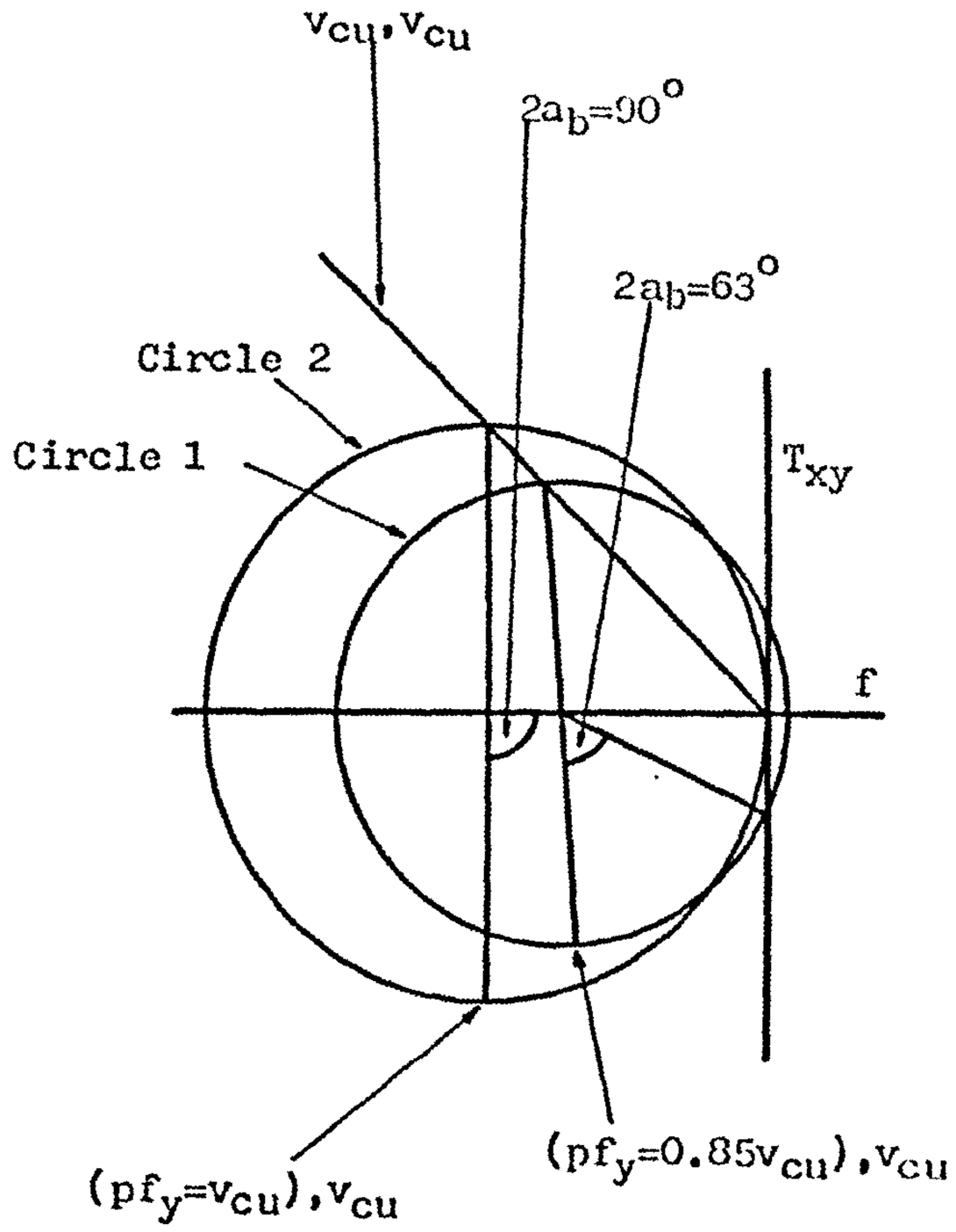

Fig. 9.5 Mattock's specimen. Strength of reinforcement derived from the angle of crack.

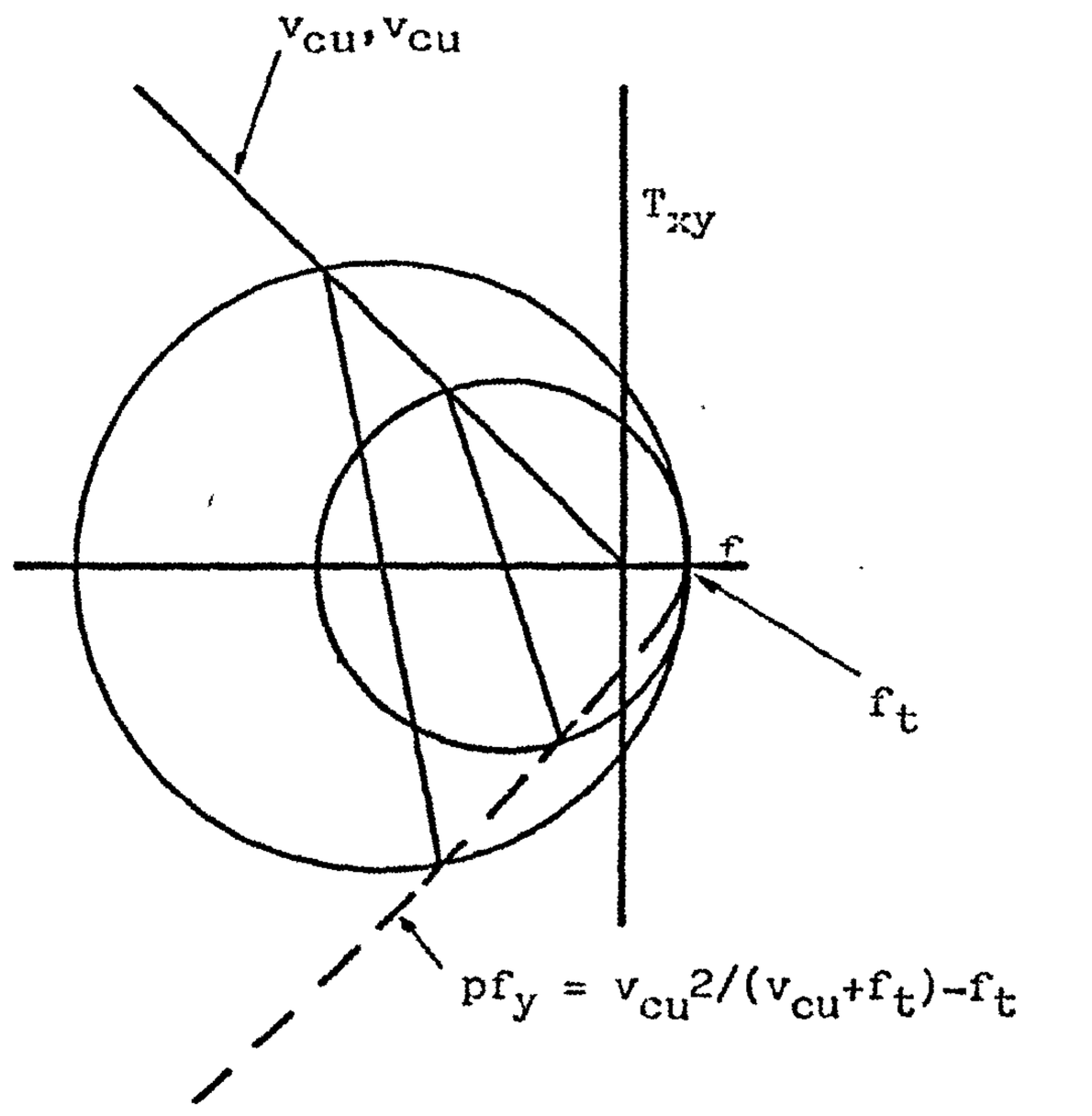

Fig. 9.6 Mattock's specimen. Strength of reinforcement derived from the tensile strength of the concrete.

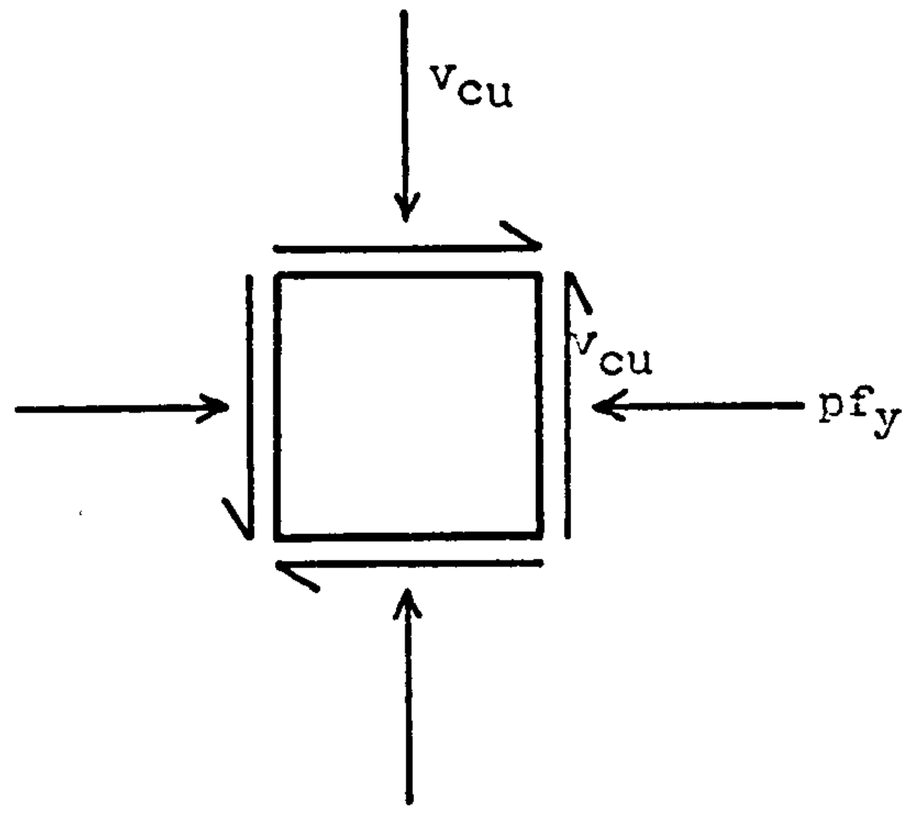

$$v_{cu}=P_e/b_c h_c$$

Fig. 9.7 Mean stresses along the shear plane of Mattock's specimen.

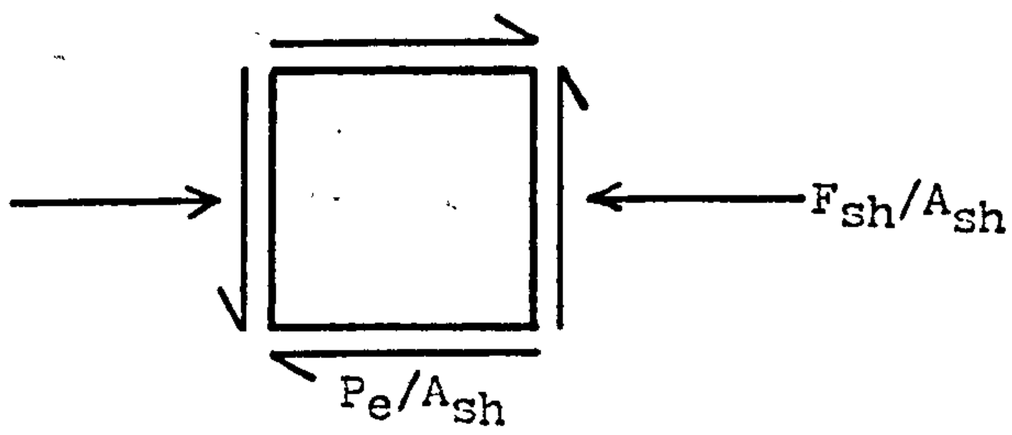

Fig. 9.8 Mean stresses along the shear plane of the push tests.

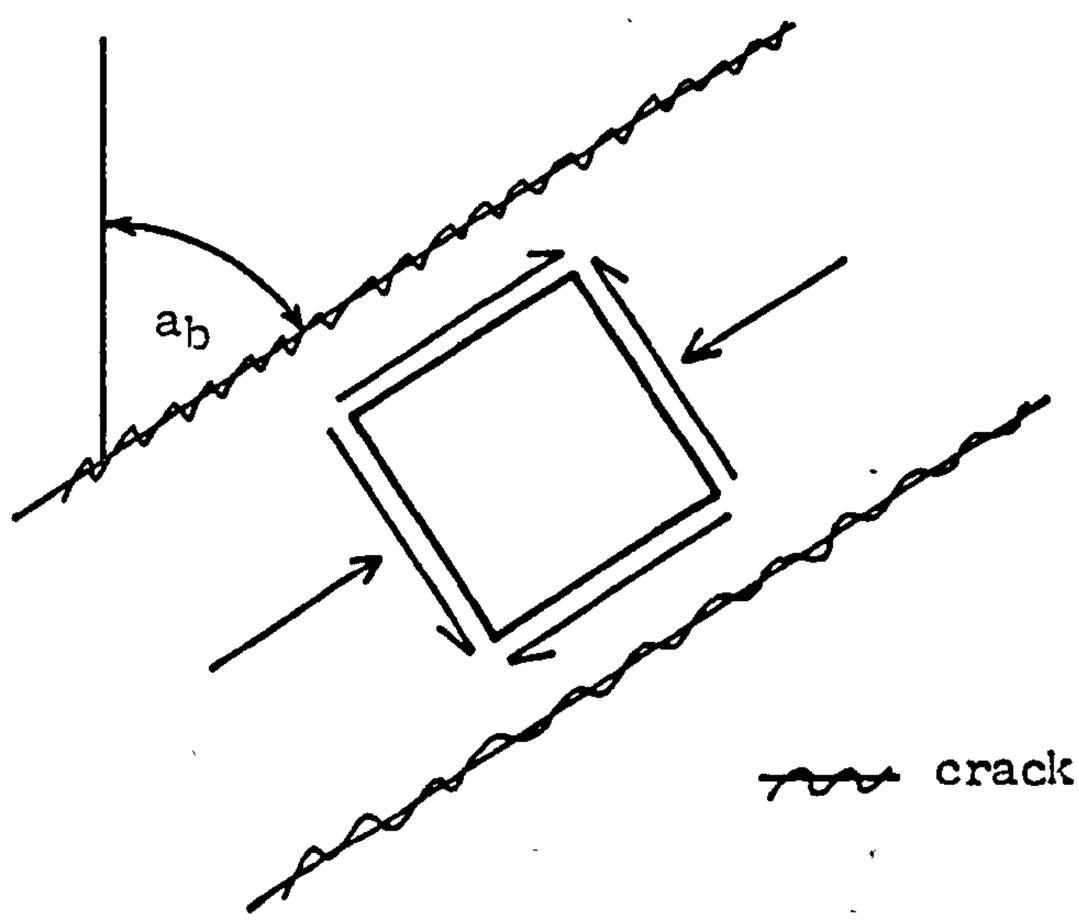

Fig. 9.9 Distribution of the stresses in the struts of concrete formed after cracking.

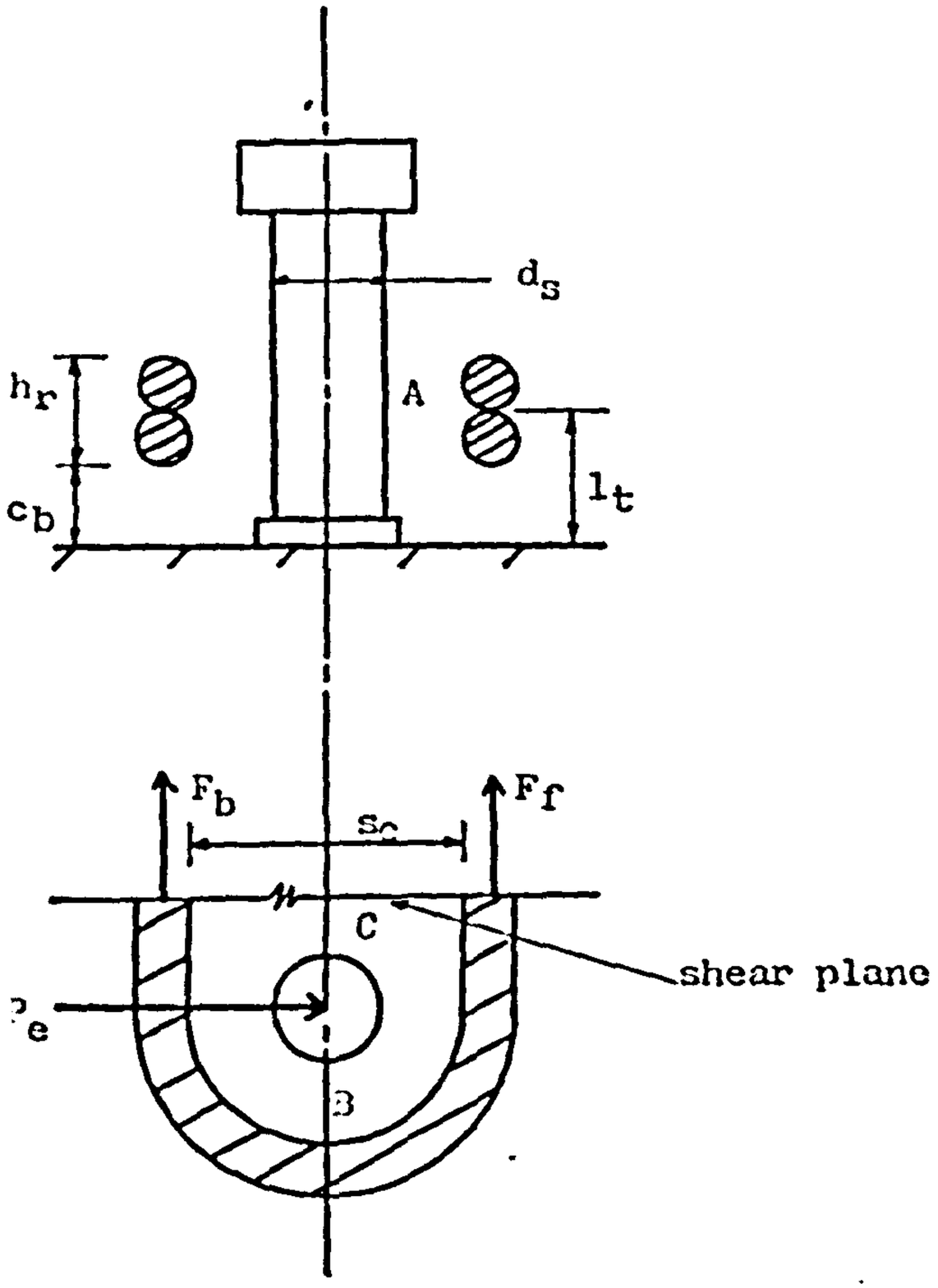

ig. 9.10 Reinforcement looped around a single stud.

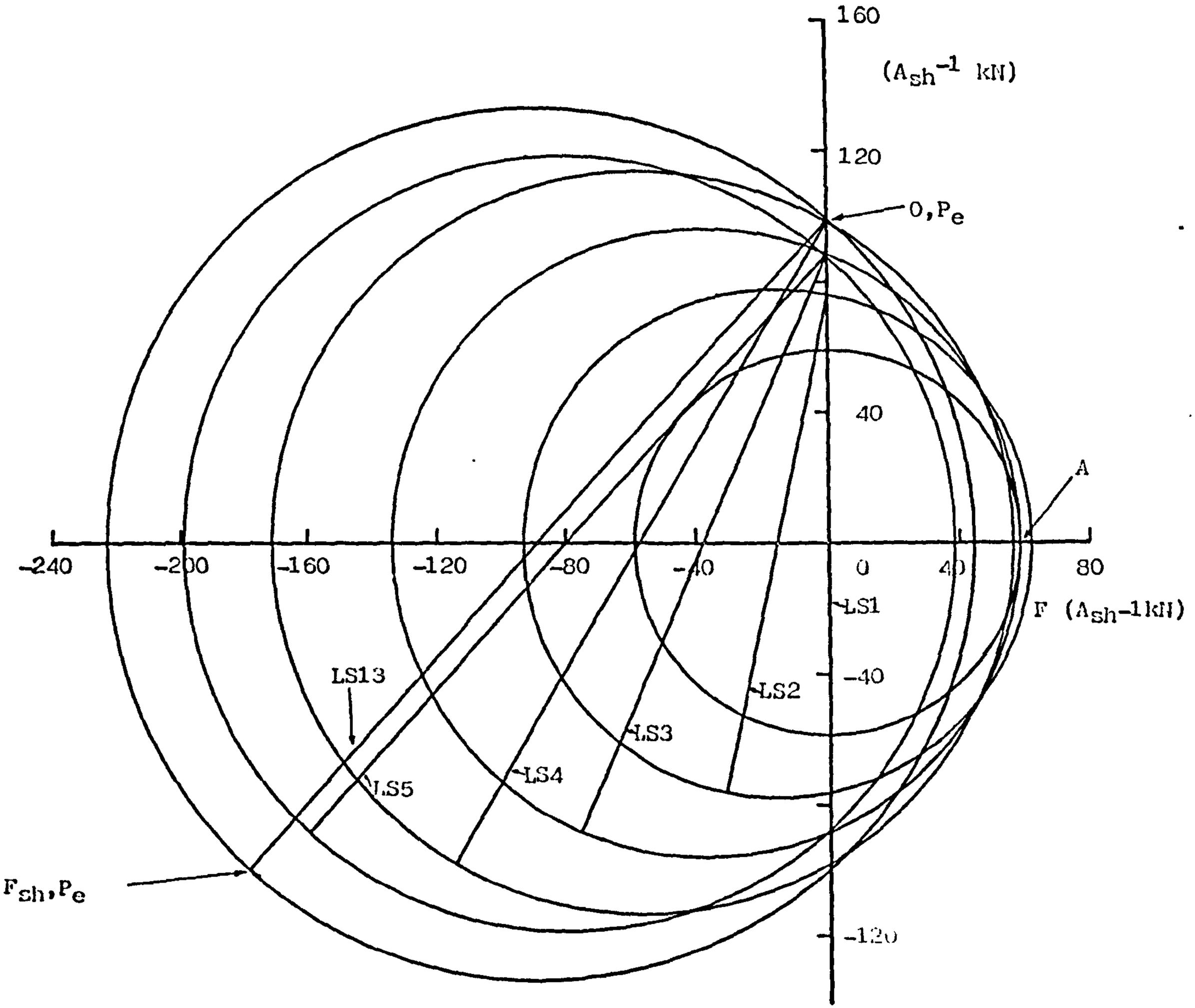

Fig. 9.11 Mohr's circles of stresses at failure from the push tests.

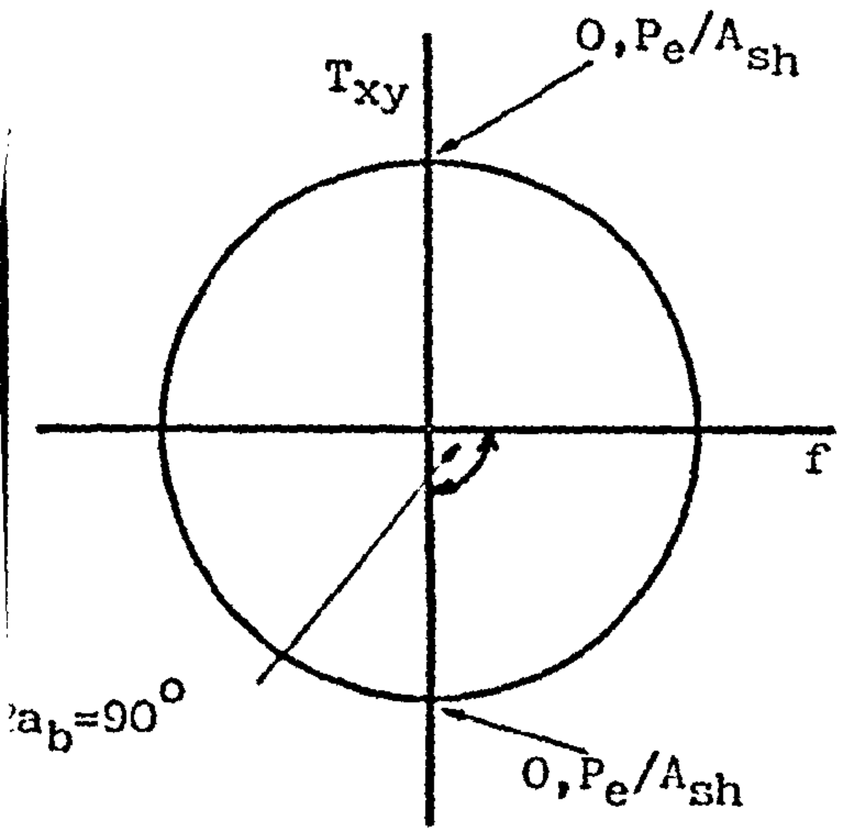

Fig. 9.12 Push test.
Angle of crack.

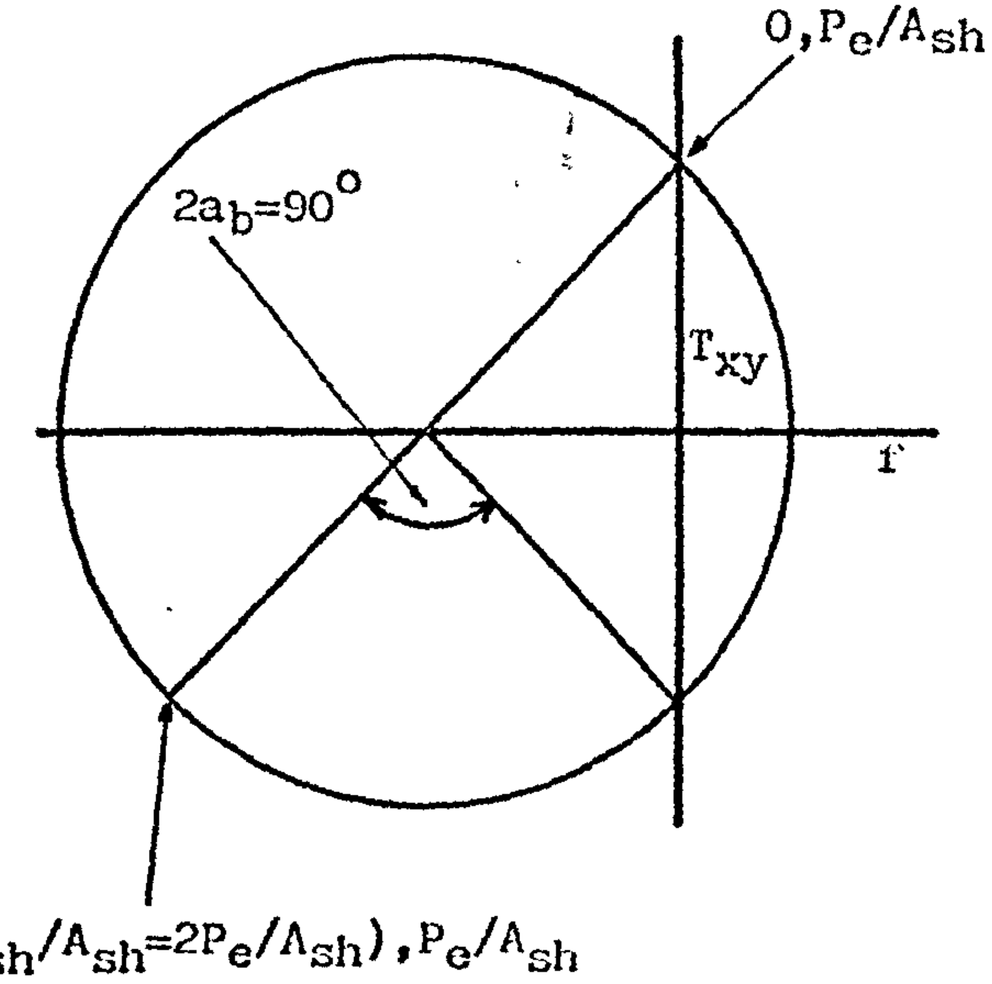

Fig. 9.13 Push test.
Strength of reinforcement
derived from the angle of crack.

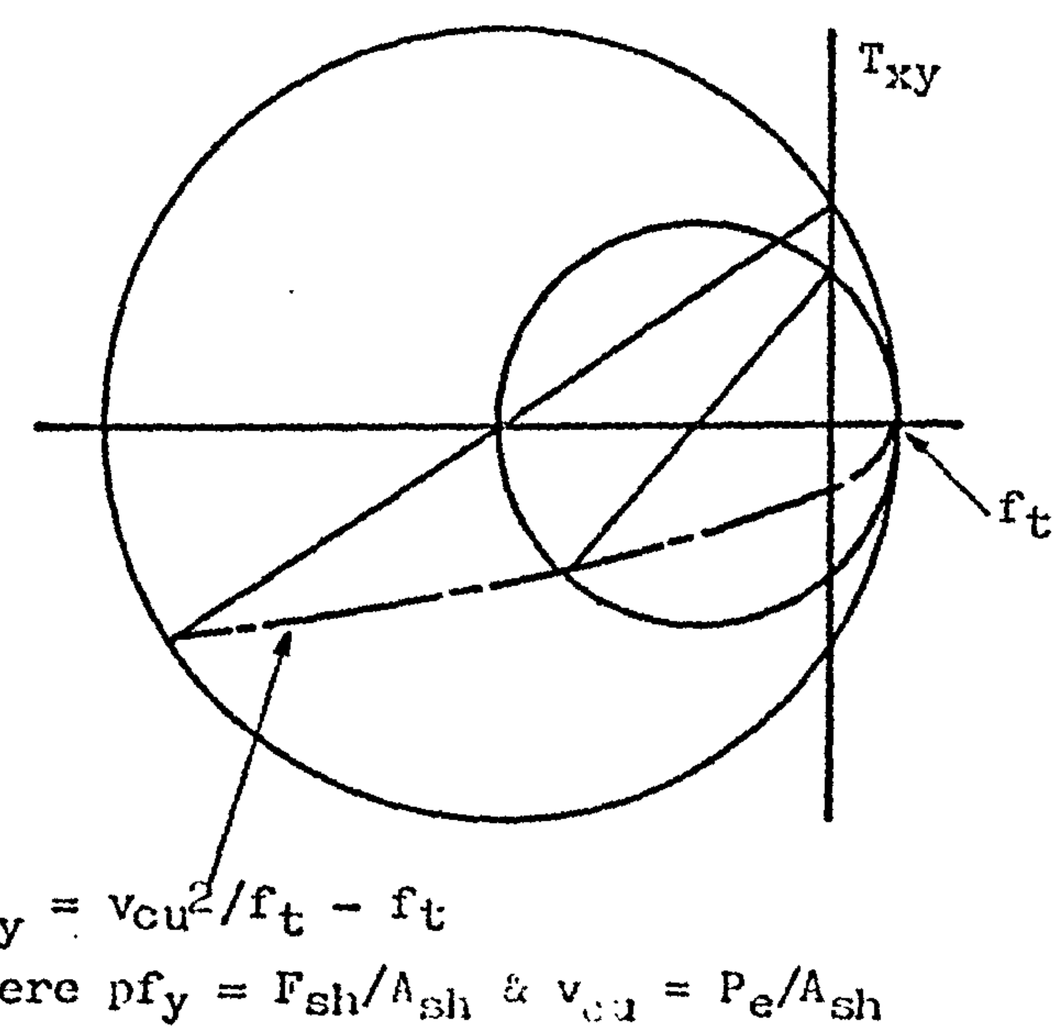

Fig. 9.14 Push test.
Strength of reinforcement derived
from the tensile strength of
the concrete.

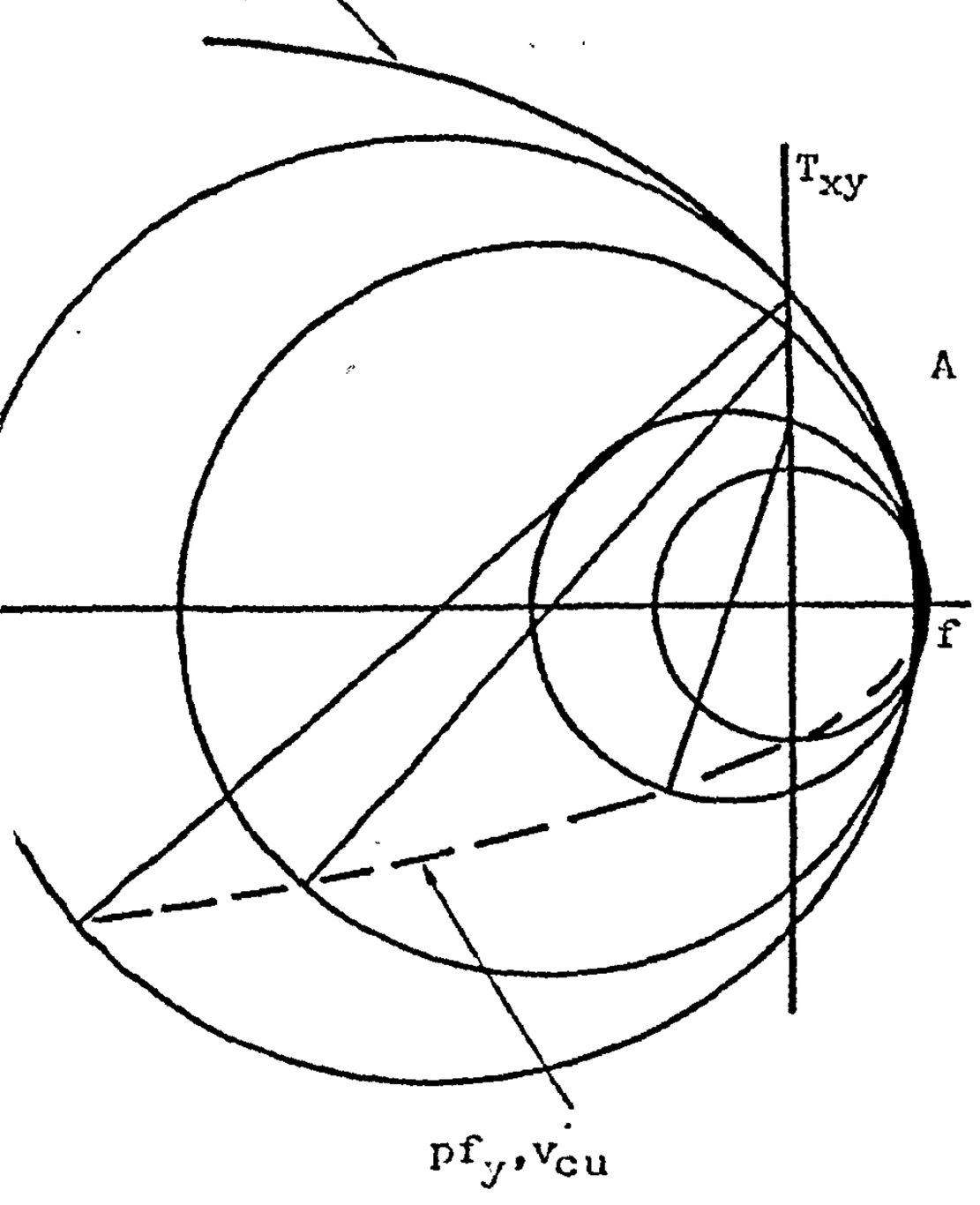

9.15 Push test. Strength of reinforcement derived from Mattock's failure envelope.

E_s = 220 kN/mm^2
v_s = 0.3
f_{su} = 620 N/mm^2

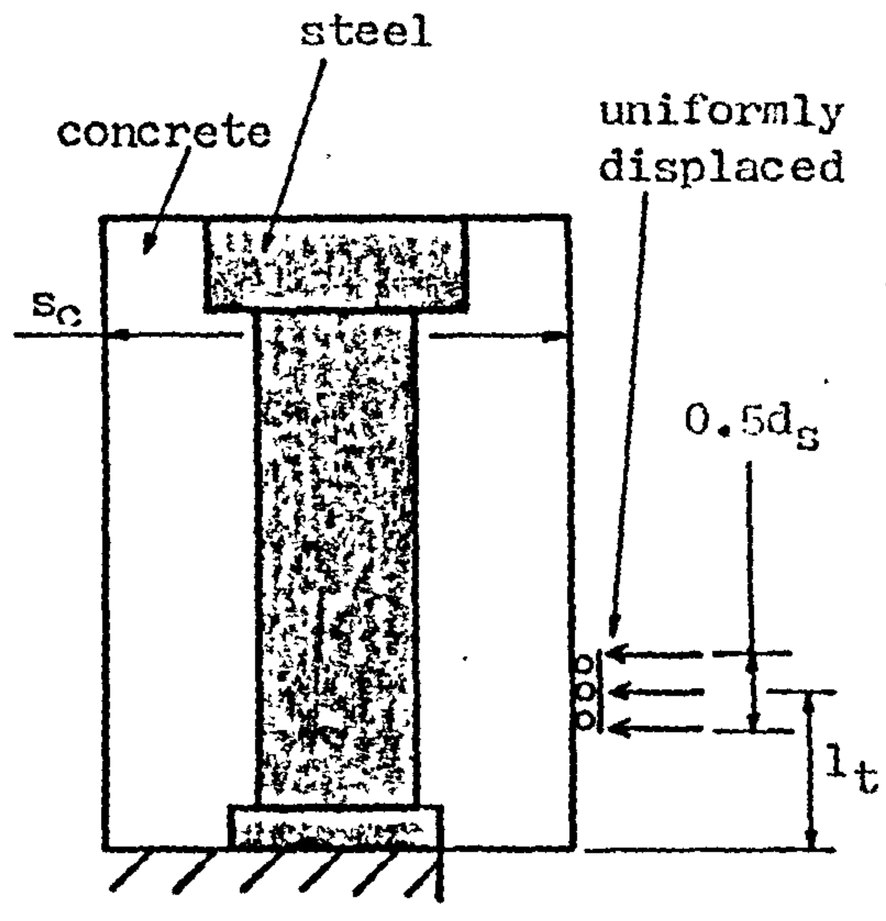

Fig. 9.16 Finite element model for varying the position of the reinforcement.

× experimental results

theoretical analyses.

$s_c = 3d_s$:
——— f_{su} exceeded
—·—·— concrete disintegrates

$s_c = 4.5d_s$:
—·— f_{su} exceeded and concrete disintegrates

——— design rule

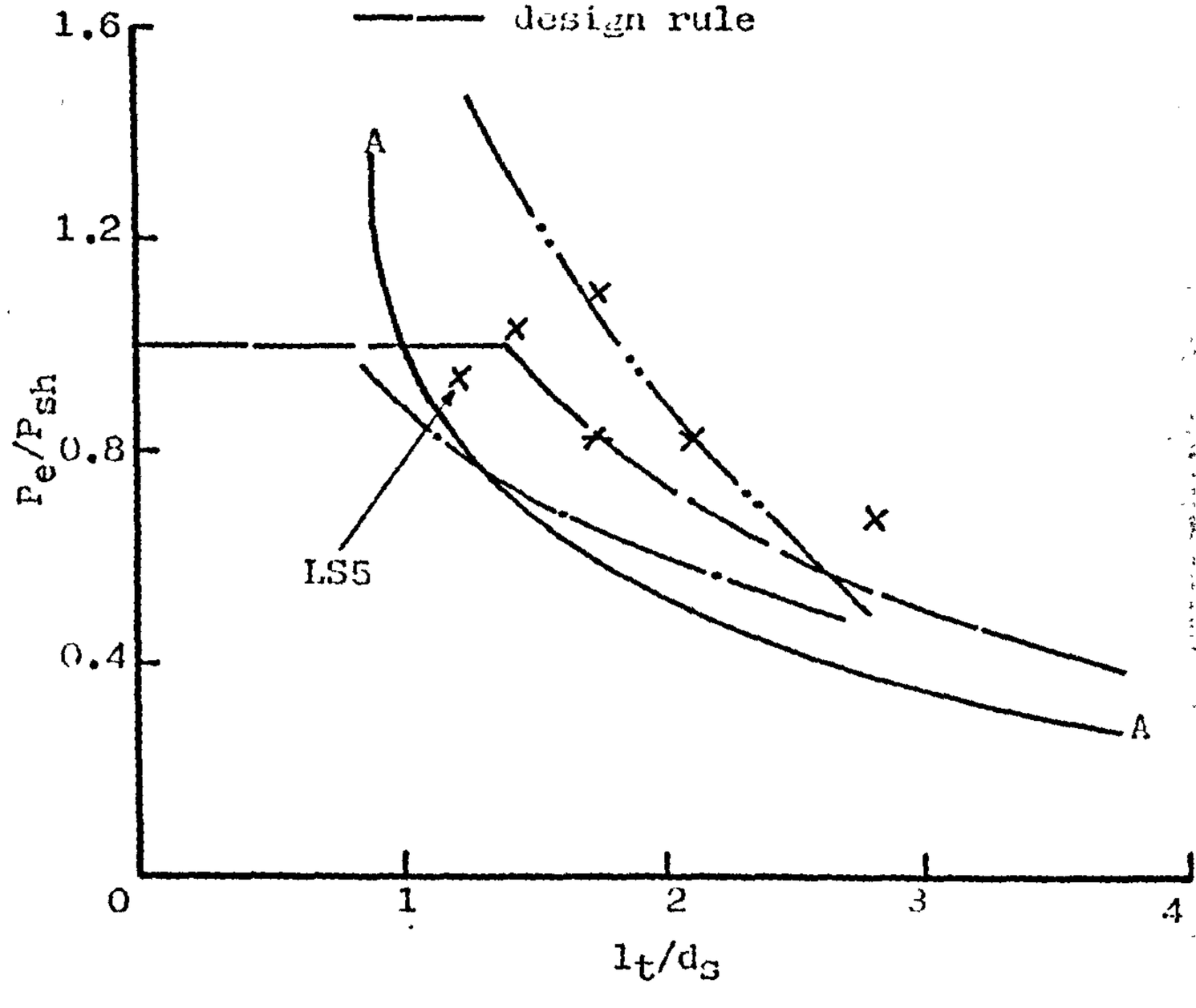

Fig. 9.17 Variation of the strength of the stud with the height of the looped reinforcement.

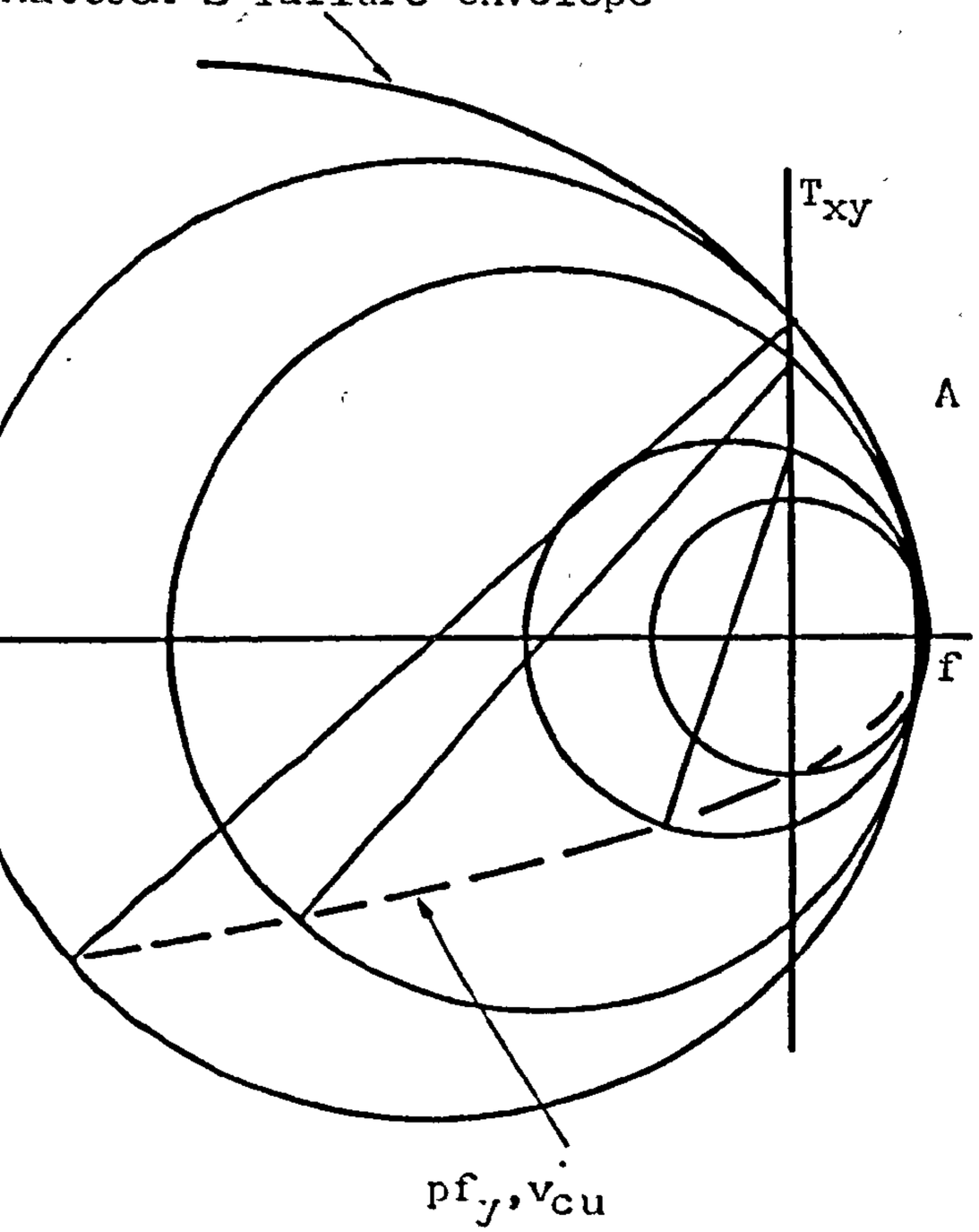

g. 9.15 Push test. Strength of reinforcement derived from Mattock's failure envelope.

E_s = 220 kN/mm^2
v_s = 0.3
f_{su} = 620 N/mm^2

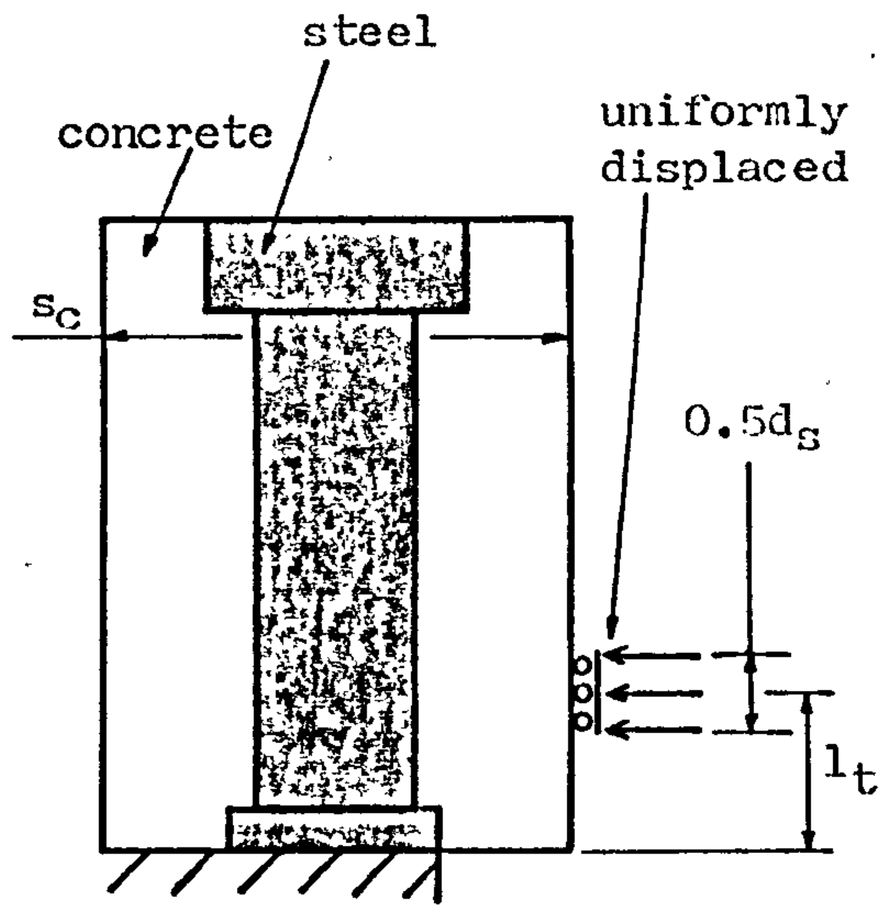

Fig. 9.16 Finite element model for varying the position of the reinforcement.

× experimental results

theoretical analyses.

$s_c = 3d_s$:
——— f_{su} exceeded
——··—— concrete disintegrates

$s_c = 4.5d_s$:
——·—— f_{su} exceeded and concrete disintegrates

—— — design rule

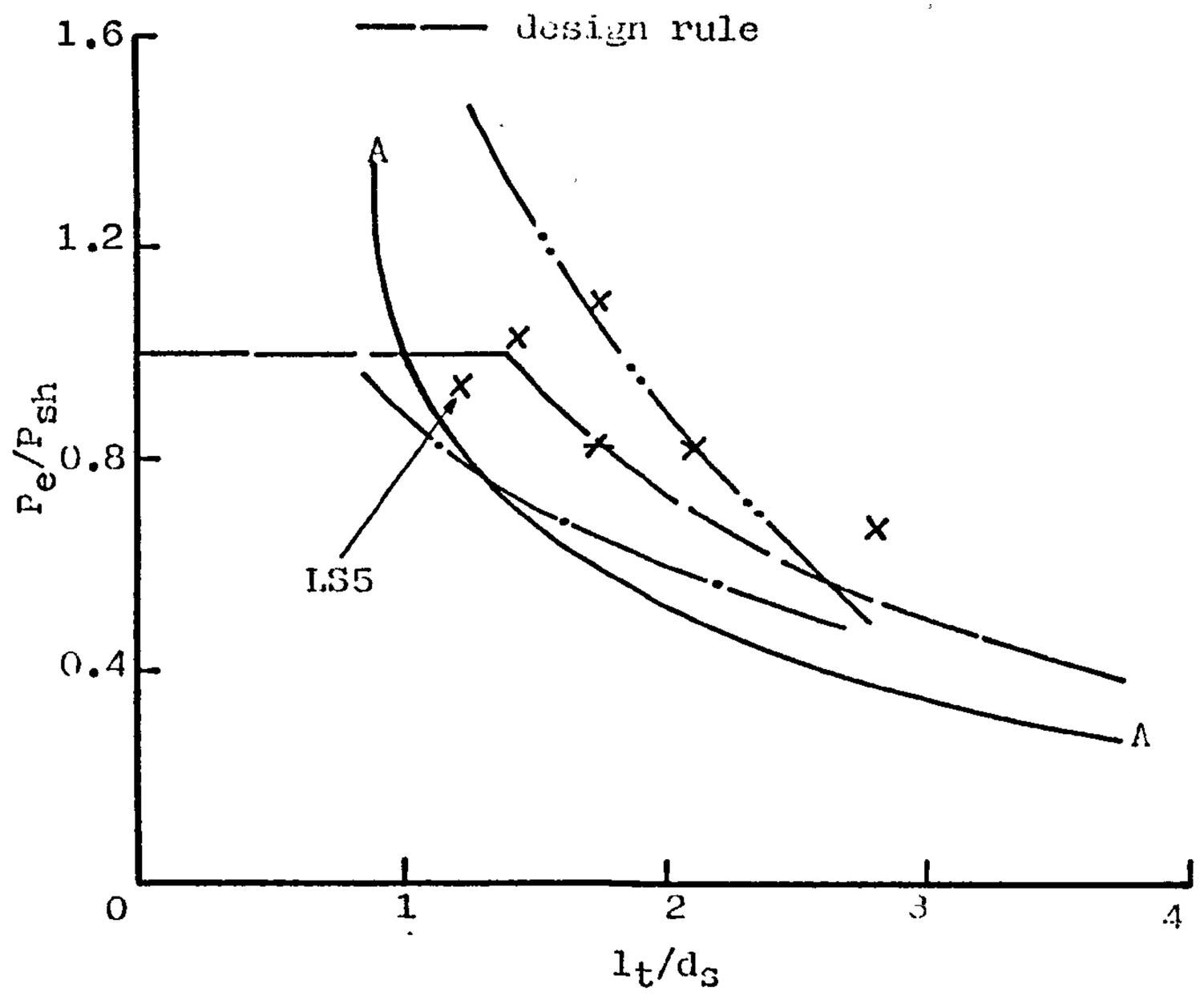

Fig. 9.17 Variation of the strength of the stud with the height of the looped reinforcement.

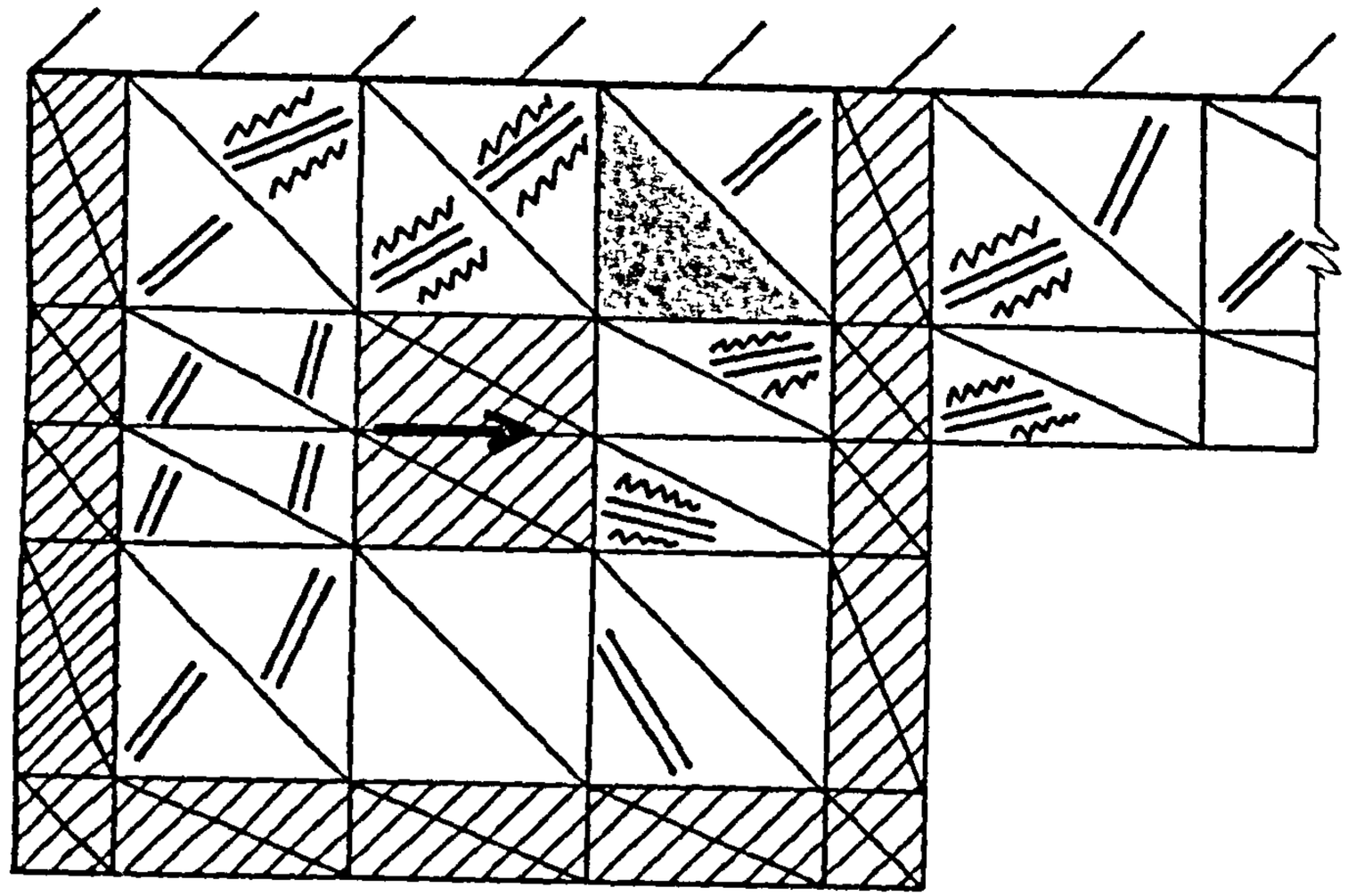

E_s=200 kN/mm^2, ν_s=0.3

A_r/A_{sh}=0.27

Fig. 9.18 Distribution of the concrete failure when the concrete first disintegrates.

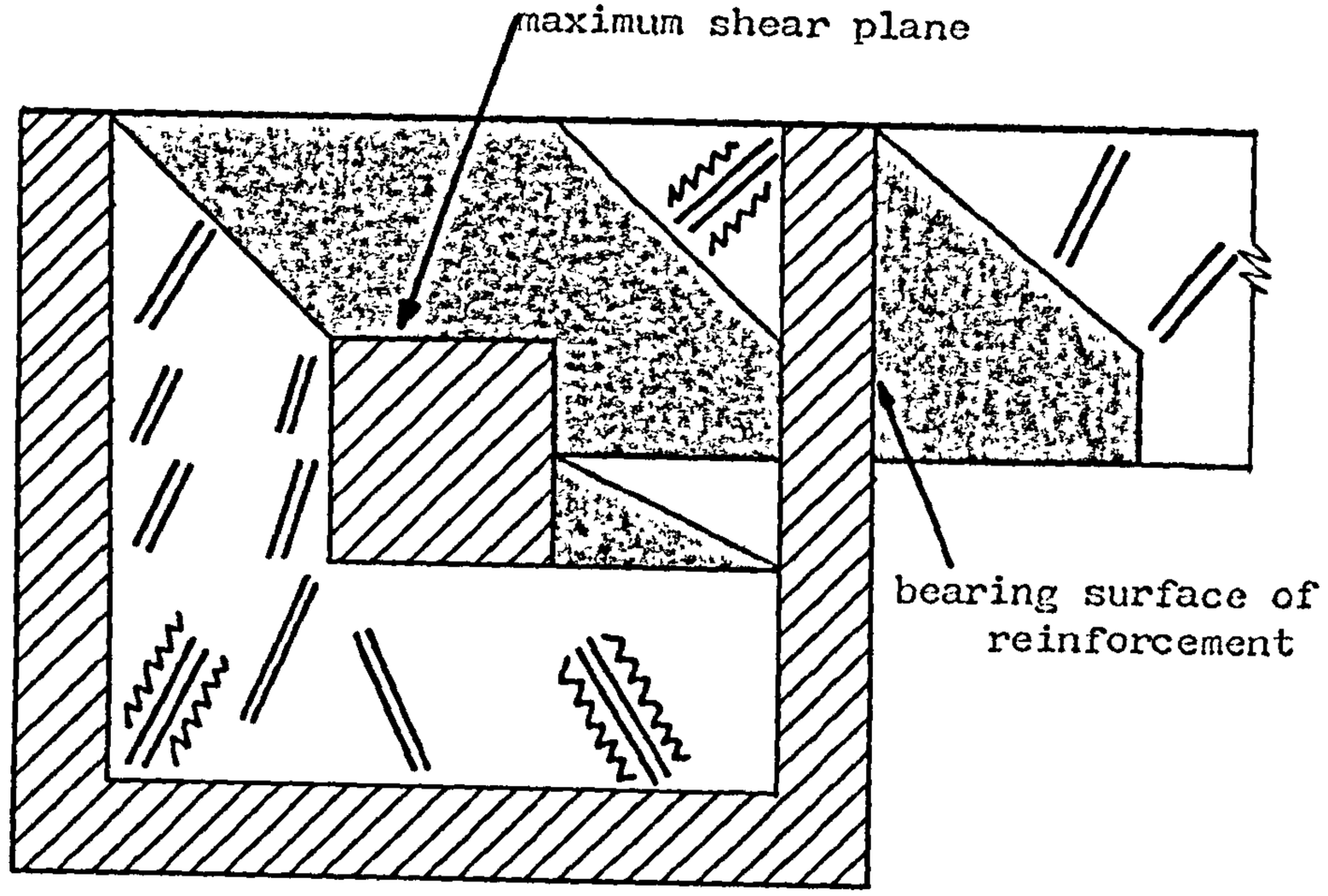

E_s=200 kN/mm^2, ν_s=0.3

A_r/A_{sh}=0.27

Fig. 9.19 Distribution of the concrete failure when the stress in the reinforcement exceeds 250 N/mm^2.

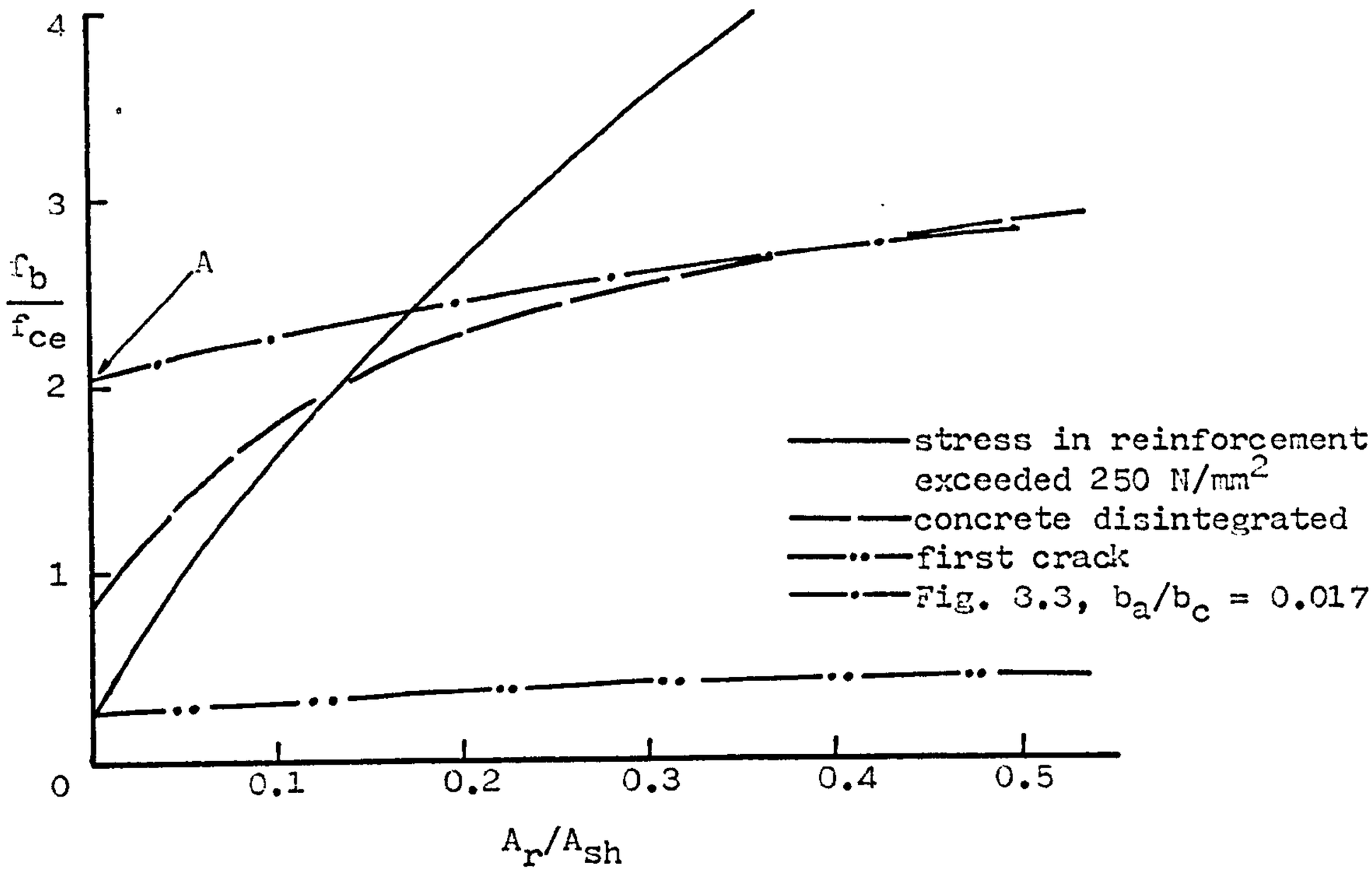

Fig. 9.20 Variation of the shear strength of a slab.

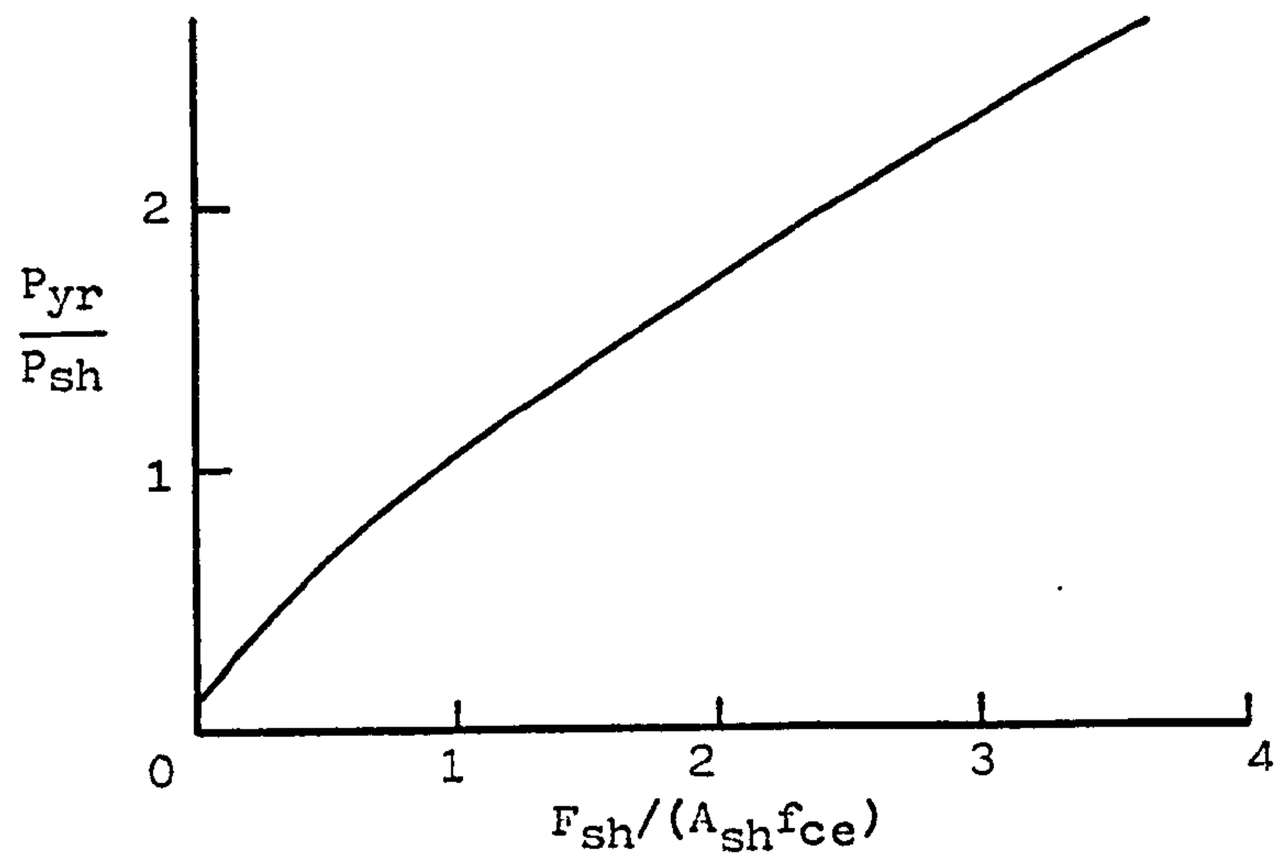

Fig. 9.21 Variation of the shear strength of the slab with the strength of the reinforcement.

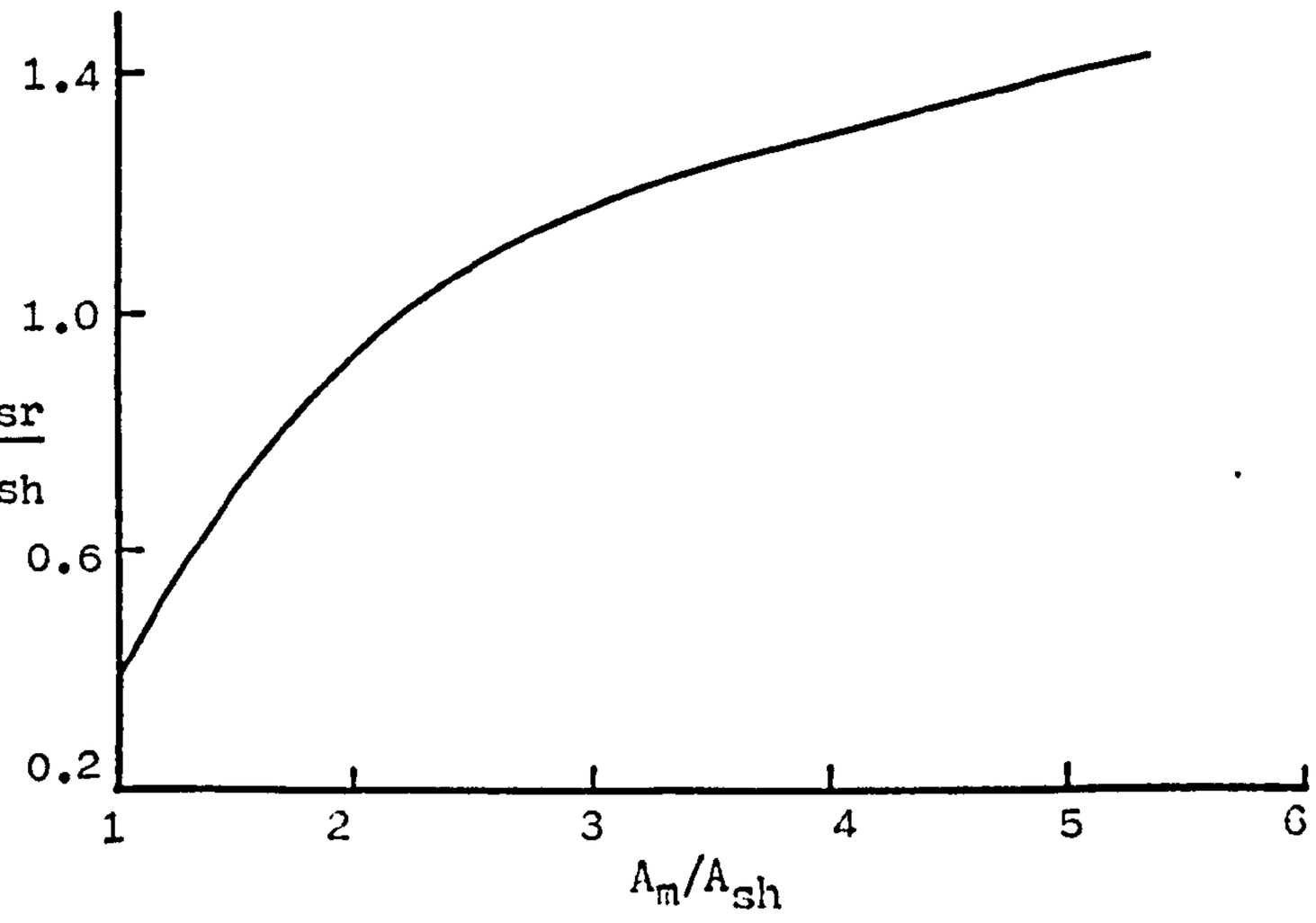

Fig. 9.22 Variation of the shear strength of the slab with the stiffness of the reinforcement.

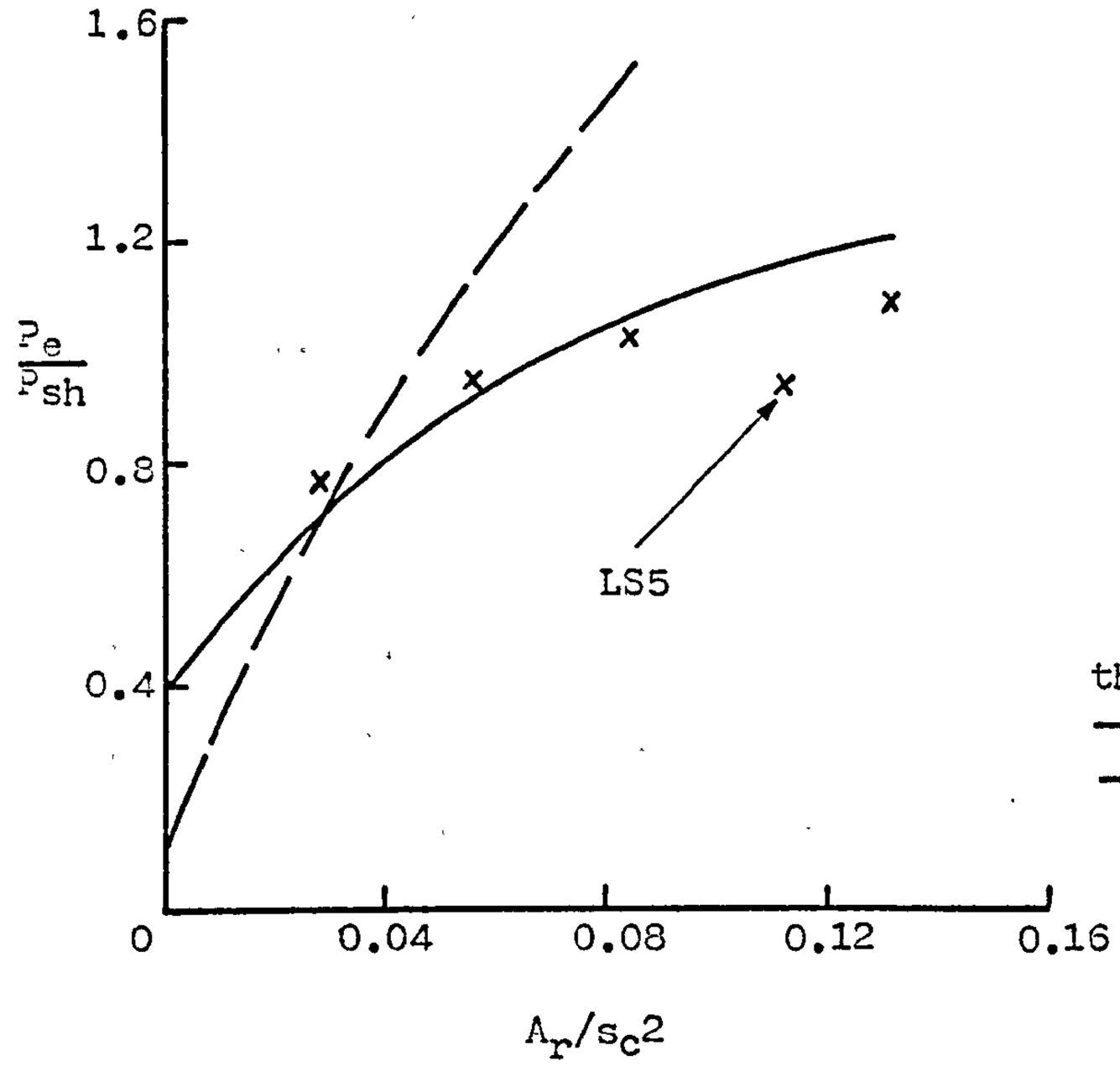

Fig. 9.23 Comparison of the theoretical and experimental shear strength of the slab.

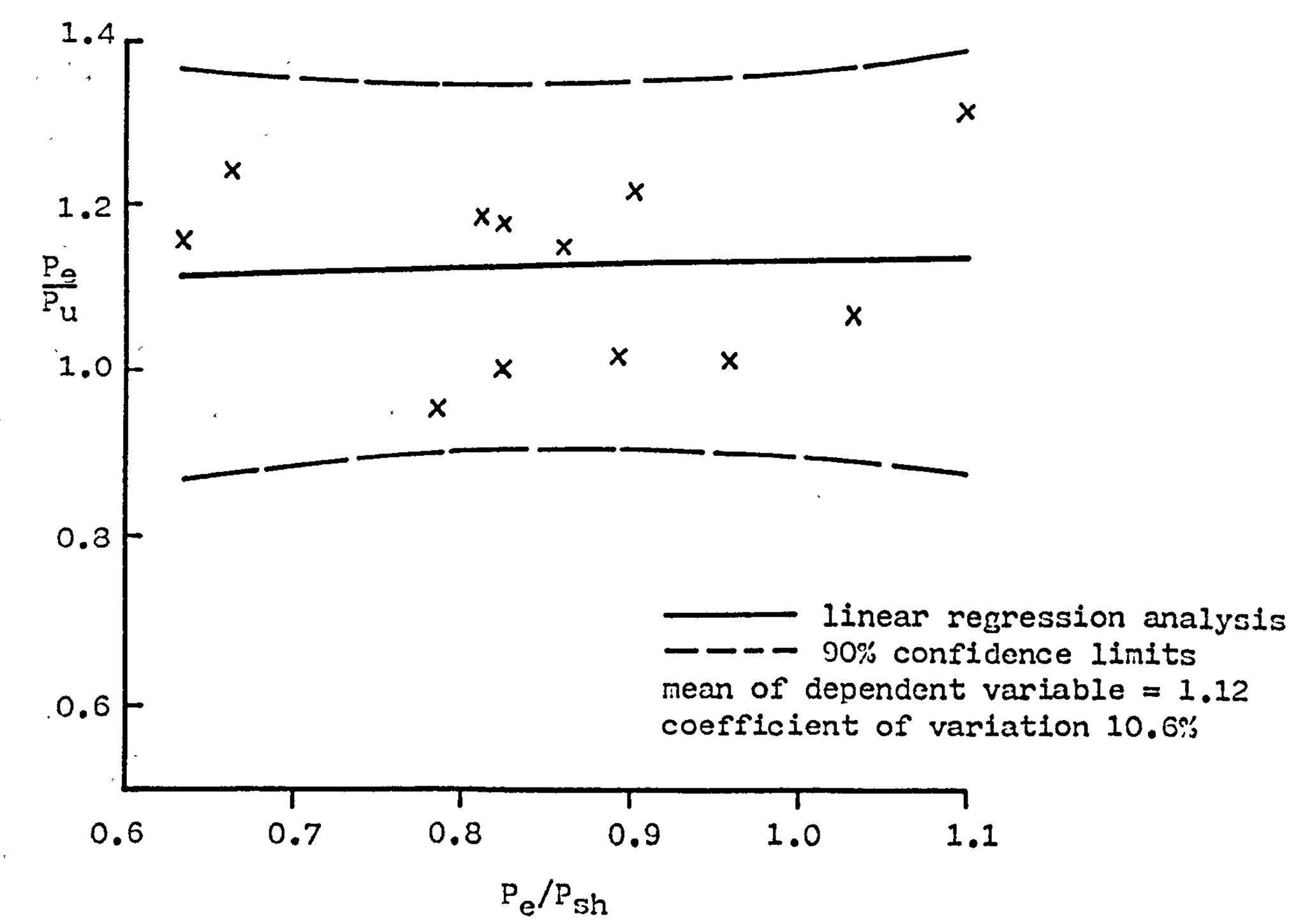

Fig. 9.24 Comparison of the theoretical and experimental results for all possible modes of failure.

Chapter Ten

VARIATION IN THE STIFFNESS

10.1 INTRODUCTION

The maximum stiffness of a stud shear connector at a particular slip is given by the load-slip curve of a connection in which the stud fails. This curve, which will be referred to as the basic curve, is derived statistically in Sect. 10.2 and the effect of splitting on the curve is discussed in Sect. 10.3.

10.2 THE BASIC LOAD-SLIP CURVE

10.2.1 Experimental data

The load-slip curves of the push tests in Tables 5.4, 5.6, 5.8, 5.10, 5.11, 5.12 and those of Fung and King in Appendix 5.1 were used in the statistical analysis. As it was shown in Sect. 6.4.1.3 that the strength of 13mm studs varies more than that of 19mm and 22mm studs, because of the size of the weld collar in relation to that of the aggregate particles, the experimental data was analysed as two groups; those with 13mm studs and those without.

10.2.2 Statistical analysis

A linear regression analysis was used to determine the variation of the slip with the cube strength, an example of which is shown in Fig. 10.1, at different proportions of the shank failure load. The slip used in the regression analysis, s_p, was the mean of the slip at both sides of the push specimen, Fig. 1.1, at the same load, and the shank failure load was either the maximum strength of the specimen when the studs failed or the theoretical load, Equ. 6.1, when the slab split.

When the slab split the falling branch of the load-slip curve, which always occurred immediately after splitting, was not included in this analysis.

10.2.3 Results

The results of the statistical analyses of the two groups of data, which are given in Tables 10.1 and 10.2 and which are also shown graphically in Fig. 10.2, can be used to construct the load-slip curves for various concrete strengths, Fig. 10.3. The results of the analyses which did not include 13mm studs, Table 10.1, have a smaller scatter than those which did, Table 10.2, and therefore give a truer representation of the load-slip curve. However, the results of the analyses which included 13mm studs, Table 10.2, are applicable over a wider range of concrete strengths and also predict a lower maximum slip and hence may be preferred for design purposes.

The scatter of the slips, Fig. 10.1, which is represented by the standard deviation in Table 10.1 and the horizontal distance between the confidence limits in Fig. 10.3 is fairly constant as the load increases. The significance of the regression, which is a measure of the dependence of the slip on the cube strength, is initially not significant, Table 10.1, but increases as the load increases. The results of unloading, Fig. 10.4, show that most of the deflection is permanent, even at low loads. It would therefore appear that the scatter of the slip is caused by the failure of the concrete at the initial stages of loading and is independent of the compressive strength of the concrete. Probable causes could be the deterioration of the concrete due to the high stress concentrations which are developed by the weld collar, Sect. 6.4.1.5, bad compaction of the concrete around the weld collar, Sect. 6.4.1.3; and the position of the aggregate particles close to the weld collar, Sect. 6.4.1.3.

It may be more appropriate to assume that the stiffness of the shear connection is dependent upon the stiffness of the concrete. Since the relationship between the cube strength and the stiffness of the concrete used in these tests is known, Fig. 5.26, the slip can be written in terms of the stiffness of the concrete:

$$s_p/d_s = A+B(6.38E_c-137) \qquad (10.1)$$

where the coefficients A and B are given in Tables 10.1 and 10.2 for different values of P/P_{sh}, and E_c is measured in kN/mm^2. The stiffness of the concrete used in these tests ranged from 21 kN/mm^2 to 32 kN/mm^2.

The slip at failure can be assumed to be that when the strength has reduced to $0.95P_{sh}$, because in only approximately half of the specimens which had reached their maximum load could the slip be measured when the load had reached this value, Tables 10.1 and 10.2.

10.3 THE EFFECT OF SPLITTING

The change in the stiffness of the transversely reinforced slabs, Table 5.10, after they had split is shown in Fig. 10.5; none of the specimens had failed at the end of the experiment.

It would appear that the design rule for the reduction in the strength of the stud when the slab splits, Equ. 8.1, is very conservative because of the large variation in the distribution of the normal force, Fig. 6.15, which causes a gradual failure of the concrete and the ability of the stud to redistribute the loads as the concrete fails. Ideally the strength should be determined from the distribution of the slip along the beam. Alternatively it may be assumed that the studs within a portion of the slab which has split must be able to develop the same maximum slip as the studs in the other regions. This maximum slip varies from $0.40d_s$ to $0.31d_s$, $P/P_{sh} = 0.95$ in Fig. 10.2, and hence the strength reduces to $0.51P_{sh}$ to $0.64P_{sh}$; Fig. 10.5.

Table 10.1 Regression analysis of the load-slip curves of 19mm and 22mm stud shear connections.

P/P_{sh}	$\bar{s}_p/d_s$	A (10^{-2})	B (-10^{-4})	S	No.	S.D.
0.1	0.015	2.22	2.02	S_n	42	0.013
0.2	0.026	3.95	3.69	S_n	42	0.018
0.3	0.034	5.23	4.76	S_n	42	0.021
0.4	0.042	6.26	5.53	S_n	41	0.023
0.5	0.052	7.95	7.26	S_p	40	0.026
0.6	0.065	10.21	9.58	S_s	37	0.027
0.7	0.079	11.99	10.15	S_p	31	0.030
0.8	0.097	14.31	10.84	S_p	25	0.025
0.85	0.108	13.82	7.23	S_p	22	0.021
0.9	0.128	15.61	7.03	S_n	18	0.025
0.95	0.169	22.29	11.93	S_n	11	0.030
0.99	0.241	31.87	16.95	S_p	10	0.033
1.00	0.276	37.14	20.83	S_s	10	0.029
1.00	0.291	40.56	25.06	S_h	10	0.030
0.99	0.321	47.50	35.62	S_h	9	0.035
0.95	0.384	45.28	17.78	S_n	5	0.048

where $\bar{s}_p$ = mean slip

$s_p/d_s = A + Bf_{cu}$

f_{cu} is measured in N/mm^2

No. = number of experimental results

S.D. = Standard deviation

Table 10.2 Regression analysis of the load-slip curves of 13mm, 19mm and 22mm stud shear connections.

P/P_{sh}	$\bar{s}_p/d_p$	A (10^{-2})	B (-10^{-4})	S	No.	S.D.
0.1	0.013	1.26	-0.08	S_n	53	0.014
0.2	0.023	2.46	0.44	S_n	53	0.021
0.3	0.032	3.58	1.21	S_n	53	0.023
0.4	0.040	4.80	2.37	S_n	52	0.025
0.5	0.051	6.70	4.60	S_n	51	0.027
0.6	0.065	9.11	7.29	S_p	48	0.029
0.7	0.081	11.31	8.84	S_p	42	0.031
0.8	0.103	14.54	11.44	S_s	36	0.031
0.85	0.118	16.16	12.19	S_s	33	0.030
0.9	0.140	18.80	13.96	S_s	29	0.034
0.95	0.180	26.06	14.59	S_p	22	0.041
0.99	0.239	27.90	11.58	S_n	21	0.047
1.00	0.269	31.01	11.97	S_n	21	0.050
1.00	0.288	34.40	16.27	S_p	21	0.049
0.99	0.309	37.61	19.87	S_p	19	0.057
0.95	0.340	36.04	6.70	S_n	13	0.067

where $\bar{s}_p$ = mean slip

$s_p/d_s = A + Bf_{cu}$

f_{cu} is measured in N/mm^2

No. = number of experimental results

S.D. = Standard deviation

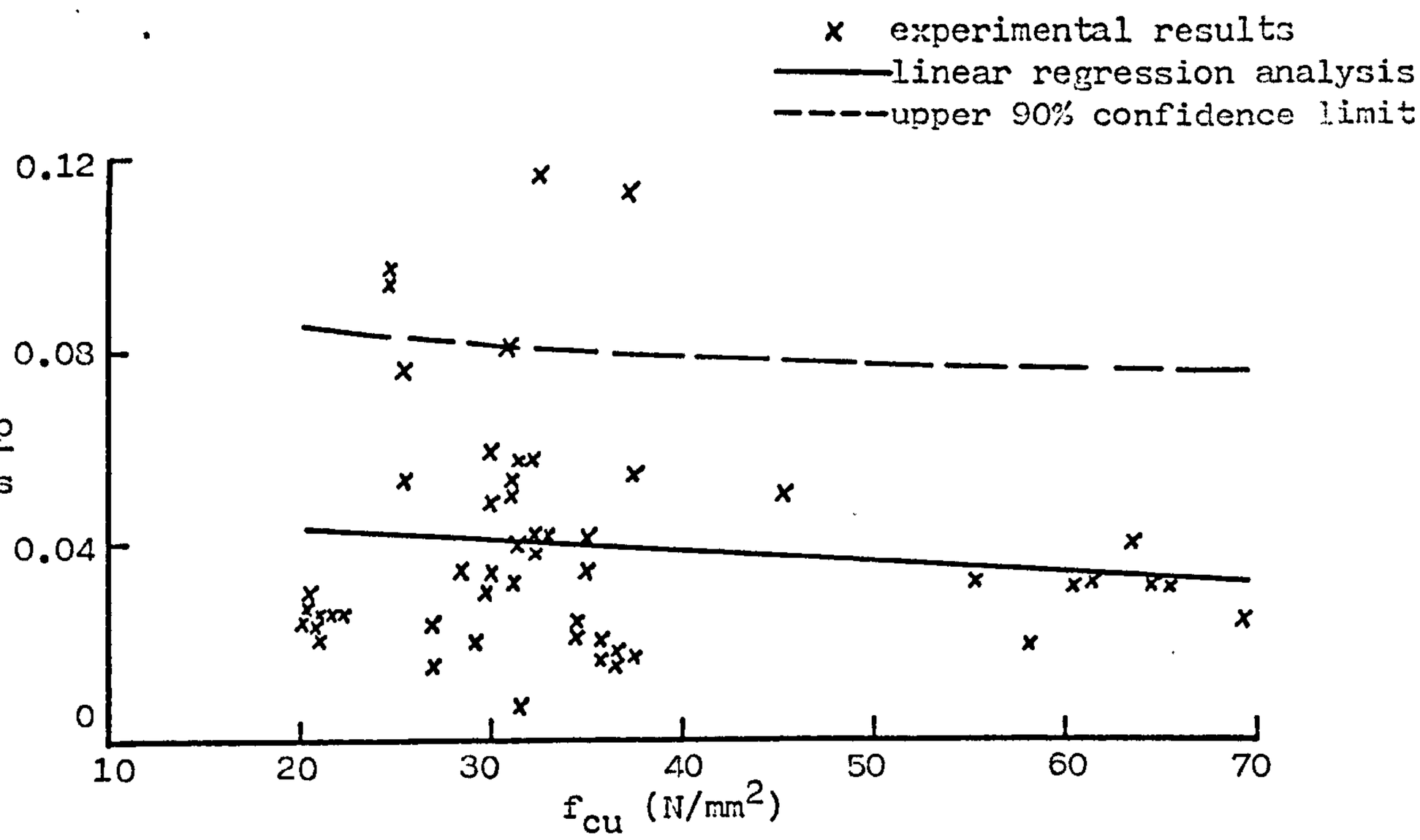

Fig. 10.1 Linear regression analysis of the slip at $P/P_{sh} = 0.4$.

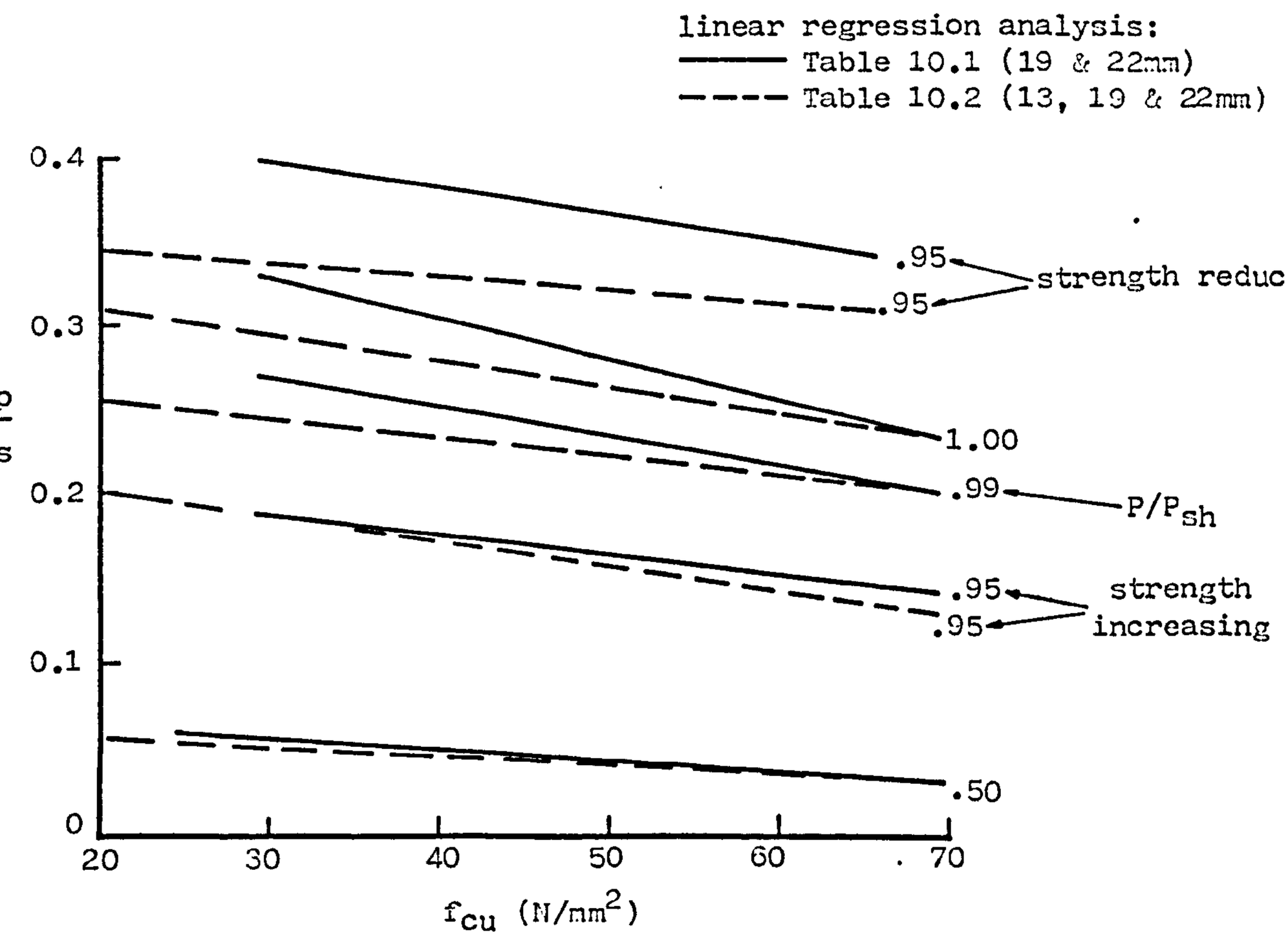

Fig. 10.2 Variation of the slip with the compressive strength of the concrete at different proportions of the shank failure load.

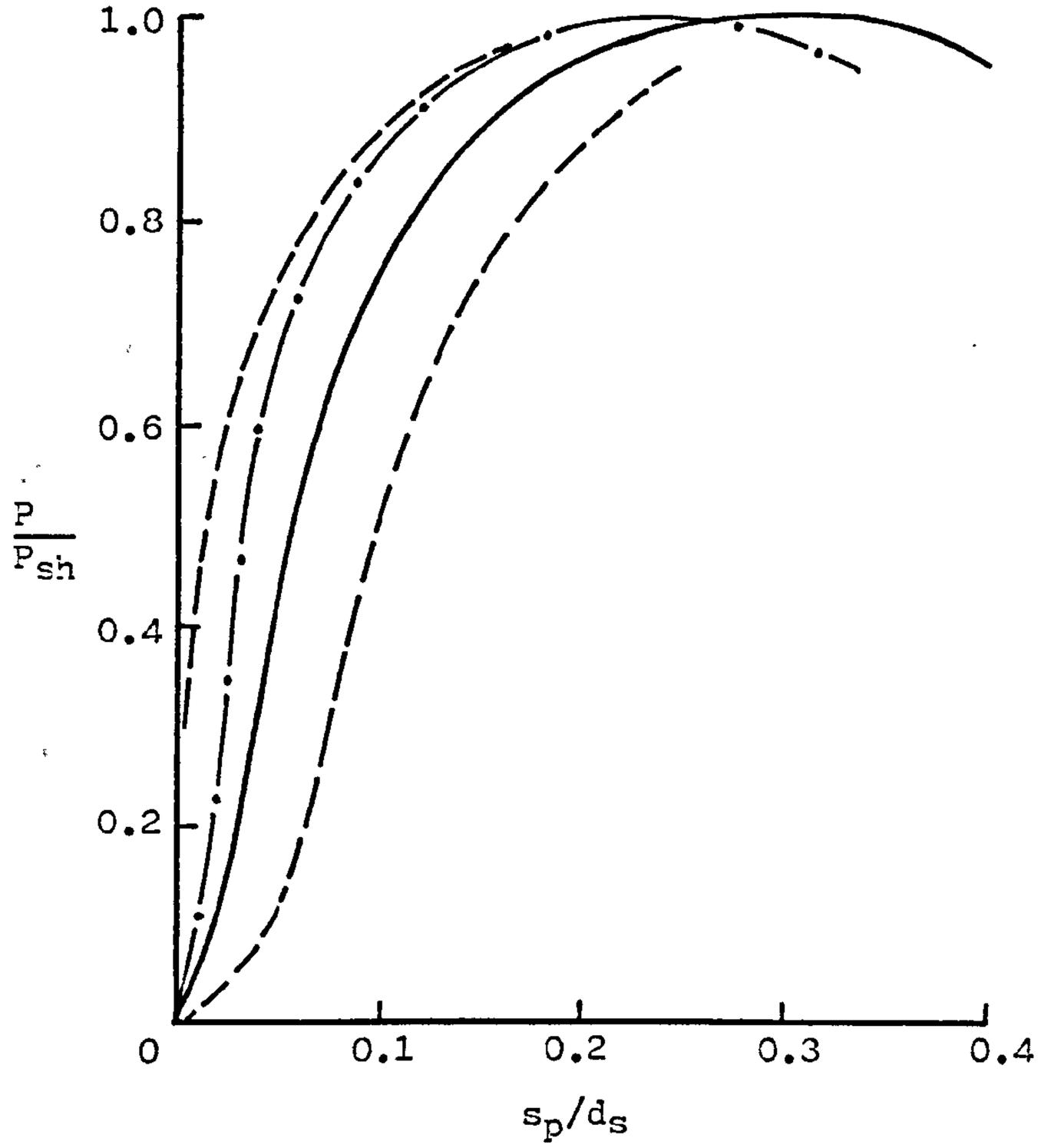

Table 10.1:
——— f_{cu} = 30 N/mm^2
– – – 90% confidence limits for f_{cu} = 30 N/mm^2
—·— f_{cu} = 65 N/mm^2

Fig. 10.3 Load-slip curves.

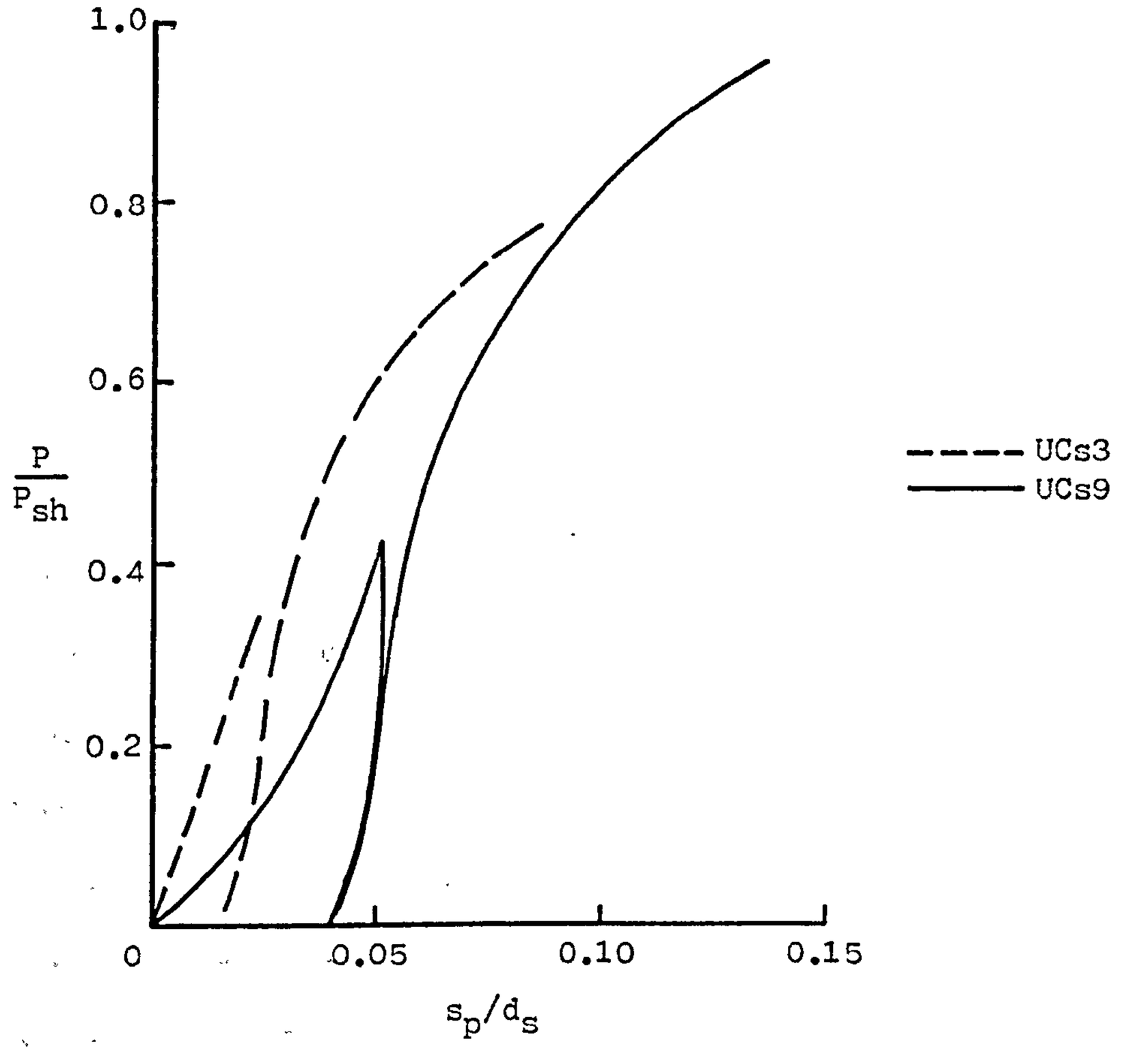

Fig. 10.4 Residual slip.

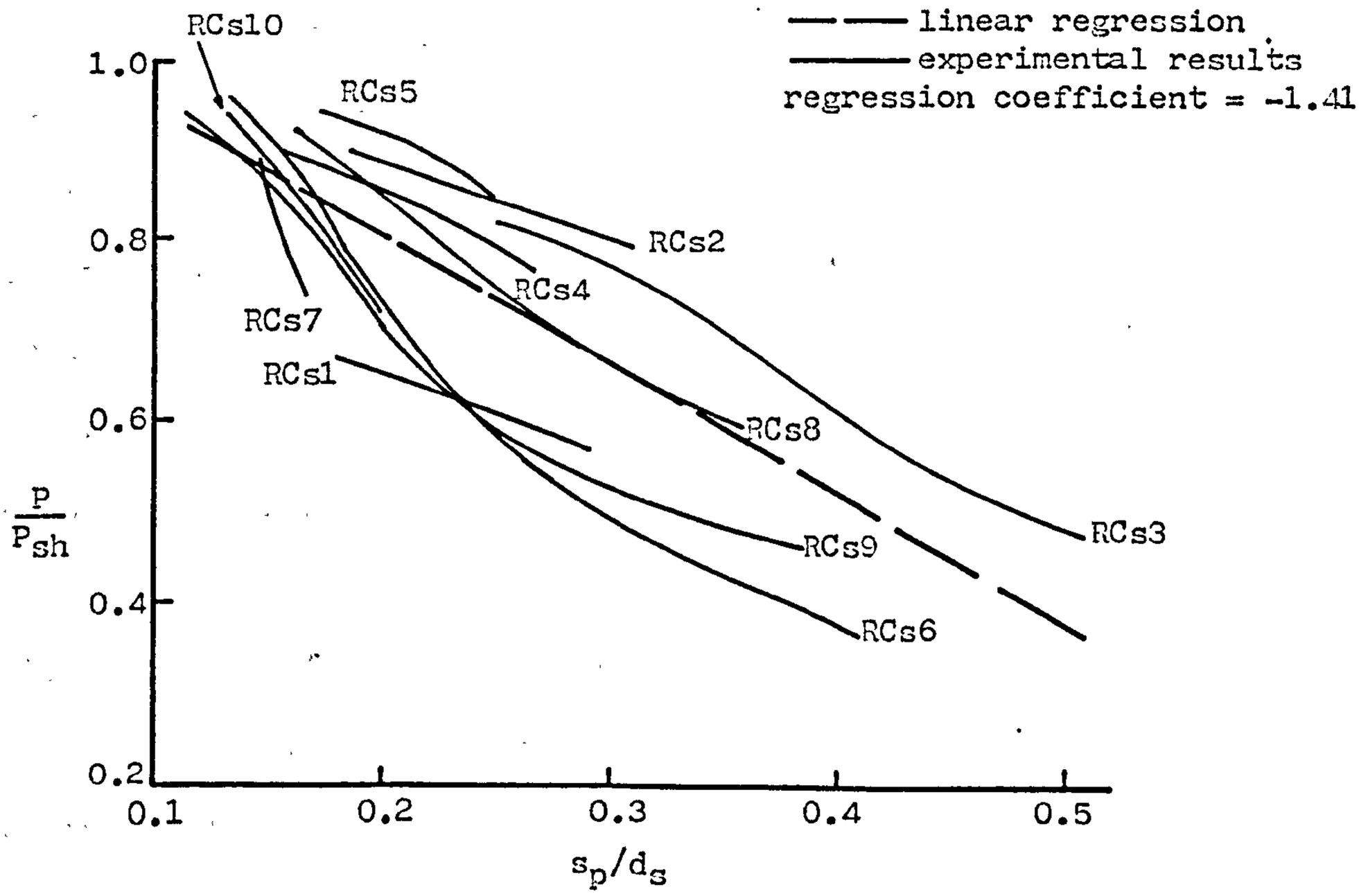

Fig. 10.5 Variation of the stiffness after splitting of reinforced slabs.

Chapter Eleven

CONCLUSIONS

11.1 INTRODUCTION

A method has been developed of determining the load-slip curves of stud shear connectors in T-beams, L-beams and haunched beams, where the number and position of the studs, amount and position of the transverse reinforcement, lateral moments and longitudinal shear flows are varied, when either the stud breaks or the slab splits. Another method has been developed of determining the strength of the shear connection in L-beams where the transverse reinforcement is looped around the stud. Both methods are applicable to concretes of all types.

11.2 LOAD-SLIP CURVES

The load-slip curve of a stud shear connection, Fig. 10.3, is dependent upon the load at which the stud breaks, the diameter of the stud, d_s, and the stiffness of the concrete, Equ. 10.1. The reduction in the strength of the shear connection after the slab has split is dependent upon the slip, Fig. 10.5; a conservative estimate would be to assume that the strength of the shear connection reduced to a half of the maximum strength of the stud at the theoretical maximum slip of the stud, Equ. 10.1.

11.3 THE MAXIMUM STRENGTH OF A STUD IN A BEAM

A stud fails when the principal stress at the weld-collar/shank interface or the weld-collar/flange interface reaches the ultimate tensile strength of the stud. The stresses in these zones is mainly caused by the 'normal force', Fig. 6.14, the distribution of which, Fig. 6.15, is dependent

upon the stiffness of the concrete, the stiffness of the stud and the height of the weld collar. The stiffness of the concrete is affected by voids, inclusions and the compressive failure of the concrete in front of the stud and the stiffness of the stud is dependent upon the height of the shank. The load at which a stud breaks is therefore dependent upon the area of the shank, the ultimate tensile strength of the stud, the stiffness and compressive strength of the concrete and the height of the stud, Equ. 6.2.

11.4 THE LOAD AT WHICH A BEAM SPLITS

When a stud applies a load to a concrete slab the dispersal of the force is balanced by the lateral tensile force in front of the stud, Fig. 7.5, which causes the slab to split when the stress reaches the split tensile strength of the concrete. The longitudinal force that the stud applies to the slab, Fig. 6.15, is not uniform because the stud is flexible and therefore the distribution of the lateral forces varies over the depth of the slab. However, it was found, Sect. 7.6.1, that an equivalent strip load, Fig. 4.17, of depth $1.87d_s$ gave the same splitting load as the stud. The splitting strength of composite slabs is therefore derived from the strength of concrete prisms of depth $1.87d_s$ which are subjected to strip loads.

When a single group of studs applies a load within a slab, Fig. 7.6, lateral tensile and compressive forces are developed in front of and behind the group; these extend a distance of $1.4b_c$ on either side of the group, where b_c is the width of the slab, and are of equal but opposite magnitude. The maximum lateral tensile stress is dependent upon the longitudinally applied force, the total width over which the studs are spaced and the width of the slab, Equ. 7.3.

When a slab supports concentrated loads, Fig. 7.35, the distribution of the lateral stresses between the groups of studs, Fig. 7.16, is composed of the superimposition of the lateral stresses developed by the individual groups, Fig. 7.6, and therefore varies along the beam.

In the region of the slab which is further than a longitudinal distance of $1.4b_c$ from the applied point loads the total lateral force between the groups, Fig. 7.16, is zero because the lateral forces which are developed by the individual groups of studs are unaffected by the change in the shear flow and therefore are uniformly distributed. The lateral tensile stresses are reduced by the superimposition of the lateral compressive forces and hence the strength of the slab increases as the spacing of the studs reduce, Fig. 7.18. The minimum strength is therefore the strength of the slab when subjected to a single group of studs, Equ. 7.3.

In the region of the slab within $1.4b_c$ from the applied point load the distribution of the lateral forces of the individual groups is not uniform and hence the mean lateral force between the groups is not zero. The maximum lateral stress, which occurs under the applied load, can be determined from the shear flow on either side of the applied load, Sect. 7.5.3.2. In longitudinal sagging regions of the beam the stress is tensile and therefore the splitting strength reduces as shown in Fig. 7.18. In hogging regions the stress is compressive.

Lateral forces which are not induced by the studs, such as occur when the slab is subjected to transverse moments, directly affect the stresses in the concrete and hence the splitting strength, Equ. 8.2. The additional lateral stiffness that transverse reinforcement provides reduces the lateral stresses in the concrete and hence increases the splitting strength, Equ. 8.2.

11.5 THE STRENGTH OF SHEAR CONNECTIONS IN WHICH THE REINFORCEMENT IS LOOPED AROUND THE STUD

It was found, Sect. 9.2, that the design rules for transverse reinforcement in the Bridge Code[7] are not directly applicable to shear connections in composite L-beams in which the reinforcement is looped around the stud.

The maximum strength of the shear connection is dependent upon six modes of failure. Compressive failure of the concrete in front of the stud, position A in Fig. 9.10, and along the bond of the reinforcement, position B, can be prevented by providing a minimum depth of reinforcement, Equs. 9.5 and 9.6. The splitting strength of the slab can be determined from Equs. 7.4 and 7.8. The strength of the connection after splitting is dependent upon the strength of the reinforcement and the shear strength of the slab, Figs. 9.21 and 9.22. The strength of the stud is dependent upon the level of the reinforcement, Fig. 9.17.

REFERENCES

1. Coble, G.G. 'Shear strength of thin flange composite specimens', Eng. J., Amer. Inst. Steel Constr., 5, 62-65, April 1968.

2. Ollgaard, J.G., Slutter, R.G. and Fisher, J.W. 'Shear strength of stud connectors in lightweight and normal-weight concrete'. Eng. J., Amer. Inst. Steel Construction, 8, 55-64, April 1971.

3. Slutter, R.G. and Driscoll, G.C. 'Test results and design recommendations for composite beams', Lehigh University, Fritz Engineering Laboratory, Report No. 279. 10, Jan. 1962.

4. Hughes, B.D. ' "Cyc-arc" stud welded concrete anchors', Civ. Eng. and Pub. Wks Review, 59, 723-7, June 1964.

5. Taylor, R., Plum, D.R. and Papasozomenos, A.G. 'Investigations on the use of deep haunches in composite construction', Proc. I.C.E., 47, 43-54, Sept. 1970.

6. Menzies, J.B. 'CP117 and shear connectors in steel-concrete composite beams made with normal-density and lightweight concrete', Struct. Engr., 49, 137-53, March 1971.

7. BS5400, Steel, Concrete and Composite Bridges:
Part 5: Design of composite bridges
British Standards Institution, London. Published in separate parts, 1978-80.

8. CP117, Composite Construction in Structural Steel and Concrete, Part 1: Simply-supported beams in building, British Standards Institution, 1965.

9. Davies, C. 'Small-scale push-out tests on welded stud shear connectors', Concrete, Sept. 1967.

10. Hainstone, R.J. and Menzies, J.B. 'Shear connectors in steel-concrete composite beams for bridges. 1: Static and fatigue tests on push-out specimens', Concrete, Sept. 1967.

11. Johnson, R.P., Greenwood, R.D. and Van Dalen, K. 'Stud shear-connectors in hogging moment regions of composite beams', Struct. Engr., 47, 345-350, Sept. 1969.

12. Teraszkiewicz, J.S. 'Static and Fatigue Behaviour of Simply Supported and Continuous Composite Beams of Steel and Concrete', Ph.D. thesis, University of London, Sept. 1967.

13. McMackin, P.J., Slutter, R.G. and Fisher, J.W., 'Combined tension and shear tests of headed concrete anchor studs', Fritz Eng. Lab. Report 200. 71. 438. 2, Lehigh University, USA, 1971.

14. Viest, I.M. 'Review of research on composite steel-concrete beams' Proc. Am. Soc. Civ. Eng., 1960, 2496 (ST6 June).

15. Davies, C., 'Steel-concrete composite beams with flexible connectors: a survey of research', Concrete, Dec. 1967.

16. Chapman, J.C., 'Composite construction in steel and concrete - The behaviour of composite beams', Structural Engineer, Vol. 42, No.4, April 1964, pp 115-125.

17. Iyengar, H.S., 'State-of-the-Art Report on Composite or mixed steel-concrete construction for buildings', American Society of Civil Engineers, 1977.

18. Johnson, R.P., 'Composite Structures of Steel and Concrete, Vol. 1', Crosby Lockwood Staples, 1975.

19. Johnson, R.P. and Buckby, R.J., 'Composite Structures of Steel and Concrete, Vol. 2, Crosby Lockwood Staples, 1979.

20. Council on Tall Buildings and Urban Habitat, 'Structural Design of Tall Steel Buildings, Vol.SB', Monograph on the Planning and Design of Tall Buildings, American Society of Civil Engineers, 1979.

21. CP110, The Structural Use of Concrete, British Standards Institution,1972.

22. Vries, W. de and Stark, J.W.B., 'Static strength of headed stud shear connectors, IBBC-TNO', Report BI-68-96, Rijswijk, The Netherlands.(A41).

23. Draft European Recommendations on Composite Beams, IABSE-CEB-FIP-CECM Joint Committee, Paris, Dec. 1976.

24. Gogoi, S., 'Interaction phenomena in composite beams and plates', Ph.D. thesis, University of London, 1964.

25. Van Dalen, K., 'Composite action at the supports of continuous beams', Ph.D. thesis, University of Cambridge, 1967.

26. Birkeland, P.W. and Birkeland, H.W., 'Connections in precast concrete construction', Journal of the American Concrete Institute, Vol. 63, No. 3, March 1966, pp 345-368.

27. Mast, R.F., 'Auxiliary Reinforcement in Concrete Connections', Proceedings, ASCE, Vol. 94, ST6, June 1968, pp 1485-1504.

28. Davies, C., 'Tests on half-scale steel-concrete composite beams with welded stud connectors', The Structural Engineer, Vol. 47, No. 1, Jan. 1969.

29. Hofbeck, J.A., Ibrahim, I.O. and Mattock, A.H., 'Shear Transfer in Reinforced Concrete', Journal of the American Concrete Institute, Feb. 1969.

30. Mattock, A.H. and Hawkins, N.M., 'Shear transfer in reinforced concrete - recent research', P.C.I. Journal, March-April 1972.

31. Johnson, R.P., 'Longitudinal shear in composite beams', University of Missouri-Columbia, Engineering experiment station bulletin series No. 67, Oct. 1969.

32. Johnson, R.P., 'Longitudinal shear strength of composite beams, ACI Journal, American Concrete Institute, Vol. 67, No. 6, pp 464-466. (A41)

33. Oehlers, D.J., 'Composite L-beams', unpublished report, University of Warwick, Department of Engineering, Nov. 1976.

34. Baldwin, J.W. and Sankar, C.D., 'Shear connections in haunched composite members', Missouri State Highway Department, University of Missouri-Columbia, Bureau of public works, Missouri cooperative highway research program, Report 68-1, 1968.

35. Chapman, J.C. and Balakrishnan, S., 'Experiments on Composite beams', The Structural Engineer, Vol. 42, No. 11, Nov. 1964, pp 369-83.

36. Fung, W. and King, J., 'The parameters affecting push-out tests on stud shear connectors', unpublished report, University of Warwick, Third year project, Department of Engineering, April 1977.

37. Dallam, N., 'Design of shear connectors in composite concrete steel bridges', University of Missouri, Report 67-7, 1967.

38. Buttrey, K.E., 'Behaviour of stud shear connectors in lightweight and normal-weight concrete, M.Sc. thesis, University of Missouri, Columbia, August 1965.

39. Hark, A.J., 'Continuous composite beams with headed-stud shear connectors', Philips Welding Reporter, No. 1967/1.

40. McGarraugh, J.B., University of Missouri, interim report, 1970.

41. Teraszkiewicz, J.S., 'Static tests on stud shear connectors in haunched slabs, Report LR223, Road Research Lab., Crowthorne, 1968.

42. Teraszkiewicz, J.S., 'Tests on stud shear connectors', Tech. Note 36, Road Research Lab., Crowthorne, Dec. 1965.

43. Davies, O.L., 'Statistical Methods in Research and Production', Oliver and Boyd, 1961.

44. Barnard, P.R., 'Research into the complete stress-strain curve for concrete', Magazine of concrete research. Vol. 16, No. 49, Dec. 1964, pp 203-210.

45. Price, W.H., 'Factors influencing concrete strength', Journal of the American Concrete Institute, A.C.I. Proceedings, Vol. 47, pp 417-432, Feb. 1951.

46. Anson, M. and Newman, K., 'The effect of mix proportions and method of testing on Poisson's ratio for mortars and concretes', Magazine of concrete research, Vol. 18, No. 56, Sept. 1966, pp 115-130.

47. Liw, T.C.Y., 'Stress strain response and fracture of concrete in uniaxial and biaxial compression', J.A.C.I., Vol. 69, pp 291-295, May 1972.

48. Hannant, D.J., 'Nomograms for the failure of plain concrete subjected to short-term multi-axial stresses', The Structural Engineer, May 1974, No. 5, Vol. 52.

49. Baker, A.L.L., 'A criterion of concrete failure', Proc. I.C.E., Vol. 45, pp 269-278, Feb. 1970.

50. Hobbs, D.W., Pomeroy, C.D., Newman, J.B., 'Design stresses for concrete structures subject to multi-axial stresses', The journal of the Institution of Structural Engineers, April 1977, Vol. 55, No. 4.

51. Arnaouti, C., 'Research into Composite Bridge Decks in Biaxial Tension', Progress report No. 6, Engineering Department, University of Warwick, July 1976.

52. Zienkiewicz, O.C., 'The Finite Element Method in Engineering Science', McGraw-Hill, 1971.

53. Desayi, P. and Krishnan, S., 'Equation for the Stress-Strain Curve of Concrete, Journal of the American Concrete Institute, Vol. 61, pp 345-50, March 1964.

54. Balmer, G.G., Jones, V. and McHenry, D., 'Shearing strength of concrete under high triaxial stress-computation of Mohr's envelope as a curve', United States Department of the Interior, Bureau of Reclamation, Structural Research Laboratory Report No. SP23, Research and Geology Division, Oct. 28, 1949.

55. Neville, A.M., 'Properties of Concrete', 2nd edition, Pitman Publishing. 1972.

56. Timoshenko, S., 'Strength of Materials, Part 1, Elementary Theory and Problems', D.Van Nostrand Company, Inc., Third edition, April 1955.

57. BS1881, Methods of testing concrete. Part 4: Methods of testing concrete for strength. Part 5: Methods of testing hardened concrete for other than strength. British Standards Institution, London. 1970.

58. Miyogi, S.K., 'Bearing Strength of Concrete - Geometric Variations', J. Struct. Div. Am. Soc. Civ. Engrs., Vol. 99, No. ST7, July 1973, pp 1471-1490.

59. Williams, A., 'The bearing capacity of concrete loaded over a limited area', Cement and Concrete Association, Technical Report 526, Aug. 1979.

60. BS812, Methods of sampling and testing of Mineral aggregates, sands and fillers. British Standards Institution, London, 1967.

61. BS18, Methods for tensile testing of metals. British Standards Institution, London. 1962.

62. Burkhardt, P., Unpublished report, University of Warwick, Department of Engineering, 1978.

63. Fung, W. and King, J., 'The Parameters Affecting Push-Out Tests on Stud Shear Connectors, University of Warwick, Department of Engineering, Third year project, April 1977.

64. Adekola, A.O., 'Interaction between steel beams and concrete floor slabs'. London University, Ph.D. Thesis, 1959.

65. Barnard, P.R., 'On the collapse of composite beams', University of Cambridge, Ph.D. Thesis, 1963.

66. Leonhardt, F., 'Prestressed concrete, design and construction', 2nd edition, Wilhelm Ernst and sohn, Berlin-Munich. 1964.

67. Plum, D.R., 'Strength of studs in composite construction', Proc. I.C.E., 51, 319-335, Feb. 1972.

68. Wheen, R.J. and Rogers, D.F., 'Anchorage zone design. Part 1 - Bearing strength of plain concrete', University of Sydney, School of Civil Engineering, Report No. R296, Oct. 1976.

69. Guyon, Y., 'Limit-state design of prestressed concrete, Vol. 2. The design of the member', Applied Science Publishers Ltd., 1974.